Doctoral Dissertation
Doctoral Program in Energy Engineering (29th Cycle)

Development of manganese oxide films for the electro-oxidation of phenol at high temperature and pressure

By
Andrea Massa

Supervisors:
Prof. Fino Debora, Supervisor
Prof. Russo Nunzio, Co-Supervisor

Doctoral Examination Committee:
Prof. Fatone Francesco, Università Politecnica delle Marche
Prof. Bolzonella David, Università di Verona
Prof. Donsì Francesco, Università di Salerno
Prof. Pugliese Massimo, Università di Torino
Prof. Pirone Raffaele, Politecnico di Torino
Prof. Ruggeri Bernardo, Politecnico di Torino
Prof. Fino Debora, Politecnico di Torino
Prof. Russo Nunzio, Politecnico di Torino

Politecnico di Torino
2016

Declaration

I hereby declare that, the contents and organization of this dissertation constitute my own original work and does not compromise in any way the rights of third parties, including those relating to the security of personal data.

Andrea Massa
2016

* This dissertation is presented in partial fulfillment of the requirements for **Ph.D. degree** in the Graduate School of Politecnico di Torino (ScuDo).

A Giuliana, per essere sempre stata
al mio fianco in questi anni e per rendermi
ogni giorno una persona migliore.

INDEX

ABSTRACT

This thesis is divided into three main parts.

In the first part, the concept of an MJ-PEM reactor will be introduced, and its design and calculations will be explained. An MJ-PEM reactor is the result of the coupling of a Multi-Junction Solar Cell (MJSC) and a Polymer Electrolyte Membrane (PEM) electrolyzer, able to work at high temperatures and pressures (up to 150°C and 30 bar). Two scenarios for the application of this system were investigated: in the first one, the anodic chamber is used for the oxidation of recalcitrant organics contained in wastewater, while the cathodic compartment is used for the evolution of H_2, for storage or direct use on site; in the second one, the H_2 produced at the cathode is sent to an anaerobic digestion process, to boost the biomethanation step, whereas at the anode O_2 is evolved and it is exploited for the digestate stabilization and disinfection. Both the scenarios proved to be feasible and effective, due to a high degree of integration between stoichiometric and thermal requirements of different systems, allowing to carry out both waste or wastewater treatment on one side, and hydrogen or natural gas production on the other side.

The second part of this work concerns the synthesis and the characterization of electrodes based on manganese oxides, for the electro-oxidation of recalcitrant organics. Phenol was chosen as target molecule, due to its high refractoriness and stability, and its wide presence in industrial plants. Manganese oxides are extensively used in electrochemistry, and they were chosen because of their low cost, high abundance, and low toxicity. Different types of manganese oxides (MnO_x) were synthesized by electrodeposition on two substrates, namely metallic titanium and titania nanotubes (TiO_2-NTs). X-Ray Diffraction (XRD) and X-Ray Photoelectron Spectroscopy (XPS) were used to analyze the oxidation states of manganese, whereas Field Emission Scanning Electronic Microscopy (FESEM) was employed to investigate the morphology of the samples and the penetration of manganese oxides inside the NTs. The electrochemical properties of the electrodes have been investigated by cyclic voltammetry (CV) and linear sweep voltammetry (LSV), showing that both calcination and electrodeposition over TiO_2-NTs gave more stable electrodes, exhibiting a marked increase in the current density. The activity of the proposed nanostructured samples towards phenol degradation has been investigated. Tetravalent manganese (α-MnO_2) resulted to be the most active phase, with a phenol conversion of 42.7%. Trivalent manganese (α-Mn_2O_3), instead, reported the highest stability, with an average working potential of 2.9 V vs. RHE, and the highest tendency for oxygen evolution reaction, reaching 0.4 mA/cm^2 at 2.5 V vs. RHE. TiO_2-NTs interlayer contributed in all cases to the decrease in the final potential reached after the reaction time of about 1 – 1.5 V, due to the improved contact with the catalyst film and the prevention of passivation of the titanium substrate.

In the third part, the most performing electrodes were selected from the ones synthesized in the second part. They were tested in High Temperature, High Pressure

(HTHP) reactor, designed in Politecnico di Torino for kinetic studies on electro-degradation of refractory organics in wastewaters, under Catalytic Wet Air Oxidation (CWAO) conditions, i.e. 150°C and 30 bar. The most stable (α-Mn_2O_3) and the most active (α-MnO_2) manganese oxides were compared, both at ambient and CWAO operative conditions, with some of the most effective electrodes used in this field: Sb-doped SnO_2 and RuO_2. Results showed that manganese oxides, especially α-Mn_2O_3, is more than tripled at 150°C and 30 bar, reaching values of phenol oxidation close to the ones of Sb-SnO_2 and RuO_2. This phenomenon can be attributed to the higher tendency of manganese in its Mn^{3+} form to oxidize water to O_2, that is wasted at ambient conditions, while is better employed at high temperatures (high kinetics, low overpotentials) and high pressures (improved O_2 solubility).

INTRODUCTION

Water is one of the most important resources for humanity, not only because it is essential for life, but also for agriculture, breeding and hygiene [1]. In the last decades, issues about the ethical and aware use of water have been raised from all over the world. World population is rapidly increasing, and modernity requires a crescent need for water for the domestic, agriculture and industrial fields. Water resources are progressively exploited up to their limits, thus leading to tensions, conflicts among users and nations, and excessive stress on the environment. One of the major problems concerns the extensive use of water per capita in developed countries, where water withdrawal per year tends to be dozens of times higher than the water consumption in developing countries and almost a hundred times higher than in developing countries [2].

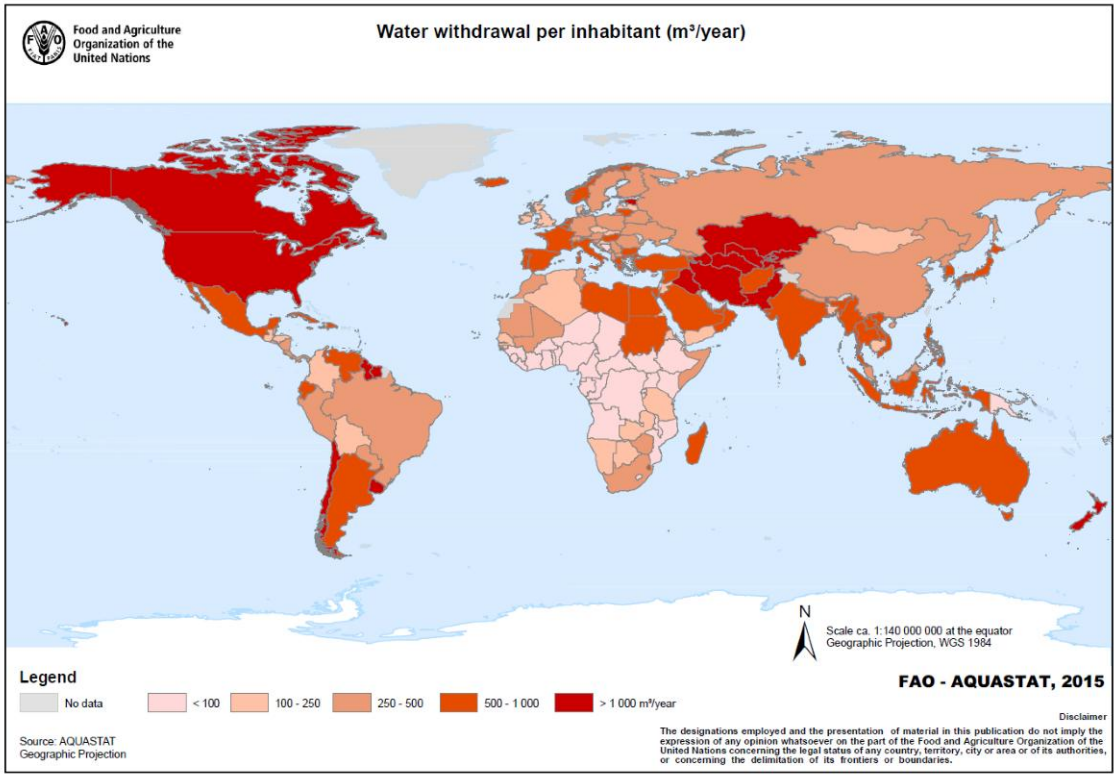

Fig. 1 – Annual water withdrawal per capita for each country

Water demand has been increasing more than twice the population in the last decades, and, even though there is no such global water lack, a high number of areas are chronically short of water resources. By 2025, 1 800 million people will be living in countries or regions with absolute water scarcity, and two-thirds of the world population could be under stress conditions [3].

According to the Millennium Development Goals Report 2012, around 800 million people, (i.e. 11% of world population), face economic water shortage or cannot access to available drinking water sources. These sources include household connections, public standpipes, boreholes, protected dug wells, protected springs and rainwater collections.

Water scarcity is an issue of poverty, and there is growing recognition that there are strong linkages between these two elements.

For poor people, lack of water is not only a matter of drought. First of all, it concerns the fair and safe access to water resources that are necessary for their sustainment. For indigent people, scarcity is due to lack of transparency and equity in decisions taken by organizations. It is due to choices about infrastructure management and development. In many places throughout the world, organizations struggle to distribute resources equitably.

Agricultural use of water for irrigation, livestock, fisheries and aquaculture is estimated as the cause of 71% of total water withdrawal, with a higher tendency for low and middle-income countries, while it is estimated that 15% of worldwide water use is for industrial purposes, especially for high-income countries [4].

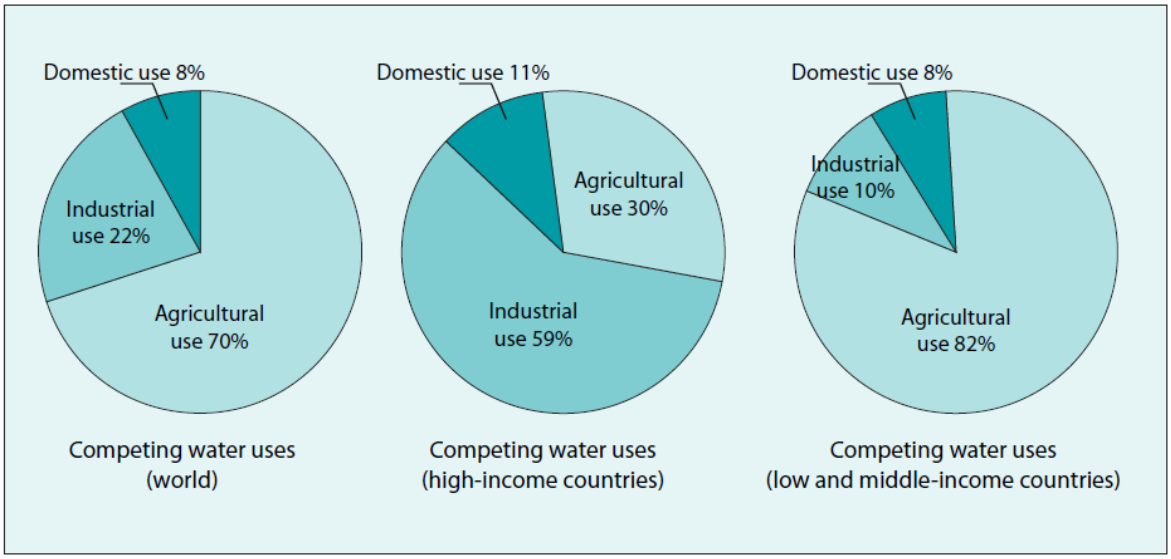

Fig. 2 – Competing for water uses according to their main sources of income

There has been a considerable reflection on environmental ethics throughout the world, and modern debates are focusing on moral imperatives, but, rather than analyzing once more the ethical issues of water management, best ethical practices should be promoted, and in particular [4]:

Human dignity: there is no life without water, people to whom it is denied are denied lives;

Participation: all people, especially the poor ones, must be involved in water management with gender and poverty issues recognized in promoting this trend;

Solidarity: upstream and downstream interdependence within a watershed continually poses challenges for water management resulting in the need for an integrated water development approach;
Human equality: all the people should be provided with the basic necessities of life on an equitable basis;
Common Good: water is a common good, and without proper water management human potential and dignity diminishes;
Stewardship: protection and careful use of water resources is needed for intergenerational and intra-generational equity and promotes the sustainable use of life-enabling ecosystems;
Transparency and universal access to information: if data is not accessible in a form that can be understood, an opportunity will arise for a party to disadvantage others;
Inclusiveness: water management policies must be addressed to the interests of all people living in a water catchment area. Minority interests must be protected, together with poor and other disadvantaged sectors.
Empowerment: the demand for participation in planning implies much more than an opportunity for consultation. Best ethical practice must be implemented to improve management.

One of the most demanding challenges for scientists and technicians is to find technologies that are more and more effective, implementable and affordable to both provide drinking water from depuration of freshwater resources and to recycle water coming from civil, agricultural and industrial use.

CHAPTER 1

WASTEWATER TREATMENT TECHNOLOGY

1.1 Introduction

The biological wastewater treatment is one of the most common processes in the world for the degradation of a large variety of compounds.

Aerobic process

An aerobic biological, or activated sludge system generally consists of the following phases (see Fig. 3):

- **Primary sedimentation / Equalization:** a primary clarifier is required to remove large solids and other undesirable substances. It is also fundamental for the equalization of the influent sent to digestion, in order to avoid large and sudden fluctuation of flow and pollutant concentration. Microorganisms, in fact, are very susceptible both to hydraulic and organic load peaks.
- **Aeration:** in this step, aerobic bacteria, also called biomass or activated sludge digest the incoming waste. They use air or oxygen fed through either air diffusers placed at the bottom of the aeration tank or incorporated by turbine mixers.
- **Settling:** after the digestion, a secondary clarifier is needed for the settling of the undigested solids and biomass. This process forms a waste sludge which must be periodically removed from the system.

Depending on the Hydraulic Retention Time (HRT) and the sludge age, three types of process can be identified:

- **high-rate** systems: with an HRT of 2-4 h and a sludge age of 1-2 days, where organic pollutants are simply fixed on the biomass and they are not fully oxidized. Volumes are small and biomass concentration is low.

– **conventional** systems: with an HRT of 5-8 h and a sludge age of 4-10 days, in which organic compounds are largely degraded in the aeration tank, but excess sludge requires additional stabilization (e.g. by anaerobic treatment). Conventional aeration systems are the most largely used for industrial and municipal wastewater treatment.

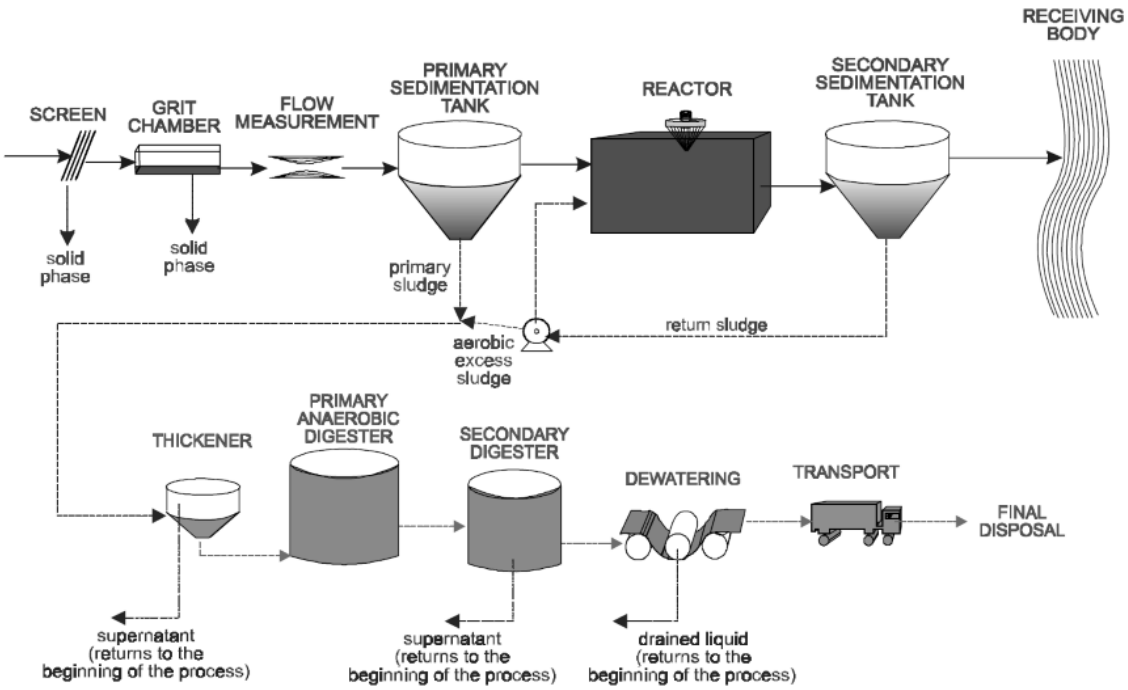

Fig. 3 – Typical flowsheet of a conventional activated sludge process

– **extended aeration** systems: with an HRT of 16-24 h and a sludge age of 14-28 days, where organic matter is completely mineralized, and the biomass is stabilized directly inside the aeration tank. Aerobic stabilization of sludge, also called endogenous respiration, requires additional oxygen, which can be significantly higher than for organic degradation (exogenous respiration). Volumes are high and biomass concentration is low.

A particular type of aerobic digester is the **Sequencing Batch Reactor (SBR)**, which houses all the main stages of a traditional activated sludge process in a single tank, thus resulting in a very compact design.
The sequence is composed of five phases:

1) *Filling*: influent raw or settled wastewater
2) *Reacting*: aeration of the liquid inside the tank
3) *Settling*: separation of the suspended solids after treatment
4) *Decanting*: withdrawal of the treated wastewater
5) *Idle*: removal of excess sludge and preparation for new cycle

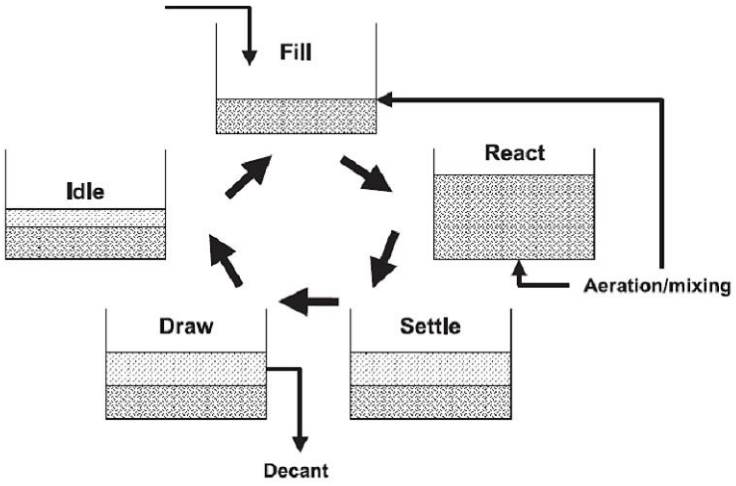

Fig. 4 - Steps of a Sequencing Batch Reactor (SBR) aerobic system

Anaerobic process

Anaerobic microbiological decomposition is a process in which microorganisms derive energy and grow by metabolizing organic material in an oxygen-free environment resulting in the production of methane (CH_4). The anaerobic digestion process can be subdivided into the following four phases (see Fig. 5), each requiring its own characteristic group of micro-organisms [5]:

- **Hydrolysis**: conversion of non-soluble biopolymers to soluble organic compounds
- **Acidogenesis**: conversion of soluble organic compounds to volatile fatty acids (VFA) and CO_2
- **Acetogenesis**: conversion of volatile fatty acids to acetate and H_2
- **Methanogenesis**: conversion of acetate and CO_2 plus H_2 to methane gas

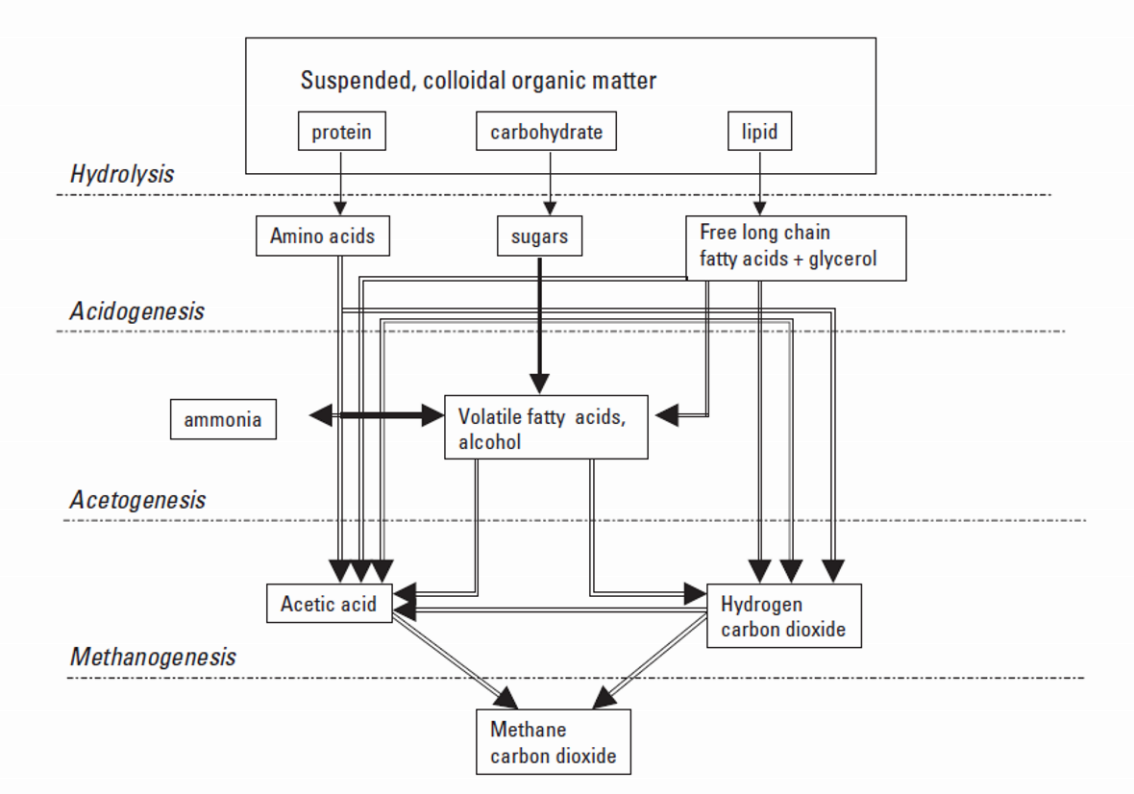

Fig. 5 – Simplified schematic representation of the anaerobic degradation process

As anaerobic digestion is a biological process, it is strongly influenced by environmental factors. Temperature, pH and alkalinity and toxicity are primary control factors.

Controlled digestion is divided in psychrophilic (10-20 ºC), mesophilic (20-40 ºC), or thermophilic (50-60 ºC) digestion [6]. As bacterial growth and conversion processes are slower under low-temperature conditions, psychrophilic digestion requires a long retention time, resulting in large reactor volumes. Mesophilic digestion requires less reactor volume. Thermophilic digestion is especially suited when the waste(water) is discharged at a high temperature or when pathogen removal is an important issue. During thermophilic treatment, high loading rates can be applied. Anaerobic digestion can occur at temperatures as low as 0°C, but the rate of methane production increases with increasing temperature until a relative maximum is reached at 35 to 37° C. At this temperature range mesophilic organisms are involved. The relation between energy requirement and biogas yield will further determine the choice of temperature. At higher temperatures, thermophilic bacteria replace mesophilic bacteria and a maximum methanogenic activity occurs at about 55°C or higher. The first steps of anaerobic digestion can occur at a wide range of pH values, while methanogenesis only proceeds when the pH is neutral. For pH values outside the range 6.5 - 7.5, the rate of methane production is lower. A sufficient amount of hydrogen carbonate (frequently denoted as bicarbonate alkalinity) in the solution is important to maintain the optimal pH range required for methanogenesis.

Advantages of anaerobic treatment are numerous and can be summarized as follows [5, 7]:

- provision of energy source through methane recovery;
- anaerobic treatment processes generally consume little energy. At ambient temperature the energy requirements are in the range 0.05-0.1 kWh/m^3 (0.18-0.36 MJ/m^3), depending on the need for pumping and recycling effluent;
- reduction of solids to be handled; excess sludge production on the basis of biodegradable COD in anaerobic treatment is significantly lower compared to aerobic processes;
- modern anaerobic treatment processes can handle very high loads, exceeding values of 30 g COD/l/day at ca. 30 °C and up to 50 g COD/l/day at ca. 40 °C for medium strength mainly soluble wastewater;
- the construction costs are relatively low;
- the space requirements of anaerobic treatment are lower than conventional systems.

Advanced Oxidation Processes (AOPs)

Whenever the type of wastewater does not meet the requirements for a biological treatment process, especially when it contains refractory organics, a different kind of approach must be employed to effectively degrade the pollutants. A lot of researchers have been addressed to this aim in the last decade pointing out the prominent role of a special class of oxidation techniques defined as advanced oxidation processes (AOPs) which usually operate at or near ambient temperature and pressure [8]. Advanced oxidation processes although making use of different reacting systems, are all characterized by the same chemical feature: production of OH· radicals. OH· radicals are extraordinarily reactive species, they attack the most part of organic molecules with rate constants usually in the order of 10^6–10^9 M^{-1} s^{-1} [9]. They are also characterized by a little selectivity of attack which is a useful attribute for an oxidant used in wastewater treatments. The versatility of AOP is also enhanced by the fact that they offer different possible ways for OH· radicals production thus allowing a better compliance with the specific treatment requirements [10].

Among the most important AOPs for the production of OH· radicals, it is worth citing:

Fenton process [11]:

$$Fe^{2+} + H_2O_2 \rightarrow Fe^{3+} + OH^- + \boldsymbol{OH}\cdot \qquad \text{Eq. 1}$$

Photo-Fenton process [12]:

$$Fe^{3+} + OH^- \overset{h\nu}{\rightarrow} Fe(OH)^{2+} \qquad \text{Eq. 2}$$

$$Fe(OH)^{2+} + H_2O_2 \overset{h\nu}{\rightarrow} Fe^{2+} + 3\boldsymbol{OH}\cdot \qquad \text{Eq. 3}$$

Photocatalytic process [13]:

$$iO_2 \xrightarrow{hv} e^- + h^+ \quad \text{Eq. 4}$$

$$TiO_2\,(h^+) + H_2O_{ad} \rightarrow TiO_2 + H^+ + \boldsymbol{OH_{ad}}\cdot \quad \text{Eq. 5}$$

Ozonation [14]:

$$OH^- + O_3 \rightarrow O_2 + HO_2^- \quad \text{Eq. 6}$$

$$HO_2^- + O_3 \rightarrow HO_2\cdot + O_3^-\cdot \quad \text{Eq. 7}$$

$$O_2^-\cdot + O_3 \rightarrow O_2 + O_3^-\cdot \quad \text{Eq. 8}$$

$$O_3^-\cdot + H^+ \rightarrow HO_3\cdot \quad \text{Eq. 9}$$

$$HO_3\cdot \rightarrow O_2 + \boldsymbol{OH}\cdot \quad \text{Eq. 10}$$

Another aspect concerning the opportunity of AOP application is that referring to the polluting load of wastes normally expressed as COD. Only wastes with relatively small COD contents (5.0 g/l) can be suitably treated by means of these techniques since higher COD contents would require the consumption of too large amounts of expensive reactants. Wastes with more massive pollutants contents can be more conveniently treated by means of wet oxidation or incineration. Wet oxidation makes use of oxygen or air to achieve pollutant oxidation at high temperatures (130–300°C) and pressure (0.5–20 Mpa) [9].

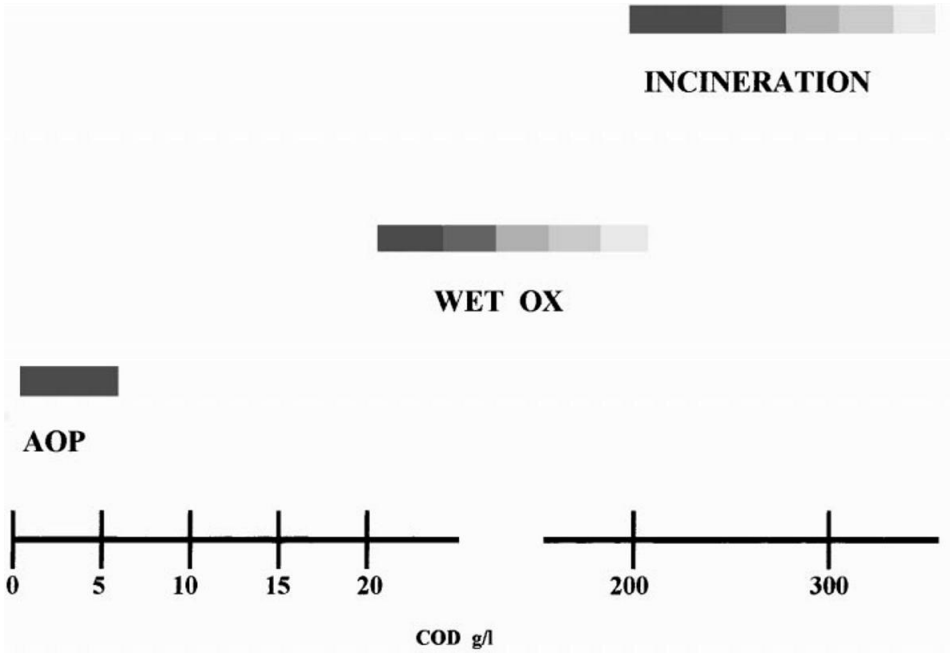

Fig. 6 - Suitability of water treatment technologies according to COD contents

1.2 Catalytic Wet Air Oxidation (CWAO)

There are many variants for the wet oxidation processes, among which the most important and widely spread are the Wet Air Oxidation (WAO) and the Catalytic Wet Air Oxidation (CWAO). As suggested by their names, they are advanced oxidation process which involves the use of either air or pure oxygen to degrade pollutants, especially recalcitrant organics, contained in aqueous solutions.

Wet Air Oxidation (WAO)

WAO is proper to a high organic loading at high flow rate and can partially cover the application range of incineration and biological methods. Especially, WAO has a great potential for the treatment of effluent containing a high content of organic matter (about 10–100 g/L of COD) and/or toxic contaminants for which direct biological treatment is not feasible. By using WAO, the organic pollutants are either partially oxidized into biodegradable intermediates or mineralized to carbon dioxide, water, and innocuous end products under elevated temperatures (125–320°C) and pressures (0.5–20 MPa) using a gaseous source of oxygen (either pure oxygen or air) as the oxidant [15].

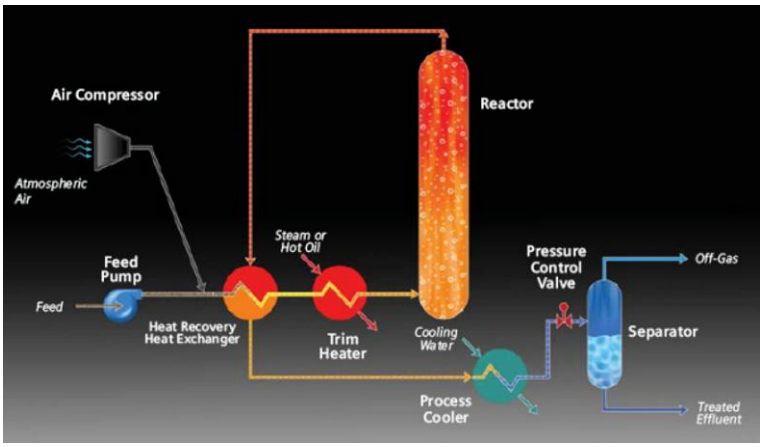

Fig. 7 - Typical Wet Air Oxidation flowsheet

The definite mechanisms and reaction pathways for WAO have not been established even for a pure compound because the oxidation of organic compounds goes through very complicated routes and leads to the formation of various intermediates. Generally, the final intermediates are short-chain organic acids such as acetic acid, etc. The identification of intermediates and by-products formed during oxidation is essential to evaluate the toxicity and to point out possible refractory compounds. Most of the studies have reported that the chemical reaction of WAO chiefly proceeds via free radical reactions. Several free radical reactions consisting of initiation, propagation, and termination of free radical have been proposed to take place during the WAO of various organic compounds.

Most of the studies on reaction pathway for WAO have employed phenol as a model compound because it is considered to be an intermediate in the oxidation of higher molecular weight aromatic compounds. Phenol oxidation follows an extremely complex pathway composed of parallel and consecutive reactions. Some authors proposed the mechanism for non-catalytic oxidation of phenol in which phenol is firstly oxidized to dihydroxybenzenes, i.e. hydroquinone and catechol, which are converted into benzoquinones. Rings of benzoquinones are then opened with the formation of appropriate acids which are further oxidized to short-chain carboxylic acids.

Catalytic Wet Air Oxidation (CWAO)

The main difference between simple WAO and CWAO is obviously the employment of a catalyst to reduce the operating temperatures and pressures, thus limiting the severity of reaction conditions but also more easily decomposing even refractory pollutants, thereby reducing capital and operational costs [16]. Though it varies with the type of wastewater, the operating cost of CWAO is about half that of non-catalytic WAO due to milder operating conditions and shorter residence time. Although the homogeneous catalysts, e.g. dissolved copper salts, are effective, an additional separation step is required to remove or recover the metal ions from the treated effluent due to their toxicity, and accordingly, increases operational costs. Thus, the development of active heterogeneous catalysts has received a great attention because a separation step is not necessary. Various solid catalysts including noble metals, metal oxides, and mixed oxides have been widely studied for the CWAO of aqueous pollutants.

The performances of various solid catalysts including noble metals such as Ru, Rh, Pd, Ir, and Pt as well as oxides of Cr, Mn, Fe, Co, Ni, Cu, Zn, Mo, and Ce for the CWAO of aqueous pollutants have been demonstrated in the last decade. Noble metals have been extensively utilized in the CWAO of model compounds as well as real wastewaters due to their excellent catalytic activities. Although noble metals show a high resistance to dissolution, they are still vulnerable to poisons including polymeric product formed during CWAO.

Among the base metal oxide catalysts, copper oxide catalysts exhibit a high activity for the CWAO of organic compounds, especially phenol. However, they are vulnerable to metal leaching under hot acidic conditions caused by acidic intermediates, i.e. short-chain carboxylic acids. Mixed metal oxides such as CeO_2-ZrO_2, CeO_2-TiO_2, $CuCeO_x$, and $MnCeO_x$ are more promising for the CWAO of organic pollutants in terms of catalytic activity and resistance to metal leaching.

Some metal oxides such as γ-Al_2O_3, TiO_2, CeO_2, etc. have been mainly used as supporting materials. Among them, ceria-based materials are one of the most promising supports due to their redox and morphological properties promoting the production of active radicals or direct redox reaction.

During the CWAO of organic compounds, heterogeneous catalysts are deactivated mainly by carbonaceous deposits and metal leaching. Coke deposition on the catalyst surface quickly deactivates the catalysts by blocking the active sites.

Generally, the complete oxidation of organic pollutants to carbon dioxide and water is hard to achieve due to the formation of more refractory intermediates like short-chain carboxylic acids. CWAO integrated with the biological process can be more attractive for the treatment of industrial wastewater containing toxic pollutants because short-chain carboxylic acids, especially acetic acid, are readily biodegradable due to their low ecotoxicity.

Further studies are necessary to develop more active and stable catalysts which can be effectively utilized on an industrial scale. It is desired to make a thorough investigation on reaction mechanisms and kinetics which provides important information for industrial applications.

1.3 Electrochemical technologies in water treatment

With the ever increasing quantity of drinking water demand and the strict environmental limits regarding the wastewater treatment, electrochemical processes have regained a primary role over the last decades. There are companies supplying facilities for metal recoveries, for treating drinking water or process water, treating various wastewaters resulting from the tannery, electroplating, dairy, textile.

Electrochemical purification systems are important as part of a more general process for the management of pollution, the cleaner processing, and the process efficiencies. Electrochemical approach to wastewater treatment concerns:

- The avoidance of polluting reagents in materials synthesis, such as zinc powder for organic reductions, by the use of direct electron transfer;
- The monitoring of pollutant concentrations through the process, in liquid effluents and gaseous emissions;
- The treatment of aqueous effluents by electrochemically generated species, such as chloride ions or hydroxyl radicals, both of which are powerful oxidizing compounds;
- The removal of environmental pollutants, such as organics and metal ions from industrial or agricultural activities;
- The transformation of chemicals to electrochemical energy, for instance by fuel cells.

Continued developments in understanding and documentation of the electrodes and membranes and electrochemical reactor design with enhanced industrial experience are resulting in a widespread availability of electrochemical processes and their characteristics.

Main advantages of electrochemical technologies:

- Electrons are clean reagents
- Transfer rate of the electron can be effectively controlled
- Reaction conditions can be easily measured
- The process can be activated/deactivated by switching the current on / off
- In some circumstances, temperature and pressure can be tuned to improve the process

Limitations and drawbacks:

- Large-scale plants are less common than traditional wastewater treatment technologies
- The cost of some components, such as electrodes, can limit the scale-up to industrial applications
- There are few electrochemical engineers for the development of this technology
- Main problems are connected to chemical reactions, corrosion, and adsorption, which can decrease performance and durability.

Particular focus was given to electrodeposition, electro-coagulation (El-C), electro-flotation (El-F) and electro-oxidation (El-Ox). Electro-coagulation is effective in recovering metals from wastewater. It is currently more applied for either iron, aluminum or the hybrid Al/Fe electrodes. The process of separation of the flocculated sludge from the treated water can be carried out by using electro-flotation. This technology is highly performing not only for the removal of colloidal particles, grease, and oil but also for the organic compounds. Usually, it is more effective than dissolved air flotation, sedimentation, impeller flotation. The newly developed active and stable electrodes for oxygen evolution at the anodes would boost the implementation of this technology. Electro-oxidation (El-Ox) is more and more applied in the field of wastewater treatment, especially in combination with other technologies. It is particularly promising in the degradation of recalcitrant pollutants on the surface of a few electrodes. Many types of the anode are used for this purpose: Titanium-based electrodes are the most commonly used, such as antimony-doped tin oxide, ruthenium oxide, boron-doped diamond film electrodes, which all show high activity and prove good stability.

1.3.1 Electrochemical recovery of metals

The electrochemical metal recovery has been employed in the field of electrometallurgy for a long time. One of the first examples of electrometallurgy in Europe was dated in the 17th century. It concerned the recovery of copper from cupriferous mine by means of electrochemical procedures. During the last decades, electrochemical applications have grown into many areas, such as chemical synthesis, metal production, surface treatment, and energy storage.

The electrochemical reaction for the recovery of metals in aqueous solution is very simple. It can be compared to a cathodic deposition of a metal ion in its zero-valence form:

$$Mn^{+} + ne^{-} \rightarrow M \qquad \text{Eq. 11}$$

There are many types of reactor for metal recovery, from very simple reactors such as tank cells, plate and frame, rotating cells, to more sophisticated 3-D reactors like fluidized bed, packed bed, or porous carbon packing cells.

Tank cells are one of the simplest and hence the most popular designs. The main application of this system is the metal recovery from highly concentrated streams, for processes such as electroplating baths, and ion-exchange systems.

The plate and frame cell, also called filter press, is one of the most applied devices. It efficiently houses anode, cathode, and membrane in only one module.

The rotating cathode cell was designed and employed to meet the requirements for improved mass transfer from the bulk of the solution to the surface of the electrode. It also has the advantage to remove the deposited material for higher efficiencies.

1.3.2 Electro-coagulation (El-C)

This process concerns the evolution of coagulants in situ by the electrical dissolution of aluminum or iron ions from their respective electrodes of metallic aluminum or iron. The generation of metal ions, which is an oxidation process, takes place in the anodic chamber, whereas hydrogen is formed at the cathode. Also, hydrogen can contribute the flocculated particles to float out of the wastewater. The Al^{3+} or Fe^{2+} ions are very performing coagulants for particulates flocculating. In general, iron is used for wastewater treatment, while aluminum is often employed for water treatment. The main advantages of electro-coagulation are high particulate removal efficiency, compact treatment plant, relatively low cost and feasibility of complete automation.

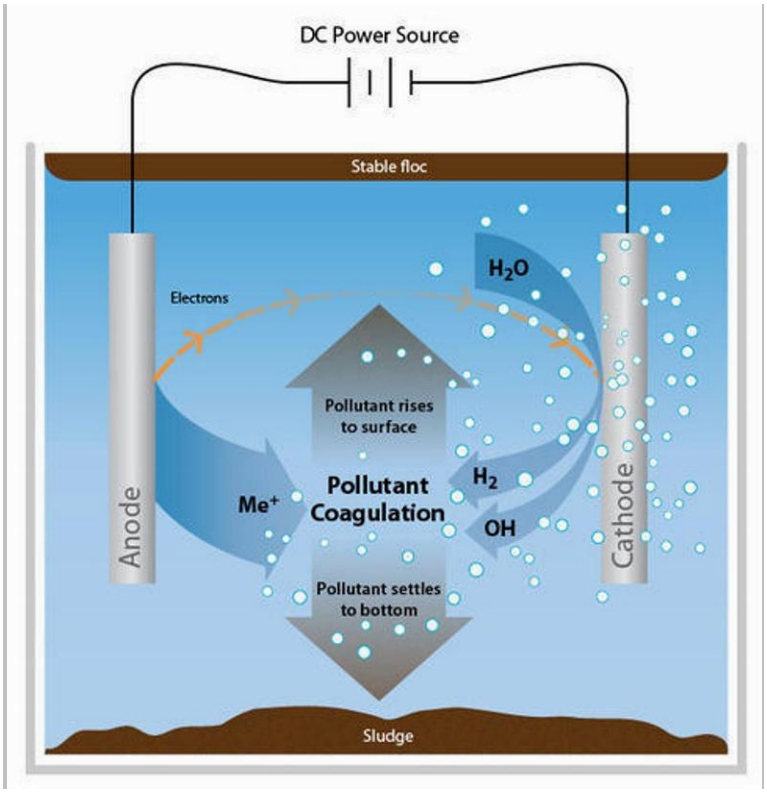

Fig. 8 - Principle of operation of the electro-coagulation system

There are many factors affecting El-C.

Current density determines the rate of Al^{3+} or Fe^{2+} released from the respective electrodes. The higher the current, the smaller the reactor.

The addition of chloride ions can significantly reduce the precipitation of Ca^{2+} or Mg^{2+} ions which are present in form of carbonates and sulfates. Indeed, they can form a passivating layer on the surface of the electrodes, thus increasing the cell voltage and reducing the current efficiency. It is therefore suggested to add a solution containing 20% Cl^-, which could also lower the power consumption, due to the increase in conductivity. Furthermore, the electro-generated chlorine is highly effective for water disinfection.

pH can affect El-C in a large number of ways: if chlorine ions are added to the wastewater, then Cl_2 evolution is influenced; aluminum and iron hydroxides tend to precipitate at basic pH; pollutants removal is usually better performed under neutral conditions, but conductivity is decreased at pH=7. Thus, a well-balanced analysis must be taken into account before application of this method.

1.3.3 Electro-flotation (El-F)

Electro-flotation process consists in the rising of pollutants to the surface of a liquid by the electro-generated bubbles of hydrogen and oxygen from water splitting.

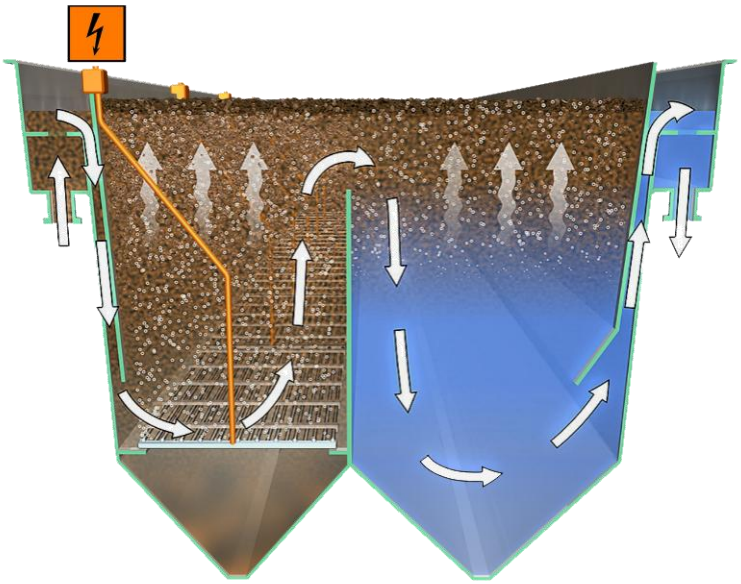

Fig. 9 - Example of an electro-flotation system

The size of the bubbles is mainly depending on the pH of the solution, as well as on the electrode material. The optimal pH for hydrogen bubbles is the neutral pH, for which they are smaller. Oxygen bubbles, instead, increase their size with pH.

The size of the bubbles depends also on the current density. The higher the current, the lower the bubbles size, at least until the value of 200 mA/cm^2. For higher values of current density, gas bubbles are little influenced by this parameter, and they are stable from 20 to 40 μm [17].

1.3.4 Electro-oxidation (El-Ox)

Hazardous effluents are continuously produced by industrial processes in huge amounts. Conventional wastewater treatments, such as biological systems, are the most widely used for this purpose. In some cases, also adsorption, ozonation, ultrafiltration, and UV disinfection are used, especially as the final step for water purification. However, these processes are not able to remove some types of compounds, in particular, recalcitrant organics.

That is why electrochemical methods for wastewater purification have gained increased attention in recent years. Electro-oxidation (El-Ox) has been employed effectively to abate different organic compounds and treat both municipal and industrial wastewaters.

El-Ox can occur according to two different processes: *indirect* and *direct*.

Indirect process

The indirect process occurs by the mediation of compounds added to the wastewater, such as chlorides. For this type of process, chlorine and hypochlorite electro-generated at the cathode to destroy pollutants. This system is very effective over a number of organic and inorganic compounds at high chloride concentration. The main drawback is the formation of chlorinated substances either in the intermediates or final products, thus limiting its application. Furthermore, salts must be added to increase the process efficiency if the chloride amount in the raw wastewater is insufficient. Pollutants can also be oxidized by the electro-generated hydrogen peroxide. Ferrous salts can be added to the wastewater or even generated in-situ from a dissolving iron electrode to carry out an electro-Fenton reaction.

Direct process

Electro-oxidation of pollutants can also be carried out directly on the surface of the anodes by either physically adsorbed or chemisorbed “active oxygen”. This process is usually called direct oxidation. The physically adsorbed “active oxygen” reacts with the organic compounds (R) to carry out their complete combustion, while the chemisorbed “active oxygen” participates in the formation of selective oxidation products. In general, hydroxyl radicals are more effective than oxygen for pollutant oxidation. Since O_2 evolution can also occur at the anode, high oxygen evolution overpotentials are required to obtain good current efficiencies. Otherwise, part of the current applied to the cell will be used for water splitting, thus lowering the overall efficiency.

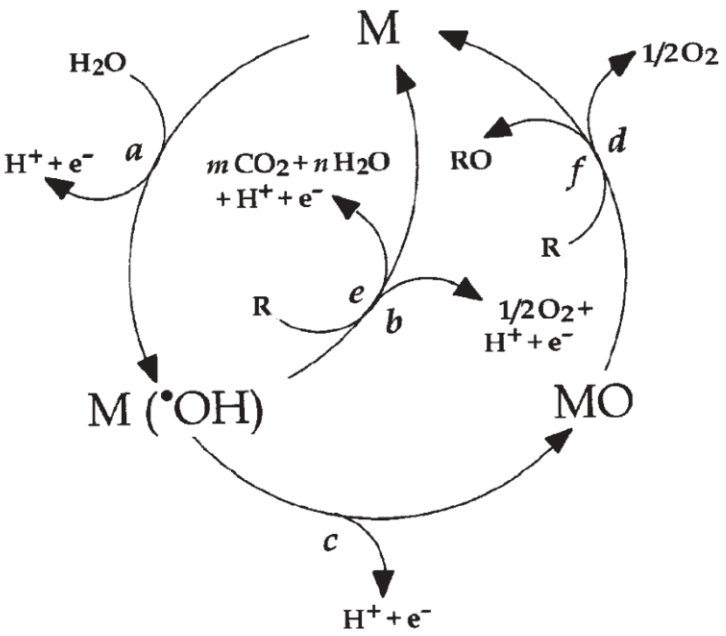

Fig. 10 - Anodic oxidation of organics with O_2 evolution on non-active anodes (*a, b,* and *e*) and on active anodes (*a, c, d,* and *f*)

Based on Fig. 10, the differences between the two limiting cases (i.e. *active* and *non-active anodes*) are reported. For both electrodes, the first reaction (Eq. 12) is water oxidation, to form adsorbed hydroxyl radicals (OH·):

$$M + H_2O \rightarrow M(HO\cdot) + H^+ + e^- \qquad \text{Eq. 12}$$

The electrochemical reactivity of adsorbed hydroxyl radicals depends on the nature of the electrode material employed in the process.

Active electrodes

With active electrodes, the interaction between the electrode (M) and the hydroxyl radical (OH·) is relatively strong. Adsorbed OH· may interact with the electrode, forming a so-called higher oxide MO (Eq. 13). This pathway may happen when higher oxidation states are available, for the anodic material, above the oxygen evolution potential (1.23 V vs. RHE).

$$M(HO\cdot) \rightarrow MO + H^+ + e^- \qquad \text{Eq. 13}$$

With active electrodes, the redox couple MO/M acts as a mediator in the oxidation of organics (Eq. 14). The latter reaction competes with the side reaction of molecular oxygen formation, which is caused by the chemical decomposition of the higher oxide (Eq. 15):

$$MO + R \rightarrow M + RO \qquad \text{Eq. 14}$$

$$MO \rightarrow M + \frac{1}{2}O_2 \qquad \text{Eq. 15}$$

The oxidative reaction of organics via the surface redox couple MO/M (Eq. 14) may be much more selective than the reaction involving hydroxyl radicals (Eq. 16). An example of an active anode is the case of IrO_2, which has a low oxygen evolution overpotential.

Non-active electrodes

With a non-active electrode, weak interactions exist between OH· and the anode surface. In this case, the oxidation of organics is mediated by hydroxyl radicals (Eq. 16) and may result in completely mineralized products (CO_2 and H_2O).

$$M(HO\cdot) + R \rightarrow M + mCO_2 + nH_2O + H^+ + e^- \qquad \text{Eq. 16}$$

In the above schematic equation, R is a fraction of an organic compound containing no heteroatoms, which needs one oxygen atom to be fully transformed into CO_2. This reaction competes with the side reaction of hydroxyl radicals (direct or indirect consumption, through the formation of hydrogen peroxide as intermediate) to oxygen (7) without any participation of the anode surface:

$$M(HO\cdot) \rightarrow M + \tfrac{1}{2}O_2 + H^+ + e^- \qquad \text{Eq. 17}$$

A non-active electrode does not participate in the anodic reaction and does not provide any catalytic active site for the adsorption of reactants and/or products from the aqueous medium. In this case, the anode serves only as an inert substrate, which can act as a sink for the removal of electrons. In principle, only outer-sphere reactions and water oxidation are possible with this kind of anode. Intermediates produced by the water oxidation are subsequently involved in the oxidation of organics in an aqueous medium. The electrochemical activity (which may be related to the overpotential for oxygen evolution) and chemical reactivity (rate of the organics oxidation with electrogenerated hydroxyl radicals) of adsorbed OH· are strongly linked to the strength of the M–OH· interaction. As a general rule, the weaker the interaction, the higher the anode reactivity for organics oxidation (fast chemical reaction); boron-doped diamond electrodes (BDD) are typical non-active electrodes, characterized by high stability and acceptable conductivity.

Photo-electrochemical process [18]

Photo-electrochemical wastewater treatment deals with the removal of water pollutants which are resistant to biodegradation. The photocatalytic method offers a large number of advantages for the removal of organics from wastewater, such as the total mineralization, the use of low-cost catalysts and the relatively easy arrangement. The first report on photo-electrochemical wastewater treatment using anodes made of TiO_2 for disinfection was reported in 1985. The working principle of photocatalysis is based on "in-situ" generation of OH· radicals, which can convert a large spectrum of recalcitrant organics into less toxic compounds, and eventually to CO_2 and H_2O. Several authors have summarized the steps of photocatalysis reaction. The semiconductor oxide (e.g. TiO2) under irradiation with light having energy higher than that of the band-gap (hv), a pair of conduction band electron (e−) and valence band hole (h+) is generated (Eq. 18). After this primary event, the charge carriers either recombine with the bulk of the material or migrate to the particle surface. Some authors suggested that, two different mechanisms may take place simultaneously either they get transferred to the adsorbed pollutant causing immediate oxidation (Mechanism 1, Eq. 19), or they are first transferred to adsorbed water molecules generating hydroxyl radicals, OH• , upon which reaction with the pollutant produce the respective oxidation products (Mechanism 2, Eq. 20).

$$Photocatalyst \xrightarrow{uv} e^- + h^+ \qquad \text{Eq. 18}$$

$$h^+ + pollutant \rightarrow {}^{\cdot}pollutant^+ \qquad \text{Eq. 19}$$

$$h^+ + OH \rightarrow OH\cdot \qquad \text{Eq. 20}$$

Mechanism 1 represents direct oxidation or direct photocatalysis, while mechanism 2 shows indirect oxidation or indirect photocatalysis. In the opinion of authors, mechanism 1 is associated with the systems which adsorb pollutants strongly at the photocatalyst surface with firm electronic contact, while mechanism 2 is dominant in systems with weak pollutant adsorption. According to principle, mechanism 2 can be as fast as mechanism 1, or it will be slower, but it is highly improbable to be faster. The electron-hole pair also initiates oxidation and reduction processes of adsorbed substrates. In aqueous solutions, the holes are scavenged by surface hydroxyl groups to generate strong oxidizing hydroxyl radicals (OH·), which can promote the oxidation and eventual mineralization of organic compounds. All studies related to photocatalysis show that the presence of molecular oxygen and water is essential during the photo-mineralization process. The trapping of charge carriers by O_2 and H_2O serves to suppress the electron-hole combination, thereby increasing the competitiveness of the light-induced redox processes.

Fig. 11 shows an example of photoelectrochemical degradation process of organic compounds on a TiO_2 electrode, and the mechanism behind the reaction.

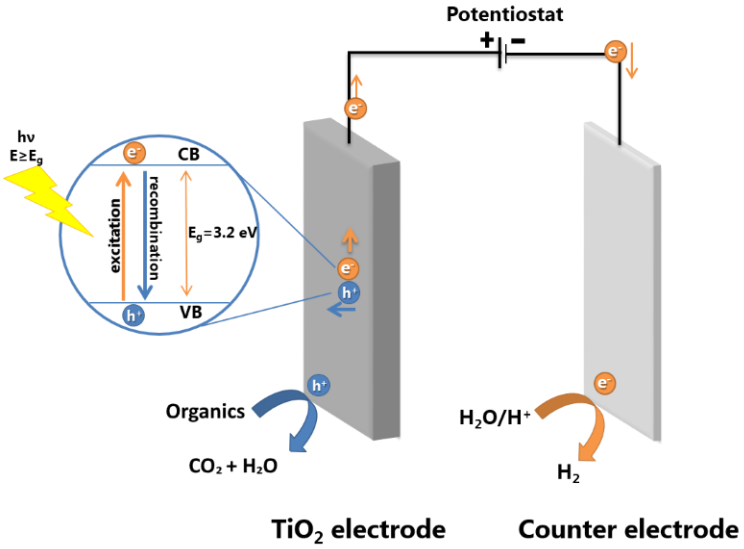

Fig. 11 – Photoelectrochemical oxidation of organics on a TiO_2 electrode

Basic principles of photocatalysis, as well as the details of rate of degradation and effect of other factors controlling the photo-oxidation, have been described in several research papers and review articles. This versatile approach for removal of a broad range of chemical pollutants in waste streams has recently become an area of wide research, particularly over the past decade.

CHAPTER 2

SOLAR POWER CONVERSION

2.1 Introduction

Due to the will to find attractive alternatives to fossil fuels, research is moving towards different types of renewable sources, as wind and solar. The latter, in particular, seems to be one of the most promising, due to the immense potential energy that the Sun provides daily to the Earth, which is normally wasted. One of the main issues that technology has to face is the improvement of the use of this source of energy.

Sunlight can be converted into electricity by exciting electrons in a solar cell. It can yield chemical fuel via natural photosynthesis in green plants or artificial photosynthesis in human-engineered systems. Concentrated or unconcentrated sunlight can produce heat for direct use or further conversion to electricity [19].

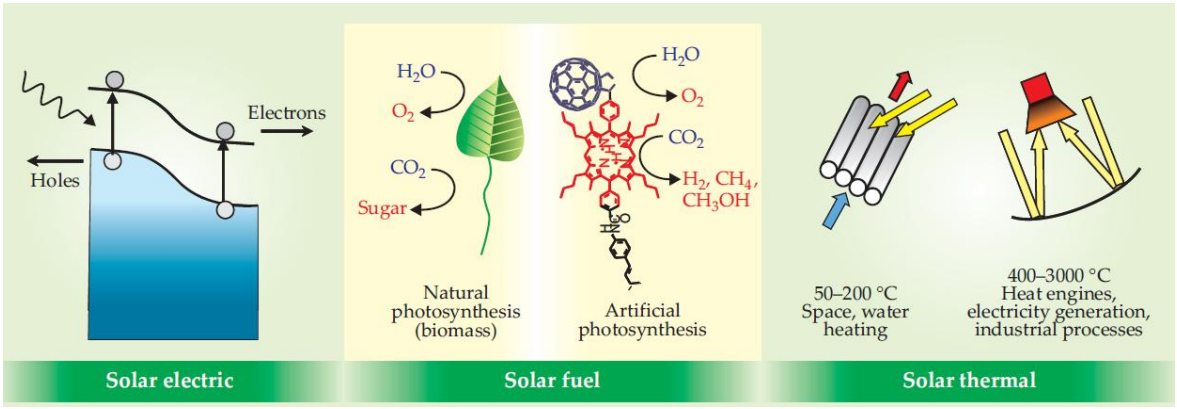

Fig. 12 – Solar conversion into three forms: electric, fuel and heat

Efficiency conversion of solar power are still low, and the costs of solar technology are very high, limiting the application of these systems. The need for better conversion technologies is a driving force behind many recent developments in biology, materials, and especially nanoscience. The gap between the energy potentially provided by the Sun and human applications is due to cost and conversion capacity. Fossil fuels meet our energy requirements in a much cheaper way than the solar source, as fossil-fuel resources are

concentrated, whereas the Sun spreads its photons uniformly over the Earth at a more modest energy density, which is more difficult to collect.

Solar energy is considered as a clean source, renewable, unlimited and equally distributed all over the planet, with some limitations towards extreme latitudes. Fossil-fuels, instead, are limited and unevenly distributed. The most important issue concerning fossil fuels, however, is related to the emissions of combustion products during the combustion process. Ideally, the combustion of any fuel should lead only to carbon dioxide (CO_2) and water. Unfortunately, this is not true, because many by-products are formed, due to the presence of molecules such as sulfur or nitrogen, which can lead to the formation of sulfur oxides (SO_x) and nitrogen oxides (NO_x). Moreover, incomplete combustion due to lack of oxygen during the combustion can form carbon monoxide (CO). Other pollutants that are worth mentioning are the uncombusted, i.e. fuel molecules which did not react. All these products are dangerous to human health and/or to the environment. N_2O, CO_2, and methane (CH_4) are powerful greenhouse gases, while carbon monoxide, benzene, and particulate matter are harmful environmental pollutants, and sulfur oxides are involved in the phenomenon of the acidic rains. In contrast, solar photons can overcome all these side effects of fossil fuels; solar power magnitude, wide availability, versatility, and beneficial effect on the environment and climate make it an appealing energy source for the future.

2.2 Solar to electricity

Presently, the world energy consumption is 10 terawatts (TW) per year, and by 2050, it is projected to be about 30 TW. The world will need about 20 TW of non-CO_2 energy to stabilize CO_2 in the atmosphere by mid-century. The simplest scenario to stabilize CO_2 by mid-century is one in which photovoltaics (PV) and other renewables are used for electricity, fuels for transportation, and heat for residential and industrial consumption. Thus, PV will play a significant role in meeting the world future energy demand [20].

A photovoltaic system can be arranged in two main ways: stand-alone and grid-connected.

Stand-alone systems

A stand-alone power system (SAPS), is an off-the-grid electricity system for locations that are not fitted with an electricity distribution system. Electricity is generated by solar panels and energy is usually stored in a battery system, but other solutions exist including fuel cells. Power drawn directly from the battery will be direct current extra low voltage (DC), and this is used especially for lighting as well as for DC appliances. An inverter is used to generate AC low voltage, which more typical appliances can be used with [21].

Stand-alone photovoltaic power systems are independent of the utility grid and may be:

- direct-coupled to the load without any electrical energy storage device, where the system is directly linked to a DC load, thus it is capable of powering such loads only during daytime. Another drawback of this system is the strict matching between power created by the solar device and the power required by the loads;
- provided with a battery pack, so that when electrical energy produced by the panels cannot immediately be used, it can be stored in an accumulator. In this way, the system is less subjected to energy fluctuation and load requirements. Energy acquired by the batteries can be then used when solar power is not available (e.g. during nighttime)

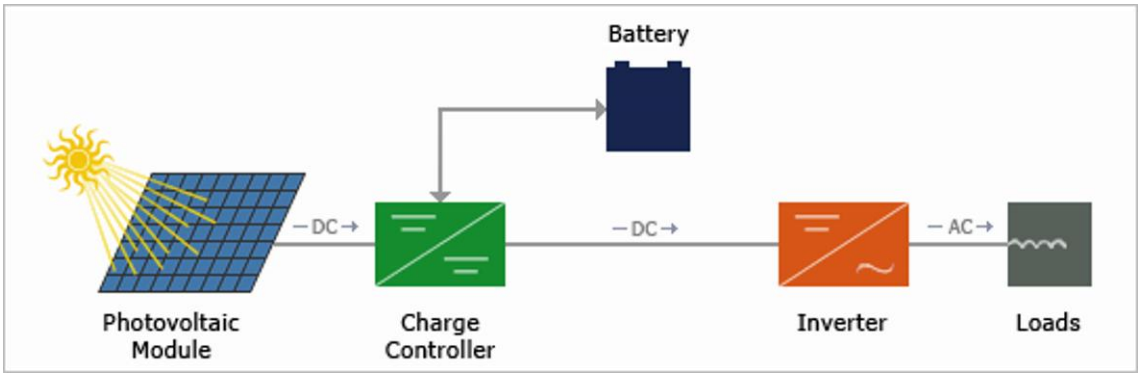

Fig. 13 – Design of a classical stand-alone photovoltaic system

Grid-connected systems

A grid-connected photovoltaic power system or grid-connected PV power system is an electricity generating solar PV power system that is connected to the utility grid. A grid-connected PV system consists of solar panels, one or several inverters, a power conditioning unit and grid connection equipment. They range from small residential and commercial rooftop systems to large utility-scale solar power stations. Unlike stand-alone power systems, a grid-connected system includes an integrated battery solution, as they are still very expensive. When conditions are right, the grid-connected PV system supplies the excess power, beyond consumption by the connected load, to the utility grid

Solar energy gathered by photovoltaic solar panels, intended for delivery to a power grid, must be conditioned, or processed for use, by a grid-connected inverter [22]. Fundamentally, an inverter changes the DC input voltage from the PV to AC voltage for the grid.

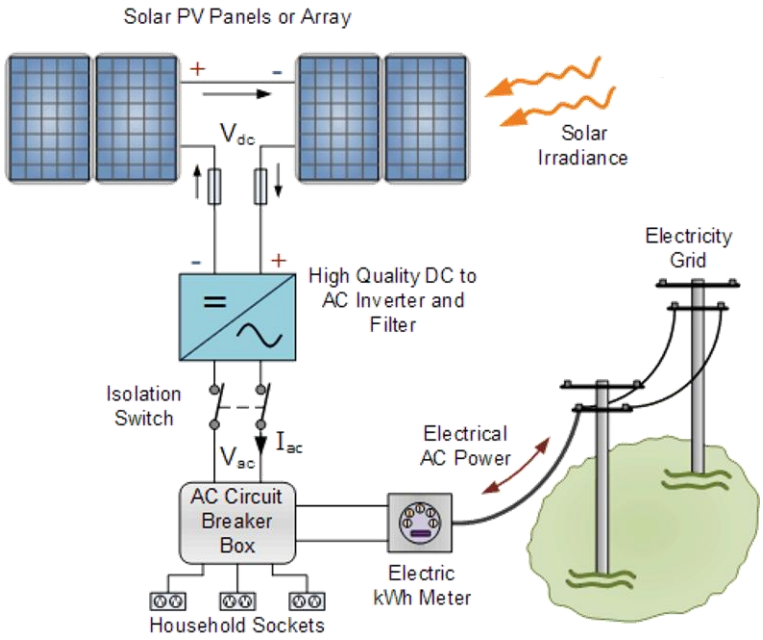

Fig. 14 – Design of a typical grid-connected photovoltaic system

Main advantages of grid-connected arrangements are: easiness of installation, due to lack of batteries often required by stand-alone systems; more efficient use of generated energy, as there are no storage losses involved; residential installation can benefit from incentives for producing electricity that is conveyed to the grid.

Main drawbacks of such systems are: impairment of power quality due to its intermittency which can cause rapid changes in voltage; protection-related requirements, as phenomena like islanding and high levels of grid-connected PV can give problems such as relay desensitization, nuisance tripping, interference with automatic reclosers, and ferro-resonance.

2.2.1 SiO_2 solar cells

The conversion of solar radiation occurs by the photovoltaic effect which was first observed by Becquerel. It is quite generally defined as the emergence of an electric voltage between two electrodes attached to a solid or liquid system upon shining light onto this system. Practically, all photovoltaic devices incorporate a p-n junction in a semiconductor across which the photovoltage is developed [23].

p-n junction

Solar cells capture photons by exciting electrons across the band-gap of a semiconductor, which creates electron–hole pairs that are then charge separated, typically by p–n junctions introduced by doping. The space charge at the p–n junction interface drives electrons in one direction and holes in the other, which creates at the external

electrodes a potential difference equal to the band-gap. The concept and configuration are similar to those of a semiconductor diode, except that electrons and holes are introduced into the junction by photon excitation and are removed at the electrodes [19].

A p–n junction is a boundary or interface between two types of semiconductor material, p-type and n-type, inside a single crystal of semiconductor. The "p" (positive) side contains an excess of electron holes, while the "n" (negative) side contains an excess of electrons. The p-n junction is created by doping, for example by ion implantation, diffusion of dopants, or by epitaxy (growing a layer of crystal doped with one type of dopant on top of a layer of crystal doped with another type of dopant). If two separate pieces of material were used, this would introduce a grain boundary between the semiconductors that would severely inhibit its utility by scattering the electrons and holes [24].

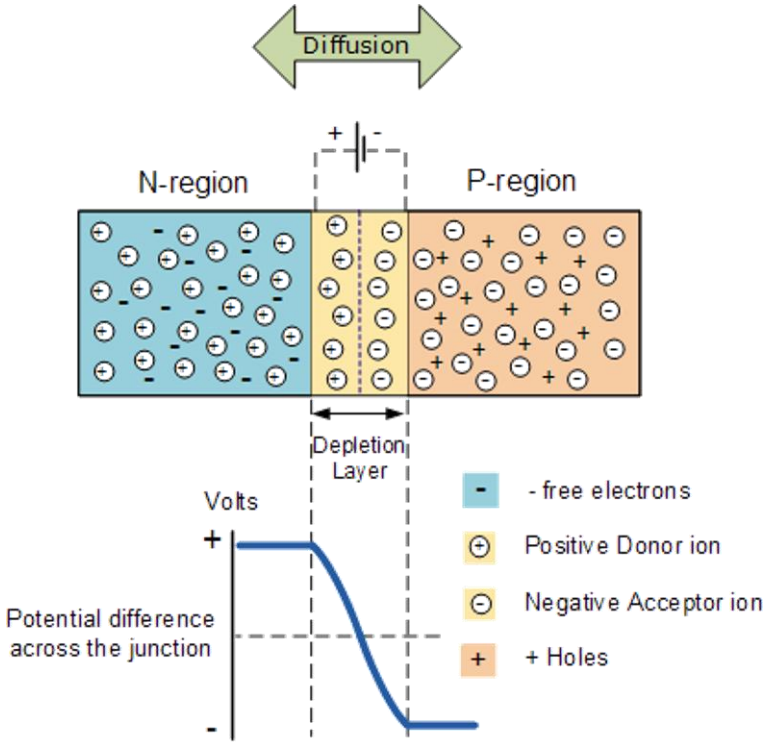

Fig. 15 – A p-n junction

Zero bias (equilibrium)

In a p–n junction, without an externally applied voltage, an equilibrium condition is reached in which a potential difference is formed across the junction. This potential difference is called “built-in potential”.

After joining p-type and n-type semiconductors, electrons from the n-region near the p–n interface tend to diffuse into the p region leaving behind positively charged ions in the n region and being recombined with holes, forming negatively charged ions in the p region. The regions near the p–n interface lose their neutrality and most of their mobile carriers, forming the space charge region or depletion layer.

Forward bias

In forward bias, the p-type is connected to the positive terminal and the n-type is connected to the negative terminal.

With increasing forward-bias voltage, the depletion zone eventually becomes thin enough that the zone's electric field cannot counteract charge carrier motion across the p–n junction, which as a consequence reduces electrical resistance. Only majority carriers (electrons in n-type material or holes in p-type) can flow through a semiconductor for a macroscopic length. The forward bias causes a force on the electrons pushing them from the N side toward the P side. With forward bias, the depletion region is narrow enough that electrons can cross the junction and inject into the p-type material. However, they do not continue to flow through the p-type material indefinitely, because it is energetically favorable for them to recombine with holes.

Reverse bias

Connecting the p-type region to the negative terminal of the battery and the n-type region to the positive terminal corresponds to reverse bias. If a diode is reverse-biased, the voltage at the cathode is comparatively higher than at the anode. Therefore, very little current will flow until the diode breaks down.

Because the p-type material is now connected to the negative terminal of the power supply, the 'holes' in the p-type material are pulled away from the junction, leaving behind charged ions and causing the width of the depletion region to increase. A similar effect occurs in the n-type region. This increases the voltage barrier causing a high resistance to the flow of charge carriers. The increase in resistance of the p–n junction results in the junction behaving as an insulator.

Semiconductors and bang-gap energy

In solid-state physics, a band-gap, is an energy range in a solid where no electron states can exist. It is the energy required to promote an electron from a valence state to a conduction state, which is free to move within the crystal lattice and serve as a charge carrier to conduct electric current. If the valence band is completely full and the conduction band is completely empty, then electrons cannot move into the solid; however, if some electrons transfer from the valence to the conduction band, then current can flow. Therefore, the band-gap is a major factor determining the electrical conductivity of a solid. Substances with large band-gaps are generally insulators, those with smaller band-gaps are semiconductors, while conductors either have very small band-gaps or none.

Crystalline Silicon (c-Si)	1,12
Amorphous Silicon (a-Si)	1,75
Germanium (Ge)	0,67
Gallium Arsenide (GaAs)	1,42
Indium Phosphide (InP)	1,34
Copper Indium Diselenide (CuInSe)	1,05
Cadmium Telluride (CdTe)	1,45
Cadmium Sulfide (CdS)	2,4

Fig. 16 – Energy band-gap of most common semiconductors

Band-gap energy in the semiconductor is fundamental for the application of the photovoltaic effect. Photons from the Sun are collected by the semiconductor and they can be exploited for the production of voltage/current. If photons have enough energy, that is, higher than the band-gap energy of the semiconductor material, then they are absorbed and their energy is converted to potential energy of holes/electrons, which can "jump" from the valence band to the conduction band. The energy that is exceeding the energy band-gap is waste as heat. On the contrary, if photons' energy is too low (i.e. lower than the energy band-gap), they pass through the system without any effect.

Thus, materials have to be chosen to obtain an energy band-gap that is high enough to reach good efficiencies and not to waste too much solar power as heat, and that is contemporary not too high in order to collect more photons as possible.

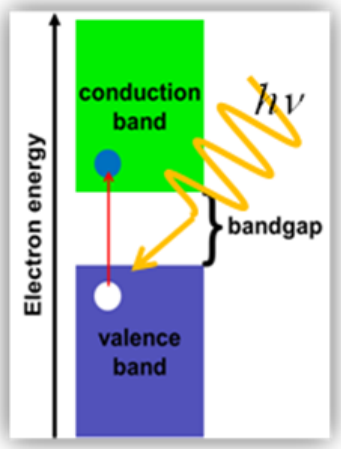

Fig. 17 – Photovoltaic effect on a semiconductor

Amorphous silicon (a-SiO_2)

A thin film material which very early appeared on the market is amorphous silicon (a-SiO_2).

The high expectancy in this material was curbed by the relatively low efficiency obtained so far and by the initial light-induced degradation for this kind of solar cells (so-

called Staebler–Wronski effect). Today, a-Si has its fixed place in consumer applications, mainly for indoor use and for low-cost solar cells. After understanding and partly solving the problems of light-induced degradation, amorphous silicon begins to enter the power market. Stabilized cell efficiencies reach 13%. Module efficiencies are in the 6–8% range [23].

Fig. 18 – An amorphous silicon (a-SiO_2) solar cell

The films are deposited by decomposition of silane (SiH_4) in a plasma. Deposition occurs at relatively low temperature but deposition rates are also low. It has been found that thinner cells exhibit higher stability, so stacked cells have been designed that utilize this effect [25].

Monocrystalline silicon (m-SiO_2)

Monocrystalline silicon solar cells are currently the fastest developing a solar cell, its composition, and production technology have been finalized, the products have been widely used for space and ground facilities. The single crystal silicon solar cells can achieve 99.999% purity. In order to reduce production costs, and now solar-terrestrial applications such as the use of solar-grade silicon rods, material performance has been relaxed.

Fig. 19 – A monocrystalline silicon (m-SiO_2) solar cell

According to the system, the user can design different size solar module solar cell composed of a variety of squares, also known as the solar array. Current SiO_2 photoelectric conversion efficiency is about 15%, whereas laboratory results have more than 20% [24].

Polycrystalline silicon (p-SiO_2)

Monocrystalline silicon solar cell production requires large amounts of high-purity silicon material, thus the process complexity and the overall cost of the production of these materials is very high. Therefore, polycrystalline silicon solar cells were developed to overcome these drawbacks.

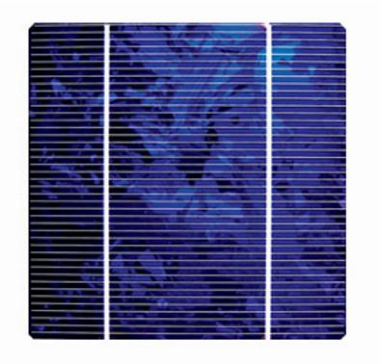

Fig. 20 – A polycrystalline silicon (p-SiO_2) solar cell

Polycrystalline material, in the form of fragments obtained from highly purified polysilicon, is placed in a quartz crucible which itself is located in a graphite crucible and melted under inert gases by induction heating. A seed crystal is immersed and slowly withdrawn under rotation.

Polycrystalline silicon solar cells reach a photoelectric conversion efficiency of about 12%, slightly lower than the silicon solar cells, but the material is simpler, and the total production costs are lower. As the technology was improved, the current conversion efficiency of polycrystalline silicon can also achieve around 14% [23].

2.2.1 Multi-Junction Solar Cells (MJSCs)

Multi-junction solar cells (MJSCs) are solar cells with multiple p–n junctions made of different semiconductor materials. Each p-n junction will produce electric current in response to different wavelengths of light. The use of multiple semiconducting materials allows the absorbance of a broader range of wavelengths, improving the cell's sunlight to electrical energy conversion efficiency.

Traditional single-junction cells have a maximum theoretical efficiency of 34%, whereas an infinite number of junctions would have a limiting efficiency of 86.8% under highly concentrated solar power.

Currently, lab examples of multi-junction cells have demonstrated performance over 46% under concentrated sunlight [26, 27]. Commercial examples of tandem cells are widely available at 30% under one-sun illumination and improve to around 40% under solar concentration [28]. However, this efficiency is gained at the cost of increased complexity and manufacturing price. To date, their higher price and higher price-to-performance ratio have limited their use to special roles, notably in aerospace where their high power-to-weight ratio is desirable. In terrestrial applications, these solar cells are emerging in concentrator photovoltaics (CPV), with a growing number of installations around the world.

The potential behind the MJSCs lies in their ability to absorb photons from sunlight in a wide range of wavelengths, unlike the traditional silicon solar cells. As previously mentioned, in fact, a solar cell can absorb only photons which exceed the band-gap energy of the material (1.12 eV in the case of crystalline Si), whereas the other photons will pass through the material (transparency loss). Thus, a low band-gap energy material should be suitable for a single junction solar cell. The drawback of this configuration, however, would be the high energy dispersion of photons, due to the fact that the excess energy between the photons and the band-gap is wasted as heat (excess excitation loss). These are the main limitations to the maximum efficiency of traditional solar cells with a single junction.

On the contrary, MJSCs are made from multiple materials, with multiple band-gaps. So, they will respond to multiple light wavelengths and some of the energy that would otherwise be lost to relaxation as described above can be captured and converted.

Following an analysis similar to those performed for single-band-gap devices, it can be demonstrated that the perfect band-gaps for a two-gap device are at 1.1 eV and 1.8 eV, while for a higher number of tandem solar cells, semiconductor materials with band-gap energy from 0.6 to 2.5 eV are needed [29].

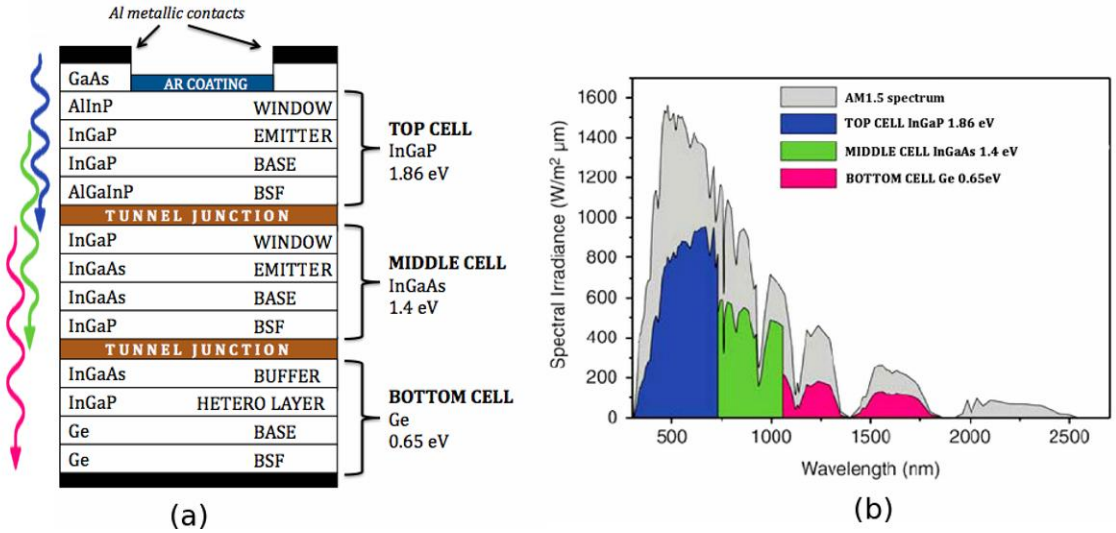

Fig. 21 – Typical structure of an MJSC (a) and spectral irradiance vs. wavelength over the AM1.5 solar spectrum (b)

To improve the overall efficiency of photons' absorption, the materials that constitute the MJSC are layered on top of each other, with the highest band-gap energy on the "top" layer and the lowest on the "bottom" layer. In this way, higher energy photons would be absorbed by the first layer, with less heat dispersion (due to a low difference between photons' energy and the solar cell band-gap), while the photons with less energy would pass through and be absorbed by the second layer, and so on. As the photons have to pass through all the cells to reach the proper layer to be absorbed, transparent conductors need to be used to collect the electrons being generated at each layer.

Producing a tandem cell is not an easy task, largely due to the thinness of the materials and the difficulties extracting the current between the layers. The easy solution is to use two mechanically separate thin film solar cells and then wire them together separately outside the cell.

The more difficult solution is the "monolithically integrated" cell, where the cell consists of a number of layers that are mechanically and electrically connected. These cells are much more difficult to produce because the electrical characteristics of each layer have to be carefully matched. In particular, the photocurrent generated in each layer needs to be matched, otherwise, electrons will be absorbed between layers. This limits their construction to certain materials, best met by the III-V semiconductors.

Materials

For optimal growth and resulting crystal quality, the crystal lattice constant of each material must be closely matched, resulting in lattice-matched devices. This constraint has been relaxed somewhat in recently developed metamorphic solar cells which contain a small degree of lattice mismatch. However, a greater degree of mismatch or other growth imperfections can lead to crystal defects causing a degradation in electronic properties.

Since each sub-cell is connected electrically in series, the same current flows through each junction. The materials are ordered with decreasing band-gaps, allowing sub-low energy light to pass to the lower sub-cells. Therefore, suitable band-gaps must be chosen such that the design spectrum will balance the current generation in each of the sub-cells, achieving current matching. Finally, the layers must be electrically optimal for high performance. This necessitates usage of materials with strong absorption coefficients, high minority carrier lifetimes, and high mobilities.

The most used materials in triple-junction tandem solar cells are: *InGaP* for the top sub-cell (Eg = 1.8 - 1.9 eV), *InGaAs* for the middle sub-cell (Eg = 1.4 eV), and Germanium (*Ge*) for the bottom sub-cell (Eg = 0.67 eV). The use of Ge is mainly due to its lattice constant, robustness, low cost, abundance, and ease of production.

The Anti-Reflective (AR) coating is generally composed of several layers in the case of MJ solar cells. The top AR layer has usually a NaOH surface texturization with several pyramids in order to increase the transmission coefficient T, the trapping of the light in the material (because photons cannot easily get out the MJ structure due to pyramids) and therefore, the path length of photons in the material. On the one hand, the thickness of each AR layer is chosen to get destructive interferences. On the other hand, the thickness of each AR layer is also chosen to minimize the reflectance at wavelengths for which the photocurrent is the lowest.

The tunnel junctions provide a low electrical resistance and optically low-loss connection between two subcells. Without it, the p-doped region of the top cell would be directly connected with the n-doped region of the middle cell. Hence, a p-n junction with opposite direction to the others would appear between the top cell and the middle cell. Consequently, the photovoltage would be lower than if there would be no parasitic diode. In order to decrease this effect, a tunnel junction is used. It is simply a wide band-gap, a highly doped diode. The high doping reduces the length of the depletion region, allowing the electrons to travel through it.

Production technologies

There are many ways to obtain a multi-junction solar cell.

The most common type of MJSC, especially used in the past years, is the *lattice-matched* [30]. The main objective is to couple the sub-cells in order to minimize the difference between the lattice constant of each compound, by tuning the relative amount of indium and gallium in the top (arsenides) and middle (phosphides) layer:

$$In_xGa_{1-x}As \rightarrow x\cdot 6.058+(1-x)\cdot 5.653$$
$$In_xGa_{1-x}P \rightarrow x\cdot 5{,}869+(1-x)\cdot 5.451$$
$$Ge \rightarrow 5.646$$

This type of lattice-matched solar cell owns good optical properties. However, the strict constraint does not allow the use of some materials, thus reducing the achievement of high efficiencies.

To overcome these issues, *lattice-mismatched* or *metamorphic* solar cells have been developed [31]. The introduction of a low lattice mismatch allows more freedom in the material choice, without decreasing the performance. Top and middle sub-cells are grown on a metamorphic buffer such that these two sub-cells are lattice-matched to each other, but are both lattice-mismatched to the Ge substrate. A step-graded buffer, which is obtained by altering the alloy ratio during film growth is introduced to reduce the strain.

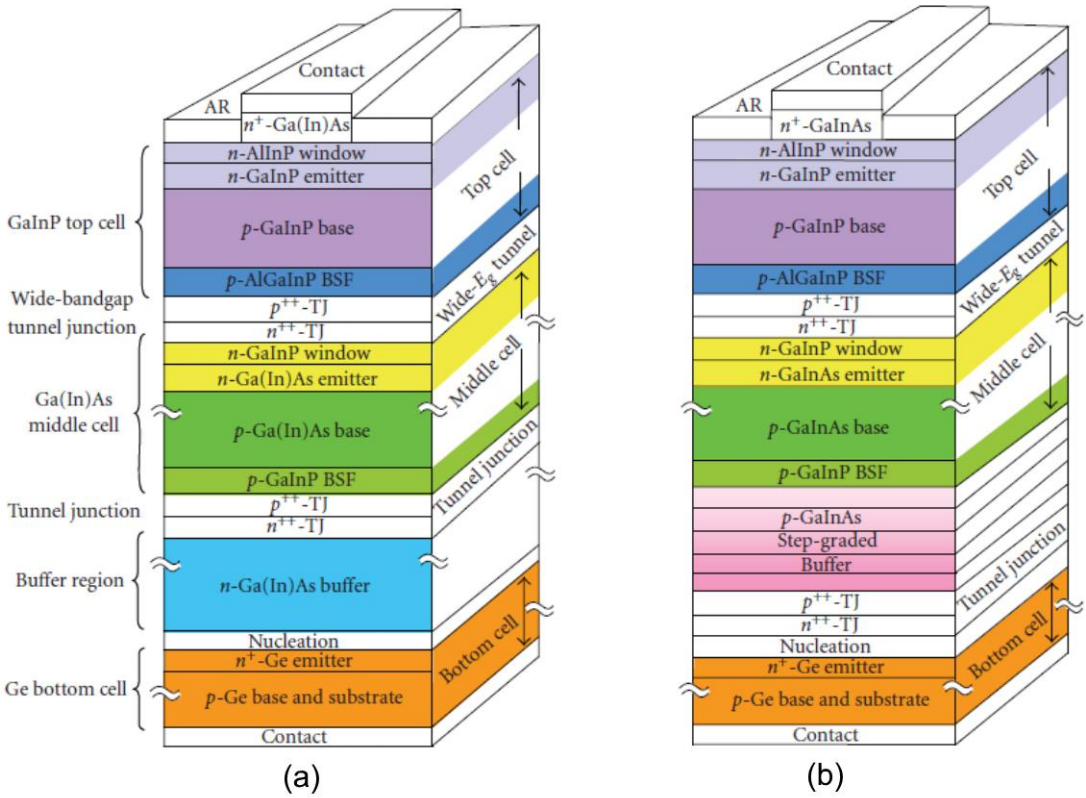

Fig. 22 – Schematic cross-sectional diagrams of lattice-matched (a) and metamorphic (b) GaInP/GaInAs/Ge 3-junction cell

One step further towards the improvement of MJSCs are the so-called *inverted metamorphic* solar cells [32]. The key concept is the same of the metamorphic solar cells, that is, allowing the use of materials with different lattice constants. In this case, however, the main objective is to replace the Ge substrate, which has a band-gap of 0,67eV with a substrate having a higher band-gap energy (~ 0,9–1 eV). A too low band-gap, in fact, increases the heat losses due to excess energy of photons reaching the substrates, thus reducing the maximum efficiency. One of the most promising materials for the bottom layer/substrate is InGaAs. The cell is grown on a substrate (usually GaAs), then bonded onto a handle, and the substrate is removed. Higher bang-gap energy in the bottom cell

would result in: lower current in Ge cell (otherwise useless); higher Ge sub-cell voltage (higher total cell voltage); lower photon energy wasted as heat.

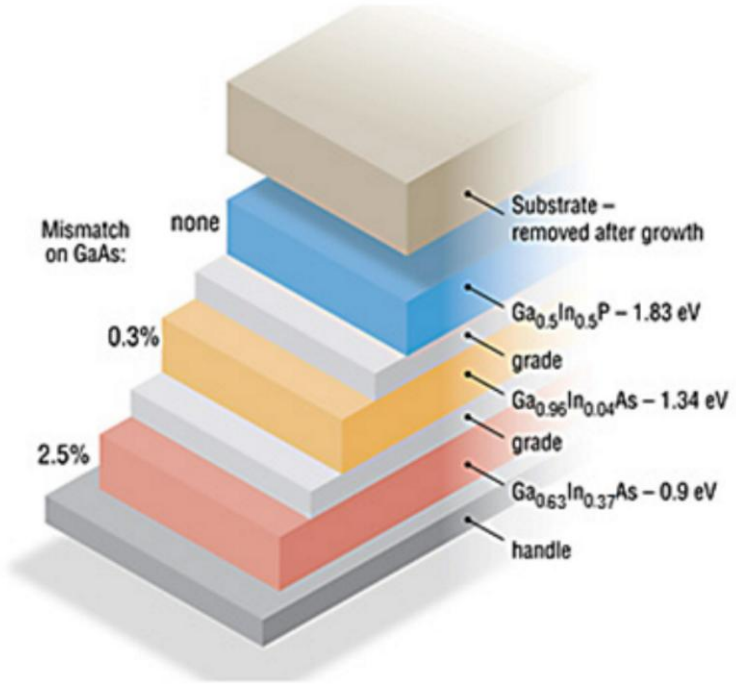

Fig. 23 – Schematic of an inverted metamorphic multi-junction solar cell

Another synthesis used for the production of MJSCs is the *direct semiconductor bonding* [33]. Two epitaxial layers are well-polished to obtain flat surfaces, which spontaneously adhere or "bond" to each other, at an atomic distance apart. Annealing at high T (500-600°C), makes the bonding permanent. However, high T may cause dopant diffusion and thermal stresses which may result in local de-bonding.

In the last few years, many processes have been tested to obtain direct bonding at room temperature, such as ultrahigh vacuum, argon beam etching, atomic hydrogen surface cleaning.

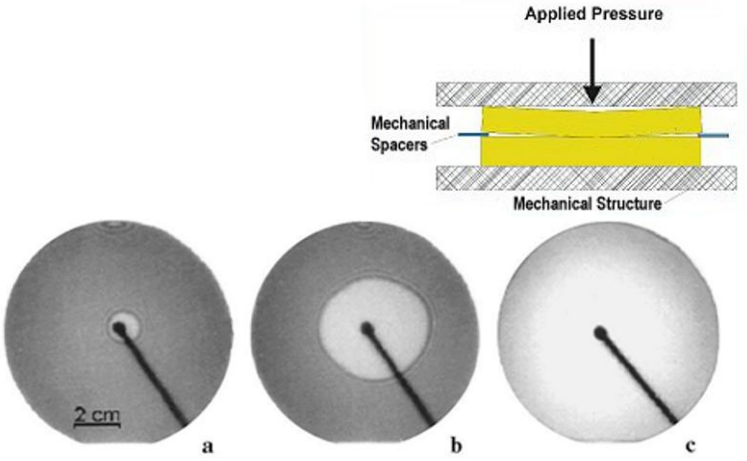

Fig. 24 – Direct semiconductor bonding technology for MJ solar cells production

Recently, studies have been carried out on MJSCs based on *nitride-based systems* [34, 35]. The band-gap energy of these materials can be tuned from 0.7 to 6.2 eV, according to the degree of doping. The re-evaluation of band-gap of InN extends the fundamental bandgap energy of III-Nitrides from near infrared (InN at 0.65 eV) to deep-ultraviolet (AlN at 6.2 eV), which provides an almost perfect match to the solar spectrum, opening up an interesting opportunity for the high-efficiency photovoltaic applications.

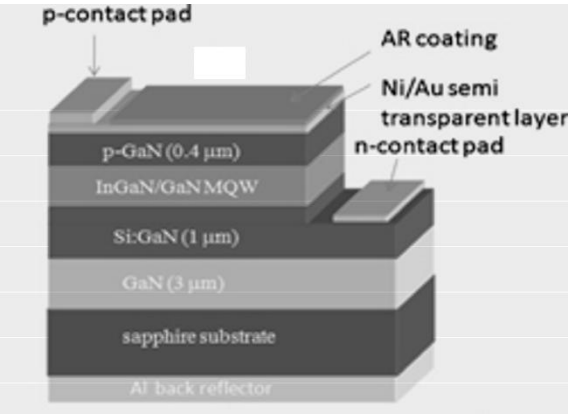

Fig. 25 – Example of an InGaN multi-junction solar cell

InGaN alloys have the advantages of high drift velocity, high radiation resistance, large absorption coefficient, and high carrier mobility. These characteristics enable the InGaN solar cells to operate also in severe environments such as the desert or space.

Influence of temperature and irradiance on MJSCs

In concentrating photovoltaics (CPV) as well as in space applications, multi-junction solar cells made from III–V compound semiconductors are widely applied as photovoltaic converters. The characterization of solar cells is usually performed at ambient temperature and under 1-sun illumination. However, in many applications, the actual operating conditions can achieve 70°C for passively cooled CPV (under 300-1000 suns), or even more than 100°C for mixed concentrated photovoltaic and thermal (CPVT) systems [36, 37].

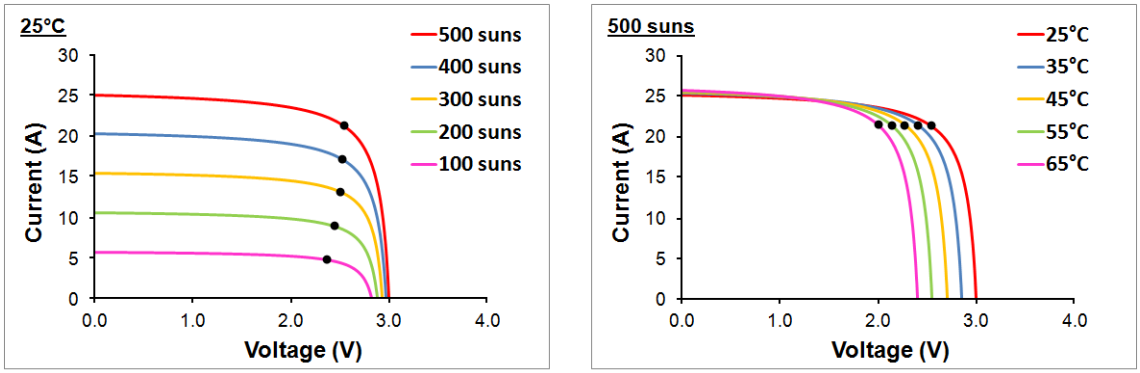

Fig. 26 – Effect of solar concentration (a) and temperature (b) on the performances of an MJSC

Fig. 26 shows the influence of the concentration factor and the temperature on the characteristic current-voltage (*I-V*) curves of a multi-junction solar cell, as well as at their maximum power point (indicated by the black dot). Obviously, an increase in the solar concentration rises the short circuit current (I_{sc}) of the MJ linearly with the concentration factor (Fig. 26a), also increasing the open circuit voltage (V_{oc}), but with a lower dependence. An increase in the system temperature, instead, tends to decrease the open circuit voltage of the solar cell (Fig. 26b), while slightly increasing the short circuit current. Thus, the maximum power point is moving towards high values when the sun concentration is rising, whereas is moving towards lower values when the temperature increases.

Voltage fall is one of the most critical points for the MJSCs when operating at high temperatures, especially for the germanium (Ge) substrates, which can reach very low values, thus compromising the efficiency of the cell. In fact, since the sub-cells are connected in series, the total current is the minimum flowing in the system, while the total voltage is the sum of the sub-cells voltages, as shown in Fig. 27.

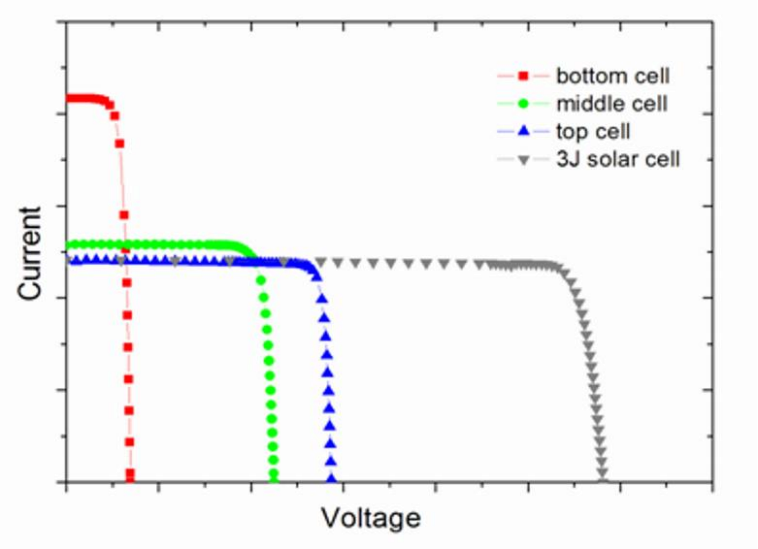

Fig. 27 – I-V characteristic of a triple-junction solar cell

Therefore, if Ge Voc tends to zero, the bottom sub-cell contribute to the total voltage is negligible. Open circuit potential is closely related to the band-gap energy of the material, which in turn is dependent on the operative temperature. Many authors proposed experimental correlations between band-gap (or V_{oc}) and temperature [36, 38]. However, the most used formulas to predict the band-gap energy and the open circuit voltage with temperature are:

$$E_g(T) = E_g(0) - \frac{\alpha T^2}{T+\beta} \qquad \text{Eq. 21}$$

where $E_g(0)$, α and β are material constants.

$$V_{oc}(T) = \frac{E_g(T)}{q} - \frac{kT}{q} \cdot ln\left(\frac{N_C N_V D_n}{N_A L_n} \cdot I_{sc}\right) \qquad \text{Eq. 22}$$

where q is the electron charge, k is the Boltzmann constant, N_c and N_v are the conduction and valence band densities, D_n is the minority carrier diffusion constant, N_A is the dopant concentration and L_n is the minority diffusion length.

In conclusion, materials with high standard band-gap energies, $E_g(0)$, are the most suitable for high-temperature applications. In addition, elevated solar concentrating factors can partially compensate the temperature influence on the open circuit voltage.

2.3 Solar to fuels

Solar energy can be stored into chemicals, usually through electrochemical conversion in electrolyzers. The main valuable products obtained by this technology are: hydrogen from water splitting and methanol from carbon dioxide reduction [39].

Solar to hydrogen

Hydrogen can play a significant role in the energy supply of a sustainable economy in the future. Electricity can be generated, e.g. directly from hydrogen using fuel cells [40], or hydrogen can be burned in conventional combustion engines [41]. Hydrogen has many advantages as it can be stored, shipped and combusted without harmful reactants.

Most systems can be classified under one of four categories [42]:

1) **Photochemical systems:** sunlight is absorbed by isolated molecules in solution. A sensitizer, that is, a molecule or semiconductor that can absorb sunlight and stimulate photochemical reactions which ultimately lead to the generation of hydrogen in reaction
2) **Semiconductor systems:** sunlight is absorbed by a semiconductor. Photovoltaic (PV) cells plus electrolyzer is certainly the most developed option at present because silicon photovoltaic cells routinely achieve efficiencies of > 15% and the efficiency of electrolyzers is often >75%.
3) **Photo-biological systems:** sunlight is absorbed by photosynthetic organisms, which carry out an energy-storing fuel production reaction. Normally, photosynthetic systems do not evolve hydrogen, but rather reduce CO_2 to carbohydrates. However, it is possible to modify conditions such that the reducing end of the photosynthetic process is coupled to a hydrogen-evolving enzyme, such as hydrogenase or nitrogenase.
4) **Hybrid systems:** involving combinations of the first three

Solar to methanol

Recently, the selective catalytic reduction of carbon dioxide (CO_2) to value added chemicals using solar energy has received a great deal of attention from the scientific community as it can indeed solve two major problems, i.e., global warming and energy crisis. The conversion of CO_2 into more useful organic fuels (like methanol) using energy that is not produced from fossil fuels is believed to have tremendous potential [39]. Methanol is the most promising photo-reduced product of carbon dioxide because it can be transformed into other useful chemicals such as gasoline (petrol) using conventional chemical technologies, or easily transported and used as fuel in the automobile vehicles without major adjustments.

There are several other motivations as listed below for producing methanol or any other useful chemical from carbon dioxide. 1) Carbon dioxide is an inexpensive, nontoxic feedstock that can frequently replace toxic chemicals such as phosgene of isocyanates. 2) Carbon dioxide is a renewable feedstock compared to oil or coal. 3) The production of chemicals from carbon dioxide can lead to new industrial productivity. 4) New routes to existing chemical intermediates and products could be more efficient and economical than current methods. 5) The production of chemicals from carbon dioxide could have a small but significant impact on the global carbon balance.

Among various routes proposed for conversion of CO_2 to methanol or to any other value added a chemical, the photoelectrochemical (PEC) cells have an edge over another process. In order to realize efficient PEC cells for this reaction, 1) an n-type semiconductor with desired band-gap and band edges for photoanode (e.g., pure TiO2, ZnO, CdS, etc.); 2) a p-type semi-conductor with desired band gap and band edges for photocathode (e.g., doped TiO2, ZnO, GaP, etc.); 3) a catalyst for performing water oxidation reaction over or near to the surface of photoanode (e.g., polyoxometallates), and 4) a catalyst to perform CO2 reduction reaction over or near to the surface of photocathode (e.g., pyridinium ions over the surface of p-GaP) are essential.

2.4 Solar to heat

Solar thermal electricity may be defined as the result of a process by which directly collected solar energy is converted to electricity through the use of some sort of heat to electricity conversion device. Mostly this is a heat engine, but there are other options such as a thermoelectric pile converter or a fan converter as in solar chimneys.

Various advanced solar thermal electricity technologies are reviewed with an emphasis on new technology and new market approaches [37, 43, 44].

Single-axis tracking systems

In single-axis tracking technology, the conventional parabolic trough collector is the mainstream established technology and is under continued development. This category is comprised of technologies in which relatively long and narrow reflectors are tracked about a single axis to keep the sun's image in focus on a linear absorber or receiver. The receiver is normally a tube or series of tubes which contain a heat transfer fluid:

- **Parabolic trough technology:** This technology uses reflectors curved around one axis using a linear parabolic shape, which has the property of collecting parallel rays along a single line focus and nearly parallel rays from the solar beam in a line image. A long pipe receiver can be placed at the focus for heating of heat transfer fluid.

- **Linear Fresnel reflector technologies:** This is a single-axis tracking technology but differs from a parabolic trough in that the absorber is fixed in space above the mirror field and the reflector is composed of many long row segments which focus collectively on an elevated long tower receiver running parallel to the reflector rotational axis.

Two-axis tracking systems

Dual axis trackers have two degrees of freedom that act as axes of rotation. These axes are typically normal to one another. The axis that is fixed with respect to the ground can be considered a primary axis. The axis that is referenced to the primary axis can be considered a secondary axis. There are several common implementations of dual axis trackers. They are classified by the orientation of their primary axes with respect to the ground. Dual axis trackers allow for optimum solar energy levels due to their ability to follow the Sun vertically and horizontally. No matter where the Sun is in the sky, dual axis trackers are able to angle themselves to be in direct contact with the Sun.

- **Paraboloidal dishes:** It is a reflective surface used to collect or project energy such as light, sound, or radio waves. Its shape is part of a circular paraboloid, that is, the surface generated by a parabola revolving around its axis. The parabolic reflector transforms an incoming plane wave traveling along the axis into a spherical wave converging toward the focus. Conversely, a spherical wave generated by a point source placed in the focus is reflected into a plane wave propagating as a collimated beam along the axis.
- **Single tower—central generation:** is a type of solar furnace using a tower to receive the focused sunlight. It uses an array of flat, movable mirrors (called heliostats) to focus the sun's rays upon a collector tower (the target). Concentrated solar thermal is seen as one viable solution for renewable, pollution-free energy.
  Early designs used these focused rays to heat water and used the resulting steam to power a turbine. Newer designs using liquid sodium have been demonstrated, and systems using molten salts (40% potassium nitrate, 60% sodium nitrate) as the working fluids are now in operation. These working fluids have high heat capacity, which can be used to store the energy before using it to boil water to drive turbines. These designs also allow power to be generated when the sun is not shining.
- **Distributed tower systems:** The basic MTSA components are a reflector field using extremely closely spaced silvered glass reflectors of a special shape to allow extremely close spacing; multiple receivers of radiation using advanced thermal and photovoltaic absorber technology; means allowing the receivers to be placed above the reflector field between 8 and 12 m high. These may be multiple small towers or posts, or else arch-like structures. For the receiver of radiation, MTSA

can simultaneously use high-temperature and photovoltaic absorbers in parallel by splitting the incoming solar beam spectrally so that electricity production is optimized.

2.5 PEM electrolyzer

Hydrogen may play an important role as an energy carrier of the future. Hydrogen may be used as fuel in almost every application where fossil fuels are being used today, but without harmful emissions. In addition, hydrogen may be converted into useful forms of energy more efficiently than fossil fuels. However, hydrogen does not occur in nature in its elemental or molecular form. Therefore, hydrogen must be produced. Although several methods have been and are being developed for the production of hydrogen from renewable energy sources, the only one currently practical is water electrolysis. Water electrolysis is a mature technology, and it is being used for hydrogen production capacities ranging from few cm^3/min to thousands m^3/h. It is relatively efficient (>70%), but because it needs high-quality energy (electricity) hydrogen produced by water electrolysis is expensive (>$20/GJ) [45].

PEM electrolysis is a process just reverse of a PEM fuel cell process (Fig. 1). Water is split into oxygen, protons and electrons on one electrode (anode) by applying a DC voltage higher than a thermo-neutral voltage (1.482 V). Protons pass through the polymer electrolyte membrane and on the cathode combine with electrons to form hydrogen. Passage of protons through the membrane is accompanied by water transport (electro-osmotic drag).

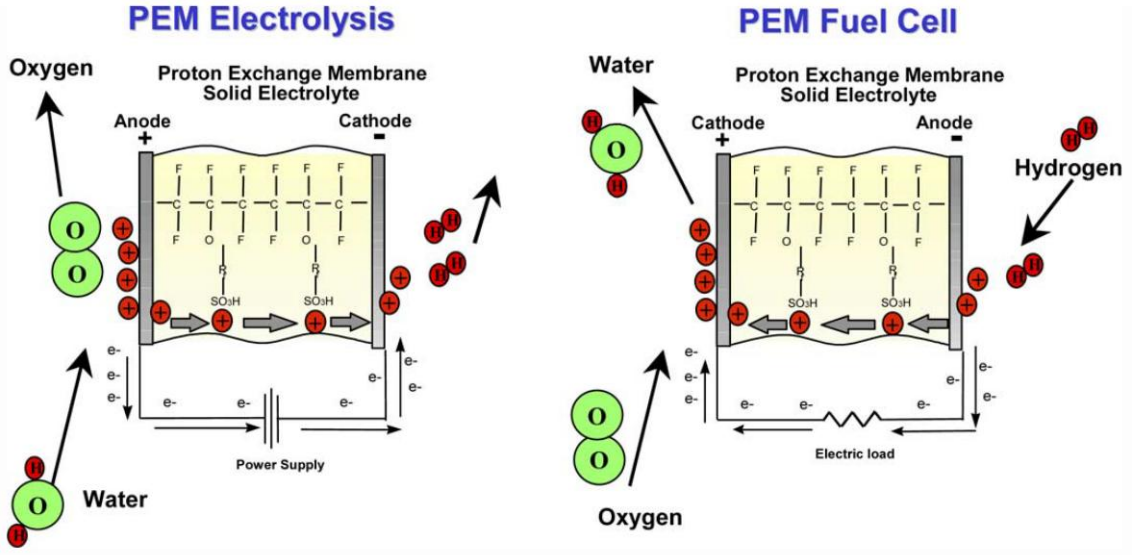

Fig. 28 - Schematic representation of PEM electrolysis and fuel cell processes

A PEM electrolyzer cell is similar to a PEM fuel cell. It has a polymer membrane and porous electrodes, flow fields, current collectors and separator plates, end plates, bus plates, manifolds. The principle of operation is just reverse of fuel cell operation. However, the materials are typically different from PEM fuel cell materials. Carbon materials, such as catalyst support, porous electrode structures (carbon fiber paper or carbon cloth) and bi-polar plates, commonly used in fuel cells cannot be used on the oxygen side of a PEM electrolyzer due to corrosion. PEM electrolyzers therefore primarily use metallic components (porous structures, flow fields, and separator plates). The catalyst is typically platinum or platinum alloys. Similarly to fuel cells, individual electrolyzer cells may be stacked into a stack, in order to get the desired output at a reasonable stack voltage.

Besides the cell stack, an electrolyzer must have a power supply/voltage regulator, water supply system, water circulation pump, water–gas separators for hydrogen and (optionally) oxygen, heat exchanger, controls and instrumentation, including the safety feature.

The efficiency of an electrolyzer is inversely proportional to the cell potential, which in turn is determined by the current density, which in turn directly corresponds to the rate of hydrogen production per unit of electrode active area. A higher voltage would result in more hydrogen production but at a lower efficiency. Typically, the cell voltage is selected at about 2 V, but a lower nominal voltage (as low as 1.6 V) may be selected, if the efficiency is more important than the size (and capital cost) of the electrolyzer. Another ‘‘source’’ of inefficiency is hydrogen permeation (loss) through the polymer membrane. This is typically insignificant at low operating pressures, but it may significantly affect the overall efficiency at very high pressures (>100 bar). In addition, there are power losses in voltage regulation and some power is needed for the auxiliary equipment (pumps, fans, solenoid valves, instrumentation, and controls). Typical industrial electrolyzers have electricity consumption between 4.5 and 6.0 kWh/Nm^3, corresponding to the efficiency of 65–80% [45, 46]. The electrolyzer efficiency is, therefore:

$$\eta_{EL} = \frac{1.482}{V_{cell}} \cdot \frac{i - i_{loss}}{i} \cdot \frac{\eta_{DC}}{1 + \xi}$$

where V_{cell} is the individual (average) cell potential (V), i is the operating current density (A/cm^2), i_{loss} is the internal current and hydrogen loss (A/cm^2), η_{DC} is the efficiency of DC/DC voltage regulator, ξ is the ratio between parasitic power and net power consumed by the electrolyzer.

CHAPTER 3

MJ-PEM REACTOR DESIGN

3.1 Introduction

As stated in the previous chapter, solar power is one of the most interesting and promising energy sources, due to its wide availability all over the Earth's surface, indefinite renewability and low impact on pollution and greenhouse gases emissions.

Among all the possible utilizations of solar power, such as the conversion to electricity by photovoltaic systems [19, 20, 44], conversion to hydrogen by direct photoelectrochemical water splitting [47-49] and conversion to heat by concentration devices [19, 43], a new concept is progressively gathering more and more attention. Thorough investigations [50-52] concern the coupling of III-V Multi-Junction Solar Cells (MJSCs) with Polymer Electrolyte Membrane (PEM) electrolyzers, as the HyCon® device designed by Fraunhofer [53].

The latter systems have several advantages over other types of device for the conversion of solar energy into hydrogen [54]:

- It has a high solar-to-hydrogen conversion efficiency (about 20%).
- The converted energy can be directly stored in the form of hydrogen.
- The only input is sunlight and de-ionized water.
- The system does not need equipment for coupling the photovoltaic array to the electrolyzer.
- The system is scalable in size and shows a favorable cost reduction potential.
- It seems to have a good long-term stability.

Thus, looking at the cathodic side of the HyCon® device, where hydrogen is formed in order to store the energy collected from the Sun, both the efficiencies and the system arrangement prove to be an optimal solution to improve the application of the photovoltaic as a valid and attractive alternative to traditional fossil fuel technologies. Moreover, thanks to the implementation of Fresnel lenses for exploitation of solar

concentration, up to 500 suns, the costs of MJSCs, which are the most relevant, are dramatically reduced, due to the reduction of the needed areas.

However, on the anodic side, water oxidation is considered only a side reaction, and the generated oxygen is a simple by-product, which is not of any interest but could be exploited for storage or wastewater treatment. In addition, solar concentration, due to high specific powers reached (as high as 1 MW/m^2 for concentrating factors of 1000 suns achievable with specific lenses [55]), is able to produce an enormous amount of thermal energy, often used in solar thermal applications [43, 44]. Also, this aspect is not considered, despite the potential benefits which can be obtained by the utilization of free heat that is naturally provided by the solar concentration system.

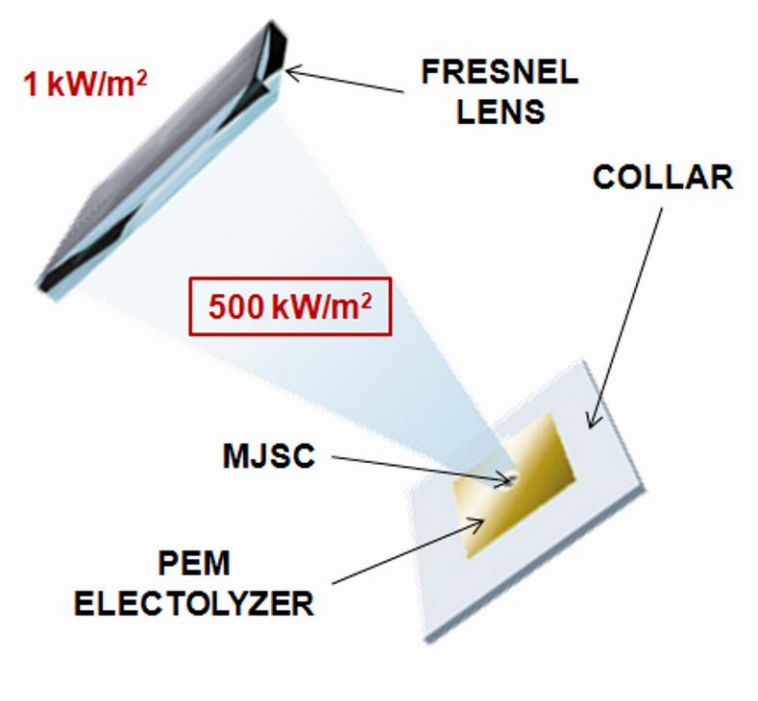

Fig. 29 - Schematics of MJ-PEM reactor under concentrated sunlight

Both these aspects, i.e. oxygen and heat exploitation, will be investigated in this chapter, to possibly increase the overall process efficiency. In particular, two main scenarios will be presented and the MJ-PEM reactor will be dimensioned to fulfill the requirements of the systems:

- Scenario I: the MJ-PEM reactor is dimensioned to treat a wastewater containing refractory organics on the anodic side, whereas hydrogen is produced at the cathode for storage purposes or for direct use on-site.

- Scenario II: the MJ-PEM reactor is matched with the biomethanation step of an anaerobic digestion plant, either mesophilic or thermophilic. The hydrogen

produced at the cathode is used for the biogas upgrading to biomethane, whereas the oxygen evolved at the anode is employed for the digestate stabilization.

3.2 Scenario I – CWAO and H_2 production

In the first scenario, the MJ-PEM reactor will be designed to work at high temperature (150 °C) and high pressure (30 bar). These demanding conditions are the minimum required for Catalytic Wet Air Oxidation (CWAO) to be carried out at the anodic side, while hydrogen can be produced in the cathodic chamber.

The wastewater considered in this study contain recalcitrant organics (with a negligible content of heavy metals), which are very susceptible to be degraded in heterogeneous catalysis by CWAO [56-58], and which can originate from many types of industries (plastics, pesticides, surfactants, pharmaceutical, etc.) or agricultural activities (wine processing and brewery, dairy, etc.).

Fig. 29 shows the design of the MJ-PEM reactor under concentrated illumination, with a concentration factor of 500 suns, obtained with a Fresnel lens. The possible role of a collar, indicated in the figure, has been studied, to individuate the proper dimensions of the PEM system in order to reach equilibrium between the heat provided and the heat dispersed.

Fig. 30, instead, shows the proposed operation scheme for a wastewater treatment with an MJ-PEM reactor assembly operating at 150°C and 30 bar.

As can be seen, wastewater (WW) enters the system after being brought to 30 bar by a "feed pump". Then, the liquid is sent to the PEM electrolyzer, on the anodic side, where oxygen is evolved on the surface of the anode, thanks to the multi-junction which converted the solar power into the bias provided to the cell. The electro-generated oxygen, which would be totally inactive towards the degradation of organic molecules in standard PEM conditions (85°C and 1 bar), and would leave the system as a simple by-product, in these circumstances would react with the refractory compounds to form, at complete mineralization, CO_2 and H_2O.

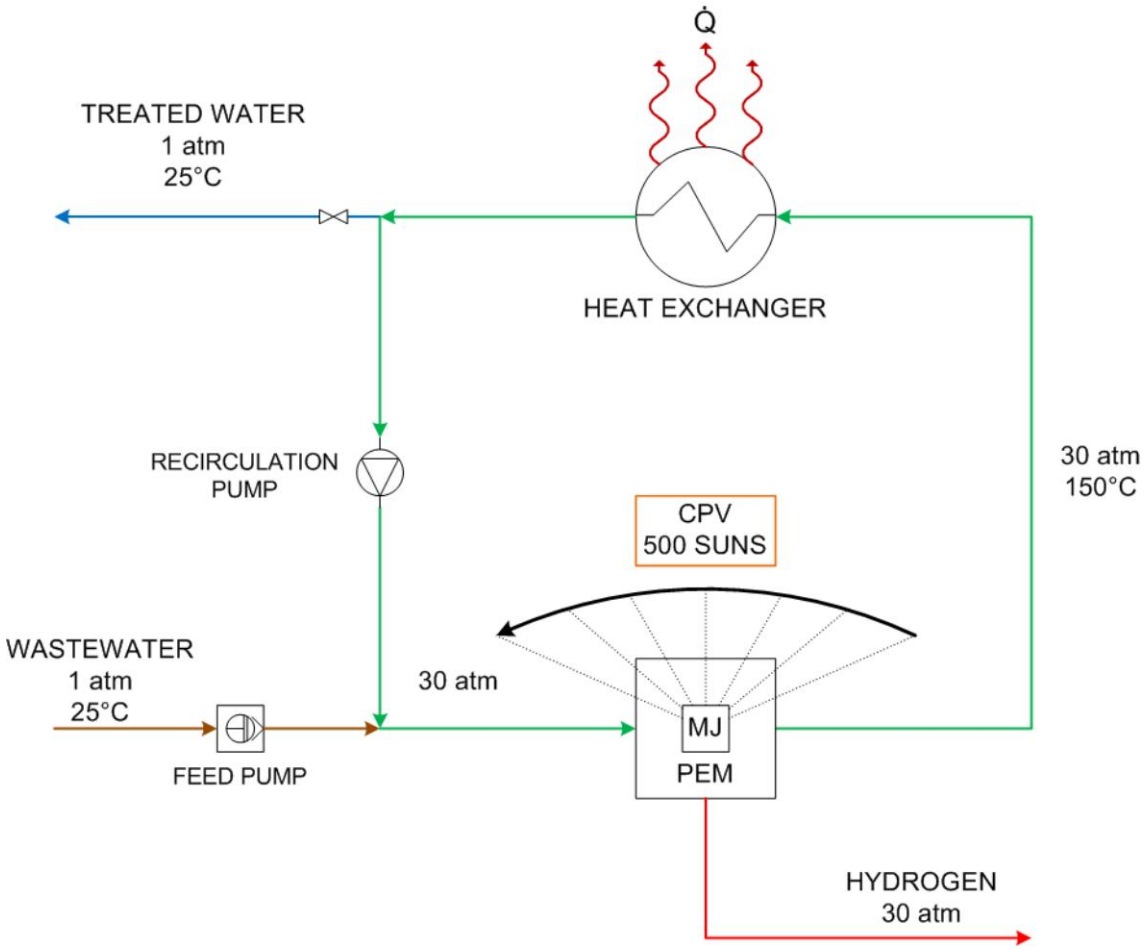

Fig. 30 - Scheme of MJ-PEM arrangement for CWAO of wastewater and hydrogen production

A concentrating factor of sunlight was chosen to be 500 suns because it is very commonly used in solar concentrators [31, 43] and some specific systems can operate even at solar concentrating factors of 1000 suns, reaching a specific solar power onto the surface of the solar cell device of about 1 MW/m^2.

MJ-PEM reactor design

First of all, the solar irradiance and exposure time to the solar light have been calculated to estimate the overall amount of energy given to the system during the daytime.

Supposing to install this device at average latitudes, e.g. in the South of Italy, at about 37°, at sea level, an "air mass coefficient" for solar radiation equal to AM 1.5 [59], can be considered. This parameter, in turn, roughly correspond to a solar irradiance of 1000 W/m^2, under clear sky conditions and for a system that is constantly perpendicular to the Sun, thus overestimating the system capacity by using ideal conditions. Thus, a value that could be representative of the real solar irradiance has been calculated for the chosen location [60], and results are shown in Table 1. At 37° latitude, the average solar irradiance weighted over a period of time of one year is about 670 W/m^2. This value has been obtained with an MJ/PEM reactor connected to a two-axis tracking solar system, in order to maximize the efficiency of the equipment. Without any solar tracking system, at a fixed inclination of the solar cell (~31° for the considered location), the average irradiance would have been ~ 583 W/m^2.

REAL SKY IRRADIANCE AT 37° LATITUDE (W/m^2)											
JAN	**FEB**	**MAR**	**APR**	**MAY**	**JUN**	**JUL**	**AUG**	**SEP**	**OCT**	**NOV**	**DEC**
530	657	724	833	917	942	883	689	584	474	417	378
AVERAGE IRRADIANCE 669 W/m^2											

Table 1 – Average real-sky irradiance calculated at 37° latitude

Next step was the estimation of the average duration of daytime which should be applied to the average solar radiation on the system. All over the world, the average duration of daytime is about 12 h, weighted over one year. An example of the daytime duration is given for the location at 37° latitude [61] and is presented in Table 2. As can be noticed, though daytime is continuously changing, the mean duration which can be taken into account for the dimensioning of the MJ/PEM system is constant for every point on the Earth's surface, and it is equal to 12 h.

DAYTIME DURATION AT 37° LATITUDE (hh:mm)												
DAY	**JAN**	**FEB**	**MAR**	**APR**	**MAY**	**JUN**	**JUL**	**AUG**	**SEP**	**OCT**	**NOV**	**DEC**
1	08:50	09:46	11:11	12:48	14:17	15:23	15:33	14:40	13:14	11:42	10:09	09:02
2	08:51	09:49	11:14	12:51	14:20	15:25	15:32	14:38	13:11	11:38	10:06	09:00
3	08:52	09:52	11:17	12:54	14:22	15:26	15:31	14:36	13:08	11:35	10:03	08:59
4	08:53	09:54	11:20	12:57	14:25	15:27	15:30	14:33	13:05	11:32	10:01	08:57
5	08:54	09:57	11:23	13:00	14:28	15:28	15:29	14:30	13:02	11:29	09:58	08:56
6	08:55	10:00	11:26	13:04	14:30	15:29	15:28	14:28	12:59	11:26	09:55	08:55
7	08:57	10:02	11:29	13:07	14:33	15:30	15:27	14:25	12:56	11:23	09:53	08:54
8	08:58	10:05	11:32	13:10	14:35	15:31	15:26	14:23	12:53	11:20	09:50	08:53
9	08:59	10:08	11:36	13:13	14:38	15:32	15:25	14:20	12:50	11:17	09:47	08:52
10	09:01	10:11	11:39	13:16	14:40	15:33	15:23	14:17	12:47	11:14	09:45	08:51
11	09:02	10:14	11:42	13:19	14:43	15:34	15:22	14:15	12:44	11:11	09:42	08:50
12	09:04	10:16	11:45	13:22	14:45	15:34	15:20	14:12	12:41	11:08	09:40	08:49
13	09:05	10:19	11:48	13:25	14:47	15:35	15:19	14:09	12:37	11:05	09:38	08:49
14	09:07	10:22	11:51	13:28	14:50	15:36	15:17	14:07	12:34	11:02	09:35	08:48
15	09:09	10:25	11:54	13:31	14:52	15:36	15:16	14:04	12:31	10:58	09:33	08:47
16	09:11	10:28	11:58	13:34	14:54	15:36	15:14	14:01	12:28	10:55	09:30	08:47
17	09:13	10:31	12:01	13:37	14:56	15:37	15:12	13:58	12:25	10:52	09:28	08:47
18	09:14	10:34	12:04	13:40	14:59	15:37	15:10	13:55	12:22	10:49	09:26	08:46
19	09:16	10:37	12:07	13:43	15:01	15:37	15:09	13:53	12:19	10:46	09:24	08:46
20	09:18	10:40	12:10	13:46	15:03	15:37	15:07	13:50	12:16	10:43	09:22	08:46
21	09:21	10:43	12:13	13:49	15:05	15:37	15:05	13:47	12:13	10:41	09:20	08:46
22	09:23	10:46	12:17	13:52	15:07	15:37	15:03	13:44	12:10	10:38	09:17	08:46
23	09:25	10:49	12:20	13:55	15:09	15:37	15:01	13:41	12:06	10:35	09:15	08:46
24	09:27	10:52	12:23	13:57	15:11	15:37	14:59	13:38	12:03	10:32	09:14	08:46
25	09:29	10:55	12:26	14:00	15:12	15:36	14:56	13:35	12:00	10:29	09:12	08:47
26	09:32	10:58	12:29	14:03	15:14	15:36	14:54	13:32	11:57	10:26	09:10	08:47
27	09:34	11:01	12:32	14:06	15:16	15:35	14:52	13:29	11:54	10:23	09:08	08:48
28	09:36	11:04	12:35	14:09	15:17	15:35	14:50	13:26	11:51	10:20	09:06	08:48
29	09:39	11:07	12:39	14:11	15:19	15:34	14:48	13:23	11:48	10:17	09:05	08:49
30	09:41		12:42	14:14	15:21	15:34	14:45	13:20	11:45	10:14	09:03	08:49
31	09:44		12:45		15:22		14:43	13:17		10:12		08:50
AVERAGE DURATION												
12.2 h												

Table 2 – Average day duration calculated at 37° latitude

This means that, averagely, every day the device receives an amount of energy of about 8000 Wh/m^2, which is equivalent to a specific solar power of 1000 W/m^2 which feeds the system for 8 h (see Fig. 31). In this way, the air mass coefficient AM 1.5 can be used, but applied to a daily period of time of 8 h, instead of 12 h. The decrease in day duration is, as stated before, due to real sky conditions.

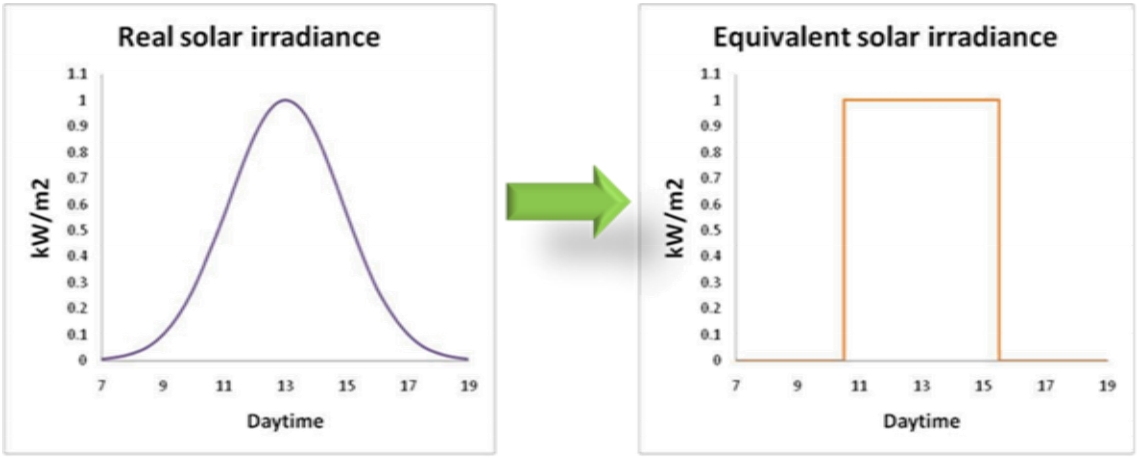

Fig. 31 – Conversion of real solar irradiance to equivalent solar irradiance

Assuming that the area of the Fresnel lens is 0.16 m^2, with a solar irradiance of 1000 W/m^2 and a concentrating factor of 500 suns, the area needed for the multi-junction solar cell to collect all the concentrated sunlight at the focal point is:

$$\boldsymbol{MJ\ area} = \frac{\boldsymbol{Fresnel\ area}}{\boldsymbol{conc\ factor}} = \frac{\mathbf{0.16\ m^2}}{\mathbf{500}} = \mathbf{3.2\ cm^2} = \mathbf{1.8x1.8\ cm^2} \qquad \text{Eq. 23}$$

While the overall solar irradiance after concentration is:

$$\boldsymbol{Irrad_{(500suns)}} = \boldsymbol{Irrad_{(1sun)}} \cdot \boldsymbol{conc\ factor} = 1000\frac{W}{m^2} \cdot 500 =$$
$$= \mathbf{500}\ \frac{\boldsymbol{kW}}{\boldsymbol{m^2}} \qquad \text{Eq. 24}$$

The PEM electrolyzer connected to the MJ solar cell can have dimensions up to the size of the Fresnel lens [53]. To reduce overvoltage losses and to work at lower current densities, high PEM electrolyzer areas would be preferred, but there are also other factors to be taken into account. Fig. 32 shows how both the concentration factor, indicated as "suns", and the ratio between the PEM electrolyzer area (EA) and the multi-junction solar cell area (MJA), shown as "EA/MJA", can strongly influence the matching of the two sub-systems, which should work at the maximum power point of the solar cell, to take advantage of all the potential of solar radiation. Therefore, even if the use of a high EA/MJA ratio (near the value of the concentration factor) could be suitable for the electrochemical process, the need for a perfect matching with the solar cell device forces to use smaller PEM electrolyzer areas.

For this study an EA/MJA ratio of 33 has been chosen, as a good compromise to meet the requirements above mentioned.

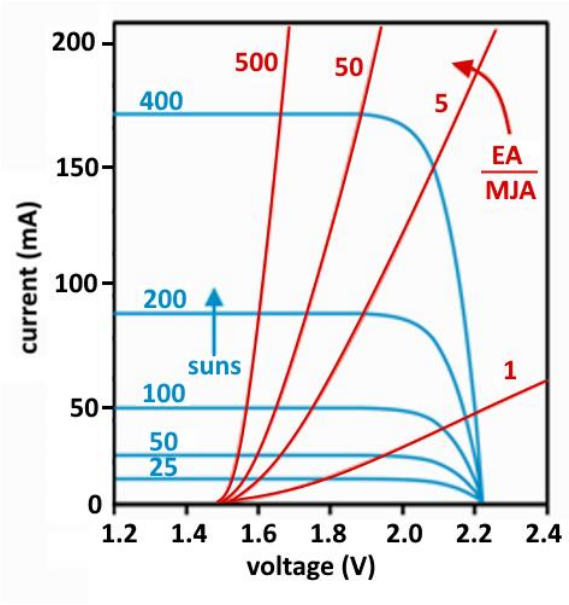

Fig. 32 – Effect of PEM area over MJ area ratio on the matching with solar cell

The electrolyzer area is then calculated:

$$\boldsymbol{A_{PEM}} = \boldsymbol{A_{MJ}} \cdot \left(\frac{\boldsymbol{EA}}{\boldsymbol{MJA}}\right) = 3.2\ cm^2 \cdot 33 = \mathbf{106\ cm^2} = \mathbf{10x10\ cm^2} \qquad \text{Eq. 25}$$

Since the PEM electrolyzer should stand high temperature and pressure, the thickness of the electrolyzer walls are supposed to be about s = 1 cm each, and composed by a $Ti_{0.95}Ta_{0.05}$ alloy [62] (suitable both for appropriate electrical contact and thermal resistance), the volume and weight of the MJ-PEM assembly are estimated:

$$\boldsymbol{V_{MJ-PEM}} = \boldsymbol{A_{PEM}} \cdot \boldsymbol{s} = 1056\ cm^2 \cdot 2\ cm = \mathbf{211\ cm^3} \qquad \text{Eq. 26}$$

$$\boldsymbol{m_{MJ-PEM}} = \boldsymbol{V_{MJ-PEM}} \cdot \boldsymbol{\rho_{Ti_{0.95}Ta_{0.05}}} = 211\ cm^3 \cdot 5.1\ \frac{g}{cm^3} =$$
$$= \mathbf{1.1\ kg} \qquad \text{Eq. 27}$$

3.2.1 Hydrogen production

The total power provided to the device is:

$$\boldsymbol{Tot\ power} = \boldsymbol{Irrad_{(1sun)}} \cdot \boldsymbol{Fresnel\ area} = 1000\ \frac{W}{m^2} \cdot 0.16\ m^2 =$$
$$= \mathbf{160\ W} \qquad \text{Eq. 28}$$

Considering an efficiency for the MJ solar cell equal to 30% and an efficiency of 67% for the PEM electrolyzer, thus assuming an overall efficiency of about 20% [53, 54, 63], the power which can be used for hydrogen production is:

$$\boldsymbol{H_2\ power} = \boldsymbol{Tot\ power} \cdot \boldsymbol{effic} = 160\ W \cdot 0.20 = \mathbf{32\ W} \qquad \text{Eq. 29}$$

By the Lower Heating Value (LHV) of hydrogen, which is also the standard enthalpy of formation of water (equal to the enthalpy associated with water splitting), the mass rate of hydrogen production can be obtained:

$$\dot{\boldsymbol{m}}_{\boldsymbol{H_2}} = \frac{\boldsymbol{H_2\ power}}{\boldsymbol{LHV_{H_2}}} = \frac{32\ W}{1.2{\cdot}10^5 \frac{J}{g}} \cdot 3600 = \mathbf{0.960\ \frac{g}{h}} \qquad \text{Eq. 30}$$

and, consequently, the volumetric rate from the ideal gas law:

$$\dot{\boldsymbol{V}}_{\boldsymbol{H_2}} = \frac{\dot{\boldsymbol{m}}_{\boldsymbol{H_2}}}{\boldsymbol{PM}_{\boldsymbol{H_2}}} \cdot \frac{\boldsymbol{RT}}{\boldsymbol{P}} = \frac{0.96\ \frac{g}{h}}{2\ \frac{g}{mol}} \cdot \frac{8.314\ \frac{J}{mol\ K} \cdot 298\ K}{101325\ Pa} = \mathbf{11.7\ \frac{Nl}{h}} \qquad \text{Eq. 31}$$

The same result would have been obtained using the water splitting potential, as the overpotential losses have been already considered in the PEM efficiency:

$$\mathbf{I} = \frac{\boldsymbol{H_2\ power}}{\boldsymbol{E_{H_2O}}} = \frac{\mathbf{32\ W}}{\mathbf{1.23\ V}} = \mathbf{26\ A} \qquad \text{Eq. 32}$$

$$\mathbf{i} = \frac{\mathbf{I}}{\boldsymbol{PEM\ area}} = \frac{26\ A}{106\ \text{cm}^2} = \mathbf{245\ \frac{mA}{cm^2}} \qquad \text{Eq. 33}$$

By Faraday's law:

$$\dot{\boldsymbol{m}}_{\boldsymbol{H_2}} = \frac{\mathbf{I}}{\mathbf{zF}} \cdot \boldsymbol{PM}_{\boldsymbol{H_2}} = \frac{26\ A}{2{\cdot}96500\ \frac{\text{C}}{\text{mol}}}\ \text{d} \cdot 2\frac{g}{mol} \cdot 3600 = \mathbf{0.968\ \frac{g}{h}} \qquad \text{Eq. 34}$$

Oxygen produced at the anodic side can be easily calculated from the stoichiometry of the water splitting reaction as:

$$\dot{\boldsymbol{V}}_{\boldsymbol{O_2}} = \frac{\dot{\boldsymbol{V}}_{\boldsymbol{H_2}}}{\mathbf{2}} = \frac{11.7\ \frac{Nl}{h}}{2} = \mathbf{5.9\ \frac{Nl}{h}} \qquad \text{Eq. 35}$$

$$\dot{\boldsymbol{m}}_{\boldsymbol{O_2}} = \frac{\boldsymbol{P} \cdot \dot{\boldsymbol{V}}_{\boldsymbol{O_2}}}{\boldsymbol{RT}} \cdot \boldsymbol{PM}_{\boldsymbol{O_2}} = \frac{101325\ Pa \cdot 5.9 \cdot 10^{-3}\ \frac{Nm^3}{h}}{8.314\ \frac{J}{mol\ K} \cdot 298\ K} \cdot 32\frac{g}{mol}$$

$$= \mathbf{7.768\ \frac{g}{h}} \qquad \text{Eq. 36}$$

3.2.2 Heat balance

The water consumed by the electrolysis reaction is:

$$\dot{m}_{H_2O\,el} = \dot{m}_{H_2} \cdot \frac{PM_{H_2O}}{PM_{H_2}} = 0.960\ \frac{g}{h} \cdot \frac{18\ \frac{g}{mol}}{2\ \frac{g}{mol}} = \mathbf{8.644\ \frac{g}{h}} \qquad \text{Eq. 37}$$

This wastewater flow is the minimum required to produce hydrogen and oxygen inside the PEM electrolyzer. Assuming that the wastewater entering the device is at 25°C and it leaves the electrolyzer at 150°C, the thermal power removed from the system is equal to:

$$\dot{Q}_{H2O\,min} = \dot{m}_{H_2O\,el} \cdot c_p \cdot \Delta T = \frac{8.644\ \frac{g}{h}}{3600} \cdot 4.186\ \frac{J}{g\ K} \cdot (150 - 25)K =$$

$$= \mathbf{1.3\ W} \qquad \text{Eq. 38}$$

while the thermal power provided to the system is:

$$\dot{Q} = Tot\ power - H_2\ power = 160\ W - 32\ W = \mathbf{128\ W} \qquad \text{Eq. 39}$$

which is a very high amount, compared to the one taken away by the minimum water flow. Some of the heat, however, is also removed as consequence of natural convection and radiance of the system.

Concerning the thermal power removed by free convection, one consideration needs to be made: natural convection is influenced by the inclination of the MJ-PEM reactor with the respect to the ground. As we are considering that the reactor is integrated with a two-axis solar tracking system, the inclination of the device is constantly changing. Therefore, an estimation of the free convection phenomenon both when the system is in vertical and in the horizontal position should be carried out, to evidence any possible difference between the two extreme cases.

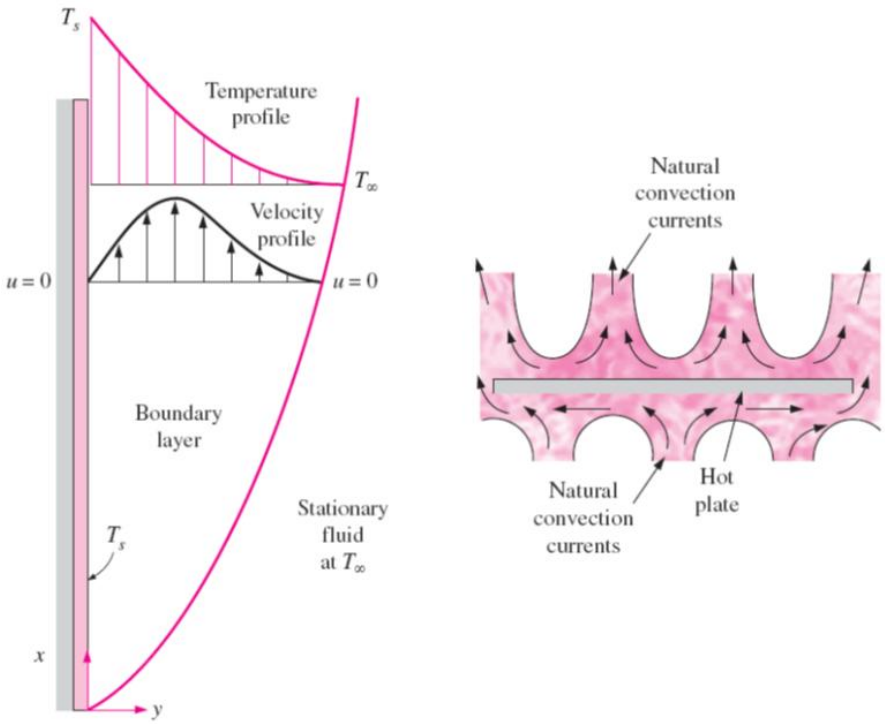

Fig. 33 – Free convection on a vertical and a horizontal plane

For this calculations, some air data are needed, in particular:

$$\rho\ (25°C) = 1.184\ \frac{kg}{m^3}$$
$$\rho\ (150°C) = 0.834\ \frac{kg}{m^3}$$
$$\mu\ (25°C) = 1.83 \cdot 10^{-5}\ Pa \cdot s$$
$$c_p\ (25°C) = 1004.80\ \frac{J}{kg\ K}$$
$$k\ (25°C) = 0.026\ \frac{W}{m\ K}$$

Heat loss by free convection (vertical plate)

If a vertical inclination is considered, then the Grashof (Gr_{vert}), Prandtl (Pr) and Rayleigh (Ra_{vert}) numbers can be determined by:

$$\boldsymbol{Gr_{vert}} = \frac{\boldsymbol{g \cdot \rho_{25} \cdot (\rho_{25} - \rho_{150}) \cdot L^3}}{\boldsymbol{\mu^2}} = \frac{\boldsymbol{9.81\ \frac{m}{s^2} \cdot 1.184\ \frac{kg}{m^3} \cdot (1.184 - 0.834)\ \frac{kg}{m^3} \cdot (0.1\ m)^3}}{\boldsymbol{(1.83 \cdot 10^{-5}\ Pa \cdot s)^2}} =$$

$$= \boldsymbol{1.32 \cdot 10^7} \qquad \text{Eq. 40}$$

where "L" is the characteristic (vertical) length of the system (i.e. the side of the PEM electrolyzer)

$$\boldsymbol{Pr} = \frac{\boldsymbol{\mu \cdot c_p}}{\boldsymbol{k}} = \frac{1.83 \cdot 10^{-5}\ Pa \cdot s \cdot 1004.8\ \frac{J}{kg\ K}}{0.026 \frac{W}{m\ K}} = \mathbf{0.71} \qquad \text{Eq. 41}$$

$$\boldsymbol{Ra_{vert}} = \boldsymbol{Gr_{vert}} \cdot \boldsymbol{Pr} = 1.32 \cdot 10^{7} \cdot 0.71 = \mathbf{9.32 \cdot 10^{6}} \qquad \text{Eq. 42}$$

If the Rayleigh number is minor than 10^9, air flow caused by free convection is in the laminar field, and the following correlation for the Nusselt number (Nu_{vert}) can be used:

$$\boldsymbol{Nu_{vert}} = \mathbf{0.59} \cdot (\boldsymbol{Ra_{vert}})^{\mathbf{0.25}} = 0.59 \cdot (9.32 \cdot 10^{6})^{0.25} = \mathbf{32.60} \qquad \text{Eq. 43}$$

The heat transfer coefficient (h_{vert}) for the natural convection in vertical orientation is:

$$\boldsymbol{h_{vert}} = \frac{\boldsymbol{Nu_{vert} \cdot k}}{\boldsymbol{L}} = \frac{32.6 \cdot 0.026\ \frac{W}{m\ K}}{0.1\ m} = \mathbf{8.25}\ \ \frac{\mathbf{W}}{\mathbf{m^2\ K}} \qquad \text{Eq. 44}$$

Finally, the heat removed by vertical natural convection (taking into account both faces of the reactor for the heat exchange) is:

$$\dot{\boldsymbol{Q}}_{\boldsymbol{vert}} = \mathbf{2} \cdot \boldsymbol{h_{vert}} \cdot \boldsymbol{L^2} \cdot \Delta \boldsymbol{T} = \mathbf{2} \cdot \mathbf{8.25} \frac{\boldsymbol{W}}{\boldsymbol{m^2\ K}} \cdot (\mathbf{0.1}\ \boldsymbol{m})^{\mathbf{2}} \cdot (\mathbf{150 - 25}) \boldsymbol{K} =$$
$$= \mathbf{21.8\ W} \qquad \text{Eq. 45}$$

Heat loss by free convection (horizontal plate)

If the system is horizontal, an "equivalent length" (L_{eq}) must be considered for the next calculations:

$$\boldsymbol{L_{eq}} = \frac{\boldsymbol{L^2}}{\boldsymbol{4L}} = \frac{(0.1\ m)^2}{4 \cdot 0.1\ m} = \mathbf{0.025\ m} \qquad \text{Eq. 46}$$

Then, the Grashof (Gr_{hor}), Prandtl (Pr) and Rayleigh (Ra_{hor}) numbers can be determined as before:

$$\boldsymbol{Gr_{hor}} = \frac{\boldsymbol{g \cdot \rho_{25} \cdot (\rho_{25} - \rho_{150}) \cdot L_{eq}^{3}}}{\boldsymbol{\mu^2}} = \frac{9.81\ \frac{m}{s^2} \cdot 1.184\ \frac{kg}{m^3} \cdot (1.184 - 0.834)\ \frac{kg}{m^3} \cdot (0.025\ m)^3}{(1.83 \cdot 10^{-5}\ Pa \cdot s)^2} =$$
$$= \mathbf{2.01 \cdot 10^{5}} \qquad \text{Eq. 47}$$

$$\boldsymbol{Pr} = \frac{\boldsymbol{\mu \cdot c_p}}{\boldsymbol{k}} = \frac{1.83 \cdot 10^{-5}\ Pa \cdot s \cdot 1004.8\ \frac{J}{kg\ K}}{0.026 \frac{W}{m\ K}} = \mathbf{0.71} \qquad \text{Eq. 48}$$

$$\boldsymbol{Ra_{hor}} = \boldsymbol{Gr_{hor}} \cdot \boldsymbol{Pr} = 2.01 \cdot 10^5 \cdot 0.71 = \mathbf{1.46 \cdot 10^5} \quad \text{Eq. 49}$$

The Nusselt number for horizontal plates must be calculated with two different correlations for the upper and the lower face. The Rayleigh number is in the range $10^4 < Ra < 10^7$, then the following formulas can be applied:

$$\boldsymbol{Nu_{hor\_up}} = \mathbf{0.54} \cdot \boldsymbol{Ra_{hor}}^{\mathbf{0.25}} = 0.54 \cdot (1.46 \cdot 10^5)^{0.25} = \mathbf{10.55} \quad \text{Eq. 50}$$

$$\boldsymbol{Nu_{hor\_low}} = \mathbf{0.27} \cdot (\boldsymbol{Ra_{vert}})^{\mathbf{0.25}} = 0.27 \cdot (1.46 \cdot 10^5)^{0.25} = \mathbf{5.27} \quad \text{Eq. 51}$$

The heat removed then is:

$$\boldsymbol{h_{hor\_up}} = \frac{\boldsymbol{Nu_{hor\_up}} \cdot \boldsymbol{k}}{\boldsymbol{L_{eq}}} = \frac{10.55 \cdot 0.026 \frac{W}{m\ K}}{0.025\ m} = \mathbf{10.68}\ \frac{\mathbf{W}}{\mathbf{m^2\ K}} \quad \text{Eq. 52}$$

$$\boldsymbol{h_{hor\_low}} = \frac{\boldsymbol{Nu_{hor\_low}} \cdot \boldsymbol{k}}{\boldsymbol{L_{eq}}} = \frac{5.27 \cdot 0.026 \frac{W}{m\ K}}{0.025\ m} = \mathbf{5.34}\ \frac{\mathbf{W}}{\mathbf{m^2\ K}} \quad \text{Eq. 53}$$

$$\dot{\boldsymbol{Q}}_{\boldsymbol{hor}} = \left(\boldsymbol{h_{hor_{up}}} + \boldsymbol{h_{hor_{low}}}\right) \cdot \boldsymbol{L^2} \cdot \Delta \boldsymbol{T} = (10.68 + 5.34)\frac{W}{m^2\ K} \cdot (0.1\ m)^2 \cdot (150 - 25)K$$

$$= \mathbf{21.1\ W} \quad \text{Eq. 54}$$

The heat removed in both cases (i.e. vertical or horizontal orientation) is approximately the same, so an average value of **21.5 W** can be supposed for free convection.

Heat loss by radiance

Hypothesizing that emissivity of Ti-Ta alloy is about ε = 0.50, then the heat dispersed by irradiation can be calculated as:

$$\dot{\boldsymbol{Q}}_{\boldsymbol{rad}} = (\mathbf{2} \cdot \boldsymbol{L^2} + \mathbf{4} \cdot \boldsymbol{L} \cdot \boldsymbol{s}) \cdot \boldsymbol{\varepsilon} \cdot \boldsymbol{\sigma} \cdot \left(\boldsymbol{T^4_{MJ-PEM}} - \boldsymbol{T^4_{\infty}}\right) =$$
$$= (2 \cdot 0.1^2 + 4 \cdot 0.1 \cdot 0.02)m^2 \cdot 0.5 \cdot 5.67 \cdot 10^{-8} \cdot (423^4 - 298^4) =$$
$$= \mathbf{20.1\ W} \quad \text{Eq. 55}$$

Therefore, the heat power which still needs to be removed is:

$$\dot{Q}_{res} = \dot{Q} - \dot{Q}_{H2O\,min} - \dot{Q}_{free} - \dot{Q}_{rad} = (128 - 1.3 - 21.5 - 20.1)\,W = \\ = \mathbf{85.1\ W} \qquad \text{Eq. 56}$$

The thermal equilibrium can be reached through two different procedures:

1) Extension of the MJ-PEM area by installation of a collar, to enhance both free convection and irradiance through the increase of the exchange surface
2) Increase in the wastewater flow inside the electrolyzer, circulating the excess in case of too low residence times for the complete mineralization of refractory organics

1) Installation of a collar

The calculations for the heat losses caused by free convection and radiance used are the same used before, without any collar.
For the sake of brevity, only the results will be showed from here on, as only the characteristic length of the system was changed, from L = 10 cm to **L = 22 cm**.

$$\mathbf{Gr_{vert} = 1.27 \cdot 10^8} \qquad \text{Eq. 57}$$

$$\mathbf{Pr = 0.71} \qquad \text{Eq. 58}$$

$$\mathbf{Ra_{vert} = 8.99 \cdot 10^7} \qquad \text{Eq. 59}$$

The Rayleigh number is again < 10^9, so the air flow is still under laminar conditions. The same correlation for the Nusselt number can be used:

$$\mathbf{Nu_{vert} = 57.45} \qquad \text{Eq. 60}$$

$$\mathbf{h_{vert} = 6.83\ \frac{W}{m^2\,K}} \qquad \text{Eq. 61}$$

$$\mathbf{\dot{Q}_{vert} = 81.0\ W} \qquad \text{Eq. 62}$$

The new equivalent length is:

$$\mathbf{L_{eq} = \frac{L^2}{4L}} = \frac{(0.22\ m)^2}{4 \cdot 0.22\ m} = \mathbf{0.055\ m} \qquad \text{Eq. 63}$$

$$\boldsymbol{Gr_{hor} = 1.99 \cdot 10^6}$$ Eq. 64

$$\boldsymbol{Pr = 0.71}$$ Eq. 65

$$\boldsymbol{Ra_{hor} = 1.40 \cdot 10^6}$$ Eq. 66

Again, the Rayleigh number is in the range $10^4 < Ra < 10^7$:

$$\boldsymbol{Nu_{hor\_up} = 18.59}$$ Eq. 67

$$\boldsymbol{Nu_{hor\_low} = 9.30}$$ Eq. 68

$$\boldsymbol{h_{hor\_up} = 8.84 \ \frac{W}{m^2 K}}$$ Eq. 69

$$\boldsymbol{h_{hor\_low} = 4.42 \ \frac{W}{m^2 K}}$$ Eq. 70

$$\boldsymbol{\dot{Q}_{hor} = 78.7 \ W}$$ Eq. 71

As can be seen, the heat transfer due to *free convection* is four times higher when the collar is installed, and it is averagely equal to **80.5 W**.

$$\boldsymbol{\dot{Q}_{rad} = 47.2 \ W}$$ Eq. 72

The heat losses by *radiation*, instead, are more than doubled.

The heat balance after the installation of a collar with dimensions 22x22 cm^2:

$$\boldsymbol{\dot{Q}_{res} = \dot{Q} - \dot{Q}_{H2O\ min} - \dot{Q}_{free} - \dot{Q}_{rad}} = (128 - 1.3 - 80.5 - 47.2)\ W = \\ = \boldsymbol{0.3 \ W}$$ Eq. 73

2) Increase of wastewater flow with recirculation

If no collar is installed, then the excess heat must be removed by increasing the water flow inside the electrolyzer. The total amount of wastewater needs to be equal to:

$$\boldsymbol{\dot{m}_{H_2O}} = \boldsymbol{\dot{m}_{H_2O\ el}} + \frac{\boldsymbol{\dot{Q}_{res}}}{\boldsymbol{c_p \cdot \Delta T}} = 8.644 \ \frac{g}{h} + \frac{85.1\ W}{4.186 \ \frac{J}{g\ K} \cdot (150-25)\ K} = \boldsymbol{595.830 \ \frac{g}{h}}$$ Eq. 74

which is a very high value compared to the one necessary for the electrolysis. Residence time inside the electrolyzer was checked, assuming that the volume inside the PEM electrolyzer is given by:

$$\mathbf{V_{PEM}} = \frac{\mathbf{A_{PEM}}}{\mathbf{2}} \cdot \mathbf{d_c} = \frac{(100\ mm)^2}{2} \cdot 2\ mm = \mathbf{10^4\ mm^3} \qquad \text{Eq. 75}$$

where d_c is the dimension of the channel, and the area is divided by two, considering the pathway of the wastewater flow as shown in Fig. 34

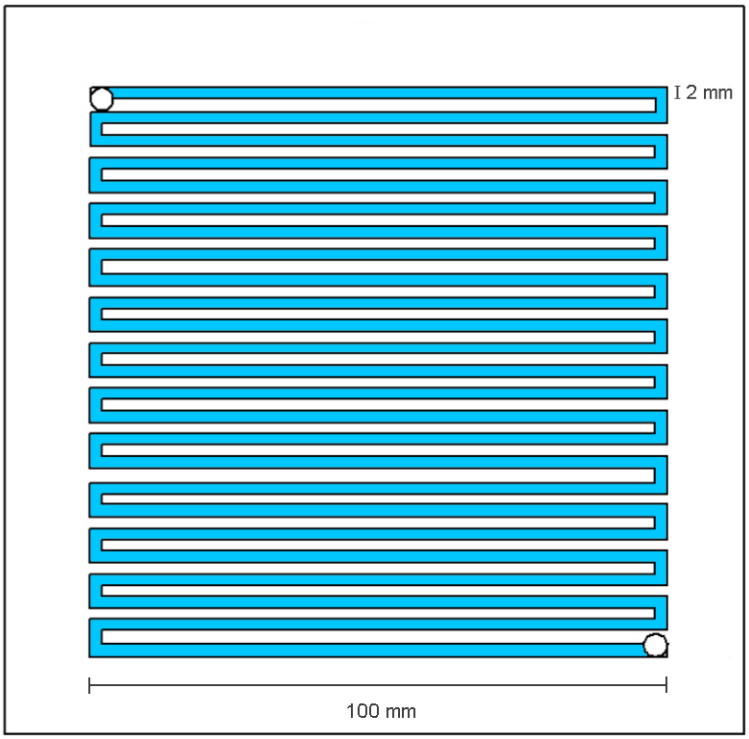

Fig. 34 - Pathway of wastewater inside the PEM electrolyzer

$$\mathbf{t_{res}} = \frac{\boldsymbol{\rho} \cdot \mathbf{V_{PEM}}}{\dot{\boldsymbol{m}}_{\boldsymbol{H_2O}}} = \frac{918\ \frac{kg}{m^3} \cdot 10^4\ \mathrm{mm}^3}{595.83\ \frac{g}{h}} \cdot \left(\frac{60}{10^6}\right) = \mathbf{1.1\ min} \qquad \text{Eq. 76}$$

This value seems very low, if compared to typical CWAO residence times, that are higher than 30 minutes [16, 56, 57]. However, due to the high current delivered to the system by the MJ solar cell (**I = 26 A**), the oxygen evolved is potentially more than enough to mineralize the wastewater. In fact, using the mass production of oxygen, calculated before, the MJ-PEM system could treat a wastewater containing a theoretical value of Chemical Oxygen Demand (COD_{th}):

$$\boldsymbol{COD_{th}} = \frac{\dot{\boldsymbol{m}}_{\boldsymbol{O_2}}}{\dot{\boldsymbol{m}}_{\boldsymbol{H_2O}}} \cdot \boldsymbol{\rho} = \frac{7.768\ \frac{g}{h}}{595.83\ \frac{g}{h}} \cdot 918\ \frac{g}{l} = \mathbf{11.96\ \frac{g}{l}} \qquad \text{Eq. 77}$$

which is very high, especially for diluted wastewaters coming from municipal, industrial or agricultural activities [64].

In addition, a possible circulation can be implemented, as represented in Fig. 30, to ensure the complete degradation of the recalcitrant organics.

Even though increasing the circulation of water seems to be more demanding than simply installing a collar, thus, the former solution could be the most suitable, especially when applied to a discontinuous process as the photovoltaic system is. Indeed, the use of a fixed-dimension collar, in the case of lower air/wastewater temperatures and the presence of strong winds could bring excessive heat losses, leading to a consequent decrease in the operative temperature. Moreover, the real problem could occur when the heat dispersion has to be increased to avoid extreme temperatures, which could compromise the device.

Thus, the choice of wastewater as thermal control should be considered as preferable in order to have a more flexible system, in addition to the possibility to exploit the heat removed in a heat exchanger (see Fig. 30).

One more consideration is made about the time required to reach the steady-state, i.e. the temperature of 150°C. Three different transients were analyzed:

a) No heat dispersion

Firstly, the heat capacity of the sole MJ-PEM device (i.e. not considering the amount of water inside the electrolyzer) was estimated.

$$\boldsymbol{C_{MJ-PEM\_1} = m_{MJ-PEM} \cdot \left(0.95 \cdot c_{p\,Ti} + 0.05 c_{p\,Ta}\right) =}$$
$$= 1.1\ kg \cdot (0.95 \cdot 540 + 0.05 \cdot 140)\ \frac{J}{kg\ K} = \mathbf{520\ \frac{J}{K}} \qquad \text{Eq. 78}$$

Only the heat power provided by the concentrated solar was considered, neglecting the heat losses due to free convection and radiation, which could not occur in real conditions, but is useful to identify the lowest limit for the heating time:

$$\boldsymbol{\Delta t_{heat\_1} = \frac{C_{MJ-PEM\_1} \cdot \Delta T}{\dot{Q}}} = \frac{520\ \frac{J}{K} \cdot (150-25)\ K}{128\ W} = \mathbf{8.5\ min} \qquad \text{Eq. 79}$$

b) MJ-PEM heat dispersion

In this case, heat losses from the minimum water flow, the free convection, and the radiance were considered, taking into account that the temperature of the device is constantly rising, thus changing the driving forces ΔT and $(T^4\text{-}T_\infty{}^4)$.

The temperature profile is indicated in Fig. 35 as a blue line.

$$\Delta t_{heat\_2} = \mathbf{10.8\ min}$$ Eq. 80

c) Collar/water increase heat dispersion

For this calculations, both the collar installation and the increase in water flow were considered, leading to the same result, shown in Fig. 35 as a green curve. As heat balance is obtained while approaching the set point temperature, T = 150°C is an asymptote, so theoretically $\Delta t_{heat\_3} \rightarrow \infty$. However, the system reaches 145°C after less than 30 minutes.

$$\Delta t_{heat\_3} = \mathbf{29.8\ min}$$ Eq. 81

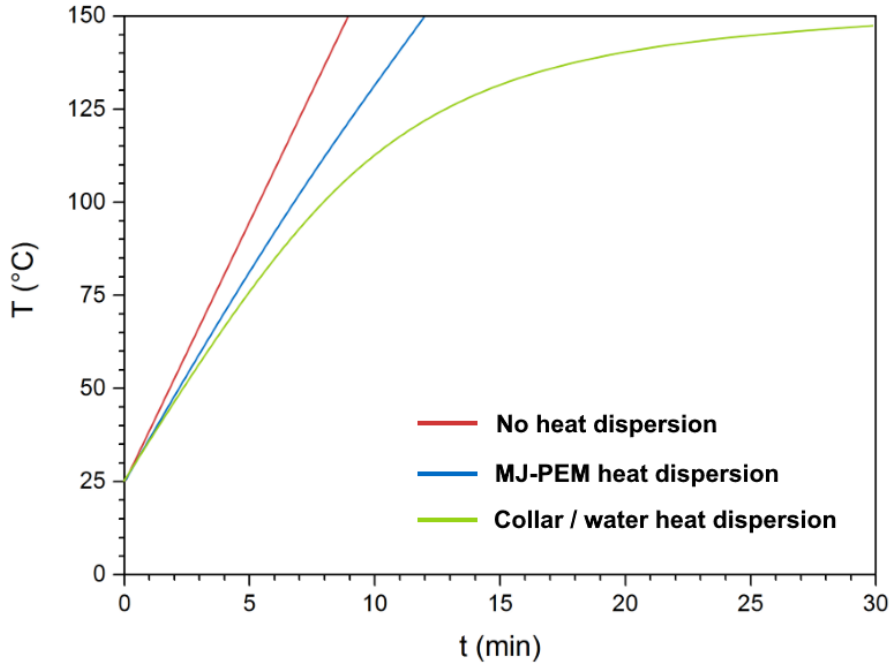

Fig. 35 - Temperature profile of the MJ-PEM during the start-up phase in different conditions

3.3 Scenario II – Matching with anaerobic digestion (AD)

In this scenario, the same MJ-PEM reactor is used for a different purpose: the system is connected in series with the methanogenic step of an anaerobic digester (AD). Hydrogen is sent to boost the upgrading of the biogas produced by anaerobic fermentation [65, 66]:

$$CO_2 + 4H_2 = CH_4 + 2H_2O \qquad \text{Eq. 82}$$

To investigate all the possible ways to match the MJ-PEM reactor with the anaerobic digestion, two processes will be taken into account: mesophilic and thermophilic digestion.

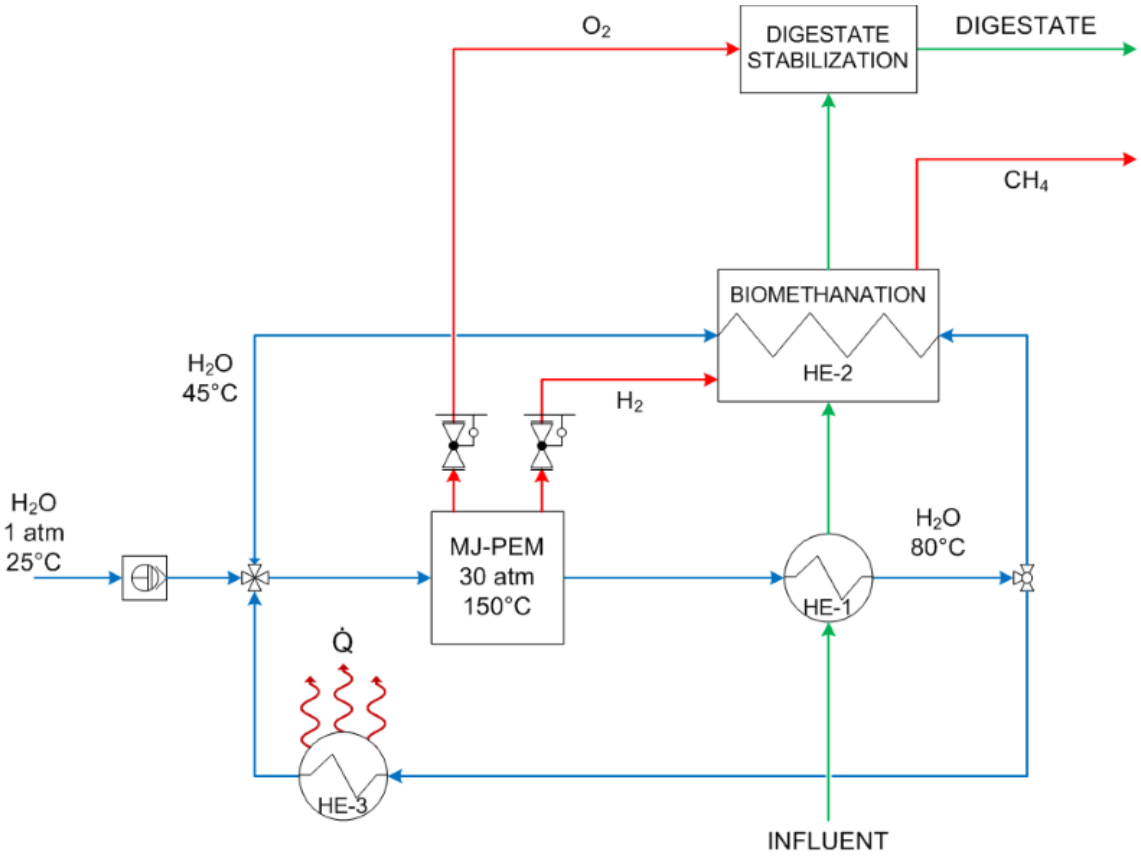

Fig. 36 - Scheme of MJ-PEM arrangement for the upgrading of biogas from an anaerobic digestion process

3.3.1 MJ-PEM and mesophilic anaerobic digestion

Typical ranges of working conditions for a mesophilic anaerobic digester are listed below in Table 3, together with the chosen operative conditions for this study:

PARAMETER	TYPICAL RANGES [5, 7, 67-69]	SELECTED VALUE
Temperature °C	30 – 38	**35**
Biogas yield Nm^3 / kg_{VS}	0.2 – 0.5	**0.3**
Organic load $kg_{VS} / (m^3_{AD}\ d)$	7.5 – 15	**10**
Residence time d	25 – 45	**35**
VS conc %	5 – 12	**8**
CO_2 conc in biogas %	25 – 45	**35**
Influent COD $kg\ O_2 / m^3$	> 20	**30**

Table 3 – Common ranges of operative conditions for a mesophilic anaerobic digester and values chosen for the design

From the biogas yield and the organic load in Table 3, the specific biogas production rate can be obtained:

$$\dot{V}_{biogas} = \textbf{biogas yield} \cdot \textbf{organic load} = 0.3\ \frac{Nm^3}{kg_{VS}} \cdot 10\ \frac{kg_{VS}}{m^3_{AD}\ d} = \mathbf{3}\ \frac{\mathbf{Nm^3}}{\mathbf{m^3_{AD}\cdot d}} \quad \text{Eq. 83}$$

which can be divided into methane and carbon dioxide specific production, according to the selected concentration of CO_2 in the biogas:

$$\dot{V}_{CH_4} = \dot{V}_{biogas} \cdot \mathbf{0.65} = 3\ \frac{Nm^3}{m^3_{AD}\ d} \cdot 0.65 = \mathbf{1.95}\ \frac{\mathbf{Nm^3}}{\mathbf{m^3_{AD}\cdot d}} \quad \text{Eq. 84}$$

$$\dot{V}_{CO_2} = \dot{V}_{biogas} \cdot \mathbf{0.35} = 3\ \frac{Nm^3}{m^3_{AD}\ d} \cdot 0.35 = \mathbf{1.05}\ \frac{\mathbf{Nm^3}}{\mathbf{m^3_{AD}\cdot d}} \quad \text{Eq. 85}$$

Hydrogen requirements

Assuming an efficiency of 90% [65, 66] for the bio-methanation reaction (Eq. 82), then the specific hydrogen rate needed for the completion of the process is:

$$\dot{V}_{H_2\,req} = \frac{\dot{V}_{CO_2}}{\mathbf{0.90}} \cdot \mathbf{4} = \frac{1.05\ \frac{Nm^3}{m^3_{AD}\,d}}{0.90} \cdot 4 = \mathbf{4.67}\ \frac{\mathbf{Nm^3}}{\mathbf{m^3_{AD}\cdot d}} \qquad \text{Eq. 86}$$

This value must be compared to the one produced by a single MJ-PEM reactor, to check how many devices are required to fulfill the needs of the anaerobic digestion process.

The volumetric rate of hydrogen (Eq. 31) evolved at the cathode of the electrolyzer is **11.7 Nl/h**. However, the daily production is limited to 8 h/d, as stated in paragraph •, due to the application of the equivalent solar irradiance:

$$MJ - PEM_{H_2} = \frac{\dot{V}_{H_2\,req}}{\dot{V}_{H_2}} = \frac{4.67\ \frac{Nm^3}{m^3_{AD}\,d}}{11.7 \cdot 10^{-3}\ \frac{Nm^3}{h} \cdot 8\ \frac{h}{d}} = 49.9\ \mathrm{m^{-3}} = \mathbf{50\ m^{-3}} \qquad \text{Eq. 87}$$

Then the number of needed MJ-PEMs for hydrogen production are 50 per volume of bio-methanation reactor.

Though they are a rather high number, the utilization of the MJ-PEM device at high temperatures (150°C) can be useful to exploit the heat excess generated by the concentrated sunlight to pre-heat and pre-treat the influent (up to 70°C or more to remove all pathogens [6, 70]) and to compensate the heat dispersion of the anaerobic reactor.

Heat requirements

Usually, in anaerobic digestion plants, the 20-30% [5] of the methane produced is used for the thermal requirements of the process above mentioned, depending on the external conditions and the latitudes [71]:

$$\dot{V}_{CH_4\,heat} = \dot{V}_{CH_4} \cdot \mathbf{0.20} = 1.95\ \frac{Nm^3}{m^3_{AD}\,d} \cdot 0.20 = \mathbf{0.39}\ \frac{\mathbf{Nm^3}}{\mathbf{m^3_{AD}\cdot d}} \qquad \text{Eq. 88}$$

$$\dot{Q}_{heat} = \dot{V}_{CH_4} \cdot LHV_{CH_4} = 0.39\ \frac{Nm^3}{m^3_{AD}\,d} \cdot 35.7\ \frac{MJ}{Nm^3} = \mathbf{13.92}\ \frac{\mathbf{MJ}}{\mathbf{m^3_{AD}\cdot d}} \qquad \text{Eq. 89}$$

Which is also similar to the most common values found in the literature. To double-check this value, another calculation has been made. Considering to heat the influent from 10°C to 35°C, and to compensate the heat dispersion through the walls of the digester (average external temperature of 20°C, weighted all over the year):

$$\dot{Q}_{heat} = \dot{m}_{in} \cdot c_p \cdot (T_{AD} - T_{in}) + U \cdot \left(\frac{A}{V}\right)_{AD} \cdot (T_{AD} - T_{ext}) =$$

$$= \frac{10 \frac{kg_{VS}}{m^3_{AD}\ d}}{0.08} \cdot 4.186 \cdot 10^{-3} \frac{MJ}{kg\ K} \cdot (35-10)K + 24 \cdot 3600 \cdot 10^{-6} \frac{MW}{m^2\ K} \cdot 0.7 \frac{m^2}{m^3} \cdot$$

$$(35-20)K = (13.08 + 0.91) \frac{MJ}{m^3_{AD}\ d} = \mathbf{13.99} \frac{\mathbf{MJ}}{\mathbf{m^3_{AD} \cdot d}} \qquad \text{Eq. 90}$$

Where c_p was estimated similar to the one of water, due to high dilution of the influent, and the overall heat transfer coefficient "U" for concrete walls was applied. The (A/V) ratio of the digester was estimated according to common digester geometries [71]. As can be seen, the two values are almost equal. Therefore the assumptions were proven to be corrected.

The heat power taken away from a single MJ-PEM system by the wastewater, which could be exploited, is:

$$\dot{Q}_{MJ-PEM} = \dot{m}_{H_2O} \cdot c_p \cdot \left(T_{MJ-PEM} - T_{min\ out}\right) =$$

$$= 596 \frac{g}{h} \cdot 8 \frac{h}{d} \cdot 4.186 \cdot 10^{-6} \frac{MJ}{g\ K} \cdot (150-45)K = \mathbf{2.10} \frac{\mathbf{MJ}}{\mathrm{d}} \qquad \text{Eq. 91}$$

where 45°C is the minimum outlet temperature, to avoid the pinch point in the second heat exchanger HE-2 in Fig. 36 (ΔT across heat exchangers is usually set between 5 and 15°C).

Therefore, the number of MJ-PEM reactors to fulfill the thermal demand of the mesophilic process are:

$$MJ - PEM_{heat} = \frac{\dot{Q}_{heat}}{\dot{Q}_{MJ-PEM}} = \frac{13.92 \frac{MJ}{m^3_{AD}\ d}}{2.10 \frac{MJ}{m^3_{AD}\ d}} = 6.6\ \mathrm{m}^{-3} = \mathbf{7\ m^{-3}} \qquad \text{Eq. 92}$$

The thermal requirements, then, could be fully satisfied by just 7 MJ-PEM devices per cubic meter of digester, which is seven times less than the systems needed for hydrogen production.

Some of the heat could be then used to disinfect the slurry, heating it up to 70°C in the first heat exchanger HE-1 in Fig. 36, which was proven to be an effective method to also enhance the biogas yield [70]. Thus, the number of MJ-PEM becomes **15 m^{-3}**.

A third heat exchanger can be implemented to recover the remaining power heat (e.g. to heat the workplace during winter), provided by the remaining 35 m^{-3} reactors used for the hydrogen production.

Oxygen requirements

The last consideration concerns the utilization of the generated oxygen, which could be sent to the stabilization of the digestate. The digestate, whose volume is approximately 90-95% and whose COD content is 20-30% of the influent volume, is largely composed of putrescible compounds which need to be stabilized, potential pathogens and viruses which must be eliminated. There are some methods suitable for this purpose, one of which is the aerobic stabilization, achievable by aerating the digestate under mechanical mixing for an adequate retention time.

Assuming the above mentioned volume and COD reductions after anaerobic digestion, the volumetric flow of digestate can be calculated:

$$\dot{V}_{dig} = \frac{\dot{m}_{in}}{\rho_{in}} \cdot \mathbf{0.90} = \frac{\frac{10}{0.08}\frac{kg_{VS}}{m^3_{AD}\ d}}{1000\ \frac{kg}{m^3}} \cdot 0.90 = 0.113 \frac{\mathrm{m}^3}{\mathrm{m}^3_{\mathrm{AD}} \cdot \mathrm{d}} = \mathbf{4.688}\ \frac{\mathbf{L}}{\mathbf{m}^3_{\mathrm{AD}} \cdot \mathrm{h}} \qquad \text{Eq. 93}$$

and the Chemical Oxygen Demand requirements:

$$\boldsymbol{COD_{dig}} = \boldsymbol{COD_{in}} \cdot \mathbf{0.30} = 30\ \frac{\mathrm{g}}{\mathrm{L}} \cdot 0.30 = \mathbf{9}\ \frac{\mathbf{g_{COD}}}{\mathbf{L}} \qquad \text{Eq. 94}$$

$$\dot{\boldsymbol{m}}_{\boldsymbol{COD}} = \boldsymbol{COD_{dig}} \cdot \dot{\boldsymbol{V}}_{\boldsymbol{dig}} = 4.688 \frac{L}{m^3_{AD} \cdot d} \cdot 9\ \frac{g_{COD}}{L} = \mathbf{42.188}\ \frac{\mathbf{g_{COD}}}{\mathbf{m}^3_{\mathrm{AD}} \cdot \mathrm{h}} \qquad \text{Eq. 95}$$

which results in a specific oxygen flow (normal conditions):

$$\dot{V}_{O_2\,req} = \dot{\boldsymbol{m}}_{\boldsymbol{COD}} \cdot \frac{\boldsymbol{R \cdot T}}{\boldsymbol{P \cdot PM_{O_2}}} = 42.188\ \frac{g_{COD}}{m^3_{AD} \cdot h} \cdot \frac{8.314\ \frac{J}{mol\ K} \cdot 298\ K}{101325\ Pa \cdot 32\ \frac{g}{mol}} = \mathbf{32.2}\ \frac{\mathbf{Nl}}{\mathbf{m}^3_{\mathrm{AD}} \cdot \mathrm{h}} \qquad \text{Eq. 96}$$

An Oxygen Transfer Efficiency (OTE) must be applied to this value, as not all the oxygen is transferred to the digestate. Average specific OTE (SOTE) values for air distributors with fine bubbles are 6%/m. If the distributors are placed at about 3 m depth of the digestate stabilization reactor, then the OTE is roughly 18%:

$$\dot{V}_{O_2\,req} = \frac{32.2\ \frac{Nl}{m^3_{AD} \cdot h}}{0.18} = \mathbf{178.9}\ \frac{\mathbf{Nl}}{\mathbf{m}^3_{\mathrm{AD}} \cdot \mathrm{h}} \qquad \text{Eq. 97}$$

Each MJ-PEM reactor can provide **5.9 Nl/h**, then:

$$\boldsymbol{MJ-PEM_{O_2}} = \frac{\dot{V}_{O_2\,req}}{\dot{V}_{O_2\,MJ-PEM}} = \frac{178.9\,\frac{Nl}{m^3_{AD}\cdot h}}{5.9\,\frac{Nl}{h}} = 30.2\ \mathrm{m}^{-3} = \mathbf{31\ m^{-3}} \qquad \text{Eq. 98}$$

3.3.2 MJ-PEM and thermophilic anaerobic digestion

Thermophilic anaerobic digester usually can produce a higher specific rate of biogas (the double or more), with lower residence times. However, biogas purity is more limited, with a higher content of CO_2. Operative parameters of thermophilic digestion are listed in Table 4:

PARAMETER	TYPICAL RANGES [5, 7, 67-69, 72]	SELECTED VALUE
Temperature °C	50 – 65	**55**
Biogas yield Nm^3 / kg_{VS}	0.4 – 0.8	**0.5**
Organic load $kg_{VS} / (m^3_{AD}\ d)$	9 – 18	**12**
Residence time d	7 – 15	**10**
VS conc %	7 – 14	**10**
CO_2 conc in biogas %	30 – 50	**40**
Influent COD $kg\ O_2 / m^3$	> 25	**50**

Table 4 – Common ranges of operative conditions for a thermophilic anaerobic digester and values chosen for the design

For the sake of brevity, calculations are shown below, in the same order as for the mesophilic digestion:

$$\dot{V}_{biogas} = \boldsymbol{biogas\ yield} \cdot \boldsymbol{organic\ load} = 0.5\ \frac{Nm^3}{kg_{VS}} \cdot 12\ \frac{kg_{VS}}{m^3_{AD}\ d} = \mathbf{3\ \frac{Nm^3}{m^3_{AD}\cdot d}} \qquad \text{Eq. 99}$$

$$\dot{V}_{CH_4} = \dot{V}_{biogas} \cdot \mathbf{0.60} = 6\ \frac{Nm^3}{m_{AD}^3\ d} \cdot 0.60 = \mathbf{3.60}\ \frac{\mathbf{Nm^3}}{\mathbf{m_{AD}^3 \cdot d}} \quad \text{Eq. 100}$$

$$\dot{V}_{CO_2} = \dot{V}_{biogas} \cdot \mathbf{0.40} = 6\ \frac{Nm^3}{m_{AD}^3\ d} \cdot 0.40 = \mathbf{2.40}\ \frac{\mathbf{Nm^3}}{\mathbf{m_{AD}^3 \cdot d}} \quad \text{Eq. 101}$$

Hydrogen requirements

Assuming again an efficiency of 90% [65, 66] for the bio-methanation reaction (Eq. 82):

$$\dot{V}_{H_2\ req} = \frac{\dot{V}_{CO_2}}{\mathbf{0.90}} \cdot \mathbf{4} = \frac{2.40\ \frac{Nm^3}{m_{AD}^3\ d}}{0.90} \cdot 4 = \mathbf{10.67}\ \frac{\mathbf{Nm^3}}{\mathbf{m_{AD}^3 \cdot d}} \quad \text{Eq. 102}$$

$$\boldsymbol{MJ - PEM_{H_2}} = \frac{\dot{V}_{H_2\ req}}{\dot{V}_{H_2}} = \frac{10.67\ \frac{Nm^3}{m_{AD}^3\ d}}{11.7 \cdot 10^{-3}\ \frac{Nm^3}{h} \cdot 8\ \frac{h}{d}} = 113.9\ \mathrm{m^{-3}} = \mathbf{114\ m^{-3}} \quad \text{Eq. 103}$$

The number of needed MJ-PEMs for hydrogen production are 114 per volume of thermophilic digester, more than the double compared with the mesophilic process, due to higher biogas yields and CO_2 concentration.

Heat requirements

$$\dot{V}_{CH_4\ heat} = \dot{V}_{CH_4} \cdot \mathbf{0.20} = 3.60\ \frac{Nm^3}{m_{AD}^3\ d} \cdot 0.20 = \mathbf{0.72}\ \frac{\mathbf{Nm^3}}{\mathbf{m_{AD}^3 \cdot d}} \quad \text{Eq. 104}$$

$$\dot{Q}_{heat} = \dot{V}_{CH_4} \cdot \boldsymbol{LHV_{CH_4}} = 0.72\ \frac{Nm^3}{m_{AD}^3\ d} \cdot 35.7\ \frac{MJ}{Nm^3} = \mathbf{25.70}\ \frac{\mathbf{MJ}}{\mathbf{m_{AD}^3 \cdot d}} \quad \text{Eq. 105}$$

With similar considerations, the heat requirement was double checked by:

$$\dot{Q}_{heat} = \dot{m}_{sludge} \cdot c_p \cdot (T_{AD} - T_{sludge}) + U \cdot \left(\frac{A}{V}\right)_{AD} \cdot (T_{AD} - T_{ext}) =$$

$$= \frac{12\ \frac{kg\ VS}{m_{AD}^3\ d}}{0.10} \cdot 4.186 \cdot 10^{-3}\ \frac{MJ}{kg\ K} \cdot (55 - 10)K + 24 \cdot 3600 \cdot 10^{-6}\ \frac{MW}{m^2\ K} \cdot 0.7\ \frac{m^2}{m^3} \cdot$$

$$(55 - 20)K = (22.60 + 2.12)\ \frac{MJ}{m_{AD}^3\ d} = \mathbf{24.72}\ \frac{\mathbf{MJ}}{\mathbf{m_{AD}^3 \cdot d}} \quad \text{Eq. 106}$$

which again confirms the adequate estimation of the parameters.

$$\dot{Q}_{MJ-PEM} = \dot{m}_{H_2O} \cdot c_p \cdot \left(T_{MJ-PEM} - T_{min\ out}\right) =$$
$$= 596\ \frac{g}{h} \cdot 8\ \frac{h}{d} \cdot 4.186 \cdot 10^{-6} \frac{MJ}{g\ K} \cdot (150 - 65)K = \mathbf{1.70}\ \frac{\mathbf{MJ}}{\mathrm{d}} \qquad \text{Eq. 107}$$

using 65°C as the minimum outlet temperature for the pinch point in the second heat exchanger in Fig. 36.

Therefore, the number of MJ-PEM reactors to fulfill the thermal demand of the thermophilic process are:

$$MJ - PEM_{heat} = \frac{\dot{Q}_{heat}}{\dot{Q}_{MJ-PEM}} = \frac{25.70\ \frac{MJ}{m^3_{AD}\ d}}{1.70\ \frac{MJ}{m^3_{AD}\ d}} = 15.1\ \mathrm{m}^{-3} = \mathbf{16\ m^{-3}} \qquad \text{Eq. 108}$$

The thermal needs, again, are fully met by less MJ-PEM devices than the ones required for hydrogen production.

Oxygen requirements

Volume and COD reduction of 10% and 70%, respectively, were hypothesized for the digestate coming from thermophilic digestion:

$$\dot{V}_{dig} = \frac{\dot{m}_{in}}{\rho_{in}} \cdot \mathbf{0.90} = \frac{\frac{12}{0.10}\ \frac{kg_{VS}}{m^3_{AD}\ d}}{1000\ \frac{kg}{m^3}} \cdot 0.90 = 0.108 \frac{\mathrm{m}^3}{\mathrm{m}^3_{\mathrm{AD}} \cdot \mathrm{d}} = \mathbf{4.5}\ \frac{\mathbf{L}}{\mathbf{m^3_{AD}} \cdot \mathrm{h}} \qquad \text{Eq. 109}$$

$$COD_{dig} = COD_{in} \cdot \mathbf{0.3} = 50\ \frac{\mathrm{g}}{\mathrm{L}} \cdot 0.3 = \mathbf{15}\ \frac{\mathbf{g_{COD}}}{\mathbf{L}} \qquad \text{Eq. 110}$$

$$\dot{m}_{COD} = COD_{dig} \cdot \dot{V}_{dig} = 4.5 \frac{L}{m^3_{AD} \cdot d} \cdot 15\ \frac{g_{COD}}{L} = \mathbf{67.5}\ \frac{\mathbf{g_{COD}}}{\mathbf{m^3_{AD}} \cdot \mathrm{h}} \qquad \text{Eq. 111}$$

$$\dot{V}_{O_2\ req} = \dot{m}_{COD} \cdot \frac{R \cdot T}{P \cdot PM_{O_2}} = 67.5\ \frac{g_{COD}}{m^3_{AD} \cdot h} \cdot \frac{8.314\ \frac{J}{mol\ K} \cdot 298\ K}{101325\ Pa \cdot 32\ \frac{g}{mol}} = \mathbf{51.6}\ \frac{\mathbf{Nl}}{\mathbf{m^3_{AD}} \cdot \mathrm{h}} \qquad \text{Eq. 112}$$

Applying the same Oxygen Transfer Efficiency (OTE) of 18% for fine bubble aeration distributors placed at 3 m beneath the surface of the reactor for the stabilization of the digestate:

$$\dot{V}_{O_2\ req} = \frac{51.6\ \frac{Nl}{m^3_{AD} \cdot h}}{0.18} = \mathbf{286.7}\ \frac{\mathbf{Nl}}{\mathbf{m^3_{AD}} \cdot \mathrm{h}} \qquad \text{Eq. 113}$$

Each MJ-PEM reactor can provide **5.9 Nl/h**, then:

$$MJ-PEM_{O_2} = \frac{\dot{V}_{O_2\,req}}{\dot{V}_{O_2\,MJ-PEM}} = \frac{286.7\ \frac{Nl}{m^3_{AD}\cdot h}}{5.9\ \frac{Nl}{h}} = 48.6\ m^{-3} = \mathbf{49\ m^{-3}} \qquad \text{Eq. 114}$$

3.4 Conclusions

Table 5 and Table 6 sum up the most important results obtained for the scenarios analyzed in the previous paragraphs (Par.s 3.2 and 0).

SCENARIO / **PARAMETER**	***CWAO + H_2 PRODUCTION***	
H_2	0.968 g/h	11.7 Nl/h
O_2	7.768 g/h	5.9 Nl/h
Gross heat (no losses)	128 W	
Net heat (free convection + radiation losses)	85.1 W	
MJ area	3.2 cm^2 (1.8 x 1.8)	
PEM area	106 cm^2 (10 x 10)	
Current density	245 mA/cm^2	
Treated wastewater	600 ml/h	
Theoretical COD	11 g/m^3	
Solar-to-hydrogen eff.	20.0 %	
Thermal eff.	53.2 %	

Table 5 – Results for "Scenario I"

In "Scenario I", one step further in the application of a concentrated multi-junction solar cell system coupled with a PEM electrolyzer for hydrogen production has been made. The MJ-PEM device operating at high temperature and pressure (i.e. 150°C and 30 bar) has a great potential for implementation in the treatment of wastewater containing recalcitrant organics, also exploiting the thermal energy provided by concentrated sunlight, thus increasing the overall efficiency of the system. Recovery of the concentrated solar heat, in fact, can help to achieve 53% of thermal efficiency, which would otherwise be null. In addition, the exploitation of the electro-generated oxygen can lead to the effective treatment of refractory wastewater up to 11 g/m^3 of COD content. Current densities of about 245 mA/cm^2 are largely feasible on an industrial scale, allowing to meet high productivities. The hypothesized solar-to-hydrogen conversion efficiencies have already

been reached by similar systems (i.e. HyCon®), thus proving that the implementation of this device is not so far from realization.

SCENARIO / **PARAMETER**	***ANAEROBIC DIGESTION***	
	Mesophilic	***Thermophilic***
Biogas production	$3\ \frac{Nm^3}{m^3_{AD}\cdot d}$	$6\ \frac{Nm^3}{m^3_{AD}\cdot d}$
CO_2 to convert	$1.05\ \frac{Nm^3}{m^3_{AD}\cdot d}$	$2.40\ \frac{Nm^3}{m^3_{AD}\cdot d}$
n° MJ-PEM (CO_2) – H_2	50 m^{-3}_{AD}	114 m^{-3}_{AD}
n° MJ-PEM (heat) – $\dot{Q}$	7 m^{-3}_{AD}	16 m^{-3}_{AD}
n° MJ-PEM (heat + pretreat)	15 m^{-3}_{AD}	19 m^{-3}_{AD}
n° MJ-PEM (digestate) – O_2	31 m^{-3}_{AD}	49 m^{-3}_{AD}

Table 6 – Results for "Scenario II"

In "Scenario II" the MJ-PEM device has been connected in series with the bio-methanation step and the digestate stabilization from anaerobic digestion. For both mesophilic and thermophilic anaerobic digestions, the hydrogen production was found to be the determining process to dimension the overall plant. In fact, in order to meet the needs of an anaerobic plant, the biogas upgrading requires twice the number of MJ-PEM than the stabilization of digestate, and about 7 times than heating of influent slurry and digester. If some of the heat is provided to pre-treat the influent up to 70°C, this value is lowered to three times for the mesophilic process. As expected, the most demanding process for the chemical and thermal matching with the MJ-PEM system was found to be the thermophilic digestion, for which the specific number of MJ-PEM reactors was more than doubled in some cases (e.g. for H_2 requirement). Nevertheless, though the conditions seem harsh, the complete independence of this integrated process from fossil sources is promising for future perspectives.

CHAPTER 4

DEVELOPMENT OF MANGANESE OXIDE ELECTRODES ON TITANIUM AND TITANIA NANOTUBES FOR ELECTRO-OXIDATION OF PHENOL

4.1 Introduction

The biological treatment of wastewater is one of the most common processes throughout the world for the abatement of a large variety of compounds. However, some organic pollutants, such as aromatic compounds, are refractory and toxic to traditional biological methods. Benzene, phenol and its derivatives (chloro-phenols and nitro-phenols), anilines, benzoquinone, and hydroquinone are some of the most common pollutants contained in industrial wastewater [73, 74].

Phenol, in particular, is one of the most studied molecules in the sector of the removal of recalcitrant organic compounds from water, due to its high refractoriness and stability, and to its extensive presence in several industrial plants, such as petroleum refineries, and plastics, pesticides and pharmaceutical factories. Advanced oxidation processes (AOPs), such as Fenton and photo-Fenton reactions [75], ozonation [76], wet air oxidation (WAO) [58], catalytic wet hydrogen peroxide oxidation (CWHPO) [77] and catalytic wet air oxidation (CWAO) [78] are all effective methods that can be used to treat this substance. However, electrochemical degradation is another attractive procedure that is being considered to remove recalcitrant organics from water, especially in low-volume applications, due to its intrinsic high efficiency [79, 80].

According to the above-mentioned classification, electro-oxidation is considered to belong to the AOP family, since OH• radicals, some one of the most powerful oxidizing agents, are produced on the surface of the electrocatalytic materials. Many catalysts have been developed for this particular application throughout the years: Pt [81-83], IrO2 [84, 85], RuO_2 [86, 87], PbO_2 [82, 88], SnO_2 [89, 90] and Boron-Doped Diamond (BDD) [91, 92].

However, only a limited amount of literature has reported the use of manganese oxides (MnO_x) as catalysts for the electro-oxidation of refractory organics [93-98]. Furthermore, in many of these works, the role of manganese oxides has not been investigated in depth because the MnO_x coating had either been deposited onto highly active intermediate substrates, such as Sb-SnO_2 [93] or RuO_2 [94, 95], or it had been doped with ions (Fe^{2+}), which can influence the performance of the electrode [96]. MnO_x have been employed extensively in electrochemistry as cathodes in alkaline batteries, in lithium-ion batteries [99, 100] and as pseudo-capacitive electrodes into supercapacitors [101-103], or for the water splitting reaction [104-109]. The main advantages of manganese oxides are their low cost if compared to Pt, IrO_2, RuO_2 and BDD, and lower toxicity than Sb-SnO_2 and PbO_2.

This work describes the fabrication and characterization of electrochemically-deposited manganese oxides over a titanium support for the electrochemical oxidation of phenol molecules in wastewater. The electrodeposition parameters, such as current density, deposition time and precursors, were tuned in order to investigate their effect on the activity. Moreover, the effect of the temperature treatment on the electrodeposited MnO_x was investigated by means of calcination in air. Additionally, the role of an interlayer between the MnO_x nanostructures and the Ti substrate was considered, in order to evaluate its effectiveness in preventing the passivation of the Ti substrate and possibly increasing the electrode surface area [110-114]. For these reasons, the optimized parameters described above were used for deposition over a TiO_2 nanotubes (TiO_2-NTs) array, grown directly on Ti foil by means of the anodic oxidation method.

TiO_2-NTs obtained from anodization have attracted considerable interest in the last few decades, since their unique properties make them useful as active elements for several applications, ranging from energy production (dye-sensitized solar cells, [48, 115] water splitting, [116, 117]) and storage (Li-ions batteries, [118, 119] supercapacitors [120]) to sensing devices, such as gas sensing, [121] and molecular sensors [122]. The main advantages of TiO_2-NTs concern their quasi-one-dimensional arrangement, which leads to a good compromise between the exposed surface area (about 40 m^2/g) and superior electron transport properties, and results in a performance enhancement in all the different fields of application [123]. Moreover, compared to other synthesis approaches, electrochemical anodization is a simple, convenient and “green” technique to fabricate uniform layers of vertically self-oriented nanostructures, which, furthermore, is easy to be scaled up for large-scale industrial productions.

4.2 Materials and methods

4.2.1 Ti substrate preparation

Several 1 x 2 cm^2 titanium (Ti) foils (Sigma-Aldrich, 99.7%, 0.25 mm thick) were mechanically polished with 320-grit sandpaper to obtain a mirror finish and were then ultrasonically washed in 2-propanol. After rinsing with DI water, the foils were degreased in a 40 % NaOH solution at 50 °C for 20 minutes and were then rinsed again and left to dry in air.

Shortly before the electrochemical process, the titanium was etched in an HF (Carlo Erba, 40% w/w) aqueous solution 1.2 % w/w, at room temperature for 1 minute, in order to obtain a fresh metal surface for NTs growth.

Titania nanotubes were synthesized on the pretreated Ti foils, by dipping 1 x 1 cm^2 into a solution of ethylene glycol, NH_4F (0.5 % w/w) and DI water (2.5 % w/w). The Ti was used as an anode, while Pt foil was used as both a cathode and a reference electrode. A constant voltage of 60 V was applied to the cell for 10 minutes and, the TiO_2-NTs were calcined at 450 °C for 30 min after a long rinsing in water. Further details on the NTs growth and characterizations can be found elsewhere [124].

4.2.2 MnO_x electro-deposition

Since no literature reports are available on the direct electrodeposition of manganese oxides onto Ti, a base-case electrode was prepared on the base of the electrodeposition parameters found elsewhere [125], used in the deposition of manganese oxide films on FTO-coated glass for water splitting application. The samples were anodically deposited by immersing 1 x 1 cm^2 of the Ti foil or the TiO_2-NTs, in an unstirred and undivided cell containing 15 ml of a 0.1 M $Mn(CH_3COO)_2$ and 0.1 M Na_2SO_4 aqueous solution, by applying a current density of 0.25 mA/cm^2 for 10 minutes (i.e. samples *A000/Ti* and *A000/NTs*).

The electrodeposition parameters (i.e. current density, deposition time and Mn-precursor concentration) were then varied to investigate their effects on the performances, as shown in Fig. 37. Also the deposition technique was modified, once the deposition parameters were optimized, using a cathodic electrodeposition method with a different precursor (i.e. a 0.01 M $KMnO_4$ and 0.1 M Na_2SO_4 aqueous solution, applying a current density of -2.5 mA/cm^2 for 10 min). Different calcination conditions were applied to some of the electrodes, in order to obtain different manganese oxidation states, and the temperature ramp was also varied to investigate its effect on the possible passivation of the Ti substrate.

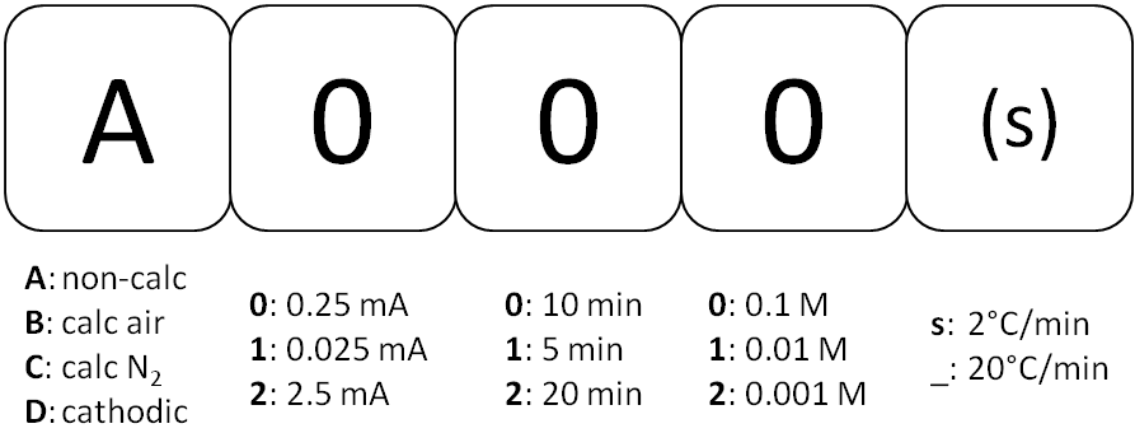

Fig. 37 – Nomenclature of the manganese oxide electrodes, electrodeposited on Ti and TiO_2-NTs

The samples were named by a letter and three numbers. The letter represents the type of synthesis: *"A"* for an anodically electrodeposited film without calcination; *"B"* for an electrode calcined in air at 500°C for 1 h; *"C"* for an electrode calcined in N_2 at 600°C for 3 h; *"D"* for a sample synthesized with the cathodic deposition in the $KMnO_4$ and Na_2SO_4 aqueous solution, then calcined in air at 500°C for 1 h. The first number represents the current density at which the electrodeposition occurs; the second number is the deposition time; the third number is the concentration of the precursor solution, either acetate or permanganate. The presence of an *"s"* after the name of the sample stands for a slow calcination ramp (2°C/min), otherwise, a fast ramp (20°C/min) is applied. Deposition on titanium or on nanotubes is explicitly indicated.

Fig. 38 presents a schematic view of all the syntheses carried out in this work.

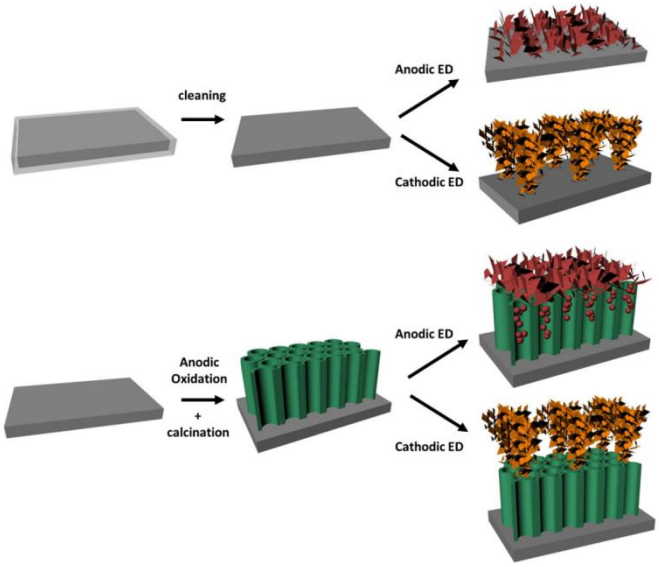

Fig. 38 - 3D scheme representing the manganese oxide electrodeposition processes over the Ti and TiO_2-NTs substrates

A BIOLOGIC VMP-300 potentiostat was used for the electrodepositions. Ti was set as the anode, Pt wire was used as the cathode and Ag/AgCl 3M KCl (+ 0.209 V vs NHE) was used as the reference electrode.

All the potentials reported in this work should be intended vs. RHE (E_{RHE} in V vs. RHE), and calculated according to Nernst's equation (Eq. 115):

$$E_{RHE} = E_{Ag/AgCl} + 0.209V + 0.059 \cdot pH \qquad \text{Eq. 115}$$

4.2.3 Characterization

The morphology, structure and physicochemical parameters of the electrodes were evaluated by means of X-Ray Diffraction (XRD, X'Pert PRO diffractometer, Cu Kα radiation λ = 1.54 Å), X-Ray Photoelectron Spectroscopy (XPS, PHI5000 VersaProbe) and Field Emission Scanning Electronic Microscopy (FESEM, Zeiss Merlin). The semi-quantitative surface composition was estimated by means of Electron Energy-Dispersive X-ray spectroscopy (EDX, Oxford X-Act).

4.2.4 Electrochemical characterization

Cyclic Voltammetries (CV) and Linear Sweep Voltammetries (LSV) were carried out in an unstirred and undivided 3-electrode cell system, containing 15 ml of a 0.1 M Na_2SO_4 solution. The scan limits were fixed between 0.5 and 2 V (vs. Ag/AgCl) and the scan rates were 20 mV/s for the CV and 5 mV/s for the LSV, respectively.

Electrochemical Impedance Spectroscopy (EIS) was conducted on some of the samples in the phenol solution (100 mg/l phenol and 0.1 M Na_2SO_4), in order to evaluate the charge transfer and charge transport properties of the films and the role of the nanotube interlayer on the electrochemical behavior of the anodes. An applied voltage of 3.3 V vs. RHE was employed, and the frequency was varied between 10^5 Hz and 1 Hz.

All the experiments were carried out on electrode areas of 1 x 1 cm^2; a Pt wire was employed as the counter electrode and an Ag/AgCl 3 M KCl (+ 0.209 V vs. NHE) was used as the reference electrode.

4.2.5 Electro-oxidation tests

The electro-oxidation tests were carried out in an unstirred and undivided glass cell containing 15 ml of phenol (C_0 = 100 mg/l) and 0.1 M Na_2SO_4 as supporting electrolyte. The prepared samples (active area of 1 x 1 cm^2) were used as the anode, while a Pt wire was set as the cathode and an Ag/AgCl, 3 M KCl (+ 0.209 V vs NHE) as the reference electrode. Constant currents were chosen in order to keep the working potential of the electrode under the limit of the instrument (10 V) over a reaction time of 5 h. The solution was then analyzed by High-Performance Liquid Chromatography (Shimadzu Prominence HPLC) with a Diode Array Detector (DAD) set at 269 nm. The column was a Rezex ROA (300 x 7.8 mm). The mobile phase was 5 mM H_2SO_4 and the flow rate was 0.5 ml/min. Chemical Oxygen Demand (COD) analyses were carried out by means of UV spectroscopy, using a HACH LANGE COD cuvette test (LCI 400) and a HACH LANGE DR5000 spectrophotometer.

4.2.6 Accelerated lifetime tests

In order to assess the durability of the synthesized electrodes accelerated lifetime tests were carried out on some of the samples in an unstirred and undivided glass cell containing 15 ml of a 1 M Na_2SO_4 aqueous solution. A Pt wire was used as the cathode and an Ag/AgCl, 3 M KCl (+ 0.209 V vs NHE) as the reference electrode. A current density of 100 mA/cm^2 was applied to the cell. The electrode was considered deactivated when the measured potential reached 10 V.

4.3 Results and discussions

For sake of brevity, some characterizations, such as XRD and FESEM, were performed only on the base-case electrodes (i.e. the *"000"* samples), used as a reference, and on the most different films, which were the *"200"* samples, deposited at high current density.

4.3.1 XRD and XPS analysis

In this paragraph, the base-case electrodes (*"000"*) and the samples deposited at high current densities (*"200"*) will be analyzed, both on Ti and on TiO_2-NTs.

- *Base-case*

Fig. 39 shows the XRD pattern of the manganese oxides electrodeposited at 0.25 mA/cm^2 for 10 minutes with 0.1 M Mn^{2+} ion concentration. The XRD spectra of the electrodes calcined at slow ramp are not shown, as they presented the same pattern of their counterpart calcined at fast ramp.

As expected, non-calcined *A000/Ti* showed no peaks that could be attributed to any crystalline phase of MnO_x, thus demonstrating that electrodeposition alone resulted in a non-crystalline material; only Ti peaks were visible [117, 125, 126].

The *A000/NTs* sample showed similar results: the non-calcined manganese oxides did not show any crystalline phase, while TiO_2 peaks and the Ti substrate were clearly visible and attributable to a tetragonal anatase phase (JCPDS 21-1272, I41/amd, a = b = 0.379 nm, c = 0.951 nm), as expected, due to the calcination of TiO_2-NTs at 450 °C.

Instead, the MnO_x electrodes calcined at 500 °C in air for 1 h, for both the slow and fast ramps (i.e. *B000(s)/Ti* and *B000/Ti*), showed the particular peaks of a cubic bixbyite crystalline phase, α-Mn_2O_3 (JCPDS 41-1442, Ia–3, a = 0.941 nm) [117, 125]. The same oxide was obtained over TiO_2-NTs (*B000/NTs*).

Moreover, it can be noticed that two peaks appeared, at 27.6° and 36.2°, on the MnO_x calcined samples, on both Ti and TiO_2-NTs. These peaks corresponded to the formation of a TiO_2 rutile phase, whose transition from anatase can start to occur at about 500 °C in air [127-131]. This observation confirmed the hypothesis of the formation of a titanium oxide layer between the Ti substrate and MnO_x coating during the heat treatment.

On the contrary, when the calcination was conducted under N_2 flow at 600°C for 3h (i.e. *C000(s)/Ti, C000/Ti,* and *C000/NTs*), the peaks of rutile were not detected, due to the absence of oxygen in the atmosphere, thus avoiding oxidation of the Ti substrate. For both the sample deposited on titanium and on nanotubes, the identified peaks were attributable

to the tetragonal hausmannite phase, Mn_3O_4 (JCPDS 1-1127 I41/amd, a = b = 0.575 nm, c = 0.942 nm), as expected from the calcination parameters [125].

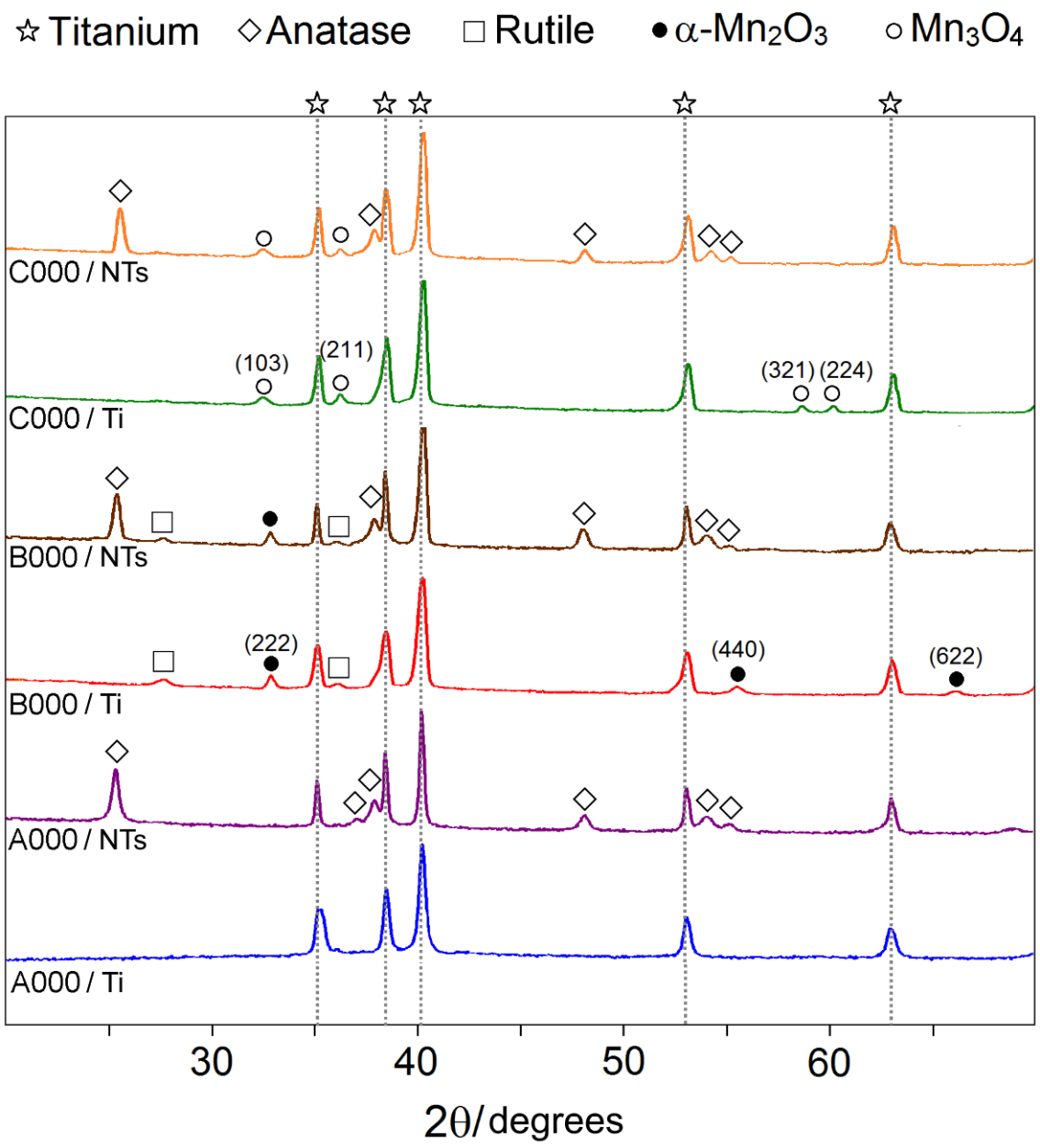

Fig. 39 – XRD patterns of MnO_x electrodeposited at 0.25 mA / 10 min / 0.1 M Mn^{2+}

- *Current density modification*

The XRD patterns of the manganese oxides electrodeposited at 2.5 mA/cm^2 are reported in Fig. 40. Such anodically deposited samples, as prepared (i.e. *A200/Ti* and *A200/NTs)*, showed only Ti and TiO_2 anatase XRD patterns, respectively, thus confirming once again that the implemented anodic electrodeposition led to a non-crystalline MnO_x material. Instead, after annealing, the XRD pattern of the *B200/Ti* sample showed a

noticeable difference, compared to the electrode deposited at 0.25 mA/cm^2. In this case, particular peaks of two MnO_x crystalline phases were detected in the spectrum: a cubic bixbyite α-Mn_2O_3 phase and a tetragonal manganese dioxide α-MnO_2 phase (JCPDS 041-1442, Ia–3, a = 0.941 nm; JCPDS 044-014, I4/m, a = b = 9.7847, c = 2.8630). This result is in contrast with the ones obtained for the same sample obtained at 0.25 mA/cm^2, and it could be possibly due to the different potentials reached during electrodeposition, because of the higher currents provided to the electrode. In fact, a change in either the potential or pH at a constant temperature can have an important effect on the equilibrium of the deposition, and can thus modify the structure of the deposited oxide [132].

In the *B200/NTs* sample, an intense peak was observed at 32.9°, thus confirming the presence of a α-Mn_2O_3 bixbyite phase in the catalyst film, while α-MnO_2 phase peaks were absent.

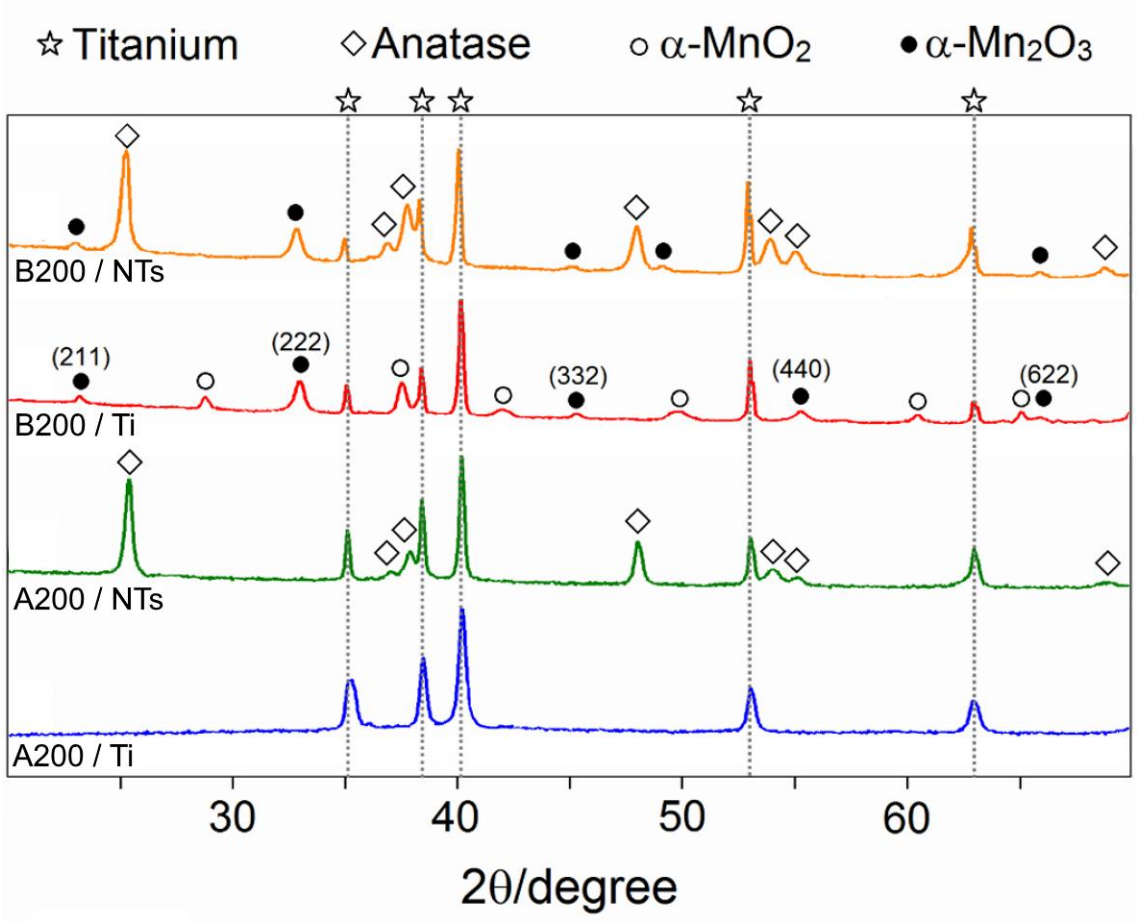

Fig. 40 – XRD patterns of MnO_x electrodeposited at 2.5 mA / 10 min / 0.1 M Mn^{2+}

➢ *Precursor modification*

Fig. 41 shows the XRD patterns of the samples obtained by cathodic electrodeposition from a precursor solution of potassium permanganate (Mn^{7+}). They were synthesized at -2.5 mA/cm^2 for 10 min in 0.01 M $KMnO_4$ and 0.1 M Na_2SO_4, then calcined at 500°C in air for 1 h. For both cathodic depositions on metallic titanium and titania nanotubes (i.e. *D201/Ti* and *D201/NTs*), the peaks of the tetragonal α-MnO_2 (JCPDS 044-014, I4/m, a = b = 9.7847, c = 2.8630) were observed, while no other peaks, apart from those of the substrates, were detected. Even though calcination conditions were identical to the anodic samples, a different phase was obtained. This behavior, again, could be attributed to the variation in deposition potential, which was negative in this case, and thus changed the thermodynamic stability of the MnO_x phase.

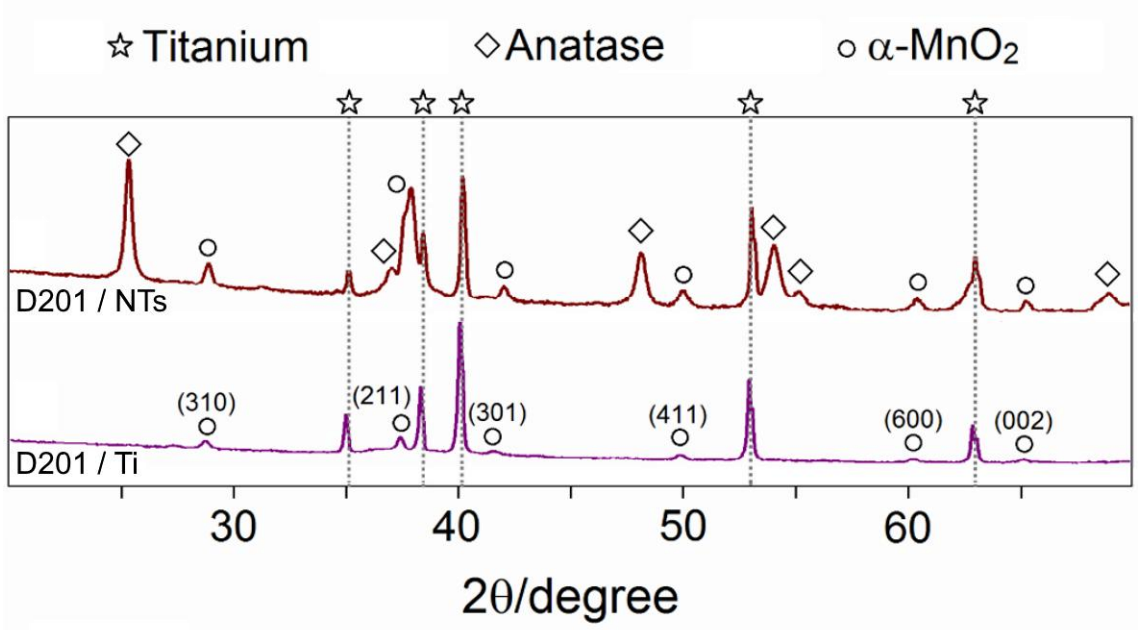

Fig. 41 – XRD patterns of MnO_x electrodeposited at -2.5 mA / 10 min / 0.01 M Mn^{7+}

In general, the MnO_x electrodes prepared at higher electrodeposition current densities did not show any formation of TiO_2 rutile, as in the case of the ones prepared at lower current density values. This could be due to the higher amount of MnO_x, which covered and protected the Ti substrate and TiO_2-NTs surface from further oxidation.

➢ *XPS analysis*

In order to investigate the surface composition of the electrodeposited MnO_x and to support the XRD analysis outcomes, XPS analysis was carried out on some of the prepared samples: i.e. *A200/Ti*, *B200/Ti*, and *D201/Ti*. The results of the Mn 3s XPS spectra, with the estimation of the Average Oxidation State (AOS) [133] of the surface of the films are reported in Fig. 42. It is easy to see that the cathodic sample (i.e. *D201/Ti*) showed the highest AOS value (i.e. 3.56), which was close to the Mn^{4+}, identified by the XRD. Instead, the AOS value for the *B200/Ti* was 3.11, which is also in agreement with the presence of a mix of Mn oxides with oxidation states of Mn^{3+} and Mn^{4+}, as revealed by the XRD measurement. Finally, the non-calcined MnO_x, *A200/Ti*, whose oxidation state could not be identified by means of XRD, gave an intermediate AOS value (i.e. 3.25), which probably means that also a mixed oxide Mn^{3+} / Mn^{4+} could have been formed after the electrodeposition, but with a slightly higher presence of Mn^{4+} than the *B200/Ti* sample.

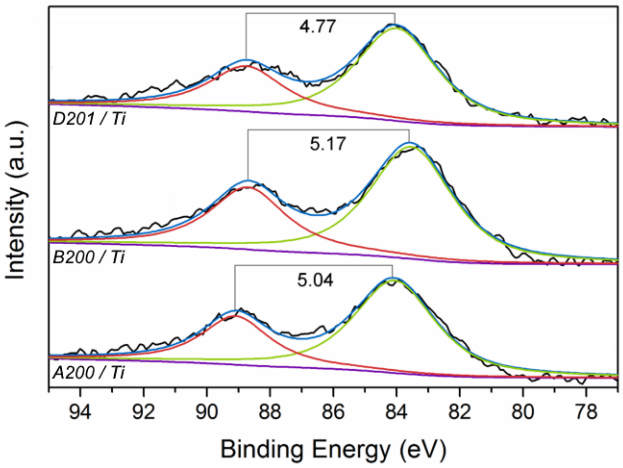

$$AOS = 8.95 - 1.13 \cdot \Delta E_s$$

Electrode	ΔE_s (eV)	AOS
D201 / Ti	4.77	3.56
B200 / Ti	5.17	3.11
A200 / Ti	5.04	3.25

Fig. 42 – A) Deconvoluted XPS spectra of Mn 3s of: *A200/Ti, B200/Ti, D201/Ti*; B) Calculation of estimated Average Oxidation State (AOS)

4.3.2 FESEM and EDX analysis

- *Base-case*

Fig. 43 reports the FESEM images of the base-case MnO_x, *"000"*, which were electrodeposited on Ti at 0.25 mA/cm^2 for 10 min at 0.1 M Mn^{2+}. After the MnO_x electrodeposition, the typical formations of nanoflake structures, which have also been observed in other works [117, 125, 134], were formed for all the different types of electrodes. The thickness of the manganese oxide layer (~ 623 nm) was quite uniform, as can be seen in the inset of *A000/Ti*. A slight change in the morphology can be noticed when *A000/Ti* is compared with *B000/Ti*, which was calcined in air with the fast ramp at 20 °C/min, however still maintaining the overall nanoflake disposition. The electrode calcined with a slow ramp, that is, *B000(s)/Ti*, instead, presented an almost unchanged nanoflakes structure with respect to *A000/Ti*. A similar trend was observed for the electrodes calcined in N_2: the sample annealed with a slow ramp, that is, *C000(s)/Ti*, showed more defined nanoflakes similar to the as-deposited sample, though they seemed more aggregated than the electrode calcined in air; the film calcined with a fast ramp (i.e. *C000/Ti*), instead, presented a structure in which the nanoflakes resulted merged and less defined.

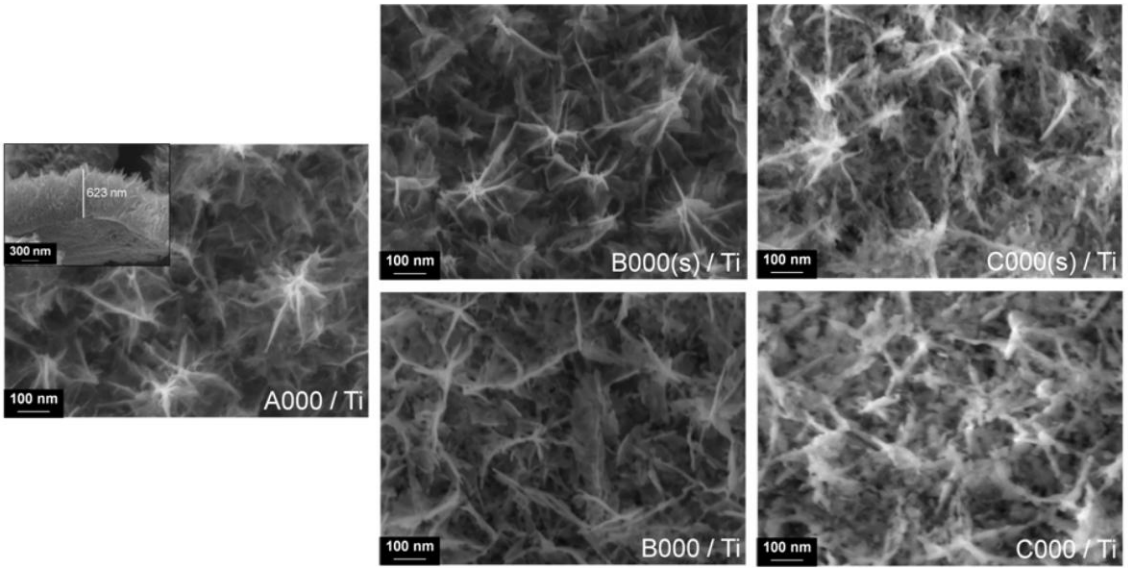

Fig. 43 – FESEM images of the samples electrodeposited on Ti at 0.25 mA / 10 min / 0.1 M Mn^{2+}

The FESEM images of the base-case MnO_x grown on TiO_2-NTs are shown in Fig. 44. The cross-section images of the TiO_2 nanotubes, after the Ti anodization and the annealing procedure, are shown on the top left of Fig. 44. The NTs were 5 µm long and vertically aligned with respect to the Ti foil. The ordered distribution of the pores can be appreciated as an inset in the figure: the inner holes had an average dimension of about 70

nm and a wall thickness of around 20 nm. All the samples grown on NTs showed nanoflakes on the top of the nanotube layer. However, the deposition of nanoflakes on the TiO_2-NTs substrate was less homogeneous than the deposition on metallic titanium, showing some uncovered areas, probably due to preferential pathways of the electrodeposition currents, where the electric resistance was lower.

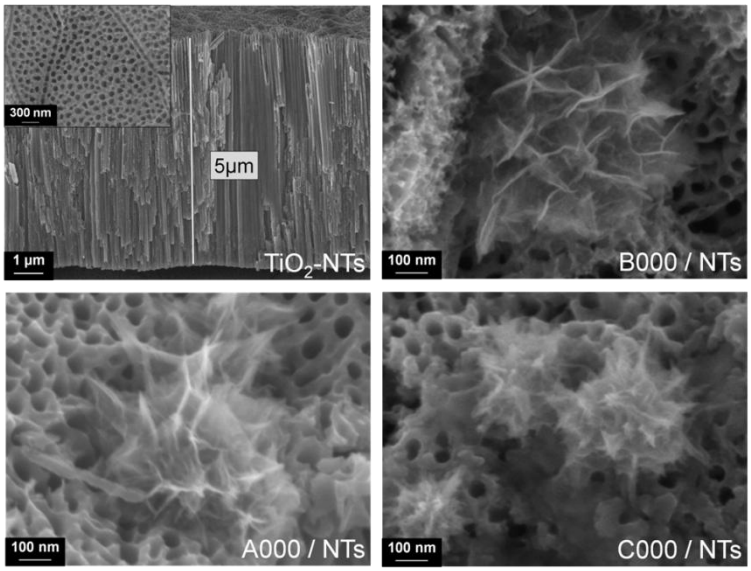

Fig. 44 – FESEM images of the samples electrodeposited on TiO_2-NTs at 0.25 mA / 10 min / 0.1 M Mn^{2+}

- *Current density modification*

Fig. 45 shows the FESEM images of the manganese oxide electrodeposited at 2.5 mA/cm^2, 10 min, 0.1 M Mn^{2+}. The non-calcined anodically deposited samples, i.e. *A200/Ti* and *A200/NTs*, still showed a similar nanoflake structure to the one seen for the sample synthesized at lower current densities. However, the nanoflakes were smaller for both electrodes, due to the higher electrodeposition current density. In fact, the nucleation rate is higher and the critical nucleation radius is decreased, as the potential and current density are increased, thus the formation and refinement of the initial grain are improved [132]. The inset in the top left allows the thickness of the MnO_x film on the *A200/Ti* sample (~ 3.7 µm), which was six times higher than the base-case samples, to be appreciated. The calcined *B200/Ti* and *B200/NTs* samples, instead, showed very fine nanoflakes, that coexisted with another type of larger crystalline nanoparticles, which were present in a greater amount on the sample grown on the titanium substrate. Such a difference in morphology can be explained by considering the larger amount of the α-MnO_2 phase in the electrode grown on Ti, as observed in the XRD analysis, which more likely composes the larger nanoparticles.

Unlike the base-case samples, the cross-sectional view of *A200/NTs* and *B200/NTs* (showed in the respective insets) exhibited evidence of the penetration of the manganese inside the nanotubes structure, similarly to the penetration of the electrodeposited Sb-doped SnO_2 films into TiO_2-NTs [110]. This phenomenon was probably due to the high electrodeposition current densities which led to smaller nanoflakes that were able to grow inside the nanotube.

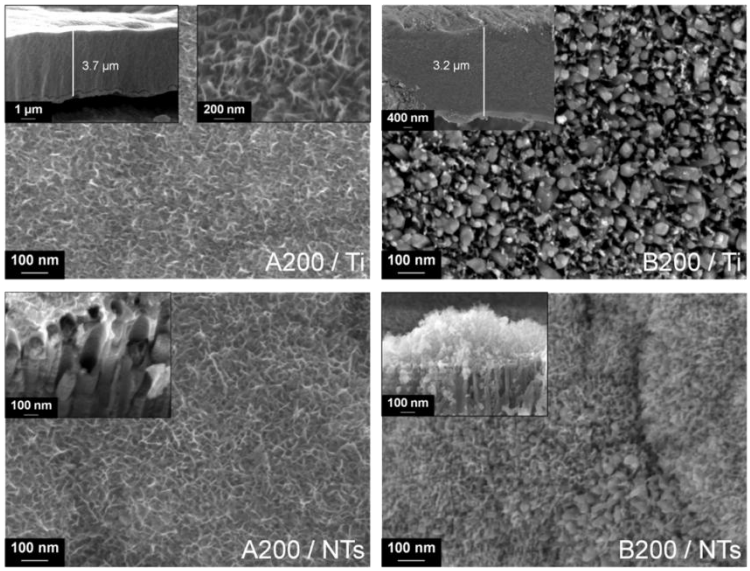

Fig. 45 – FESEM images of the samples electrodeposited at 2.5 mA / 10 min / 0.1 M Mn^{2+}

- *Precursor modification*

The FESEM images of the MnO_x samples, that is, prepared by cathodic deposition, *D201/Ti*, and *D201/NTs*, pointed out a totally different morphology from the anodically deposited MnO_x, as shown in Fig. 46. The nanoflakes formed a layer directly over the nanotubes, from which polycrystalline rod-like structures of a noticeable thickness (~ 3.6 µm) grew. In this case, the cross-section of the *D201/NTs* sample, shown as an inset in the right picture, did not report a deep penetration of manganese oxide inside the nanotubes. This could be due to either a different wettability of the nanotubes by the $KMnO_4$ solution from the $Mn(CH_3COO)_2$ used in the anodic deposition, or a different electric field induced inside and on the top of the nanotubes.

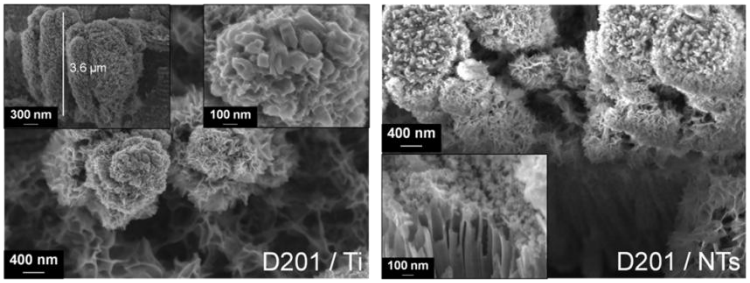

Fig. 46 – FESEM images of the samples electrodeposited at -2.5 mA / 10 min / 0.01 M Mn^{7+}

- *EDX analysis*

Table 7 and Table 8 show some of the data from the EDX surface composition analyses of all the manganese oxides over Ti and TiO_2-NTs. As can be noticed, for all the base-case samples, synthesized at 0.25 mA/cm^2, the atomic ratio (Mn/Ti) is comparable, with a slightly higher manganese content for the non-calcined electrode grown on nanotubes (i.e. *A000/NTs*).

	MnO_x phase	**Mn/Ti**
A000/Ti	non-crystalline	0.12
B000(s)/Ti	α-Mn_2O_3	0.10
B000/Ti	α-Mn_2O_3	0.11
C000(s)/Ti	Mn_3O_4	0.09
C000/Ti	Mn_3O_4	0.08

	MnO_x phase	**Mn/Ti**
A000/NTs	non-crystalline	0.16
B000/NTs	α-Mn_2O_3	0.11
C000/NTs	Mn_3O_4	0.08

Table 7 – EDX results for the base-case electrodes

For samples synthesized at ±2.5 mA/cm^2, the atomic ratio, Mn/Ti, is up to 10 or even 100 times higher than the one reported for the electrodes synthesized at lower current densities, as a greater amount of manganese oxide was deposited on these samples. Moreover, the Mn/Ti values measured for the films grown on Ti were considerably higher than the ones registered for those grown on the nanotubes, and this could be due to the higher electric resistance of the TiO_2-NTs than the metallic Ti, which limited the total amount of manganese oxide deposited. However, because of the higher surface area of the TiO_2-NTs, it is more likely that the lower Mn/Ti ratios observed in the NTs than on Ti were due to the better distribution of MnO_x on the top of the TiO_2-NTs, as well as inside the NTs pores (Fig. 45).

	MnO_x phase	**Mn/Ti**
A200/Ti	non-crystalline	15.2
A200/NTs	non-crystalline	2.1
B200/Ti	α-Mn_2O_3 / α-MnO_2	18.2
B200/NTs	α-Mn_2O_3	1.6

	MnO_x phase	**Mn/Ti**
D201/Ti	α-MnO_2	13.4
D001/NTs	α-MnO_2	7.4

Table 8 – EDX results for the electrodes synthesized at ±2.5 mA/cm^2

4.3.3 Electrochemical characterization

- *Base-case*

Cyclic Voltammetries (CVs) and Linear Sweep Voltammetries (LSVs) were carried out in a 0.1 M Na_2SO_4, without phenol, to test the electrochemical behavior of the samples in neutral conditions, similar to most of the literature [135-138].

Fig. 47, Fig. 48 and Fig. 49 show the CVs of the base-case electrodes (*"000"*), synthesized at 0.25 mA/cm^2, 10 min and 0.1 M Mn^{2+}, both on titanium and titania nanotubes. The graphs were individually plotted in order to clearly evidence the shape of the CV and the stability of the electrocatalytic film. Fig. 50 and Fig. 51, instead, show the LSVs of the same anodes (deposited on Ti and TiO_2-NTs, respectively), gathered to compare their electrochemical activity. As can be seen, many differences emerged from the CVs among the non-calcined, air-calcined and N_2-calcined samples. Indeed, the as-deposited film of MnO_x on metallic Ti (i.e. *A000/Ti in* Fig. 47a) presented pseudo-capacitive behavior, which is usually a characteristic of crystalline MnO_2, or non-crystalline MnO_x phases [116]. Moreover, the stability of this electrode is not very high, as the observed current density at ~ 2.6 V_{RHE} halved after 5 cycles.

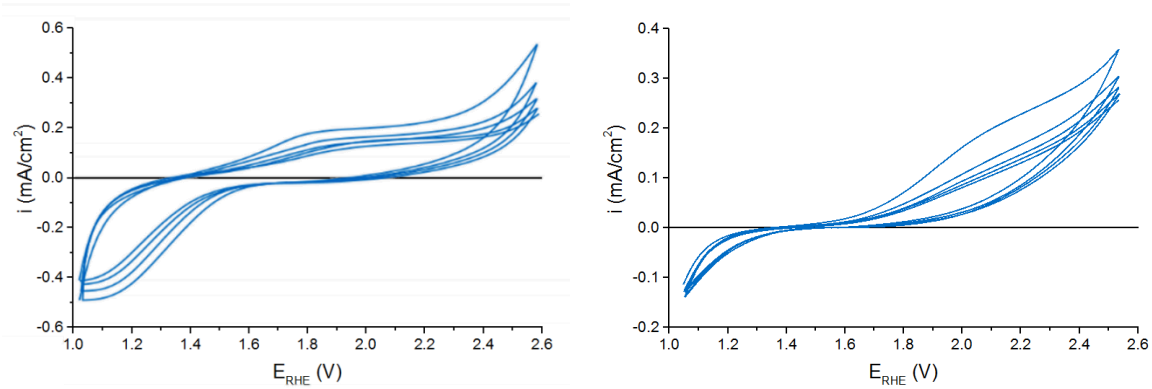

Fig. 47 – CV in 0.1M Na_2SO_4 of a) *A000/Ti* and b) *A000/NTs*. Scan rate 20 mV/s

After calcination, either in air or in N_2, the pseudo-capacitance of manganese oxide films on Ti was no more detected by the CVs (Fig. 48a, b and Fig. 49a, b). This phenomenon could either be due to the change in the crystalline phase, from non-crystalline to α-Mn_2O_3 [117], or because of the variations in the morphology (growth in the particle sizes) of the deposited film after the thermal treatment [139].

For the samples calcined in air "*B000"*, also the stability was greatly affected: even though current densities achieved at 2.6 V_{RHE} were lower than the *A000/Ti* sample, the cycles were almost overlapped, especially for the *B000/Ti* calcined with the fast ramp. On

the contrary, the "*C000"* anodes, obtained by calcination in N_2, showed low stability, similar to the non-calcined electrode.

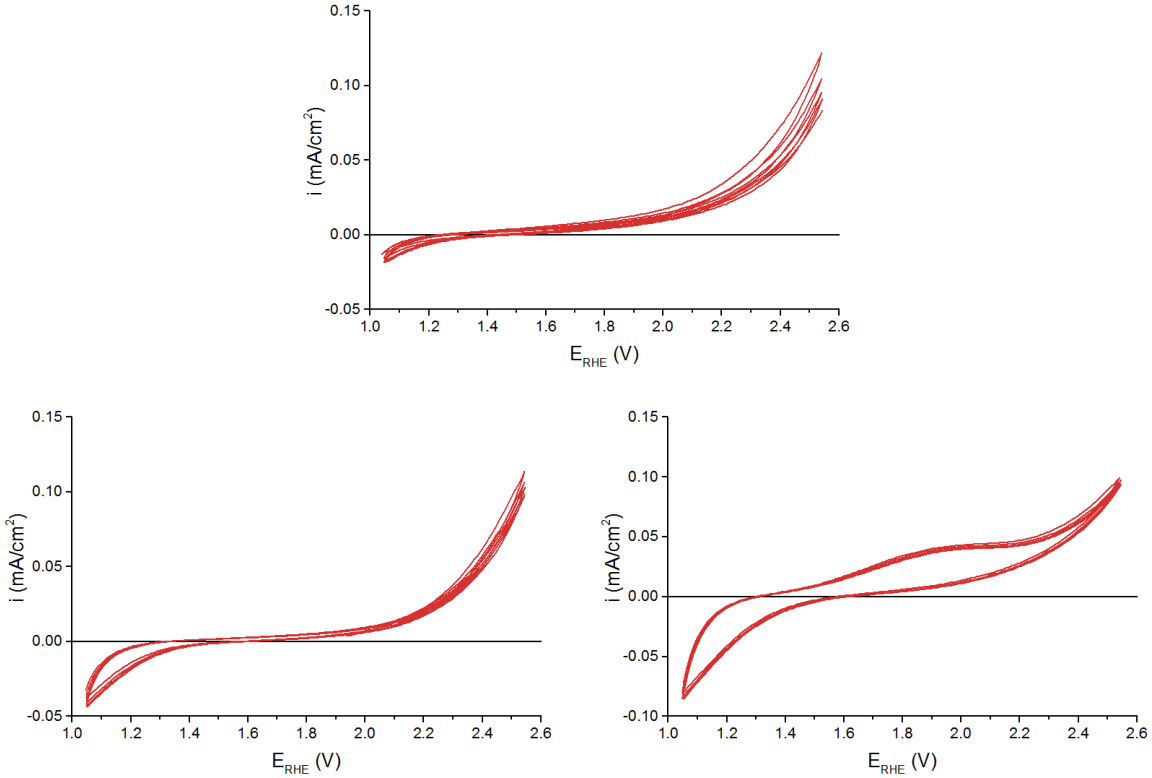

Fig. 48 – CV in 0.1M Na_2SO_4 of a) *B000(s)/Ti,* b) *B000/Ti* and c) *B000/NTs*. Scan rate 20 mV/s

Concerning the depositions on TiO_2-NTs (Fig. 47b, Fig. 48c, and Fig. 49c), it can be noticed that the pseudo-capacitive behavior is observed for all the types of synthesis, even for the calcined films, which did not show any pseudo-capacitive tendency when the deposition occurred on Ti metal. This phenomenon could be due to the presence of the titania nanotubes in the interlayer [116, 118, 119].

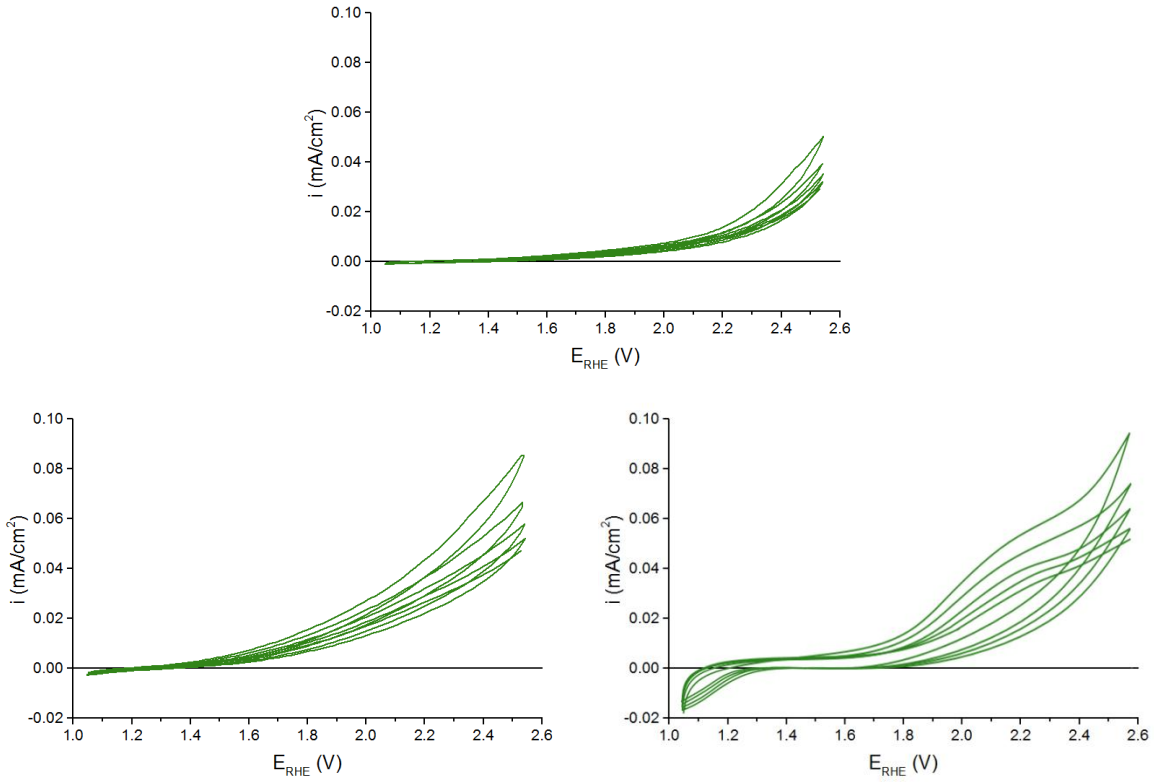

Fig. 49 – CV in 0.1M Na_2SO_4 of a) *C000(s)/Ti*, b) *C000/Ti* and c) *C000/NTs*. Scan rate 20 mV/s

The pseudo-capacitance in the MnO_x phase was caused by the electron transfer at the Mn surface sites, the charge transfer being balanced by either the chemisorption/desorption of the electrolyte cations or by the insertion/disinsertion of the protons [116, 140]. In the case of TiO_2, due to its semiconducting properties, electrons are accumulated in the material when it behaves like a cathode (i.e. presence of negative current values) and they are then released when the electrode polarity is inverted and acts as an anode [116].

Another interesting effect related to the presence of the nanotubes interlayer is the influence on the stability. Indeed, although the current densities were comparable, the manganese oxides grown on nanotubes showed a slight increment in the stability after 5 CV cycles.

The LSVs of the base-case electrodes deposited on titanium are shown in Fig. 50. The non-calcined sample (i.e. *A000/Ti*) showed the higher current density at ~ 2.6 V_{RHE}, followed by the electrodes calcined in air, (i.e. *B000(s)/Ti* and *B000/Ti*), while the samples calcined in N_2 gave the lowest current densities. Therefore, the electrochemical activity towards water oxidation followed the order: MnO_x > α-Mn_2O_3 > Mn_3O_4, which was not the same trend observed for the same syntheses on FTO reported in other works [125], where the α-Mn_2O_3 phase reported the highest activity, followed by non-crystalline MnO_x and Mn_3O_4.

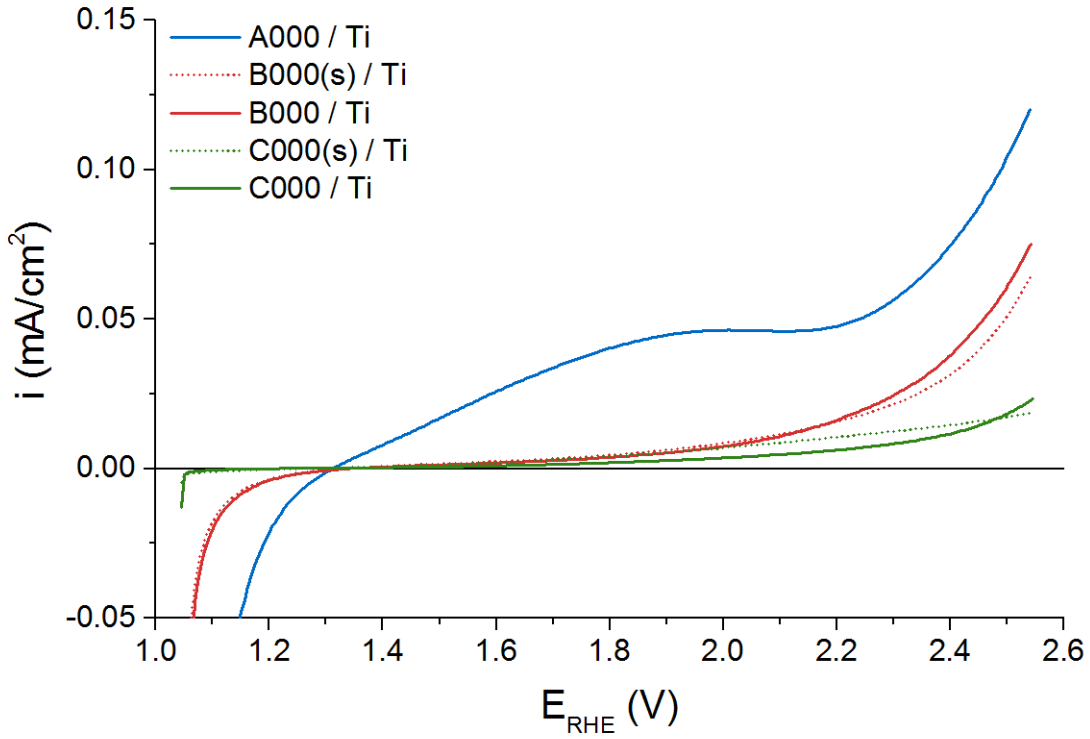

Fig. 50 – LSV in 0.1M Na_2SO_4 of base-case electrodes deposited on Ti. Scan rate 5 mV/s

The same sequence of activity was observed for the samples grown on TiO_2-NTs, with similar current densities to films deposited on Ti. Some change in the shape of the LSVs of the calcined samples was detected, due to the pseudo-capacitive behavior of the nanotubes, as described above.

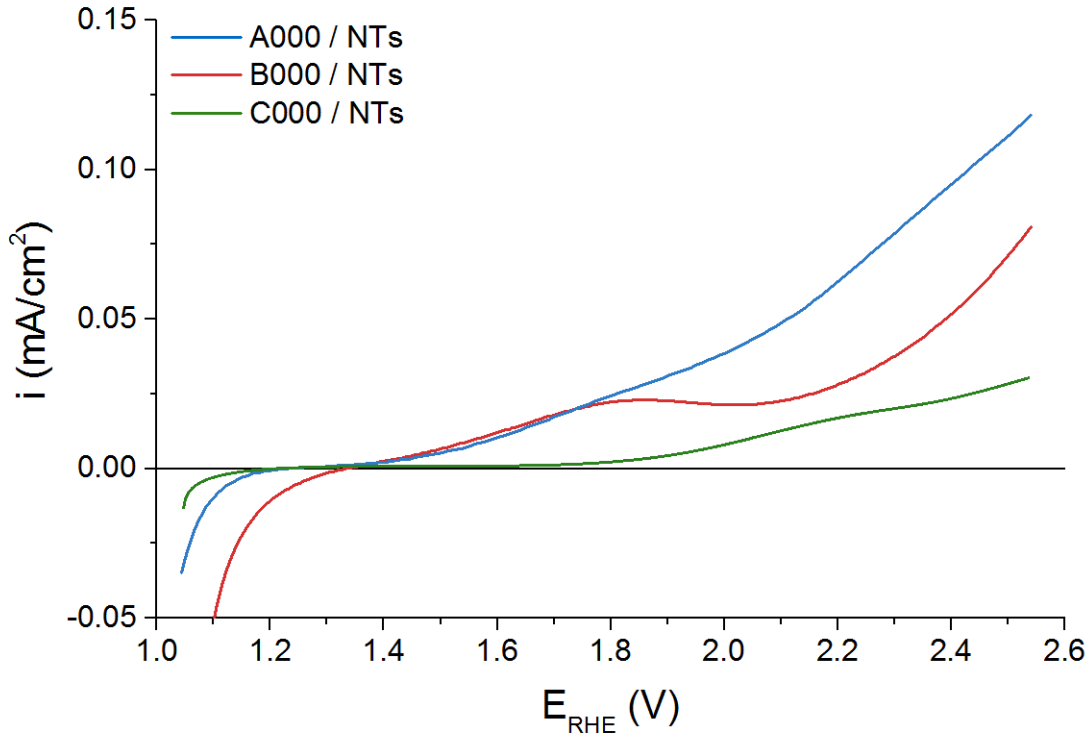

Fig. 51 – LSV in 0.1M Na_2SO_4 of base-case electrodes deposited on NTs. Scan rate 5 mV/s

Due to the poor activity and stability of the hausmannite films and to the apparently moderate influence of the nanotubes interlayer on the CVs and LSVs, further electrodepositions with modifications of deposition time and Mn^{2+} concentration were conducted only on Ti, either without calcination (i.e. *"A"* samples) or with calcination in air (i.e. *"B"* samples).

- *Deposition time modification*

The time employed for the electrodeposition of manganese oxide was varied to analyze its effect on the performances of the catalytic film. Fig. 52 showed the CVs of non-crystalline MnO_x synthesized at 0.25 mA/cm2, for 5 min (*A010/Ti*, Fig. 52a) and 20 min (*A020/Ti*, Fig. 52b), at 0.1 M Mn^{2+}. It is clearly evidenced that in both cases the pseudo-capacitive behavior due to the MnO_x phase is still present, and the film instability is remarkable (current density is halved after 5 CV cycles). Moreover, the average current densities achieved by these two samples were half than the *A000/Ti* base-case anode. Therefore, if it was somehow expected a decrease in performances for the electrode obtained with 5 min of deposition time, an increase in deposition time was not beneficial for the efficiencies of the samples deposited for 20 min.

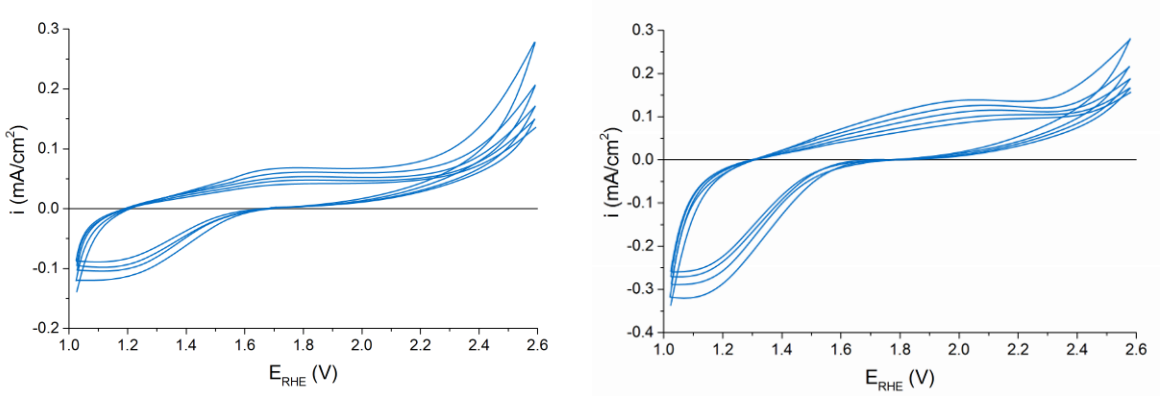

Fig. 52 – CV in 0.1M Na_2SO_4 of a) *A010/Ti* and b) *A020/Ti*. Scan rate 20 mV/s

A similar behavior was evidenced for the two electrodes calcined in air, as shown in Fig. 53. Both the electrodes showed no pseudo-capacitance, and the stability was better than the non-calcined electrodes. The sample deposited for 5 min (*B010/Ti*, Fig. 53a) reached less than half of the current obtained by the *B000/Ti* samples, while the one deposited for 20 min (*B020/Ti*, Fig. 53b) showed similar activities, but a more marked decrease in the current density after 5 cycles.

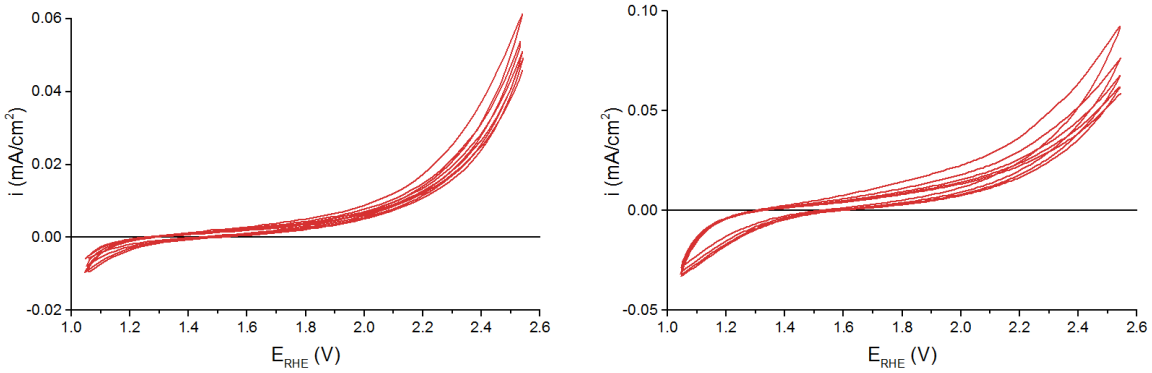

Fig. 53 – CV in 0.1M Na_2SO_4 of a) *B010/Ti* and b) *B020/Ti*. Scan rate 20 mV/s

A comparison between these samples was obtained by the LSVs reported in Fig. 54. The most active electrode was the non-crystalline sample synthesized at 20 min, then the one synthesized at 5 min. The two electrodes air-calcined gave lower current densities, as before, with a slightly higher effectiveness for the sample deposited for 20 min.

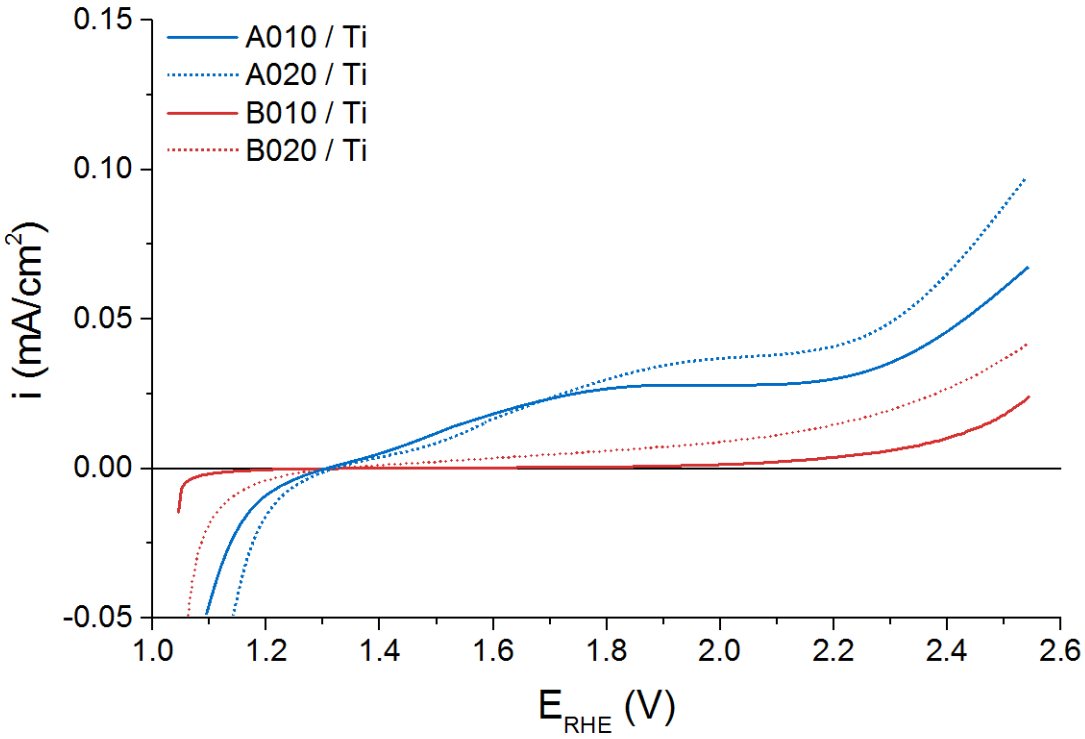

Fig. 54 – LSV in 0.1M Na_2SO_4 of electrodes deposited on Ti at different times. Scan rate 5 mV/s

Thus, also in this case, a change in the deposition time did not evidence any improvement in the electrochemical performances of the manganese oxide electrodes.

➢ *Concentration modification*

Some works [141, 142] use very low concentrations of precursor in the deposition solution, so the possible influence of the manganese acetate concentration was analyzed. Fig. 55 and Fig. 56 show the CVs of the electrodes deposited from solutions containing 0.01 M and 0.001 M Mn^{2+}, without and with calcination in air.

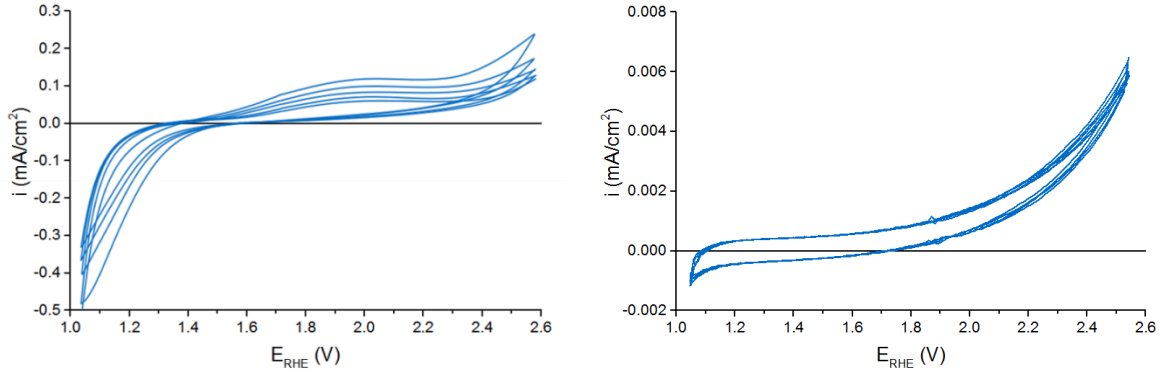

Fig. 55 – CV in 0.1M Na_2SO_4 of a) *A001/Ti* and b) *A002/Ti*.
Scan rate 20 mV/s

In both cases, the current densities were lower with respect to the base-case, and pseudo-capacitance and stability were not affected.

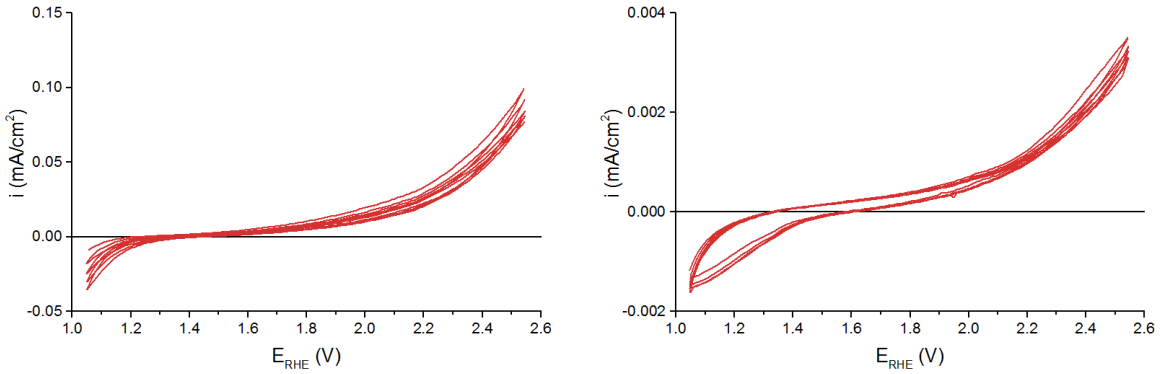

Fig. 56 – CV in 0.1M Na_2SO_4 of a) *B001/Ti* and b) *B002/Ti*.
Scan rate 20 mV/s

For very low concentrations of 0.001 M Mn^{2+} (i.e. *A002/Ti* and *B002/Ti* samples), the currents were lowered more than one order of magnitude, as clearly evidenced by the LSVs reported in Fig. 57, while for the *A001/Ti* and *B001/Ti* samples the currents were almost halved with respect to the base-case.

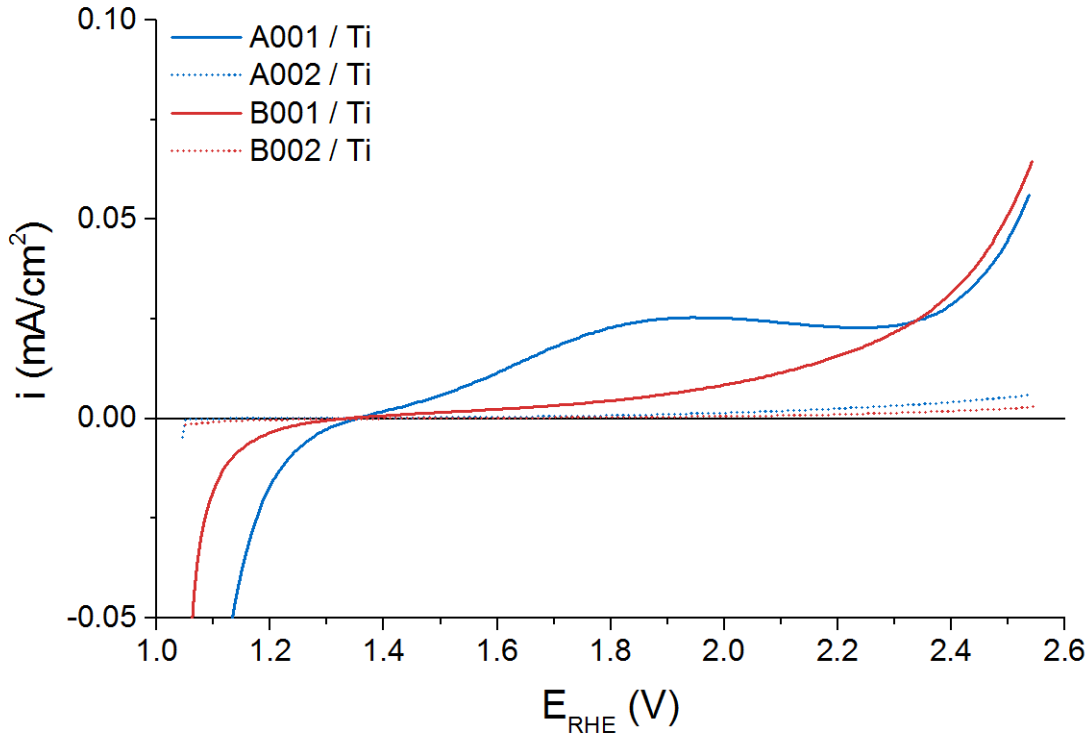

Fig. 57 – LSV in 0.1M Na_2SO_4 of electrodes deposited on Ti at different Mn^{2+} concentrations. Scan rate 5 mV/s

In conclusions, the most suitable concentration of manganese acetate precursor for this type of synthesis was found to be 0.1 M $Mn(CH_3COO)_2$.

- *Current density modification*

The last parameter changed for this investigation was current density. Fig. 58 and Fig. 59 show the CVs for the electrodes deposited on Ti with a current density of 0.025 mA/cm^2 (Fig. 58a and Fig. 59a) and 2.5 mA/cm^2 (Fig. 58b and Fig. 59b), or for the samples grown on TiO_2-NTs employing a current density of 2.5 mA/cm^2 (Fig. 58c and Fig. 59c).

The non-crystalline film obtained with low currents (i.e. *A100/Ti*) showed a less capacitive behavior than the base-case *A000/Ti* sample, probably because of the lower amount of deposited material. The achieved currents, on the contrary, were only slightly lower than the base-case electrode, even though the instability was found to be similar, as the currents at 2.6 V_{RHE} halved after the end of the CV. On the other hand, the calcined sample synthesized at 0.025 mA/cm^2, that is, *B100/Ti*, showed a decreased current, together with a more questionable stability than the *B000/Ti* sample. Therefore, low current densities were considered not suitable for the electrodeposition of manganese oxide films on Ti.

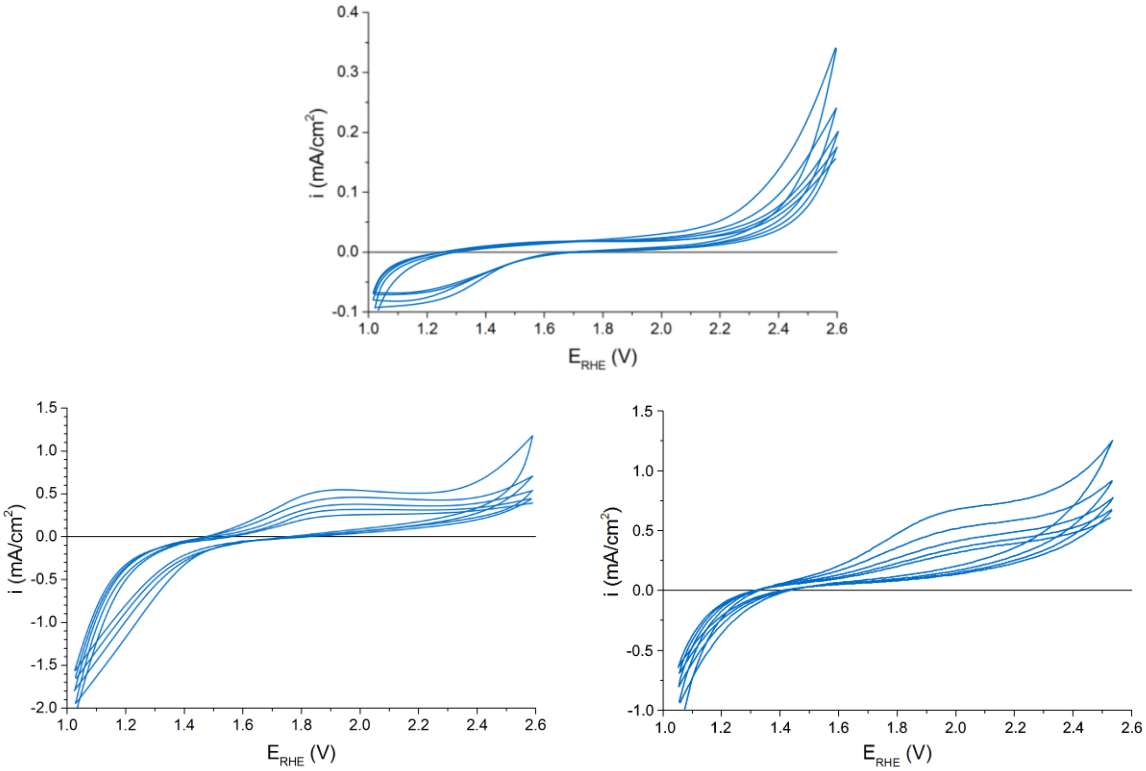

Fig. 58 – CV in 0.1M Na_2SO_4 of a) *A100/Ti*, b) *A200/Ti* and c) *A200/NTs*. Scan rate 20 mV/s

The non-calcined samples synthesized with higher current densities (i.e. *A200/Ti* in Fig. 58b), on the contrary, achieved high currents at potentials ~ 2.6 V_{RHE}, with a noticeable capacitive behavior, which was probably due to the higher amount of deposited MnO_x on the substrate. The stability of the film layer, however, was not improved by the change in the electrodeposition current. The same pseudo-capacitance is detected for the same film obtained on TiO_2-NTs (i.e. *A200/NTs* in Fig. 58c), and stability is again slightly enhanced thanks to the presence of the nanotubes.

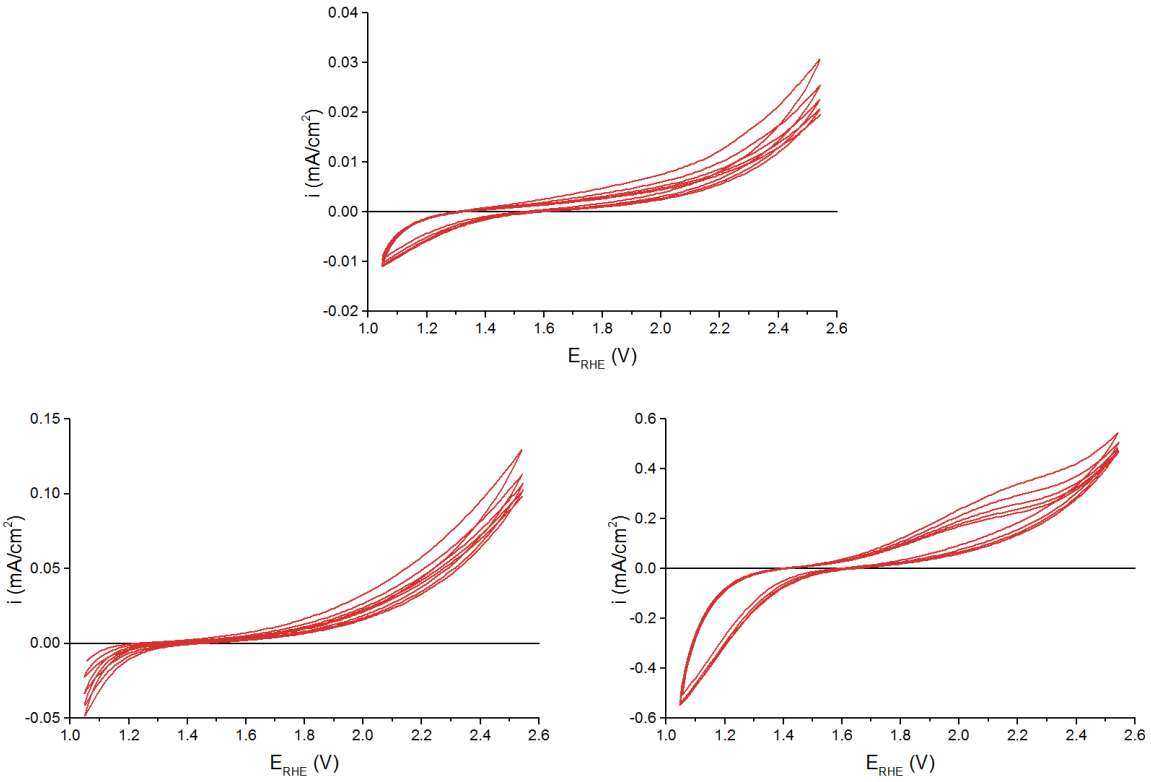

Fig. 59 – CV in 0.1M Na_2SO_4 of a) *B100/Ti*, b) *B200/Ti* and c) *B200/NTs*. Scan rate 20 mV/s

Similar results, in terms of pseudo-capacitance, were reported for the calcined sample on nanotubes (i.e. *B200/NTs* in Fig. 59c), compared to the same film grown on Ti (i.e. *B200/NTs* in Fig. 59b). The pseudo-capacitive behavior of an electrode, in fact, was exclusively due to either the type of material (non-crystalline) or the presence of the nanotubes. Concerning the stability obtained during the CV analysis, the samples grown on TiO_2-NTs reported again the best results. This phenomenon could be explained by the penetration of the MnO_x nanoflakes inside the nanotubes, which improved the contact area and limited the detachment of the film from the interlayer, as can be appreciated in the cross-section of the FESEM images in Fig. 45.

➢ *Precursor modification*

As far as the MnO_x cathodically deposited on Ti is concerned (Fig. 60a), although the prevalent phase formed after their thermal treatment was α-MnO_2, they did not show a pseudo-capacitive behavior. Such phenomena could be explained by considering the different rod-like morphologies of these MnO_x samples, which have less exposed surface area than the nanoflakes, and this could lead to a lower capacitive effect. It has been reported that differences in MnO_2 morphology under different electrodeposition conditions and the post-thermal treatments could contribute to the differences in the capacitive behaviors [143, 144]. Indeed, a lower capacitance effect has been observed for a smaller nanosheets spacing and more compactness of the structure, which make ion diffusion within the structure difficult [143]. Moreover, the interaction with the substrate seems to play a crucial role in the capacitive behavior of manganese oxide films and also leads to different morphologies, which in turn affects the electrochemical characteristics of the electrode [145, 146].

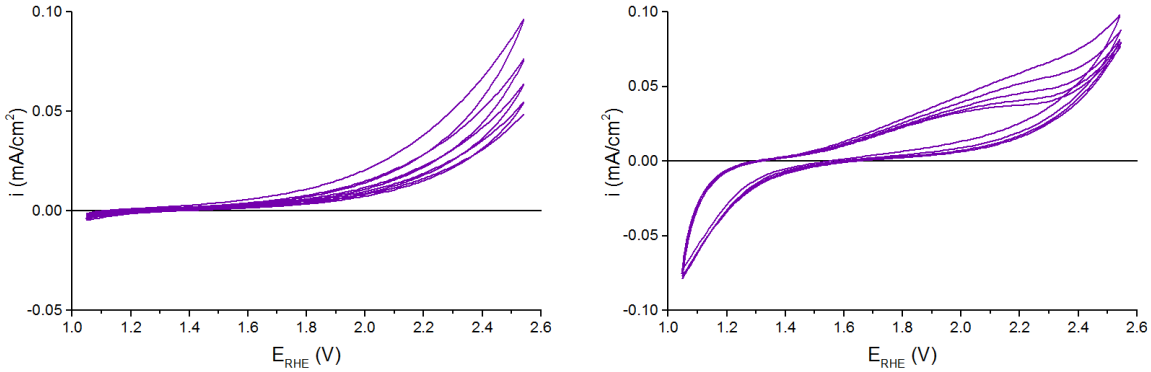

Fig. 60 – CV in 0.1M Na_2SO_4 of *D201/Ti*.
Scan rate 20 mV/s

On the contrary, pseudo-capacitance of the cathodically deposited MnO_x was again observed for the film grown on TiO_2-NTs (Fig. 60b), thus confirming that such behavior was due to the presence of the nanotubes interlayer.

Fig. 61 and Fig. 62 show the LSVs for the samples synthesized on Ti and TiO_2-NTs, respectively, at different current densities and with the permanganate precursor. As previously stated, the anodes synthesized by low current densities, that is, 0.025 mA/cm^2, presented the lowest currents at 2.6 V_{RHE}, probably because of the low amount of material deposited on the substrate.

For samples deposited on Ti, the non-crystalline MnO_x (*A200/Ti*) demonstrated again to be the most active film in the LSV. As can be noticed, the cathodic MnO_x sample grown on both Ti and TiO_2-NTs (i.e. *D201/Ti* and *D201/NTs*) showed a flat LSV and low current densities (< 0.05 mA/cm^2 at ~ 2.6 V_{RHE}) towards the water oxidation. This was

probably due to the presence of the α-MnO_2 phase, which had a lower tendency for that type of reaction [147].

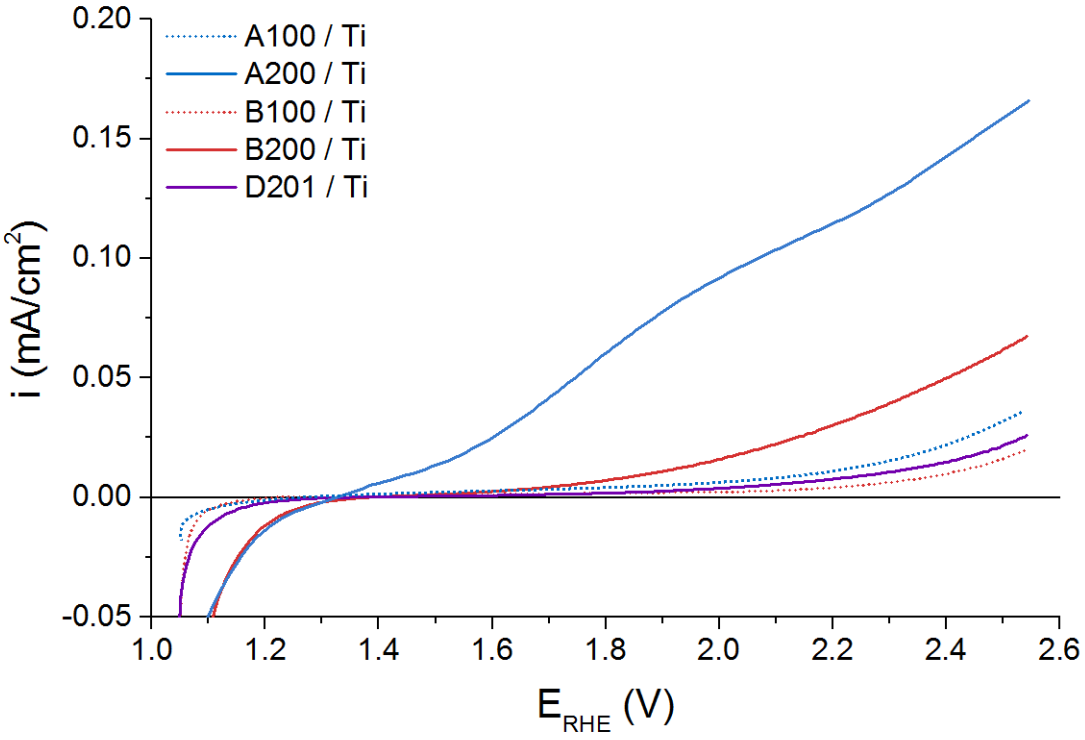

Fig. 61 – LSV in 0.1M Na_2SO_4 of electrodes deposited on Ti at different currents and precursor. Scan rate 5 mV/s

When analyzing the LSVs obtained by the electrodes grown on TiO_2-NTs, an interesting phenomenon was found in Fig. 62. The *B200/NTs* sample produced the highest final current density (~ 0.4 mA/cm^2 at 2.5 V vs. RHE, see Fig. 62), which was one order of magnitude higher than the similar MnO_x film deposited on Ti (*B200/Ti*,), and than the cathodically deposited films (*D201/Ti* and *D201/NTs*). Moreover, it was two times higher than the current densities obtained for the respective non-calcined samples, on both Ti and TiO_2-NTs. This trend was in agreement with the predominance of the α-Mn_2O_3 phase revealed by the XRD analysis on the calcined electrodes containing TiO_2-NTs, which is capable of higher oxygen evolution rates than α-MnO_2 [95, 104, 125], thus justifying the improved behavior for the water oxidation reaction. On the contrary, the presence of α-MnO_2 detected on the *B200/Ti* sample, as well as in the cathodically deposited MnO_x, led to a decrease in the water oxidation activity [147-149], which instead should be beneficial for the degradation of organic molecules (e.g. phenol) with a higher Nernst potential than water oxidation.

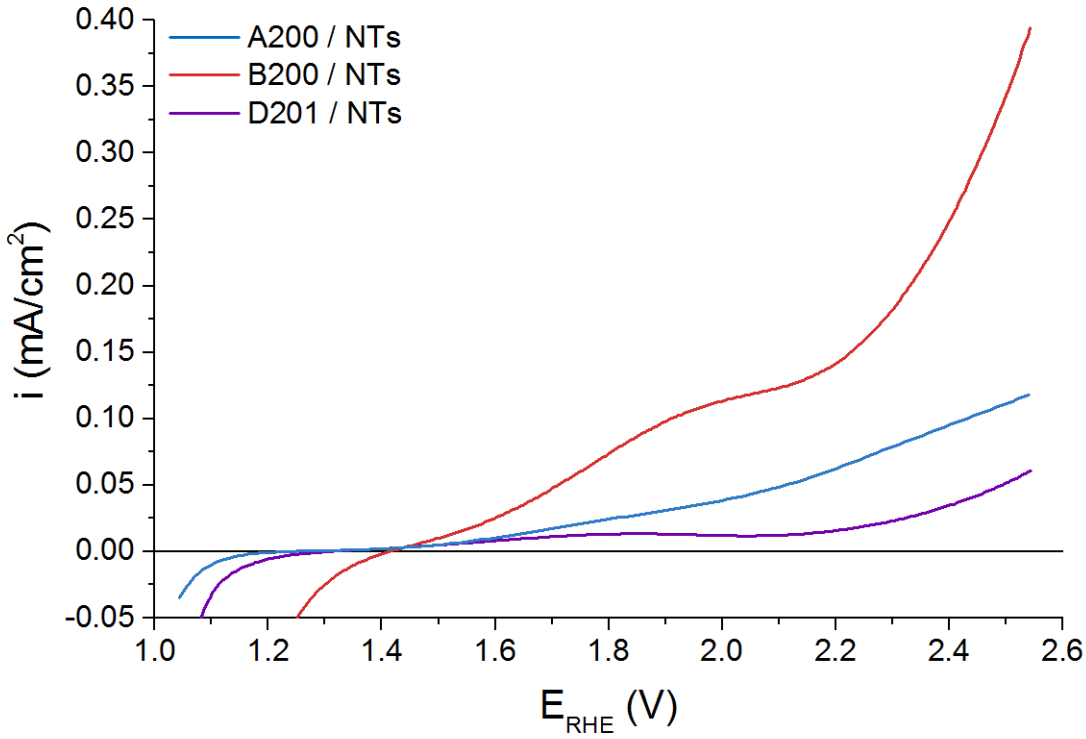

Fig. 62 – LSV in 0.1M Na_2SO_4 of electrodes deposited on NTs at 2.5 mA / 10 min

4.3.4 Phenol electro-oxidation tests

Fig. 63 shows the phenol degradation results obtained for all the electrodes synthesized in this work. The results obtained for the two substrates (Ti and TiO_2-NTs), without any catalyst, are also reported for comparison purposes. The effects of the electrodeposition parameters (time, Mn^{2+} concentration, current density and type of precursor) are separated to better evidence the effect of these parameters on the film activity.

- *Base-case and substrates*

El-Ox tests for the base-case electrodes were carried out at 0.25 mA/cm^2, not to exceed the limit of the potentiostat (10 V), and to start the process at around the same value of potential (~ 3 V_{RHE}).

Although the conversions were rather low, an interesting trend can be observed: the nanotubes interlayer seems to have a beneficial effect on both the degradation and the maximum potential reached after 5 h of reaction. In particular, the non-calcined *A000/NTs* sample reported the highest phenol conversion, that is, of about 12%.

It is also worth noticing (see the last box of Fig. 63a) that the blank test with the TiO_2-NTs substrate showed a slight conversion of phenol (about 4%), unlike the Ti foil, which was totally inactive. Moreover, after the tests, Ti was passivated and its surface changed from gray to a brownish color, indicating that a poor conductive oxide layer was formed as a result of the current passed through the electrode. The nanotubes resulted in a comparable conversion to that of the calcined electrodes, which indicates a higher selectivity of the non-crystalline MnO_x than of the sample containing α-Mn_2O_3 for this reaction; however, the reduction of the potential (more than 3 V) necessary to perform the reaction in the presence of the manganese oxide catalysts on the TiO_2-NTs, is clear, which confirmed the effectiveness of these materials for phenol degradation. Probably, the role of TiO_2-NTs is related to a decrease in the charge transfer resistance (*i.e.* kinetics of reaction), which could be induced by the good distribution and penetration of the manganese oxide on the high surface area and by the porosity provided by this 3D nanostructure, which enhance the diffusion of the electrolyte to the active material [93, 110, 111, 144].

As far as the effect of the temperature ramp during calcination is concerned, the electrode calcined at the slow ramp of 2 °C/min (*B000(s)/Ti*) did not lead to any conversion and resulted in a higher final potential than the similar sample calcined with a fast heating ramp (20 °C/min, sample *B000/Ti*). Therefore, the latter condition was implemented for the subsequent studies. Under such a condition, calcination improved the stability of all the samples and acted positively on phenol conversion in the case of the sample on the Ti substrate (*B000/Ti)*. Calcined electrodes, in fact, were the only ones which remained under 4 V_{RHE} for all the duration of the test.

Films calcined in N_2, instead, presented no conversion in all cases, i.e. calcined at slow or fast ramp, either on titanium or on nanotubes, proving that the hausmannite (Mn_3O_4) phase is non-active for the electro-degradation of phenol. Moreover, their working potentials resulted to be the highest for the samples grown over Ti, or comparable to the non-calcined electrodes for the film deposited on TiO_2-NTs.

- *Deposition time modification*

The synthesis conducted at different deposition times (i.e. 5 and 20 min) are also presented in Fig. 63a, in the second box. The *A010/Ti* and *A020/Ti* samples, which were the non-calcined ones, showed little or no phenol and COD degradation, similarly to the electrode deposited at 10 min, which gave 1.2% phenol conversion. Also the samples calcined in air, i.e. *B010/Ti* and *B020/Ti*, did not show any increment in the oxidation effectiveness towards phenol, thus confirming the results obtained by the electrochemical characterization: the deposition times investigated did not significantly affect the performances of the MnO_x films.

On the contrary, when looking at the working potentials in Fig. 63b, all the time-modified samples presented higher final potentials than the base-case counterparts. Thus,

all the following electrodes were synthesized with a deposition time of 10 min, which proved to provide the most stable performances.

- *Concentration modification*

The third boxes in Fig. 63 show the performances of the electrodes synthesized at different concentrations of Mn^{2+} precursor, either non-calcined or calcined in air. Both the samples obtained with 0.01 M Mn^{2+} (i.e. *A001/Ti* and *B001/Ti*) gave similar conversions to the base-case electrodes, with similar or slightly higher working potentials, therefore confirming the hypotheses of the electrochemical characterization, in which the difference between 0.1 M and 0.01 M Mn^{2+} was not determining. On the contrary, the samples obtained at 0.001 M Mn^{2+} were totally non-active, and their working potentials were higher than the base-case, probably due to the low amount of deposited material on the substrate.

Thus, the precursor concentration for further syntheses was 0.1 M Mn^{2+}.

Table 9 - Electrooxidation results for all tested electrodes

Electrode	**Faradaic efficiency (%)**	**TON (mol_{Phenol} / mol_{Mn})**	**Relative conversion (mol_{Phenol} / mol_{Mn}·W·h)**
A000 / Ti	7.8	0.25	37.2
A000 / NTs	33.2	2.36	469.0
B000(s) / Ti	0.0	–	–
B000 / Ti	10.7	0.86	212.6
B000 / NTs	37.1	1.15	314.8
C000(s) / Ti	0.0	–	–
C000 / Ti	0.0	–	–
C000 / NTs	0.0	–	–
Ti	0.0	–	–
TiO_2-NTs	22.4	–	–

a – Base-case electrodes and substrates

Electrode	Faradaic efficiency (%)	TON (mol_{Phenol} / mol_{Mn})	Relative conversion (mol_{Phenol} / mol_{Mn}·W·h)
A010 / Ti	0.0	–	–
A020 / Ti	11.7	0.19	27.9
B010 / Ti	9.8	1.58	390.1
B020 / Ti	15.6	0.63	230.6

b – Time modification

Electrode	Faradaic efficiency (%)	TON (mol_{Phenol} / mol_{Mn})	Relative conversion (mol_{Phenol} / mol_{Mn}·W·h)
A001 / Ti	10.7	0.86	212.6
A002 / Ti	0.0	–	–
B001 / Ti	3.9	0.13	18.6
B002 / Ti	0.0	–	–

c – Concentration modification

Electrode	Faradaic efficiency (%)	TON (mol_{Phenol} / mol_{Mn})	Relative conversion (mol_{Phenol} / mol_{Mn}·W·h)
A100 / Ti	0.0	–	–
A200 / Ti	43.3	0.51	17.1
A200 / NTs	42	0.48	20.1
B100 / Ti	0.0	–	–
B200 / Ti	45.9	0.35	25.1
B200 / NTs	26.7	0.26	25.7
D201 / Ti	44.6	0.82	43.7
D201 / NTs	45.3	0.75	46.7

d – Current and precursor modification

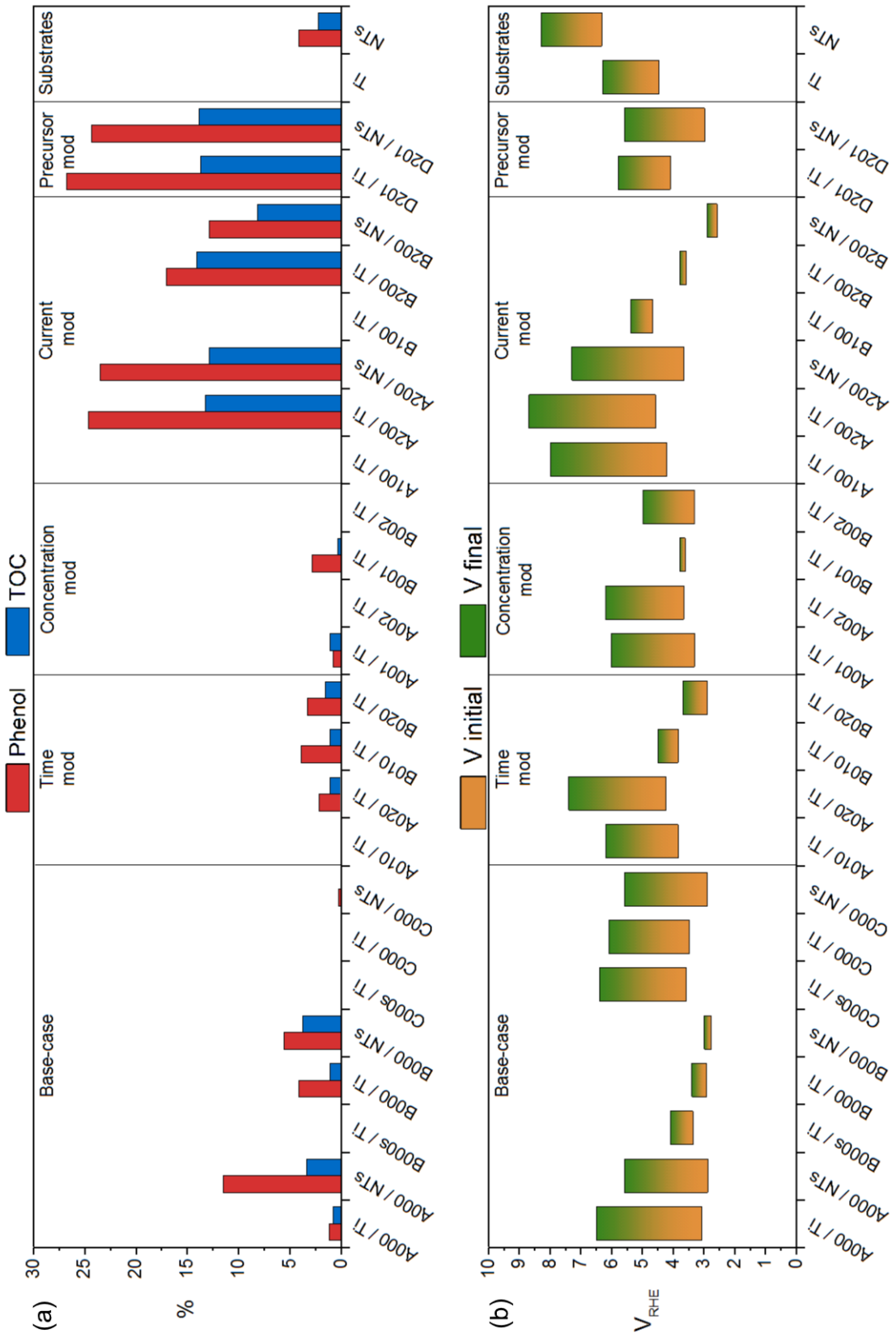

Fig. 63 - Phenol and COD conversion (a), initial and final potentials (b) for all the electro-oxidation tests

- *Current density and precursor modification*

Fig. 63 shows the performances obtained for the samples deposited at different current densities and with the cathodic method, on the right side of the bar charts. The electrodes obtained by electrodeposition at 0.025 mA/cm^2 were tested at 0.25 mA/cm^2 (due to poor stability), whereas the samples deposited at ±2.5 mA/cm^2 were tested at an El-Ox current density of 0.75 mA/cm^2. It was not possible to carry out the tests for Ti and TiO_2-NTs under the El-Ox current density of 0.75 mA/cm^2, as the two substrates reached the limit potential of the instrument (10 V) after just a few minutes.

First of all, it is worth noting that both the electrodes synthesized at 0.025 mA/cm^2, non-crystalline and calcined (i.e. *A100/Ti* and *B100/Ti*), showed no activity and their working potentials resulted in the highest among their type of material, even though the El-Ox current was only 0.25mA/cm^2. Therefore, no more consideration was given to this type of deposition.

Concerning the samples deposited at ±2.5 mA/cm^2, the as-prepared electrodes containing non-crystalline manganese oxides reported similar phenol conversion efficiencies, probably because of the higher thickness of the MnO_x on the top of the NTs substrate, whose activity prevailed over that of the material within the pores. Nonetheless, the role of NTs played in reducing the final reaction potential was again confirmed.

The highest conversion was obtained for the *D201/Ti* electrode, while the lowest one was reached for *B200/NTs*. Interestingly, as revealed by the XRD analysis, the higher the presence of α-MnO_2, the higher the conversion, while the higher the presence of α-Mn_2O_3, the lower was the degradation efficiency. The lower effectiveness of the latter type of electrodes could be due to the higher production of molecular oxygen, as Mn_2O_3 (Mn^{3+}) is considered the most active phase for water splitting [117, 125, 147, 148], and it leads to the indirect oxidation of phenol through a reaction with O_2. MnO_2 (Mn^{4+}) is instead more active for phenol oxidation [96, 97] or in heterogeneous catalysis [149, 150], due to its ability to degrade organic molecules by producing hydroxyl radicals (OH·). This has also been confirmed by the XPS analysis, which showed they were the samples with the highest AOS values (i.e. closer to the oxidation state of Mn^{4+}).

Although the presence of nanotubes in the calcined material, induced a small reduction in the activity (~5%), the final potential was about 1 V lower in the *B200/NTs* sample than for the *B200/Ti* sample. This can be explained by considering the induced formation of both the α-Mn_2O_3 and α-MnO_2 phases on the TiO_2-NTs substrate. The LSV of the *B200/NTs* sample resulted in the highest current densities in 0.1 M Na_2SO_4 (Fig. 7), which showed a higher tendency of this electrode towards the water splitting reaction. This feature, i.e. greater stability and oxygen evolution activity, is worth exploiting using this type of electrode in mild Catalytic Wet Air Oxidation (CWAO) conditions (Temperature, T < 200 °C; Pressure, P < 30 bar), in order to be able to exploit the O_2 produced to degrade phenol in a high T - high P electrochemical multifunctional reactor.

The Faradaic efficiency (FE) was calculated from the COD conversion, using Eq. 116:

$$FE = \frac{COD - COD_0}{8I\Delta t} \cdot FV_r \qquad \text{Eq. 116}$$

where COD_0 and COD are the chemical oxygen demand before and after the test, F is Faraday's constant (96487 C/mol), V is the reaction volume (l), I is the applied current (A) and Δt is the reaction time (s).

The Faradaic efficiency of the base-case electrodes was higher for the samples grown on the nanotubes (see Table 9a), because of the good performances obtained in terms of COD conversion. By changing the deposition time and the Mn^{2+} concentration, the variation of faradaic efficiency was negligible (see Table 9b, c)

The Faradaic efficiency was generally higher for the electrodes deposited at ±2.5 mA/cm^2 (see Table 9d), than for the ones observed for the samples synthesized at lower current densities, due to the fact that the conversion of both phenol and COD was much improved. In this case, with the exception of the *B200/NTs* electrode (α-Mn_2O_3), the FE was similar for all the electrodes, even for those samples which showed a lower phenol conversion. This implies that phenol can be readily converted into more oxidized molecules, such as benzoquinone or maleic acid [151, 152], but any further degradation is more difficult, thus a difference between the phenol and COD conversions have been observed.

Even though the complete removal of phenol was not achieved, the specific activities of the MnO_x-based electrodes were quite high, as shown in Table 9. The theoretical amount of Mn that was deposited on the electrode surfaces during the electrodeposition experiments can be calculated according to Faraday's law as:

$$I \cdot \Delta t = z \cdot \frac{m}{MW_i} \cdot F \qquad (3)$$

where I is the electrodeposition current (A), Δt is the electrodeposition time, z is the number of electrons involved (2 for anodic deposition, 3 for cathodic deposition), m is the mass deposited (g), MW_i is the molecular weight of the ionic species (g/mol) and F is Faraday's constant (96487 C/mol). Hence, the theoretical amount of Mn in the electrodes deposited at 0.25, 2.5 or -2.5 mA/cm^2 for 10 min were 0.043, 0.427 and 0.285 mg_{Mn}/cm^2, respectively.

The Turn Over Number (TON) referred to the Mn (active sites) was then calculated as mols of phenol degraded by mols of Mn in the electrodes (see Table 9a, d). In the same manner, a conversion efficiency related to the energy consumption was calculated by dividing the TON by the total applied energy (in Wh) provided to the electrode during the 5h of the degradation test and the results are also reported in the last column of Table 9a and Table 9d.

The TON for the electrodes deposited at 0.25 mA/cm^2 was lower for the samples grown on Ti than the one obtained for the films synthesized over the nanotubes, especially for the non-calcined samples. The energy relative conversion followed the same trend, with the best performances being observed for samples on the TiO_2-NTs.

The electrodes deposited at 2.5 mA/cm^2, in general, led to lower TONs than the electrodes synthesized at 0.25 mA/cm^2, probably due to the elevated thickness of the films, which did not allow all the deposited manganese oxide to be exploited. As for the phenol degradation, the anodically deposited and calcined films and the samples grown on nanotubes were slightly less performing than the samples over titanium. However, the energy related conversion, had an inverse trend, with better results for the above-mentioned electrodes. This was due to the improved stability and, thus, to the lower potential reached during the electrooxidation process.

The cathodic manganese oxides proved to be the best performing synthesized electrodes, for all the analyzed parameters (phenol degradation, COD reduction, TON and energy relative conversion).

A comparison was made with one of the most effective SnO_2-Sb sample on the TiO_2-NTs electrode [111], that converted 90% of phenol in 1.7h, at a current density of 10 mA/cm^2, which corresponds to a working potential of about 2.85 V vs RHE. For this type of electrode, the deposited mass was 2.50 mg/cm^2 and the TON was 0.88 mol_{Phenol} / mol_{SnSb}, which is similar to the one obtained for *D201* and lower than the electrodes grown at 0.25mA/cm^2 on the TiO_2-NTs. When the energy given to the electrode for 1.7 h was considered, the conversion related to the energy consumption was of 18.2 $mol_{Phenol}/(mol_{SnSb} \cdot Wh)$, that is, 58 % less than our best electrode (*D201/Ti*) which achieved 43.7 $mol_{Phenol}/(mol_{SnSb} \cdot Wh)$.

4.3.5 EIS analysis

Electrochemical Impedance Spectroscopy (EIS), a well-known technique that is often employed to characterize electrochemical systems with the aim of comparing their charge transfer and transport properties [47, 48, 116], was also performed on the phenol solution. An applied DC potential of 3.3 V_{RHE}, which was the average initial potential achieved during the El-Ox process for all the considered samples, was employed for the EIS analyses. The results are reported in Fig. 64B and Fig. 66B (Nyquist plots) and in Fig. 65 and Fig. 67 (Bode plots: phase and modulus of impedance |Z| vs. frequency).

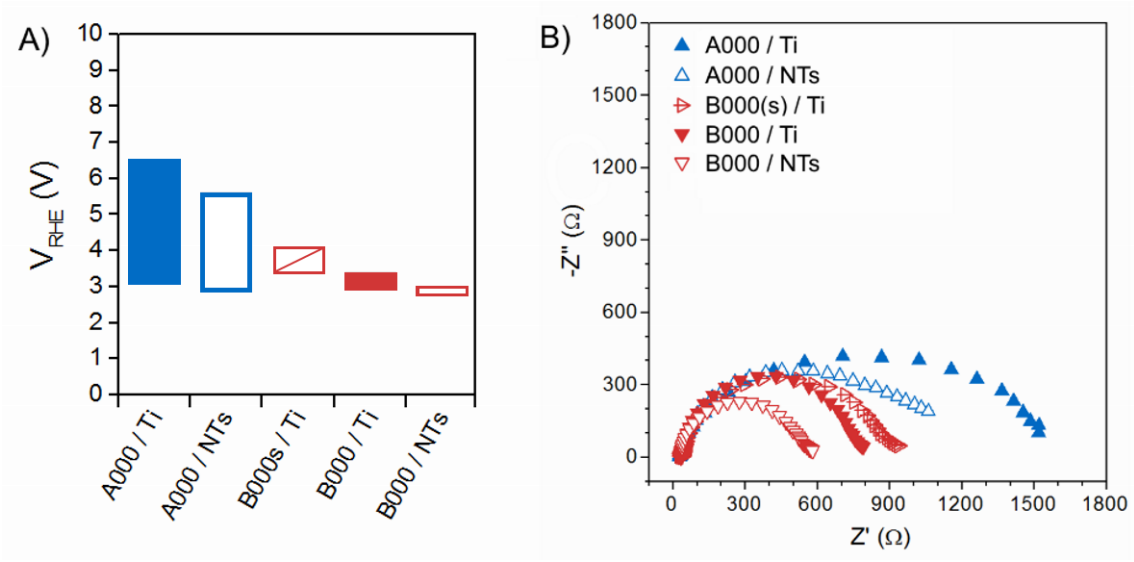

Fig. 64 – (A) Electro-oxidation potentials and (B) Nyquist plots of the EIS measurements at 3.3 V vs. RHE of base-case samples

The most stable electrodes that were able to sustain the constant potential (i.e. for which the total increase of potential over time was lower than 0.5 V) were found to be the calcined anodically deposited MnO_x electrodes over both the Ti and TiO_2-NTs substrates (see Fig. 64A and Fig. 66A), which can be attributed to the presence of highly stable α-Mn_2O_3 crystalline phase. Accordingly, the Nyquist plots of the same samples in Fig. 64B and Fig. 66B show that they evidenced lower impedance values for these electrodes than for the other electrodes, which in turn indicated an increase in the number of electrons transferred through the electrode/electrolyte interface on those materials. In fact, a reduction in the diameter of the semicircle in the Nyquist plots indicated a lower resistance to the charge transfer because of an enhancement of the reaction kinetics, which, in this case, depends on the surface properties of the MnO_x-based electrode materials [117]. Nevertheless, it was not possible to identify which was the prevalent reaction between water oxidation and phenol degradation from these electrochemical measurements, and, the phenol and COD conversion were therefore chemically determined as reported in Par. 4.3.4.

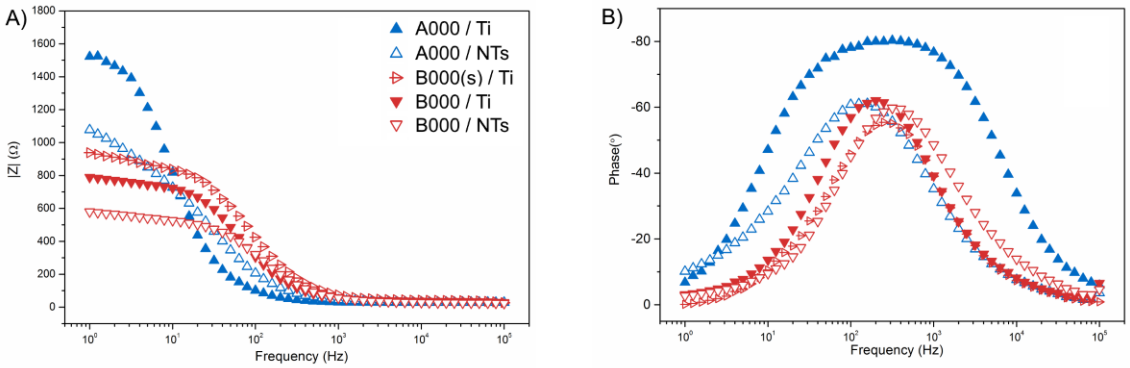

Fig. 65 – Bode plots of EIS at 3.3 V_{RHE} of base-case electrodes in 100 mg/l phenol and 0.1 M Na_2SO_4: Impedance modulus (A) and phase (B)

Instead, all the non-calcined MnO_x samples (see Fig. 64A and Fig. 66A) reached very high potentials, of up to 8.6 V. An intermediate behaviour was observed for the thermal-treated cathodically deposited MnO_x samples, which were constituted by rod-like α-MnO_2, and steadily increased the potential up to 6 V.

Interestingly, in all the samples, TiO_2-NTs contributed to the reduction of the applied potential for phenol El-Ox (from 0.5 to 1.5 V) with respect to the Ti substrate. In particular, the *B000/Ti* and *B200/Ti* samples settled at a higher potential (of about 0.4 V and 1 V, respectively) than the similar materials deposited on the TiO_2-NTs substrates. This trend can be attributed to the presence of a certain amount of α-MnO_2 for the *B200/Ti* sample, but not for the other material.

Besides, the difference between the El-Ox potential of the MnO_x on the Ti, for the non-crystalline MnO_x electrodes (Fig. 64A and Fig. 66A), with respect to that on the TiO_2-NTs substrate increased during the time-course of the reaction. On the other hand, TiO_2-NTs interlayer in cathodically deposited electrodes (Fig. 66A), did not decrease the potential with respect to the sample on Ti in the same extent as the anodically deposited MnO_x, but a certain improvement was also achieved in this case. A possible explanation for such behavior could be the lower tendency of the cathodically deposited manganese oxide to enter the nanotube pores, as already observed in the FESEM cross-sections (Fig. 46), and, to a certain extent, could also be due to a loss of adhesion of the MnO_2 to the substrate.

In short, the positive influence of the NTs substrate on the behaviour of the electrodes was evident as it increased the reaction kinetics and led to a lowering of the necessary potential, which was also demonstrated by the lower impedance of the MnO_x samples deposited on TiO_2-NTs than their counterparts supported on the Ti foils, as can be seen in Fig. 64B and Fig. 66B and in the modulus of impedance |Z| at 1 Hz reported in Fig. 65 and Fig. 67.

Since the charge transport differences in the samples were not so evident in the Nyquist plots in Fig. 64B and Fig. 66B, the EIS measurements were also plotted in the

form of Bode diagrams (Fig. 65 and Fig. 67). Bode plots are usually useful to separate charge transfer and charge transport processes in electrochemical systems because the latter is characterized by faster time constants [47, 104]. The phase spectra in Fig. 65 and Fig. 67 show a clearly distinguishable peak for all the electrodes in the range between 100 and 1000 Hz (approx. centered at about 200 Hz for most of the samples), which can be attributed to the charge transport process in such electrodes. Instead, the charge transfer process at the electrode/electrolyte interface can be analyzed from the |Z| at frequencies lower than 100 Hz, in the same way as for previous works [116, 117]. For comparison purposes, the |Z| values at 200 Hz and at 1 Hz could be ascribed to a measure of the charge transport and charge transfer resistances, respectively, of the different electrodes. As expected, the values of |Z| at 1 Hz followed an equivalent trend to the diameter of the Nyquist plots semicircles, and the same conclusions as before can, therefore, be drawn.

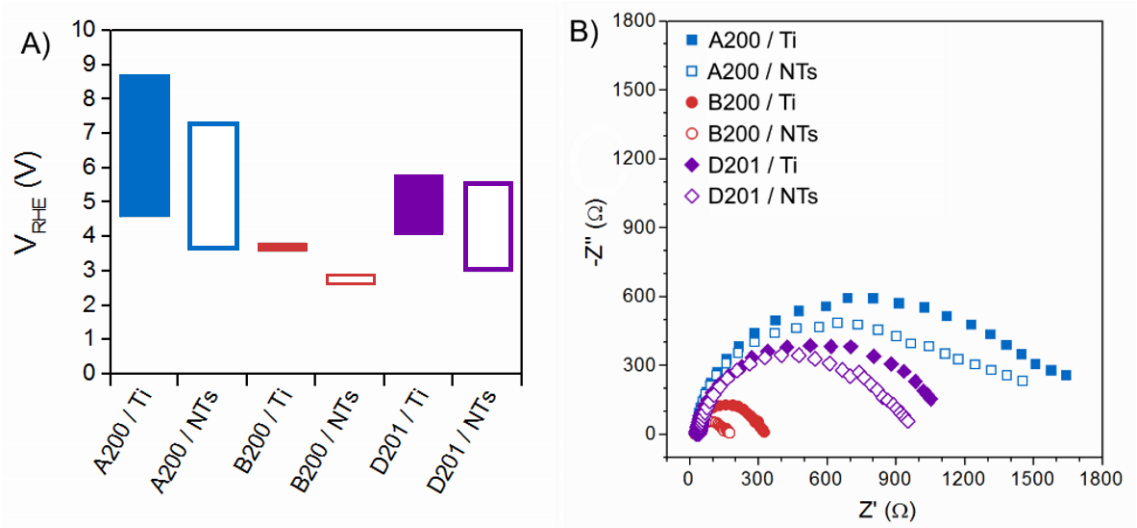

Fig. 66 – (A) Electro-oxidation potentials at and (B) Nyquist plots of the EIS measurements at 3.3 V vs. RHE of samples synthesized at ±2.5 mA/cm^2

In the thin samples (see the FESEM images in Fig. 43) deposited at 0.25 mA/cm^2, the highest conductivity of the Ti substrate is confirmed by the low |Z| values (e.g. 58 Ω at 200 Hz) of the non-calcined MnO_x sample supported on Ti foil (i.e. *A000/Ti*). Obviously, such resistance values also accounted for the resistivity of the non-crystalline MnO_x film towards the electrons flow and, consequently, it could not be null. As a consequence, the charge transport resistance was higher for the sample deposited on the TiO_2-NTs, with a |Z| value of 118 Ω at 200 Hz, which can be attributed to the lower conductivity of TiO_2 than the metallic Ti.

However, after the thermal treatment, the charge transport was similar, with a higher value of |Z| for all the samples. The sample calcined with the slow ramp, *B000/Ti (s)*, showed the highest impedance (i.e 257 Ω at 200Hz), while the fast heating ramp decreased the impedance to 172 and 198 Ω in the *B000/Ti* and *B000/NTs* samples, respectively. Considering that all these calcined samples contained α-Mn_2O_3, their charge

transfer properties can be attributed to the formation of the TiO_2 passivation layer on the surface of the Ti foil (as observed from the XRD), which caused a considerable drop in the metallic behaviour of this substrate, especially for the slow heating ramp, which exposed the sample to high temperatures for longer times.

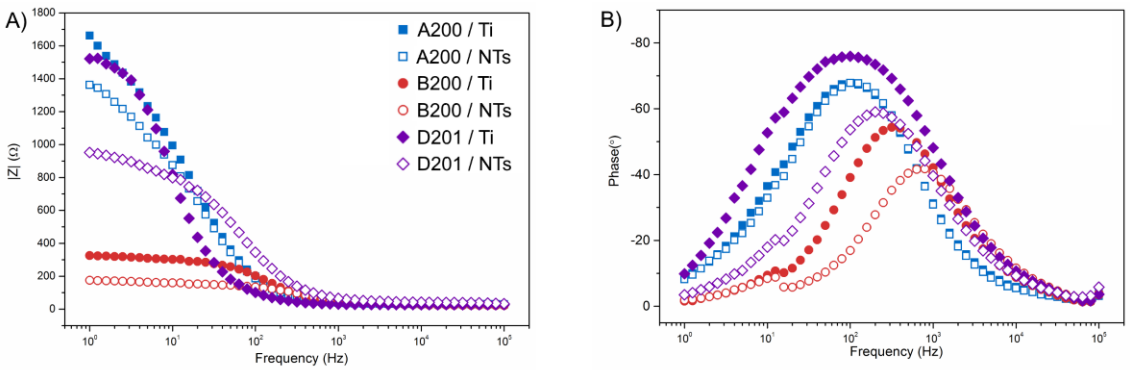

Fig. 67 – Bode plots of EIS at 3.3 V_{RHE} of electrodes synthesized at ±2.5 mA/cm^2 in 100 mg/l phenol and 0.1 M Na_2SO_4: Impedance modulus (A) and phase (B)

The electric conduction properties of the TiO_2 nanotube arrays are mainly related to defects produced during the electrochemical growing process (anodization), which lead to the well-known n-type semiconducting behavior. Oxygen vacancies and Ti^{3+} states in TiO_2 nanotubes, which dominate optical and electrical properties of the material to a great extent [123] are particularly important. In comparison to a compact oxide layer, such as the thermal oxide formed under the MnO_x (on Ti) after annealing, the doping level obtainable inside the crystalline TiO_2 nanotubes is generally very high (10^{20} cm^{-3}, as calculated by Mott–Schottky analysis in a previous work [119]). This can explain the different behavior observed for the *A000/Ti* and *B000/Ti* samples in comparison with their counterparts in TiO_2 NTs. The metallic behavior of titanium in the non-crystallized sample leads to a higher charge transport from the MnO_x to the current collector, while the rutile layer without defects that is formed on the top of the metal substrate after calcination at 500 °C becomes less effective than the self-doped nanotubular carpet, despite their different thicknesses.

On the other hand, when the MnO_x amount and the film thickness is increased, after an increase in the electrodeposition current to 2.5 mA/cm^2, both of the non-calcined samples on Ti foil and TiO_2-NTs reported similar |Z| values (i.e. 100 Ω at 200 Hz). After the thermal treatment, their charge transport resistance increased slightly, showing |Z| values of 133 and 115 Ω, respectively, at 200 Hz, which once again is probably due to the formation of a passivating layer after the calcination. Moreover, the impedance modulus was higher for the *B200/Ti* sample, which contained α-Mn_2O_3 and α-MnO_2, unlike the sample on the TiO_2-NTs which only contained α-Mn_2O_3, as observed from the XRD analyses.

In the case of the calcined cathodically deposited samples, although both were constituted by α-MnO_2, the one on the Ti substrate reported a lower charge transport resistance than the similar sample on TiO_2-NTs, which had a |Z| value at 200 Hz of about 59 Ω and 200 Ω, respectively. In this case, the poor charge transport could be due to the limited contact area between the α-MnO_2 film and the nanotubes, as shown by the cross section of the FESEM images.

4.3.6 Accelerated lifetime tests

The accelerated lifetime tests were carried out on some of the synthesized samples: the base-case anodes and the electrodes obtained at high current densities, either anodically and cathodically deposited.

It was not possible to perform durability tests on the non-calcined electrodes, deposited at 0.25 mA/cm^2 or at 2.5 mA/cm^2, and on the electrodes calcined in N_2, as those electrodes immediately reached 10 V. As a consequence, it is possible to state that calcination was essential to reach a resistant film that could withstand high current densities, without being damaged or reaching too high working potentials.

Fig. 68 shows the tests that were carried out on the calcined electrodes electrodeposited at 0.25 mA/cm^2 and it can be observed that films grown on TiO_2-NTs were able to resist up to 3 h, while the samples on Ti had a lifetime of about 2 h, with a slight increase in durability when the calcination occurred at a fast ramp.

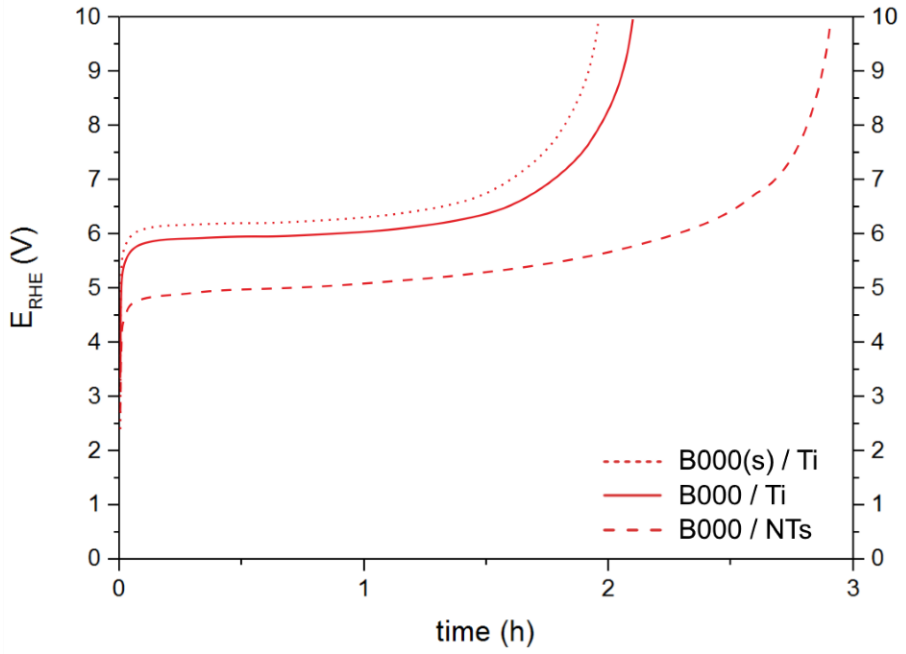

Fig. 68 – Accelerated lifetime test at 100 mA/cm^2 in 1 M Na_2SO_4 of base-case samples

Fig. 69 reports the results of the durability tests on the calcined electrodes electrodeposited at ±2.5 mA/cm^2, among which the *B200/NTs* sample reached about 15 h of an accelerated lifetime, while the same film deposited on metallic titanium stopped at 12 h. Both the *D201/Ti* and *D201/NTs* cathodic electrodes resisted for about 7 h, thus confirming that the calcined anodic samples were the most durable electrodes. If compared to previous literature works, the results obtained on the most stable sample were comparable in order of magnitude to the durability tests carried out for similar electrodes based on SnO_2-Sb synthesized via electrodeposition over TiO_2-NTs, which had durabilities of about 36 h [113].

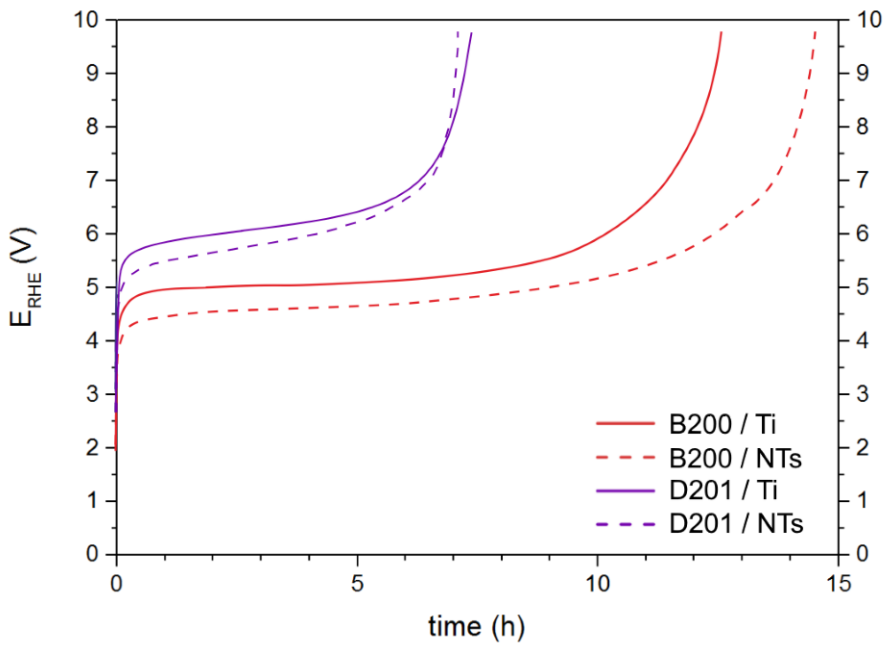

Fig. 69 – Accelerated lifetime test at 100 mA/cm^2 in 1 M Na_2SO_4 of samples synthesized at ±2.5 mA/cm^2

4.4 Conclusions

In conclusion, MnO_x electrodeposited on titanium and titania nanotubes were synthesized, fully characterized and tested. Various techniques, which led to different morphologies and phases of manganese oxides, were employed, as reported by means of the FESEM, XRD and XPS investigations.

Electro-deposition parameters such as time, precursor concentration, deposition current and type of precursor were varied to investigate their effects on the performances of the films. For the anodic deposition from a Mn^{2+} precursor (i.e. manganese acetate), 2.5 mA/cm^2 for 10 min in 0.1 M Mn^{2+} was found to be the best synthesis, which led to the highest conversions. For the cathodic deposition in potassium permanganate, the best combination was -2.5 mA/cm^2 for 10 min in 0.01 M Mn^{7+}.

Also the ramp applied during the calcinations was studied, proving that a fast ramp at 20°C/min provided better results than the slow ramp at 2°C/min.

Concerning the activities of the different phases, α-MnO_2 on titanium demonstrated the highest activity for the electro-degradation of phenol, while α-Mn_2O_3 on titania nanotubes provided the highest stability during the reaction. Hausmannite Mn_3O_4, on the contrary, gave the lowest activity and stability, therefore it was no more considered after the preliminary tests.

Synthesis on TiO_2-NTs allowed the manganese oxide to penetrate inside the nanotube array when the anodic deposition was carried out, while cathodic deposition did not show any relevant growth of manganese oxide inside the nanotube structure. MnO_x deposited on TiO_2-NTs resulted in lower working potentials (about 1-1.5 V) during the electro-oxidation of phenol, than the same electrodes grown on Ti metal. This result was investigated through an EIS analysis, which confirmed the fundamental role of TiO_2-NTs in enhancing the charge transfer properties and improving the conduction from the metal substrate to the MnO_x film, especially in calcined electrodes, as the formation of a passivating layer of rutile on the metallic Ti was avoided. Thus, excellent performances were obtained on the optimized substrates, even though total phenol and COD conversions were not reached in this work. However, it is important to underline that the electro-oxidations were carried out at very low current densities with respect to those adopted in most of the literature. Furthermore, these results should be considered in relation to the amount of deposited material, which was lower than for the other reported syntheses, due to the fast electrodeposition times.

Moreover, the durability tests proved that the electrodes anodically deposited at high current densities had the longest lifetime, which was further increased by the presence of the nanotubes layer (up to 15h), thanks to the better adhesion obtained from the penetration of the MnO_x film inside the nanotubes. More studies are required in order to better understand the deactivation causes, in order to be able to further improve the lifetime of these materials.

The easiness of the procedure and the thermal energy saving obtained with the proposed synthesis method should be considered as positive points, since there is no need for long layer by layer preparations, such as the one used to deposit alternate layers of Sb and Sn from their respective precursors solutions and for which the calcination times are higher. Hence, further improvements should be made to increase both the performance and stability of such electrodes, in order to find an interesting alternative to the commonly used, and more expensive (e.g. IrO_2, RuO_2) or more toxic electrodes (e.g. PbO_2) for the treatment of organics in wastewater. Moreover, the here presented results open interesting perspectives for additional phenol degradation studies, even under intensified process conditions, with the aim of boosting phenol conversion at high temperatures and high pressures (CWAO conditions).

CHAPTER 5

ELECTRO-OXIDATION OF PHENOL AT HIGH TEMPERATURES AND PRESSURES

5.1 Introduction

After having performed the characterizations and the electro-oxidation (*El-Ox*) tests at ambient conditions, to compare the activities of the MnO_x-based anodes with the state-of-the-art, tests under high temperatures and high pressures (HTHP) were carried out on some of the most promising samples. In particular, the *B200/Ti* sample (i.e. anodically deposited with α-Mn_2O_3 / α-MnO_2 phases), and the *D201/Ti* sample (i.e. cathodically deposited with α-MnO_2 phase) were selected among the others, due to their high activity and/or stability.

As reported in chapter 4, in fact, cathodic electrodes (type *D*) showed the higher efficiency of degradation phenol, while the anodic samples (type *B*) proven to give a stable working potential throughout all the El-Ox tests.

Tests on the samples deposited on TiO_2-NTs will not be shown, as the nanotubes interlayer resulted too fragile for the operative conditions employed in the experiments, and both the film and the nanotubes detached from the substrate of titanium foil.

The manganese oxide electrodes were compared with two of the most performing types of anode used for this application: electrodeposited antimony-doped tin oxide (SnO_2-Sb^{5+}) film on titanium and thermally deposited ruthenium oxide (RuO_2) over titanium.

Two main results are expected:

1) the increase of the efficiency for phenol removal and the degree of mineralization, due to the improved exploitation of the current given to the system (evolved O_2 is used as well as hydroxyl radicals for the oxidation of phenol, instead of being wasted as a by-product)
2) the decrease of the cell potential for the reaction, since the higher temperatures should favor the electrolyte conductivity and improve the charge transfer

5.2 Materials and methods

5.2.1 Ti substrate preparation

Titanium foils (Sigma-Aldrich, 99.7%, thickness 250 µm) of 40 cm^2 were prepared according to the procedure described in Par. 4.2.1 [153]: polishing with 320-grit sandpaper, ultrasound cleaning in 2-propanol for 15 minutes. degreasing in 40% NaOH at 50°C for 20 minutes, and etching for 1 minute in HF solution 1.2% w/w shortly before the deposition process to remove the native oxide layer.

5.2.2 MnO_x electrodes synthesis

Electrodeposition of manganese oxides was conducted under similar conditions to Par. 4.2.2, with a BIOLOGIC VMP-300 potentiostat. Ti was set as the anode, Pt wire was used as the cathode and Ag/AgCl 3M KCl (+ 0.209 V vs NHE) was used as the reference electrode.

The *B200/Ti* sample was prepared by anodic deposition, by dipping the titanium foil (40 cm^2) in 150 ml of a solution containing 0.1 M of $Mn(CH_3COO)_2$ as Mn precursor and 0.1 M Na_2SO_4 as supporting electrolyte. A current density of 2.5 mA/cm^2 was applied to the system for 10 min.

The *D201/Ti* sample was deposited by cathodic deposition, by dipping the Ti foil (40 cm^2) in 150 ml of 0.01 M of $KMnO_4$ and 0.1 M Na_2SO_4 solution and applying a current density of -2.5 mA/cm^2 for 10 min.

Both the samples were calcined in a muffle oven at 500°C for 1 h, with a temperature ramp of 20°C/min.

5.2.3 SnO_2–Sb^{5+} electrodes synthesis

Synthesis of antimony-doped tin oxide films was carried out with a procedure described elsewhere [110]. The Ti foil (40 cm^2) was alternatively dipped in precursor solutions of $SbCl_3$ (Fluka, > 99.0%)and $SnCl_4 \cdot 5H_2O$ (Fluka, 98.0%). Sb^{3+} ions were first electrodeposited on the Ti substrate in a solution containing 0.01 M of $SbCl_3$ and 0.05 M citric acid (Sigma Aldrich, 99%) for 1 min at a constant current density of -2 mA/cm^2. After rinsing with DI water, the electrode was then dipped in a solution containing 0.1 M of $SnCl_4$ and 0.05 M H_2SO_4 (Fluka, 95-98%), and a current density of -2 mA/cm^2 was

applied for 25 min. This procedure was repeated for 2 times to obtain a layer-by-layer electrodeposited material. The sample was then rinsed and left to dry in air.

Finally, the electrode was annealed in a muffle oven at 550°C for 6 h, with a calcination ramp of 20°C/min.

5.2.4 RuO_2 electrodes synthesis

The film of ruthenium oxide was obtained via the thermal deposition method, described elsewhere [154]. The precursor solution was 0.1 M $RuCl_3 \cdot xH_2O$ (Sigma Aldrich, 38-42% Ru basis) dissolved in 2-propanol (Sigma Aldrich, 99.5%), with the addition of some drops of HCl (Fluka, 37%). The solution was applied to the surface of the Ti foil (40 cm^2) by brush coating, dried at 80°C in air for 10 min, and then calcined in a muffle oven at 500°C for 15 min. The procedure was repeated 10 times. Finally, the sample was annealed at 500°C in air for 2 h.

5.2.5 Standard electro-oxidation tests

Firstly, all the electrodes were synthesized on a Ti foil of 1 cm^2, to test them in standard El-Ox conditions (i.e. at ambient temperature and pressure). Experiments were carried out in an undivided and unstirred cell containing 15 ml of phenol (C_0=100 mg/l) and 0.1 M Na_2SO_4 as supporting electrolyte. The samples were employed as the anode, while Pt wire was set as the cathode. A constant current density of 2.5 mA/cm^2 was applied to the system for 5 h. This value is far lower than those commonly used in literature (around 10-20 mA/cm^2). It was chosen as it is the minimum theoretical current, needed to completely oxidize phenol, according to Eq. 117 and Eq. 118:

$$C_6H_6O + 7O_2 = 6CO_2 + 3H_2O \qquad (28e^-) \qquad \text{Eq. 117}$$

$$\boldsymbol{i = \frac{I}{A_{el}} = \frac{z \cdot F \cdot \frac{C_{0_{phenol}}}{PM_{phenol}} \cdot V_{sol}}{\Delta t \cdot A_{el}}} = \frac{28 \cdot 96500 \frac{C}{mol} \cdot \frac{100}{94} \frac{mol}{l} \cdot 0.015\ l}{3600 \cdot 5\ h \cdot 1\ cm^2} = \mathbf{2.40\ \frac{mA}{cm^2}} \qquad \text{Eq. 118}$$

rounded up to **2.50 mA/cm^2**. In this way, the TOC conversion coincides with the faradaic efficiency (FE), defined as:

$$\boldsymbol{FE = \frac{TOC_{fin} - TOC_{in}}{\Delta TOC_{theor}}} \qquad \text{Eq. 119}$$

Higher current densities could have been applied, but the reaction overpotential would have reached higher values, thus decreasing the Faradaic efficiency of the process.

5.2.6 High-Temperature High-Pressure electro-oxidation tests (HTHP El-Ox)

HTHP El-Ox tests were carried out in a prototype reactor at Politecnico di Torino. The lab-scale reactor consists of two separate chambers (500 ml each), where anodic and cathodic reactions take place. A pipe connects the two compartments, where a membrane can be placed, in case separation of the two chambers is required, e.g. to have wastewater treatment on the anodic side and hydrogen production from clean water on the cathodic side.

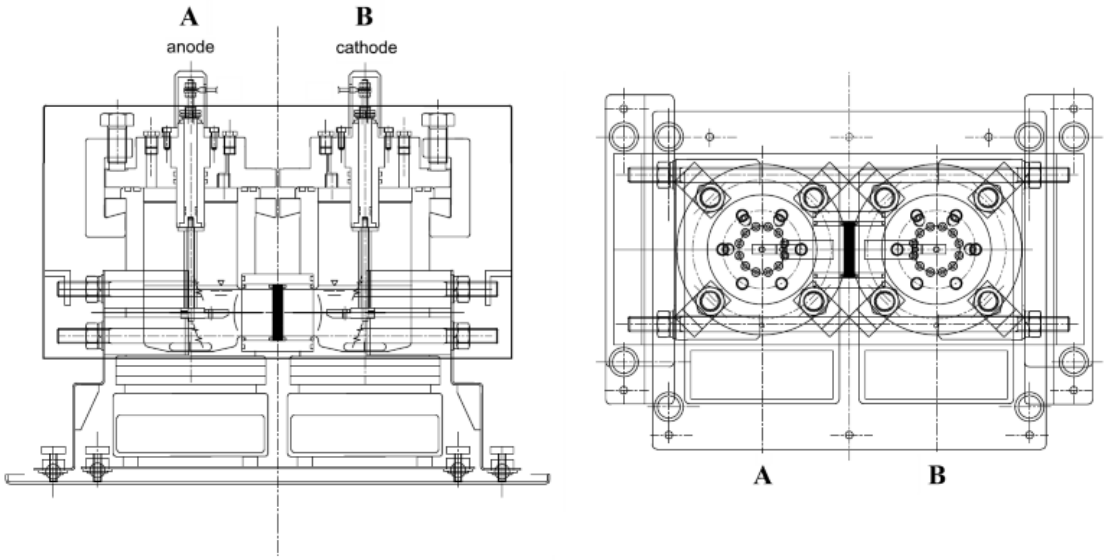

Fig. 70 – Scheme of the HTHP reactor

The equipment is made of AISI 316 stainless steel and can resist to 50 bars and 200°C. A magnetic hotplate stirrer provides both the heat and the mixing. There are temperature and pressure sensors on the top of the chambers. The system works in batch conditions, but it could also operate in continuous conditions (liquid inlet and outlet lines are predisposed on the top of the reactor). Gas outlets are provided with back pressure regulation and pressure relief valves so that they could be connected to a gas chromatograph for further analysis.

Different conditions were employed during the tests. Firstly, an experiment was conducted at 85°C and 30 bar, i.e. similar to some PEM electrolysis conditions [155], to investigate the potential application of the manganese oxide samples in standard PEM electrolyzer. Then, a test was carried out at 150°C and 30 bar, which are comparable with

mild CWAO conditions [56]. The synthesized electrodes were used as the anode, while a Pt foil (~ 15 cm^2) was employed as the cathode. No reference electrode and membrane were employed.

For both the experiments the electric charge passed through the system was the minimum for complete the mineralization of phenol, calculated by:

$$q = I \cdot \Delta t = z \cdot F \cdot \frac{C_{0_{phenol}}}{PM_{phenol}} \cdot V_{sol} = \frac{28 \cdot 96500 \frac{C}{mol} \cdot \frac{100}{94} \frac{mol}{l} \cdot 1\,l}{3600} = \mathbf{798\ mA \cdot h}$$

Eq. 120

rounded up to **800 mA·h**. Therefore, also for these tests, the faradaic efficiency is equal to the TOC conversion.

5.2.7 Ohmic drop compensation

As one of the critical issues in the employment of the HTHP device is the high distance between the anode and cathode (~ 10 cm), a preliminary characterization of the reactor by Electrochemical Impedance Spectroscopy (EIS) was made, to evaluate the ohmic drop in different conditions of temperature and pressure. The same procedure was carried out for the standard El-Ox tests. Measured cell potentials were then compensated by the ohmic overvoltage, in order to allow the comparison among all the samples and the operative conditions.

5.2.8 HPLC and TOC analysis

High-Performance Liquid Chromatography (Shimadzu Prominence HPLC, with a Diode Array Detector DAD, set at 269 nm) and Total Organic Carbon (Shimadzu TOC-V_{CPH} Carbon Analyzer) analysis were performed to determine the phenol degradation and the degree of mineralization.

HPLC was also used to determine the intermediates formed during the degradation, in order to compare the reaction pathways with the ones presented in the literature.

5.3 Results and discussion

5.3.1 Ohmic drop compensation analysis

Tests in beaker at ambient conditions

Firstly, the measurement was carried out in the beaker, where, the standard El-Ox tests were performed. Two Pt wires were used for the experiment. A cell potential of 4.5 V, which is commonly reached in electro-oxidation treatments [152], and an alternate current (AC) frequency of 10^5 Hz were set, to determine the resistance of the solution. Results showed that the initial solution (100 mg/l phenol and 0.1 M Na_2SO_4), has a resistance of 30-35 Ω when the electrodes are placed at a distance of ~ 2 cm. Thus, the cell overpotential due to the ohmic drop is about 0.08 V, if a current density of 2.5 mA/cm^2 is applied to an anode of 1 cm^2.

Tests in the HTHP reactor

In order to investigate the response of the system to the variation of the operative conditions, the impedance analysis for the ohmic drop measurement was carried out in a wide range of temperatures and pressures. This would also be useful to understand the trend of the electrolyte resistance with both temperature and pressure.

The cell potential was set at 4.5 V and the AC frequency was set at 10^5 Hz, as for the ambient conditions test. Two Pt foils were employed as electrodes. For the same solution (100 mg/l phenol and 0.1 M Na_2SO_4), and a distance of ~ 10 cm between anode and cathode, the following ohmic drops were found at different operative conditions:

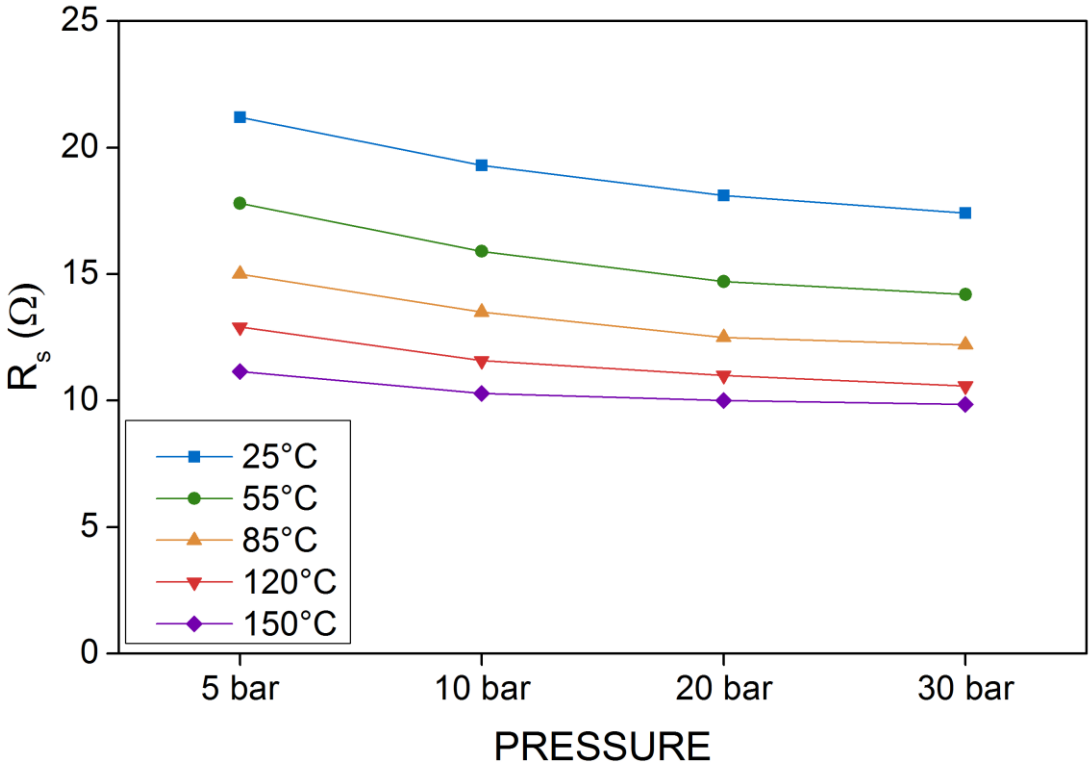

Fig. 71 – Effect of the pressure on the electrical resistance of the solution

As shown in Fig. 71, the influence of the pressure on the electrolyte resistance resulted very small, especially at high temperatures, where the resistance decreased from a value of 11.1 Ω to a value of 9.9 Ω (at 150°C). At 25°C, instead, the solution resistances fell from 21.2 Ω to 17.4 Ω. Also the pressure range affected the trend of the resistance: from 5 to 10 bar, the decrease was more pronounced than in the range 10-30 bar, in which a very small change was observed. Indeed, in the first pressure interval (5-10 bar), the drop of resistance was almost equal to the decrease in the second part (10-30 bar), and this trend was detected for all the temperatures analyzed.

Probably, this effect was due to two phenomena [156]:

1) the increase of the pressure partially compressed the volume of the solution thus slightly increasing the concentration of the electrolyte (Na_2SO_4). However, this enhancement should account only for a part of the total effect;
2) the change in the dissociation equilibrium of sodium sulfate could have improved the amount of Na^+ and SO_4^{2-} ions in the solution;

At such low pressures, the effect of the rise in the liquid viscosity could be neglected.

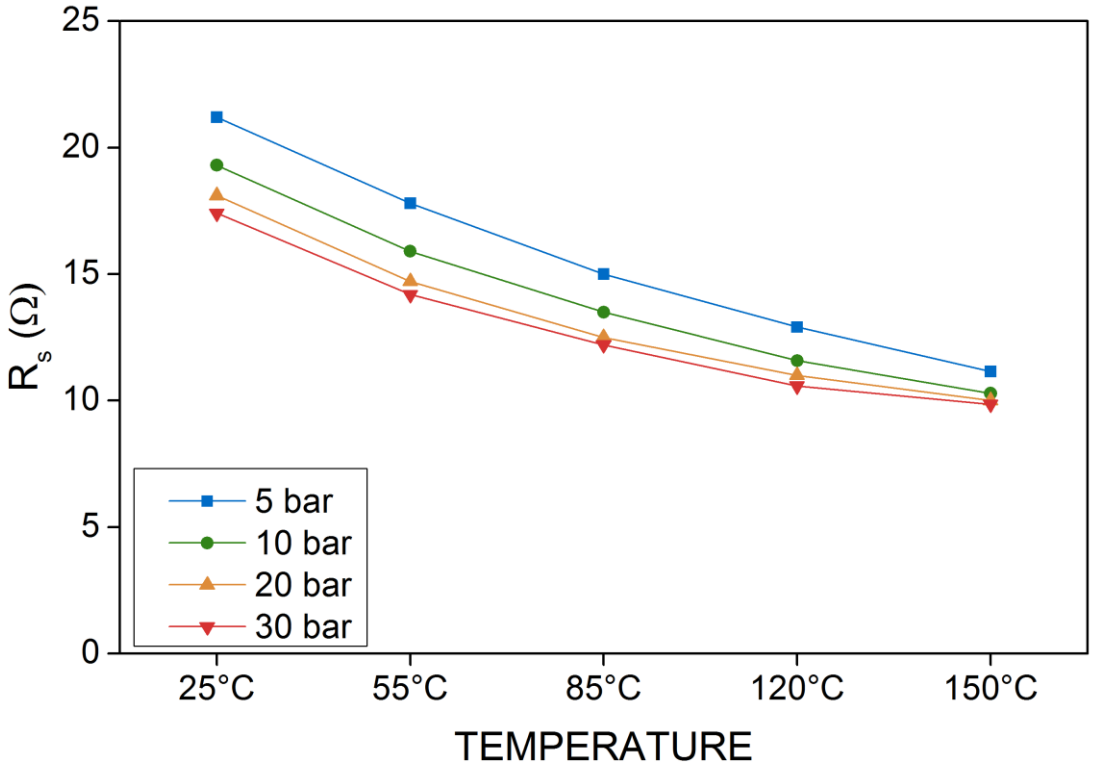

Fig. 72 – Effect of the temperature on the electrical resistance of the solution

The effect of the temperature on the electrolyte resistance is shown in Fig. 72. The strong influence of this parameter on the conductivity of the solution is clearly evidenced, as expected [157]. Great differences were observed, moving from ambient temperature (i.e. 25°C) to 150°C. The variation was not perfectly linear, but it was slightly more accentuated in the range of the lower temperatures. The drop of resistance from 25°C to 150°C was more noticeable for 5 bar (21.2 Ω to 11.1 Ω) than for 30 bar (17.4 Ω to 9.9 Ω).

The strong effect of the temperature is easily explained by the enhanced ion mobility, due to the drop in the solution viscosity, which is a more determining factor than pressure influence.

The electrolyte resistance at 25°C is lower in the HTHP reactor than in the beaker, even though the distance between the electrodes is higher. According to Eq. 121, this phenomenon is due to the fact that the area in which current is carried (A) is larger because of the different geometry, thus compensating the higher distance (l). Since the electrolyte solution is the same, the resistivity (ρ, Ω·m) is unvaried

$$R_s = \rho \cdot \frac{l}{A} \qquad \text{Eq. 121}$$

5.3.2 Standard electro-oxidation tests

Fig. 73 shows the performances of the electrodes containing the manganese oxides, namely *B200/Ti* and *D201/Ti*, compared to the bare substrate of titanium foil, and the electrodes of antimony-doped tin oxide (named *SnO_2-Sb*) and ruthenium oxide (named *RuO_2*).

As can be seen, Ti foil is totally non-active, as previously described in Chapter 4, and it is moreover easily oxidizable. Indeed, when it is used as anode, even at low current densities it tends to form an oxide layer, which passivates the electrode and increase the potential required to carry on the reaction. This phenomenon occurred during the experiment at 2.5 mA/cm^2 in ambient conditions: few minutes after the beginning of the test, the cell voltage reached the limit of the potentiostat (> 10 V) and the surface of the Ti foil became darker. The experiment was then stopped just after 3-4 min.

The *B200/Ti* sample, which was obtained by anodic deposition and presented a mixed manganese oxide film, that is, α-Mn_2O_3 / α-MnO_2, showed the lowest electro-degradation efficiency of phenol (22.3%), with a poor degree of mineralization, as indicated by the TOC analysis (11.3%). This behavior, as previously explained in Chapter 4, was due to the presence of the α-Mn_2O_3 phase, which is mainly active towards the water splitting reaction [117, 125, 147, 148]. As a consequence, a large part of the current provided to the system was wasted for the oxygen evolution reaction.

On the contrary, when the *D201/Ti* sample, which was synthesized by cathodic electro-deposition, the overall phenol abatement, and TOC reduction were greatly improved (42.7% and 27.6%, respectively), achieving efficiencies double than the ones obtained by the tests on the anodic sample. This trend is reasonably explicable by the composition of the cathodic film of manganese oxide, which contained only the α-MnO_2 phase. In fact, α-MnO_2 is largely considered as the most active for the electro-oxidation of organic compounds [96, 97].

If the two types of manganese oxide are compared from the stability point of view, instead, the employment of the anodic sample resulted in a lower cell voltage and in a smaller increase of the potential during the El-Ox experiment. Averagely, *B200/Ti* worked at ~ 5 V (almost constant), instead of ~ 6 V showed by *D201/Ti*, which reached 6.5 V at the end of the test (after 5 h).

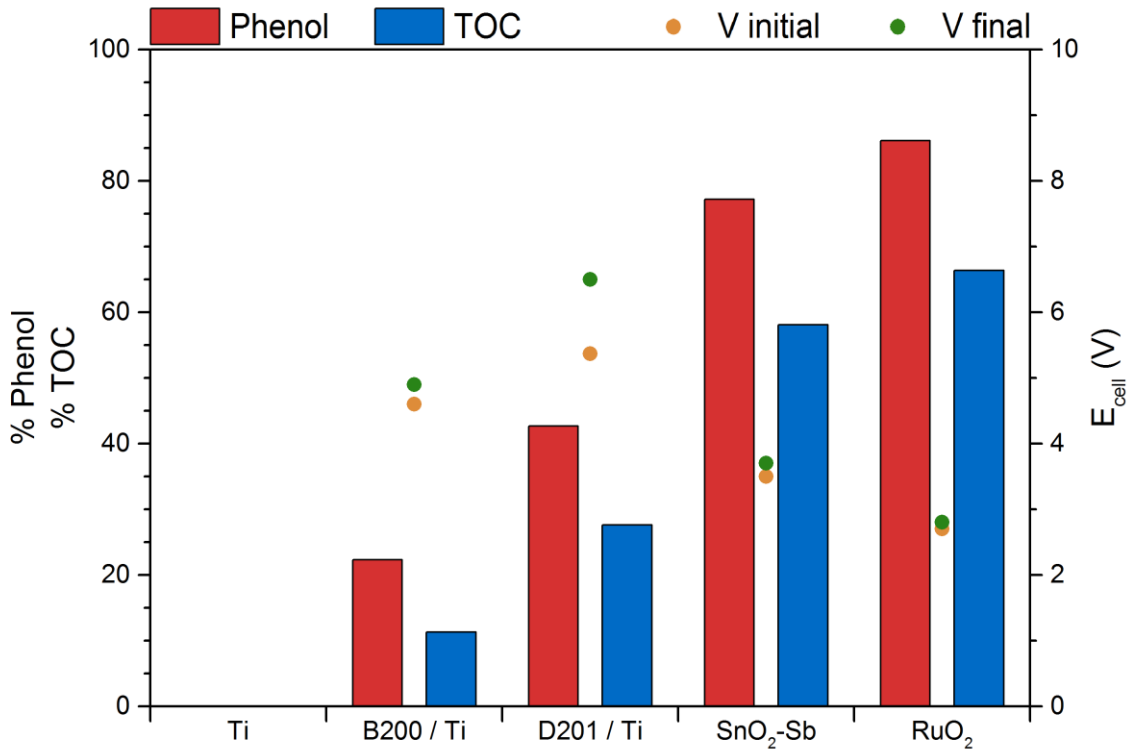

Fig. 73 – Phenol and TOC reduction, initial and final potentials for El-Ox tests carried out in ambient conditions at 2.5 mA/cm^2

The two "reference" anodes, which represent the state-of-the-art in the field of the electro-degradation of recalcitrant organics, effectively managed to reduce the concentration of phenol to acceptable values, considering that the current provided to the cell was slightly more than the minimum required to achieve 100% of TOC reduction.

The *SnO_2-Sb* sample, which was obtained by cathodic layer-by-layer electro-deposition, reached a phenol conversion of 77.2% and a TOC reduction of 58.1%, which were the double of the cathodic deposited MnO_x electrode (i.e *D201/Ti*) and four times than the anodic sample (i.e *B200/Ti*). The high oxygen evolution overpotential attributed to this type of electrode is well-known in the literature [88, 158-163], and is the main factor that allows antimony-doped tin oxide films to reach high efficiencies. The working cell potential employed with the *SnO_2-Sb* electrode was about 3.6 V, almost constant thoroughly the experiment.

The electrode based on the thermally brush-coated *RuO_2* proved to be the best performing anode for phenol electro-degradation, achieving phenol conversions as high as 86.1% and degree of mineralization equal to 66.4%. Such efficiencies of the ruthenium oxide film lie in its high activity towards a number of electrochemical reactions, including water electrolysis [164, 165], chlorine evolution [165, 166] and organics abatement [84, 86, 154, 167]. The cell potential achieved in the test was ~ 2.7 V and was unchanged during all the reaction time.

Although the phenol and TOC conversion obtained with the MnO_x electrodes were not complete, the specific activities of the MnO_x-based electrodes were quite high, as shown in Fig. 74. The weight of the MnO_x samples and the *SnO_2-Sb* electrode were estimated with the Faraday's law, and they resulted equal to 0.427 mg_{Mn}/cm^2 for *B200/Ti* and 0.285 mg_{Mn}/cm^2 *D201/Ti*, while *SnO_2-Sb* gave a value of 2.170 mg_{Sn}/cm^2, respectively. The ruthenium oxide electrode, instead, was weighed on a microbalance (Mettler Toledo UMX2, with 0.1 µg of resolution) after the brush-coating deposition, obtaining a value of 4.312 mg_{Ru}/cm^2.

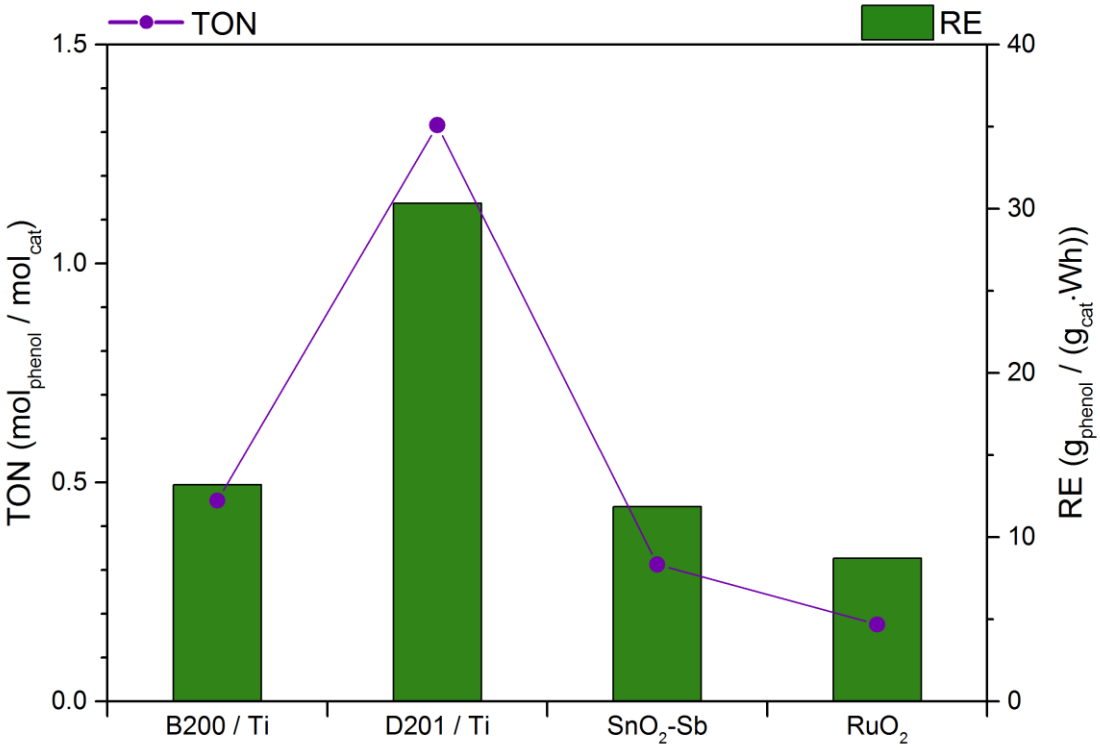

Fig. 74 – Turn Over Number (TON) and Relative Efficiency (RE) for El-Ox tests carried out in ambient conditions at 2.5 mA/cm^2

Both the Turn Over Numbers (TONs) and the Relative Efficiencies (REs) of the MnO_x samples were far higher than the ones obtained from the tin and ruthenium oxide electrodes, which was largely due to the lower amount of material deposited on the Ti foil. Layer-by-layer electrodeposition of the *SnO_2-Sb* film, in fact, required an overall deposition time of about 1 h, mainly for tin oxide, which is 6 times higher than the one employed for the synthesis of the manganese oxide samples.

Thermal brush-coating deposition of *RuO_2* deposited even more material on the surface of the titanium foil, which is one of the drawbacks of this methods, due to the lack of control over the amount of metal oxide.

As shown in Fig. 74, even though the anodic MnO_x electrode provided a phenol conversion of about 22%, its TON and RE were comparable to the ones obtained with the two reference samples, whereas the cathodic sample demonstrate to have a good compromise between absolute and relative conversion, achieving around 43% of phenol oxidation and showing a TON and an RE three times higher than the state-of-the-art electrodes.

5.3.3 HTHP electro-oxidation tests

Blank tests

Before starting with the experiments on the electrodes, two blank tests were carried out in the HTHP reactor to assess the thermal stability of phenol in the most demanding conditions of temperature and pressure. For this purpose, 1 l of phenol solution (100 mg/l) was put in the HTHP reactor, then heated up to 150°C and compressed with N_2 up to 30 bar. After 5 h the reactor was cooled and pressure released.

In the first blank test, no purge with a nitrogen flux was done on the solution before heating and compressing. As a consequence, some dissolved air remained in the starting solution, and a certain degree of degradation was expected due to the presence of oxygen which could react with phenol.

On the contrary, the second blank test was conducted after purging the system with a nitrogen flow for 1 h, thus removing the largest part of the dissolved oxygen in the solution.

Both HPLC and the TOC analysis for the degradation of phenol were carried out on the solution after the blank tests. Table 10 sums up the results obtained.

	Phenol conversion	**TOC conversion**
Blank test – no N_2 purge	8.6%	4.6%
Blank test – N_2 purge 1 h	2.3%	1.1%

Table 10 – Phenol and TOC conversions for the blank tests in the HTHP reactor

As can be seen, the effect of residual oxygen gas inside the starting solution was far from being negligible, as it reduced the concentration of phenol by 8.6% and the TOC by 4.6%.

This phenomenon was due to the reactivity of molecular oxygen towards the organic molecules in operative conditions similar to Catalytic Wet Air Oxidation (CWAO), which were the ones reached in the blank test. Moreover, the residence time of the solution inside the reactor was sufficient for the partial mineralization of phenol to CO_2 and H_2O.

By purging the solution before entering the CWAO region, the degradation was limited to 2.3%, with a degree of mineralization equal to 1.1%, which means that less oxygen was present in the system during the experiment.

Fig. 75 – Reactor used for the High-Temperature High-Pressure (HTHP) tests

i) 85°C, 30 bar, high current densities

The first test was carried out at 85°C and 30 bar, which are operative conditions similar to a PEM electrolyzer. A current density of 10 mA/cm^2 was applied to the system for a reaction time of 2 h. Under this conditions, the total charge passed should be the minimum required to complete mineralize phenol in the solution, as described in par. 5.2.6.

Fig. 76 shows the performances of the synthesized electrodes, in addition to the Ti substrate.

The test with bare titanium foil was carried out to investigate possible activity towards the reaction in HTHP conditions. As stated before, Ti inert for phenol oxidation and easily oxidizable in ambient conditions, reaching rapidly high potentials due to the formation of an inert oxide layer.

Surprisingly, at 85°C and 30 bar titanium foil gained some small activity for the El-Ox reaction, achieving ~ 20% and ~12% of phenol and TOC abatement, respectively.

Also the degradation efficiency of anodic manganese oxide (i.e. *B200/Ti*) was improved, and the phenol conversion resulted more than doubled at 85°C, 30 bar, reaching values of phenol and TOC reduction (55.6% and 43.9%, respectively) even higher than the cathodic MnO_x sample (i.e. *D201/Ti*). This trend could be attributed to the higher tendency

of manganese in its Mn^{3+} form, which is present in the anodic film, to oxidize water to O_2, that would be wasted in ambient conditions, while should be reactive at high temperatures and high pressures.

The same phenomenon was observed for Ti, which also improved the working potential of the cell. This effect could be explained considering the influence of the temperature on kinetics and overpotential. Higher temperature, in fact, should improve the charge transfer, the solution conductivity (as seen in par. 5.2.6), and the reaction overpotential, thus allowing also titanium to evolve oxygen without passivation. On the other hand, pressure should enhance gas solubility in the aqueous solution, avoiding the loss of oxygen as the bubbles are formed on the surface of the anode.

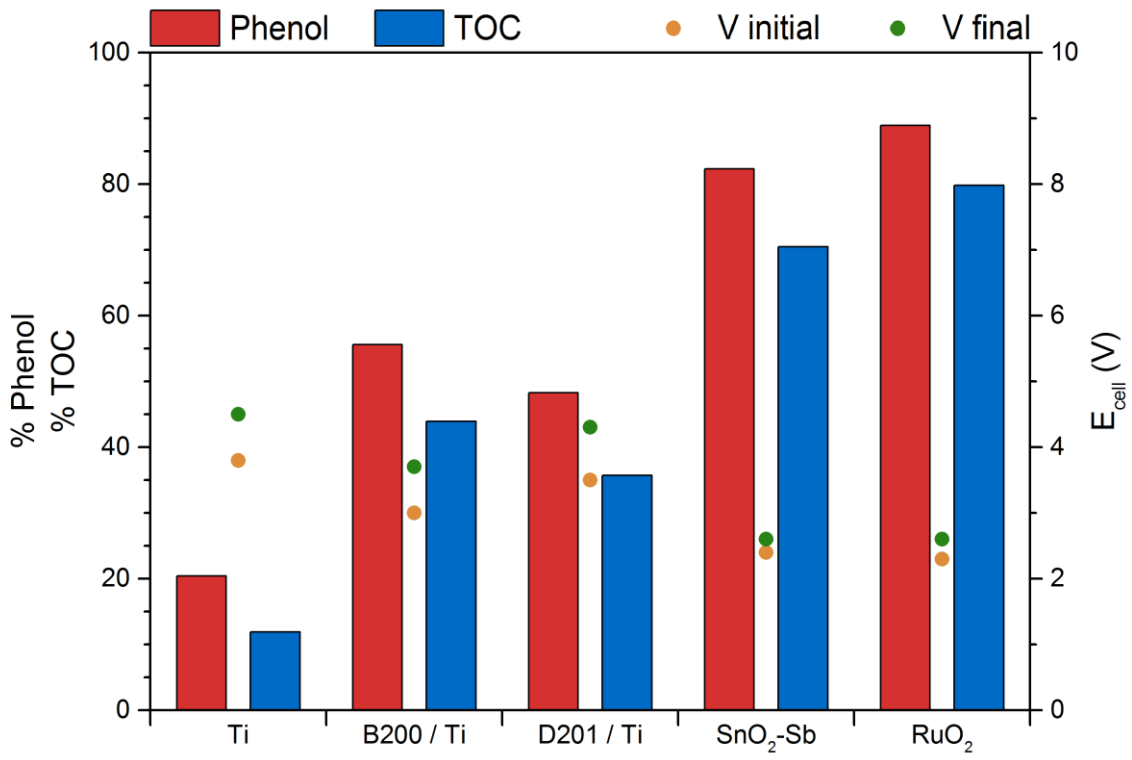

Fig. 76 - Phenol and TOC reduction, initial and final potentials for El-Ox tests carried out at 85°C, 30 bar at 400 mA

The cathodic sample (i.e. *D201/Ti*), instead, did not increase its efficiency with respect to the ambient El-Ox test. This can be attributable to the absence of the α-Mn_2O_3 phase, more active for water splitting. Thus, no boost of the phenol and TOC degradation (48.3% and 35.7%) was observed for this electrode, due to the O_2 evolution.

A similar behavior was obtained with the employment of the two reference anodes: *SnO_2-Sb* and *RuO_2*. In both cases, in fact, only a slight increase in the efficiency was reported: phenol conversion was 82.3% for *SnO_2-Sb* and 88.9% for *RuO_2*. On the contrary,

the TOC reduction was noticeably enhanced, proving the beneficial effect of temperature and pressure, which contributed to a higher degree of mineralization of the wastewater.

ii) 85°C, 30 bar, low current densities

Another test was conducted in the same operative conditions, concerning temperature and pressure. However, in this case, a current density of 5 mA/cm^2 was applied to the system, but for a reaction time of 4 h, thus leaving unvaried the total amount of charge needed to completely degrade phenol and TOC. In this way, the effect of the last two parameters (current and time) on the efficiency of the process was analyzed. As expected, a halved current density with doubled residence times resulted in higher faradaic efficiencies, since the TOC reduction was increased for all the samples.

Averagely, for bare titanium and for the manganese oxide electrodes, both the phenol and TOC reduction raised of about 15-20%, whereas the increment for the two references, i.e. *SnO_2-Sb* and *RuO_2*, was more limited (less than 5%), as represented in Fig. 77.

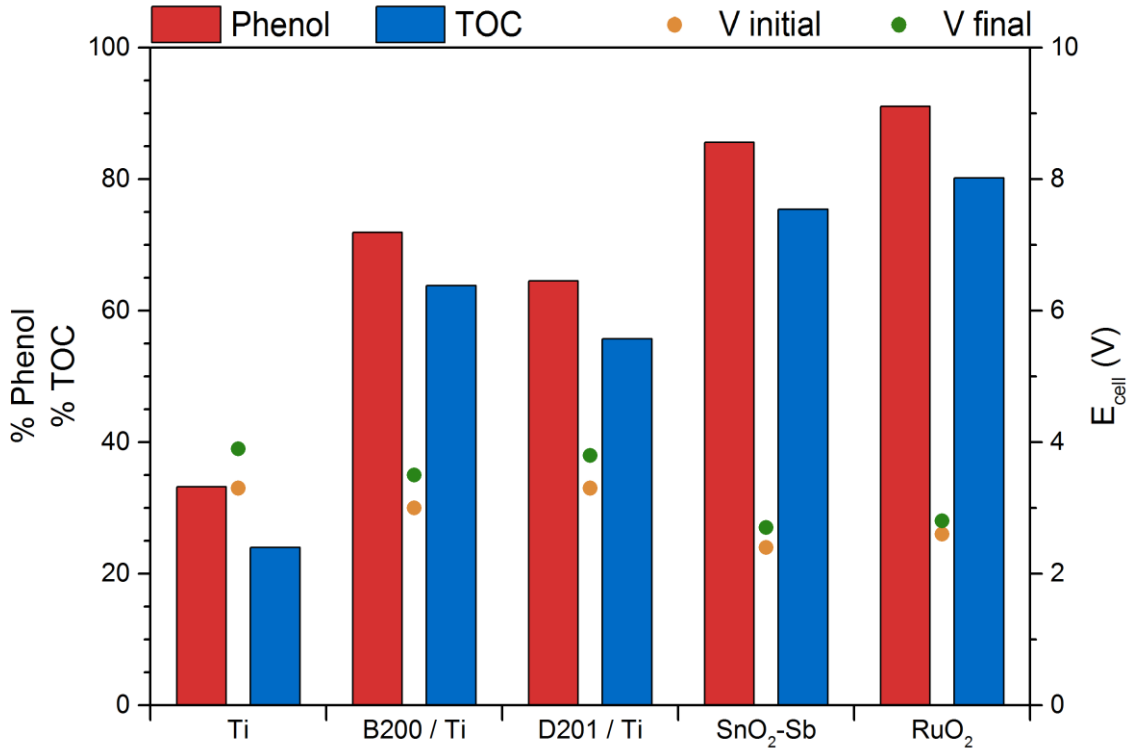

Fig. 77 - Phenol and TOC reduction, initial and final potentials for El-Ox tests carried out at 85°C, 30 bar at 200 mA

This steep increase in the performances of the MnO_x samples was most probably due to the reduction of irreversibilities which are usually caused when the system is brought far from the equilibrium, represented by the open circuit potential. Indeed, the higher the applied current density, the greater the influence of phenomena such as ohmic drop, polarization and mass transfer limitation. Besides, improved exploitation of the O_2 evolved at the anode could be an additional explanation for this trend. In fact, if the employed current density is too high, the amount of oxygen at the surface of the electrode is formed too quickly to react with the organic molecules, as the mass transfer of phenol from the bulk of the solution becomes the limiting factor. Therefore, not all the O_2 electro-generated is used for electro-degradation but could be wasted as gas bubbles.

iii) 150°C, 30 bar, high current densities

The second set of tests in HTHP conditions was conducted at 150°C and 30 bar. In the first experiment, a current density of 20 mA/cm^2 was passed through the system for 1 h, and the results are shown in Fig. 78.

If compared to the tests at 85°C, the performances of all the electrodes, especially for MnO_x electrodes, were visibly improved. The phenol and TOC conversion for manganese oxides were comparable with the test *ii* (85°C, 30 bar at low current), but in this case, the current density was four times higher. This high effectiveness, despite the demanding operative conditions, was probably due to the fact that the reaction was carried out under CWAO conditions, so the O_2 reactivity towards the degradation of phenol was boosted and prevailed over the irreversibilities and the mass transfer limitations described before.

Also the working potential of the system was kept at limited values (after ohmic drop compensation), even though the applied current was elevated, thus proving the beneficial effect of the temperature on the electrochemical process.

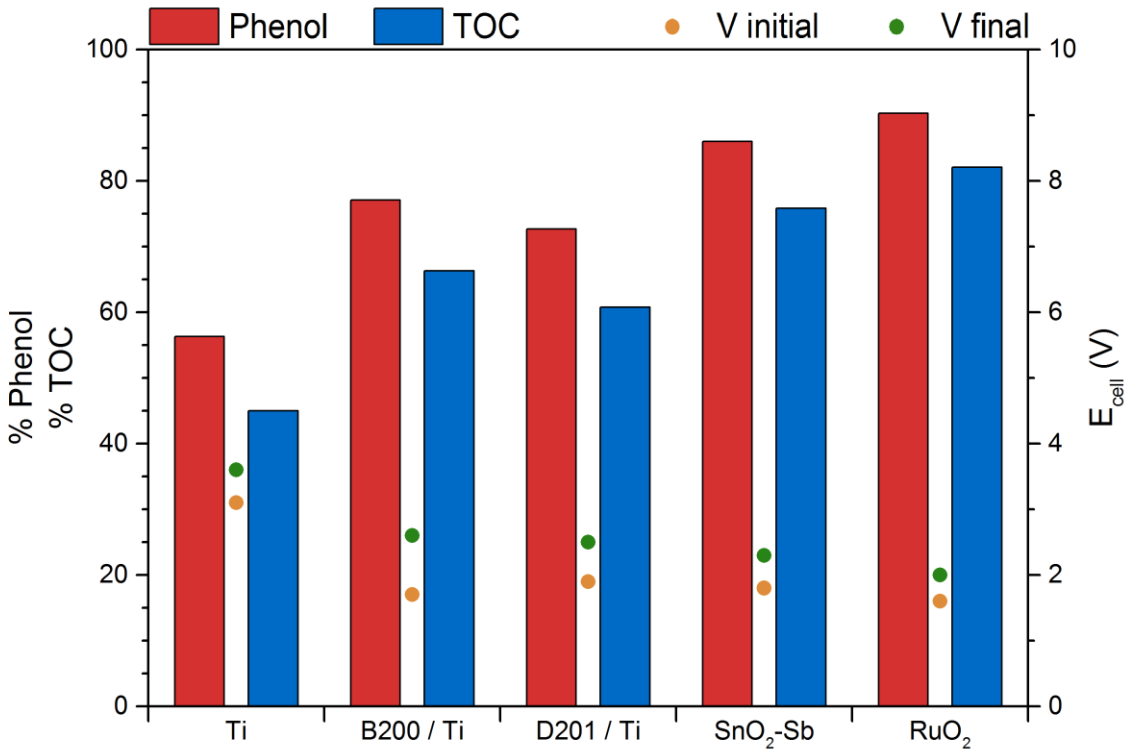

Fig. 78 - Phenol and TOC reduction, initial and final potentials for El-Ox tests carried out at 150°C, 30 bar at 800 mA

The overall performance of both the *B200/Ti* and the *D201/Ti* electrodes was then similar to the one of the reference anodes, thus encouraging the application of these materials for the electro-oxidation of recalcitrant organics.

iv) 150°C, 30 bar, low current densities

The last test was carried out in CWAO conditions, by applying a current density of 4 mA/cm^2 for 5 h, to investigate the performances of the system in the absence of mass transfer limitations of the organic reagent.

The results obtained, which are shown in Fig. 79, are surprisingly good for all the sample examined, and even for the bare titanium foil. The conversion of phenol was > 85% for Ti and > 90% all the coated anodes. TOC reduction, which is numerically equal to the faradaic efficiency, was between 80% and 90% for the manganese oxides and between 85% and 90% for *SnO_2-Sb* and *RuO_2*.

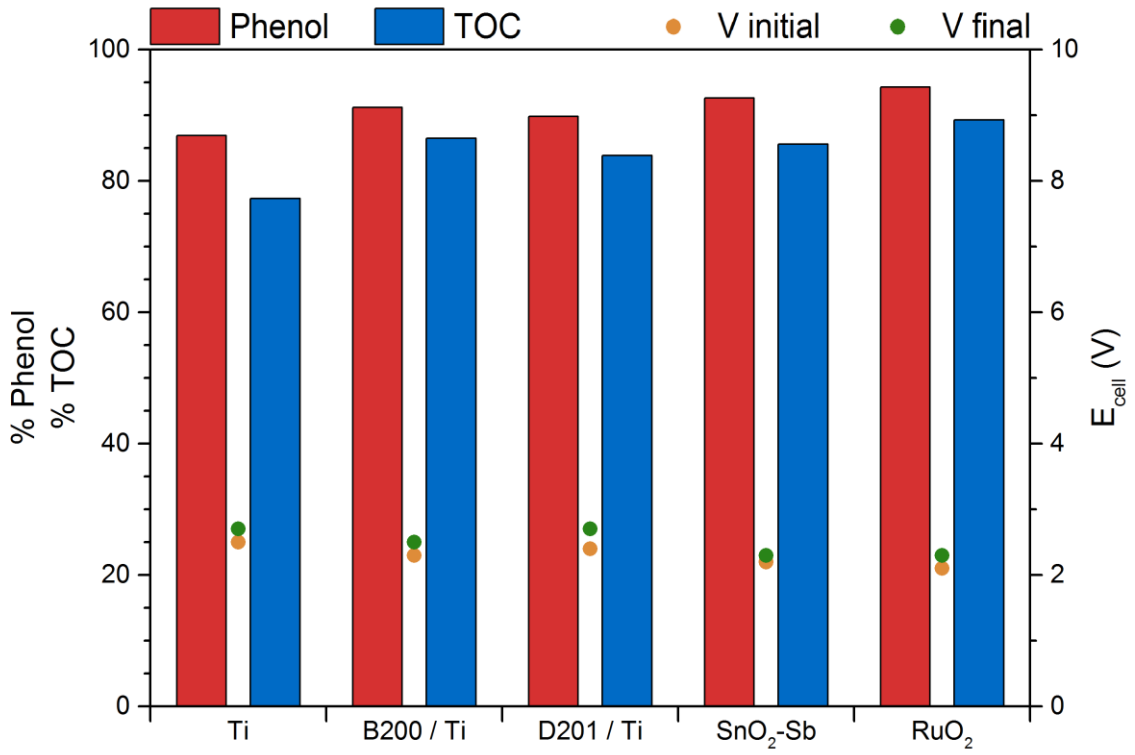

Fig. 79 - Phenol and TOC reduction, initial and final potentials for El-Ox tests carried out at 150°C, 30 bar at 160 mA

The beneficial effect of a higher residence time, with a decreased current, was again confirmed by the test in CWAO conditions. Giving the electro-generated oxygen enough time to react with the organics, the conversion achieves almost the complete mineralization, moreover obtaining elevated current efficiencies.

Of course, by increasing the charge passed through the system more than the minimum (stoichiometric) needed for the mineralization, the residence time could be reduced to meet industrial-scale demands. This method would obviously require higher current density, thus decreasing the faradaic efficiency.

The last comparison between the HTHP tests was made by analyzing the TurnOver Numbers (TONs) and the Relative Efficiencies (REs) of the coated electrodes.

To calculate these parameters, the amount of deposited material was measured by weighing the electrodes after the deposition process. The values of the film weights are reported in Table 11:

	B200 / Ti	***D201 / Ti***	***SnO_2-Sb***	***RuO_2***
Weight (mg)	16.118	10.804	87.137	180.448

Table 11 – Weights of catalyst on coated samples

The purple dots in Fig. 80 represent the TONs for the tested anodes. Only one value for each sample is showed, as the weight was considered equal for all the syntheses. As can be seen, the TON for the manganese oxides is much higher than the one obtained for the references. In particular, the *B200/Ti* sample, gave a TON that was 4 times higher than *SnO_2-Sb* and 8 times higher than *RuO_2*, whereas the *D201/Ti* sample provided a TON 5 and 10 times greater than *SnO_2-Sb* and *RuO_2*, respectively.

The REs are represented by the bar chart and followed the same trend of the TONs: higher efficiencies for the MnO_x electrodes and lower for the references. In this case, however, the values changed with the type of experiment, as the REs depends on the energy given to the system, that is, current, time and potential. Therefore, they are useful to analyze the influence of the operative conditions on the effectiveness of the process. The operative conditions as indicated in the legend of Fig. 80 are recalled here below:

i) *85°C, 30 bar, 10 mA/cm^2, 2 h*

ii) *85°C, 30 bar, 5 mA/cm^2, 4 h*

iii) *150°C, 30 bar, 20 mA/cm^2, 1 h*

iv) *150°C, 30 bar, 4 mA/cm^2, 5 h*

As clearly shown, the changes in the operative conditions strongly influenced the manganese oxide electrodes, especially when moving towards CWAO ranges and/or slower reaction rates. The trend is less accentuated for the reference anodes since the original conversions were already high and the HTHP reactions did not noticeably affect their performances.

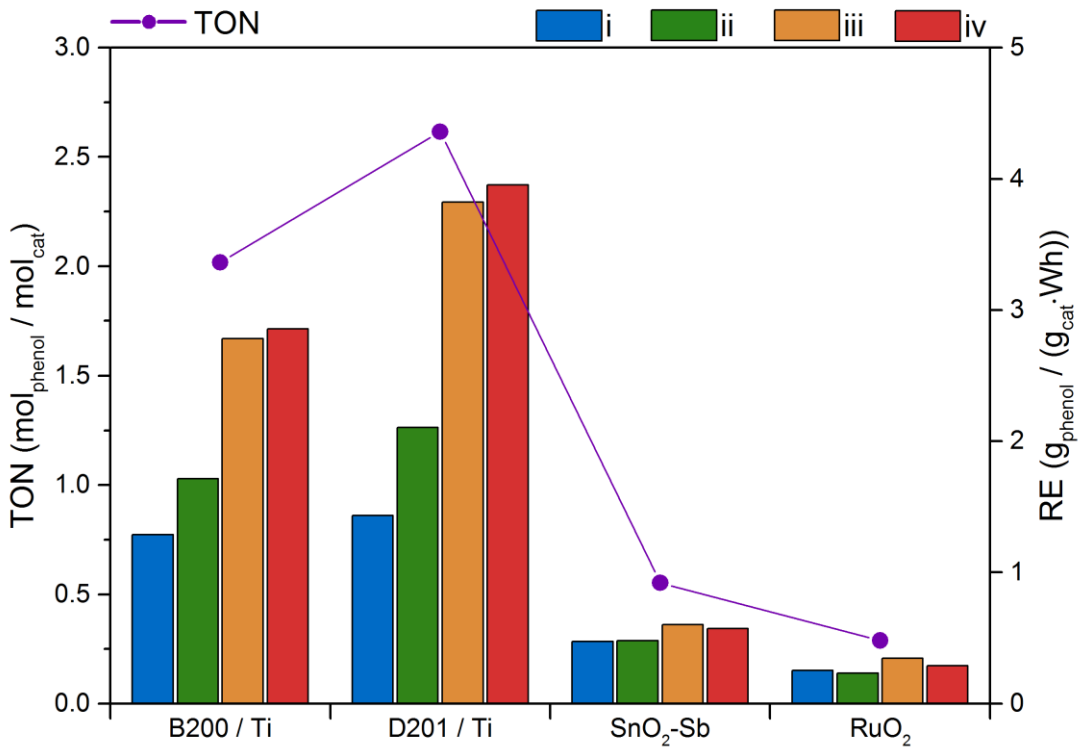

Fig. 80 - Turn Over Number (TON) and Relative Efficiency (RE) for El-Ox tests carried out in HTHP conditions

5.3.4 HPLC spectra analysis

Since few works exist on the electro-oxidation of phenol on manganese oxide electrodes, and no works, as far as is known, concerns the El-Ox of phenol in such operative conditions, an investigation on the intermediates produced during the reaction was carried out by the analysis of the HPLC spectra.

First of all, the HPLC analysis was performed on the solutions treated in ambient conditions (see Fig. 83). Then, after a literature review, some standard solutions with pure compounds, which were hypothesized to be the intermediates of the phenol electro-degradation, were prepared and analyzed at the HPLC to detect their retention times, in order to compare them with the ones obtained by the treated solutions.

A large number of intermediate products were recognized in the various solutions treated with different types of electrode. Fig. 81 shows all the spectra of the identified compounds and their retention times. It is worth mentioning that no quantitative analysis of the intermediates was made, as their concentrations were estimated to be around 1-2 ppm, or even less, for each compound. In addition, the intensity of the peaks is not associated with the relative amount of the by-products, as some substances tend to absorb more than others at the considered UV wavelength (~ 206 nm). For instance, maleic and fumaric

acids always showed the highest peaks, even though their concentration was similar to other compounds.

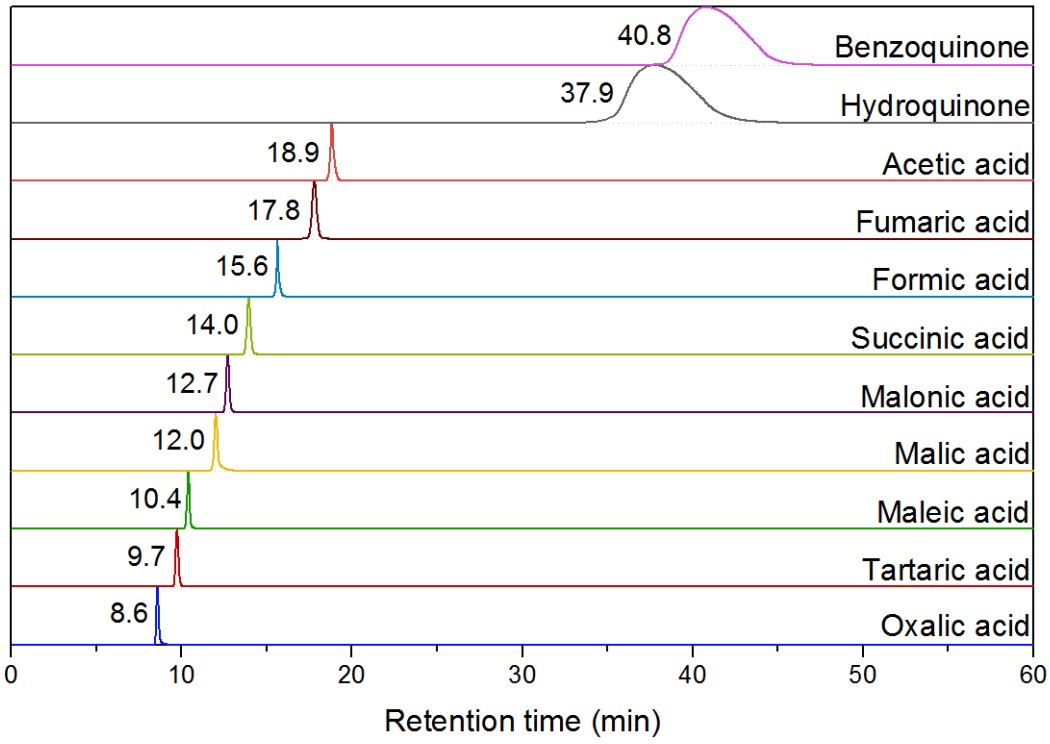

Fig. 81 – Retention times of standard solution of detected intermediates for the phenol El-Ox reaction by HPLC analysis

In particular, benzoquinone (t_R = 40.8 min) and hydroquinone (t_R = 37.9 min) were found in the final solutions, as aromatic intermediates, which are usually in redox equilibrium, since the cell is undivided and the benzoquinone could migrate and be reduced at the cathode. This is commonly recognized as the first step in the electrochemical degradation of phenol, after the formation of phenoxy radicals, which are also the responsible for possible fouling of the electrodes when reacting with quinones to form insoluble polymeric compounds [151, 152, 160, 168, 169]. Their peaks are clearly distinguishable, since their retention times are noticeably higher than the other intermediates, which are all organic acids (mainly dicarboxylic acids).

The main acidic compound detected in this group is the maleic acid (t_R = 10.4 min), which is also the most absorbing in the UV range used for the analysis, so it was the most easily recognizable. It is largely accepted that the step following the formation of the redox couple benzoquinone and hydroquinone is the aromatic ring opening, which leads to maleic acid [151, 152, 160, 168, 169] and its *trans* isomer: fumaric acid (t_R = 17.8 min) [151, 168]. Other lower molecular weight intermediates were identified. Succinic acid (t_R = 14.0 min) [151, 152] is directly derived from the couple maleic/fumaric acid, by reduction at the cathode, which is not uncommon [152]. Further oxidation could occur, by formation of malic (t_R = 12.0 min) [151, 169] and tartaric acid (t_R = 9.7 min) [169]. All these acids,

composed by four carbons, can be transformed into malonic acid (t_R = 12.7 min) [152, 168, 169], which is a three-carbon molecule. From malonic acid two different intermediates could be obtained: oxalic acid (t_R = 8.6 min) [151, 152, 160, 168, 169] as the lowest weight dicarboxylic acid, which in turn could be mineralized; acetic acid (t_R = 18.9 min) [152, 168], which could be degraded to formic acid (t_R = 15.6 min) [151, 168] and, finally, to CO_2 and water.

Fig. 82 illustrates the proposed reaction mechanism of the electrochemical degradation of phenol, described above, including all the substances individuated by HPLC analysis.

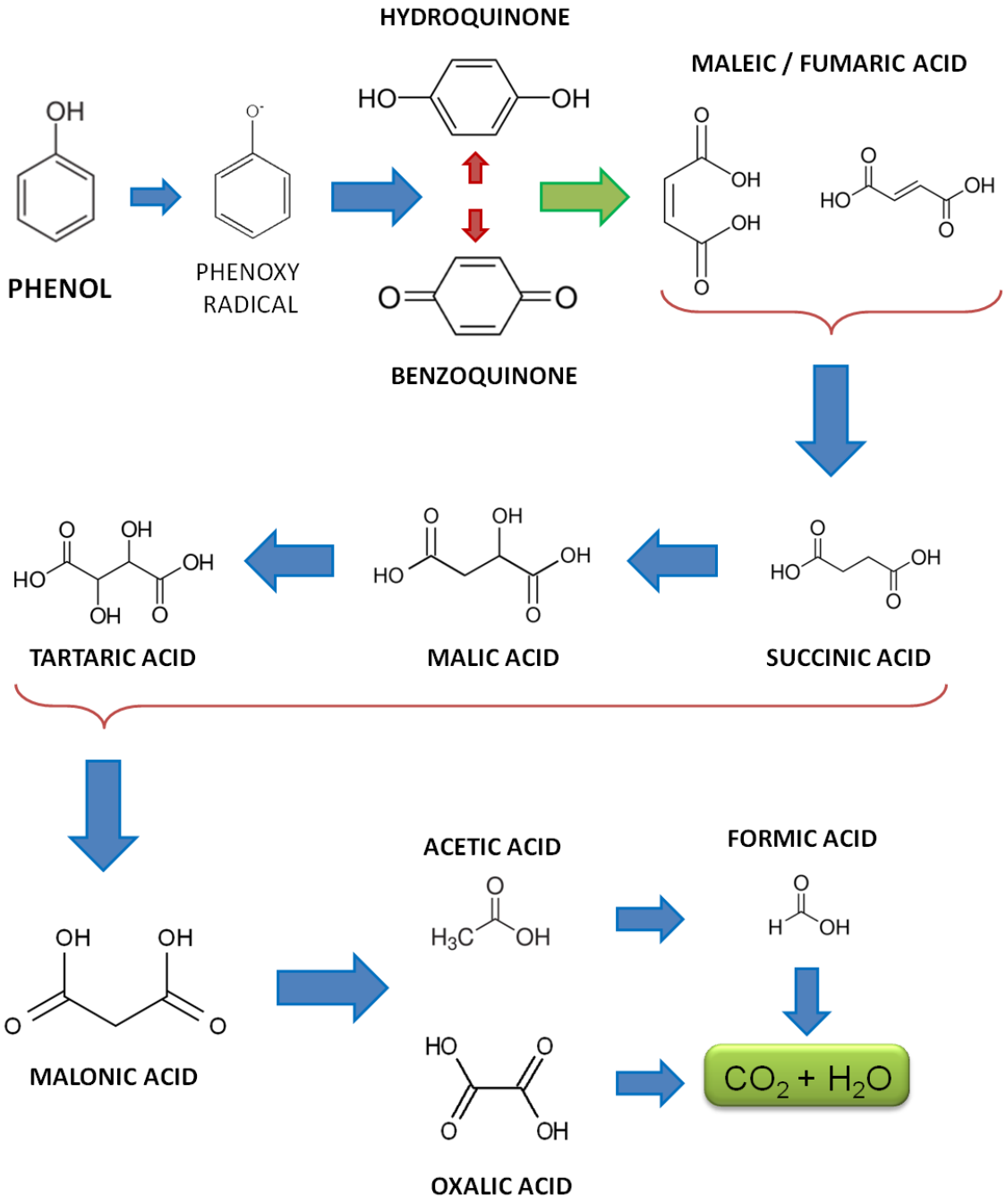

Fig. 82 – Reaction pathway of phenol El-Ox

For all the electrodes tested at ambient conditions (Fig. 83), with the obvious exception of the Ti foil, peaks of intermediates were detected in the HPLC spectra. Averagely, all the samples showed the presence of the most important by-products, such as maleic, fumaric and oxalic, thus proving that the reaction mechanism should be similar for all the catalytic films. Small residuals of benzoquinone and hydroquinone were detected in the *SnO_2-Sb* and *RuO_2* samples. The presence of these couple of by-products means that probably, in both the electrodes, some difficulty in the ring opening step was encountered.

On the other hands, in the MnO_x electrodes, no trace of quinones was found, showing that this type of electrodes was not limited by the ring opening step. A difference between the intermediates of the *B200/Ti* and *D201/Ti* samples was detected: the cathodic sample, in fact, presented two peaks corresponding to malic and acetic acid, which were absent in the anodic sample, whereas the tartaric acid was present only for the anodic sample.

The *SnO_2-Sb* and *RuO_2* samples mainly showed maleic, fumaric and oxalic acids, with some amount of tartaric and malonic acids in their treated solutions.

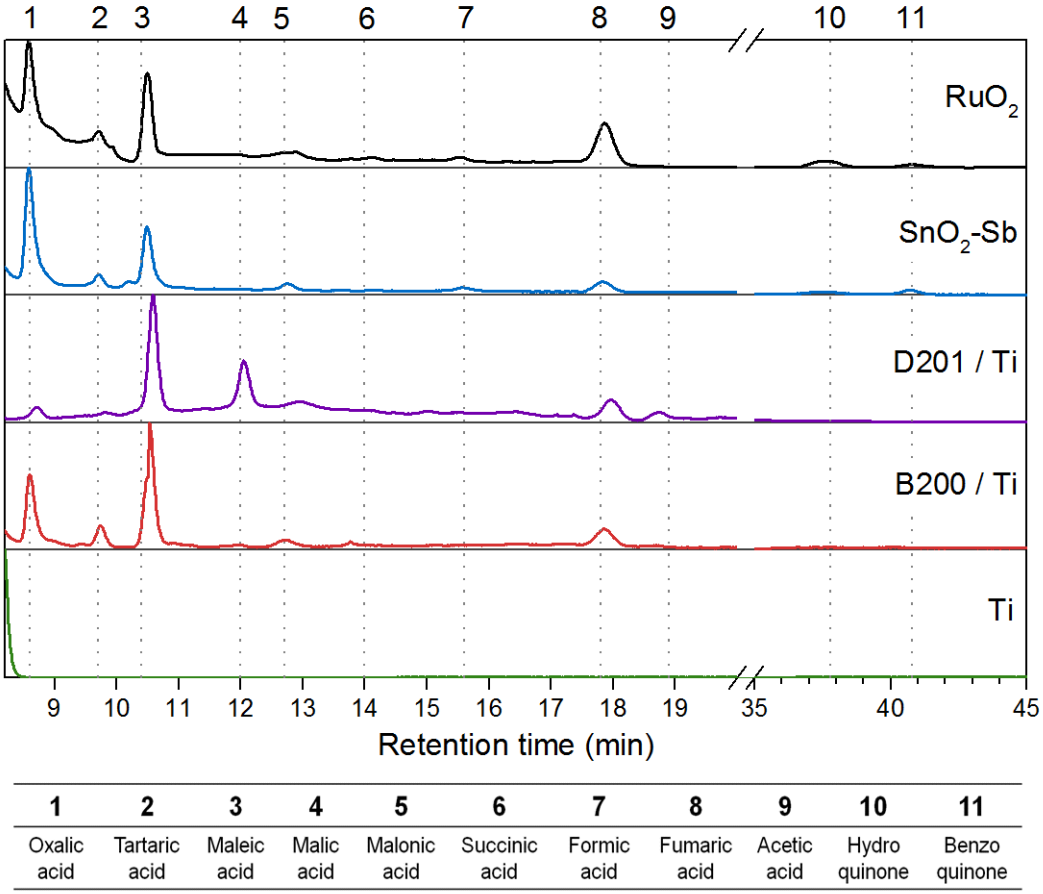

Fig. 83 – HPLC spectra for El-Ox tests carried out at ambient conditions at 2.5 mA

The following images (from Fig. 84 to Fig. 87) show the spectra of solutions treated in the different HTHP conditions.

Fig. 84 shows the results of test *i)*, at 85°C, 30 bar and high current densities (10 mA/cm^2). Since also Ti presented some activity, here some intermediates were found in its HPLC spectra, such as maleic, fumaric, succinic, malonic and oxalic acids. For the manganese oxide anodes, the by-products were similar to the standard experiment, with no detection of aromatic intermediates (i.e. the quinones). For the *SnO_2-Sb* electrode, the predominant peak was the maleic acid, together with the oxalic acid. *RuO_2* presented more intermediate compounds than the other electrodes. For both the reference anodes, benzoquinone was found in the solution, while hydroquinone was absent. This phenomenon could be explained by the geometry of the reactor, and especially by the higher distance between anode and cathode, which did not allow the formed benzoquinone to migrate to the cathode and to be reduced to hydroquinone (at least in a relevant amount).

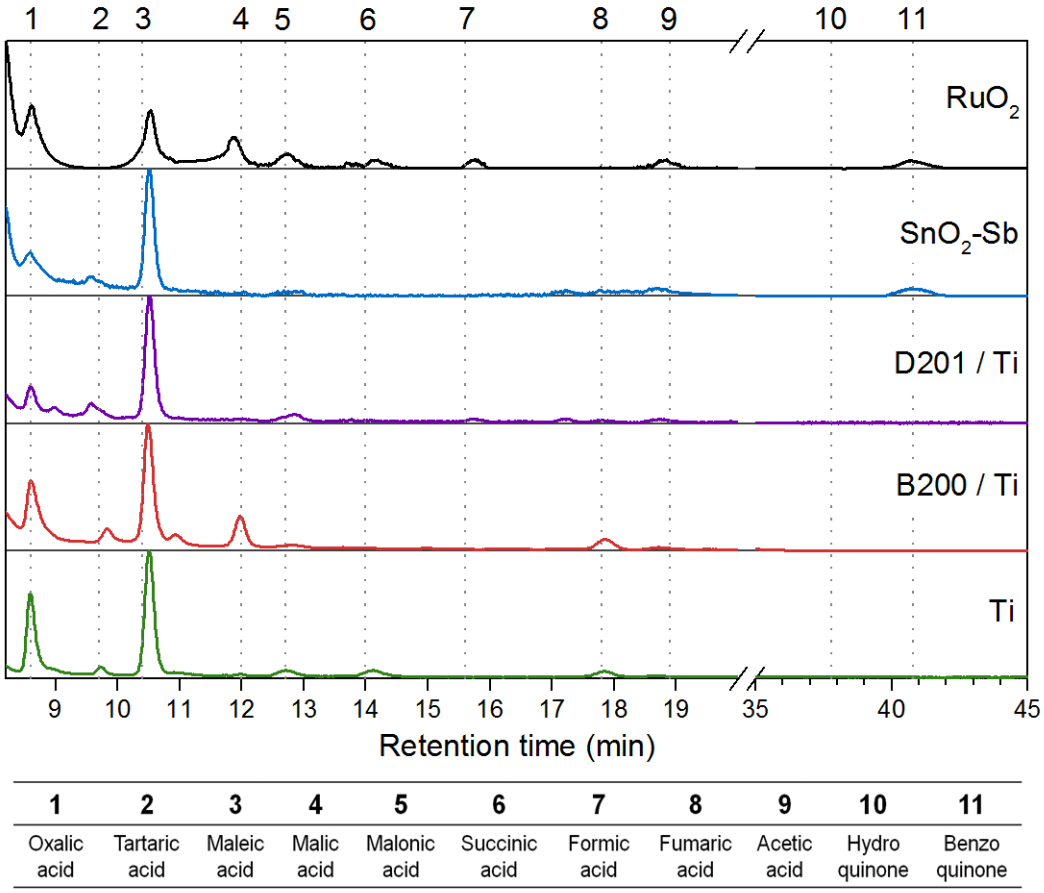

Fig. 84 – HPLC spectra for El-Ox tests carried out at 85°C, 30 at 400 mA

Fig. 85 shows the results for the solutions treated at 85°C, 30 bar and low current densities (5 mA/cm^2). Just like previous considerations, for manganese oxide anodes, the predominant by-products found were maleic and oxalic acids, with some malic acid. In this case, the two HPLC spectra for the *B200/Ti* and *D201/Ti* samples are similar, probably because of milder reaction conditions, with higher reaction times, which allow the intermediates to react almost completely. All the TOC conversions, in fact, were improved

in this experiment. Concerning the two reference anodes, a greater amount of tartaric and malic acid were observed, with some traces of aromatics (mainly benzoquinone). The Ti foil gave maleic, oxalic and fumaric acid as intermediates.

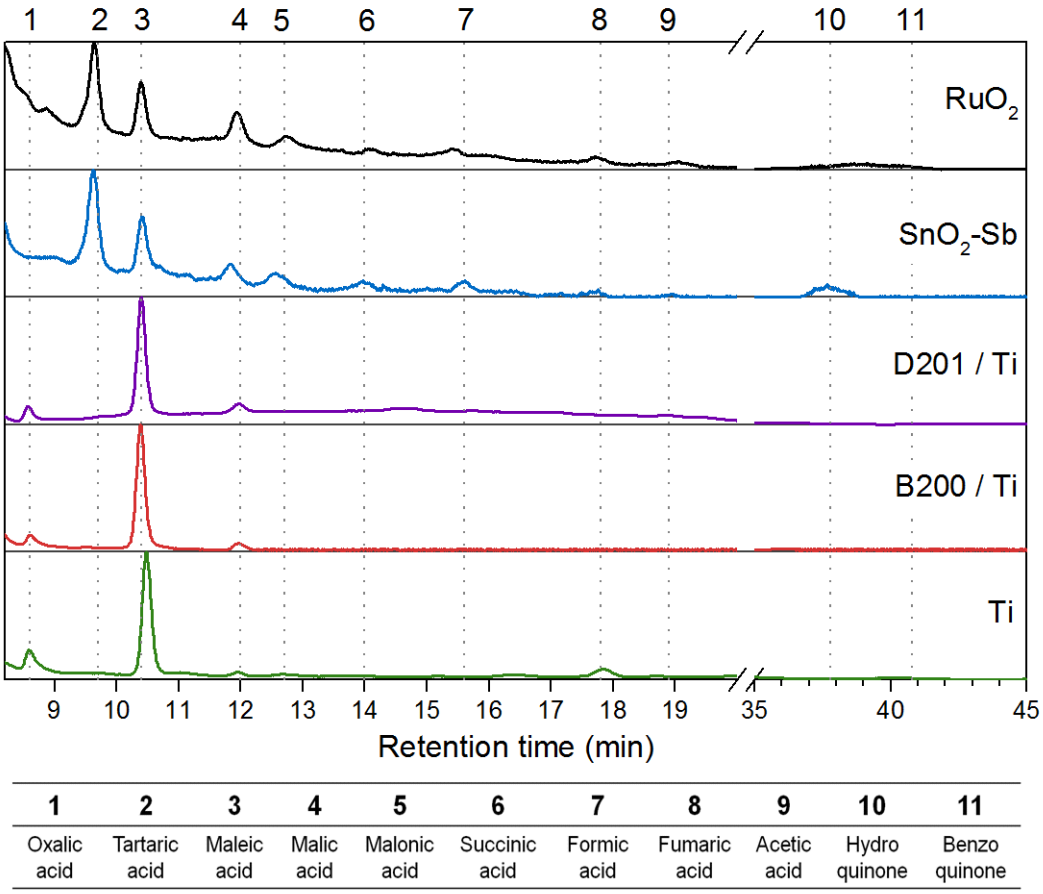

1	2	3	4	5	6	7	8	9	10	11
Oxalic acid	Tartaric acid	Maleic acid	Malic acid	Malonic acid	Succinic acid	Formic acid	Fumaric acid	Acetic acid	Hydro quinone	Benzo quinone

Fig. 85 – HPLC spectra for El-Ox tests carried out at 85°C, 30 at 200 mA

The last analyzed groups of solutions are the one tested under CWAO conditions, at 150°C, 30 bar and 5 or 20 mA/cm^2, as shown in Fig. 86 and Fig. 87. Even though, as stated before, the HPLC analysis was not carried out to quantify the concentration of the intermediates, a reduction in the intensity of the peaks occurred in experiments at 150°C, with a decrease also in the number of compounds. Indeed, if compared with standard El-Ox tests, only maleic, fumaric and oxalic acids were largely observed in HTHP conditions. This trend is in accordance with the steep increase in TOC conversion and could be possibly due to increased kinetics and lower overpotentials, which contributed to further mineralization of the intermediates.

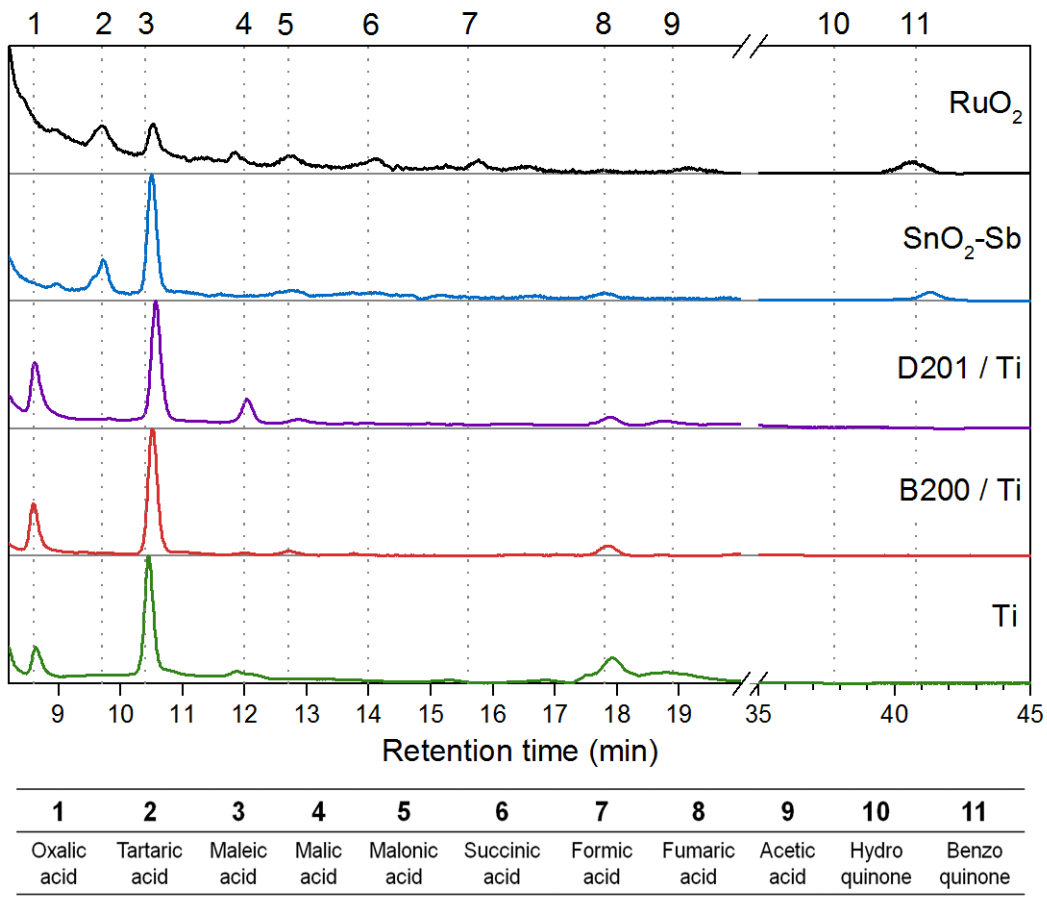

1	2	3	4	5	6	7	8	9	10	11
Oxalic acid	Tartaric acid	Maleic acid	Malic acid	Malonic acid	Succinic acid	Formic acid	Fumaric acid	Acetic acid	Hydro quinone	Benzo quinone

Fig. 86 – HPLC spectra for El-Ox tests carried out at 150°C, 30 at 800 mA

Therefore, is possible to state that experiments at high temperatures and pressures did not directly influence the reaction pathways for the degradation of phenol but improved transformation into lower weight molecules, and finally into CO_2 and H_2O.

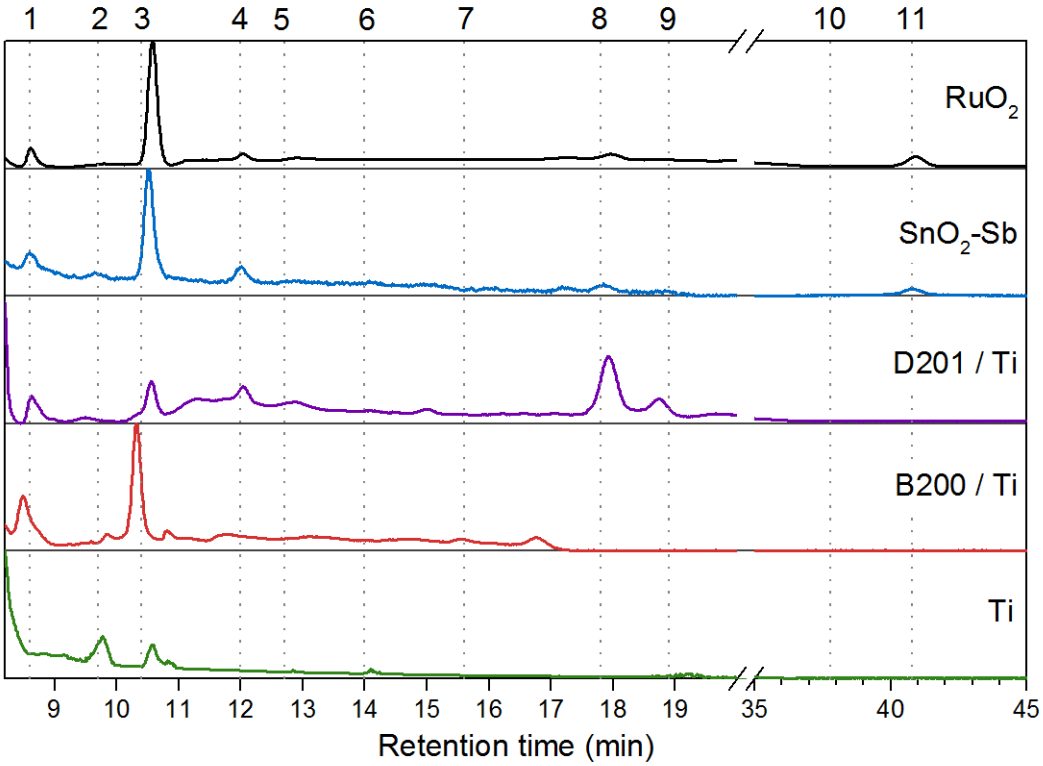

1	2	3	4	5	6	7	8	9	10	11
Oxalic acid	Tartaric acid	Maleic acid	Malic acid	Malonic acid	Succinic acid	Formic acid	Fumaric acid	Acetic acid	Hydro quinone	Benzo quinone

Fig. 87 – HPLC spectra for El-Ox tests carried out at 150°C, 30 at 160 mA

5.4 Conclusions

Two types of MnO_x-based electrodes deposited on titanium were synthesized. One sample was obtained by anodic electrodeposition from a Mn^{2+} precursor (i.e. manganese acetate), whereas the other one was synthesized by cathodic electrodeposition from a Mn^{7+} precursor (i.e. manganese permanganate). Both these electrodes were tested at ambient temperature and pressure, to investigate their activity for the electrochemical degradation of phenol in wastewater. In standard electro-oxidation conditions, the anodic sample showed a poor conversion (~ 22%), while the cathodic electrode proved a moderate activity (~ 43%). This behavior was attributed to the different composition of the catalytic film: in the anodic sample a mixed manganese oxide was detected by the XRD analysis, that is, α-Mn_2O_3 / α-MnO_2; the cathodic sample, instead, presented only the α-MnO_2 phase.

α-Mn_2O_3 is commonly recognized as the most active for water splitting reaction, with a lower oxygen evolution overpotential. Therefore, its activity for the degradation of recalcitrant organics is lower, being the water electrolysis the preferred reaction. On the contrary, α-MnO_2 is largely accepted as the most active phase for electrochemical abatement of refractory organics, due to higher production of active OH· radicals. The results were compared to the bare Ti substrate and two of the most performing electro-catalysts: layer-by-layer electrodeposited *SnO_2-Sb* and brush coated *RuO_2*. Both these reference anodes showed high activities (~ 77% and ~ 86%, respectively), whereas the metallic Ti was rapidly passivated and the test was stopped after few minutes.

To investigate the effect of high temperature and pressure (HTHP) on the electro-oxidation of phenol, the two manganese oxides were tested in a lab-scale HTHP reactor. The experiments were carried out at 85°C and 30 bar (similar to PEM electrolyzers) and at 150°C and 30 bar (mild CWAO conditions). Also the influence of the current density was studied, applying a higher and a lower value for each operative conditions. As hypothesized, by increasing T and P, the MnO_x anodes, especially the anodic one, boosted their efficiency, due to the beneficial effects of the operative conditions. Temperature contributed to improve kinetics and lower overpotentials, while pressure enhanced the oxygen dissolution, thus allowing its exploitation for phenol degradation. Surprisingly, even the bare Ti foil increased its conversions, and the passivation was avoided. On the other hand, the references *SnO_2-Sb* and *RuO_2* did not show any noticeable benefit from the employment of high T and P, probably because of their lower tendency to evolve O_2.

At 85°C and high current densities (10 mA/cm^2) the anodic sample more than doubled its efficiency (~ 55%), whereas the cathodic electrode was almost stable (~ 48%). At half of the current, the anodic MnO_x gave almost 72% phenol conversion, while the cathodic sample reached only ~ 64%. In CWAO conditions conducted at high current densities (20 mA/cm^2), the anodic sample achieved comparable efficiency to the state-of-the-art reference anodes (~ 77%), and the cathodic one was slightly less performing (~ 72%). When the current density was lowered to 5 mA/cm^2, all the conversions exceeded

90%, and even Ti obtained ~ 85%, thus proving that electro-generated oxygen is highly reactive towards organics and can be easily exploited for recalcitrant organics degradation, without using expensive or toxic anodes, such as RuO_2, BDD, and PbO_2.

HPLC analysis of the treated solutions detected a large number of intermediates, commonly observed also in other works, such as benzoquinone and hydroquinone, or maleic and oxalic acids. The change in the operative conditions and in the electrocatalyst did not evidence any noticeable trend, showing that the reaction mechanism is similar for all materials and it is not influenced by temperature and pressure.

REFERENCES

[1] S. N. Pollalis, A. Georgoulias, S. J. Ramos and D. Schodek, *Infrastructure sustainability and design*, Routledge, 2013.

[2] FAO, *AQUASTAT website*, Food and Agriculture Organization of the United Nations (FAO), (2016) Website accessed on [2016/10/18]

[3] Watkins, *Beyond scarcity: Power, poverty and the global water crisis*, United Nations Development Programme, New York, (2006)

[4] J. Liu, A. Dorjderem, J. Fu, X. Lei, H. Liu, D. Macer, Q. Qiao, A. Sun, K. Tachiyama, L. Yu and Y. Zheng, *Water Ethics and Water Resource Management*, Ethics and Climate Change in Asia and the Pacific (ECCAP) Project, Working Group 14 Report, (2011)

[5] T. De Mes, A. Stams, J. Reith and G. Zeeman, *Methane production by anaerobic digestion of wastewater and solid wastes*, Bio-methane & Bio-hydrogen, (2003) 58-102

[6] H. N. Gavala, U. Yenal, I. V. Skiadas, P. Westermann and B. K. Ahring, *Mesophilic and thermophilic anaerobic digestion of primary and secondary sludge. Effect of pre-treatment at elevated temperature*, Water Res., 37 (2003) 4561-4572

[7] L. Appels, J. Baeyens, J. Degrève and R. Dewil, *Principles and potential of the anaerobic digestion of waste-activated sludge*, Prog. Energy Combust. Sci., 34 (2008) 755-781

[8] P. R. Gogate and A. B. Pandit, *A review of imperative technologies for wastewater treatment I: oxidation technologies at ambient conditions*, Advances in Environmental Research, 8 (2004) 501-551

[9] R. Andreozzi, V. Caprio, A. Insola and R. Marotta, *Advanced oxidation processes (AOP) for water purification and recovery*, Catal. Today, 53 (1999) 51-59

[10] P. R. Gogate and A. B. Pandit, *A review of imperative technologies for wastewater treatment II: hybrid methods*, Advances in Environmental Research, 8 (2004) 553-597

[11] S. H. Lin and H. G. Leu, *Operating characteristics and kinetic studies of surfactant wastewater treatment by Fenton oxidation*, Water Res., 33 (1999) 1735-1741

[12] Y. Samet, E. Hmani and R. Abdelhédi, *Fenton and solar photo-Fenton processes for the removal of chlorpyrifos insecticide in wastewater*, Water Sa, 38 (2012) 537-542

[13] H. Choi, E. Stathatos and D. D. Dionysiou, *Photocatalytic TiO2 films and membranes for the development of efficient wastewater treatment and reuse systems*, Desalination, 202 (2007) 199-206

[14] A. E. Segneanu, C. Orbeci, C. Lazau, P. Sfirloaga, P. Vlazan, C. Bandas and I. Grozescu, *Waste water treatment methods*, InTech Publishing, 2013.

[15] M. Luan, G. Jing, Y. Piao, D. Liu and L. Jin, *Treatment of refractory organic pollutants in industrial wastewater by wet air oxidation*, Arabian Journal of Chemistry, (2012)

[16] K.-H. Kim and S.-K. Ihm, *Heterogeneous catalytic wet air oxidation of refractory organic pollutants in industrial wastewaters: a review*, J. Hazard. Mater., 186 (2011) 16-34

[17] G. Chen, *Electrochemical technologies in wastewater treatment*, Sep. Purif. Technol., 38 (2004) 11-41

[18] R. Das, *Application Photocatalysis for Treatment of Industrial Waste Water—A Short Review*, Open Access Library Journal, 1 (2014) 1

[19] G. W. Crabtree and N. S. Lewis, *Solar energy conversion*, Physics today, 60 (2007) 37-42

[20] T. M. Razykov, C. S. Ferekides, D. Morel, E. Stefanakos, H. S. Ullal and H. M. Upadhyaya, *Solar photovoltaic electricity: Current status and future prospects*, Solar Energy, 85 (2011) 1580-1608

[21] A. Fragaki and T. Markvart, *Stand-alone PV system design: Results using a new sizing approach*, Renewable Energy, 33 (2008) 162-167

[22] M. Meinhardt and G. Cramer, *Past, present and future of grid connected photovoltaic- and hybrid-power-systems*, Power Engineering Society Summer Meeting, 2000. IEEE, 2 (2000) 1283-1288

[23] A. Goetzberger, J. Luther and G. Willeke, *Solar cells: past, present, future*, Sol. Energy Mater. Sol. Cells, 74 (2002) 1-11

[24] A. Goetzberger, C. Hebling and H.-W. Schock, *Photovoltaic materials, history, status and outlook*, Materials Science and Engineering: R: Reports, 40 (2003) 1-46

[25] A. Goetzberger and C. Hebling, *Photovoltaic materials, past, present, future*, Sol. Energy Mater. Sol. Cells, 62 (2000) 1-19

[26] F. Dimroth, T. N. D. Tibbits, M. Niemeyer, F. Predan, P. Beutel, C. Karcher, E. Oliva, G. Siefer, D. Lackner, P. Fu, x00Df, Kailuweit, A. W. Bett, R. Krause, C. Drazek, E. Guiot, J. Wasselin, A. Tauzin and T. Signamarcheix, *Four-Junction Wafer-Bonded Concentrator Solar Cells*, IEEE Journal of Photovoltaics, 6 (2016) 343-349

[27] Fraunhofer, New world record for solar cell efficiency at 46%. French-German cooperation confirms competitive advantage of European photovoltaic industry, Last Update: 01 December 2014, Last access: 15 November 2016

[28] K. Tanabe, *A review of ultrahigh efficiency III-V semiconductor compound solar cells: multijunction tandem, lower dimensional, photonic up/down conversion and plasmonic nanometallic structures*, Energies, 2 (2009) 504-530

[29] M. F. Huq, Z. I. Chowdhury, M. Hasan and Z. H. Mahmood, *The efficiency of the single junction and multijunction In x Ga 1-x N solar cell using AMPS-1D simulator*, Journal of Bangladesh Academy of Sciences, 37 (2013) 65-72

[30] M. S. Leite, R. L. Woo, J. N. Munday, W. D. Hong, S. Mesropian, D. C. Law and H. A. Atwater, *Towards an optimized all lattice-matched InAlAs/InGaAsP/InGaAs multijunction solar cell with efficiency> 50%*, Appl. Phys. Lett., 102 (2013) 033901

[31] R. R. King, D. C. Law, K. M. Edmondson, C. M. Fetzer, G. S. Kinsey, H. Yoon, D. D. Krut, J. H. Ermer, R. A. Sherif and N. H. Karam, *Advances in high-efficiency III-V multijunction solar cells*, Advances in OptoElectronics, 2007 (2007)

[32] H. Yoon, M. Haddad, S. Mesropian, J. Yen, K. Edmondson, D. Law, R. R. King, D. Bhusari, A. Boca and N. H. Karam, *Progress of inverted metamorphic III–V solar cell development at Spectrolab*, Photovoltaic Specialists Conference, 2008. PVSC'08. 33rd IEEE, (2008) 1-6

[33] D. Bhusari, D. Law, R. Woo, J. Boisvert, S. Mesropian, D. Larrabee, W. Hong and N. Karam, *Direct semiconductor bonding technology (SBT) for high efficiency III-V multi-junction solar cells*, Photovoltaic Specialists Conference (PVSC), 2011 37th IEEE, (2011) 001937-001940

[34] O. Jani, I. Ferguson, C. Honsberg and S. Kurtz, *Design and characterization of GaN/ InGaN solar cells*, Appl. Phys. Lett., 91 (2007) 132117

[35] L. Sang, M. Liao, N. Ikeda, Y. Koide and M. Sumiya, *Enhanced performance of InGaN solar cell by using a super-thin AlN interlayer*, Appl. Phys. Lett., 99 (2011) 161109

[36] H. Helmers, M. Schachtner and A. W. Bett, *Influence of temperature and irradiance on triple-junction solar subcells*, Sol. Energy Mater. Sol. Cells, 116 (2013) 144-152

[37] H. Helmers, A. W. Bett, J. Parisi and C. Agert, *Modeling of concentrating photovoltaic and thermal systems*, Progress in Photovoltaics: Research and Applications, 22 (2014) 427-439

[38] R. Pässler, *Parameter sets due to fittings of the temperature dependencies of fundamental bandgaps in semiconductors*, physica status solidi(b), 216 (1999) 975-1007

[39] I. Ganesh, *Conversion of carbon dioxide to methanol using solar energy-a brief review*, Materials Sciences and Applications, 2 (2011) 1407

[40] G. Ercolino, M. A. Ashraf, V. Specchia and S. Specchia, *Performance evaluation and comparison of fuel processors integrated with PEM fuel cell based on steam or autothermal reforming and on CO preferential oxidation or selective methanation*, Applied Energy, 143 (2015) 138-153

[41] C. White, R. Steeper and A. Lutz, *The hydrogen-fueled internal combustion engine: a technical review*, Int. J. Hydrogen Energy, 31 (2006) 1292-1305

[42] J. R. Bolton, *Solar photoproduction of hydrogen: a review*, Solar energy, 57 (1996) 37-50

[43] S. A. Kalogirou, *Solar thermal collectors and applications*, Prog. Energy Combust. Sci., 30 (2004) 231-295

[44] D. Mills, *Advances in solar thermal electricity technology*, Solar Energy, 76 (2004) 19-31

[45] F. Barbir, *PEM electrolysis for production of hydrogen from renewable energy sources*, Solar energy, 78 (2005) 661-669

[46] S. Grigoriev, V. Porembsky and V. Fateev, *Pure hydrogen production by PEM electrolysis for hydrogen energy*, Int. J. Hydrogen Energy, 31 (2006) 171-175

[47] S. Hernández, M. Tortello, A. Sacco, M. Quaglio, T. Meyer, S. Bianco, G. Saracco, C. F. Pirri and E. Tresso, *New transparent laser-drilled fluorine-doped tin oxide covered quartz electrodes for photo-electrochemical water splitting*, Electrochim. Acta, 131 (2014) 184-194

[48] A. Lamberti, A. Sacco, S. Bianco, M. Quaglio, D. Manfredi and C. F. Pirri, *Enhancement of electron lifetime in dye-sensitized solar cells using anodically grown TiO2 nanotube/nanoparticle composite photoanodes*, Microelectron. Eng., 111 (2013) 137-142

[49] T. K. Mallick, P. C. Eames and B. Norton, *Using air flow to alleviate temperature elevation in solar cells within asymmetric compound parabolic concentrators*, Solar Energy, 81 (2007) 173-184

[50] M. Armandi, D. Drago, M. Pagani, B. Bonelli and M. Santarelli, *Direct coupling of H 2 production through a high pressure PEM electrolyzer and its storage by physisorption on microporous materials*, Int. J. Hydrogen Energy, 37 (2012) 1292-1300

[51] P. Millet, *GenHyPEM: an EC-supported STREP program on high pressure PEM water electrolysis*, (2006)

[52] F. Marangio, M. Pagani, M. Santarelli and M. Cali, *Concept of a high pressure PEM electrolyser prototype*, Int. J. Hydrogen Energy, 36 (2011) 7807-7815

[53] F. Dimroth, G. Peharz, U. Wittstadt, B. Hacker and A. Bett, *Hydrogen production in a PV concentrator using III-V multi-junction solar cells*, 2006 IEEE 4th World Conference on Photovoltaic Energy Conference, 1 (2006) 640-643

[54] G. Peharz, F. Dimroth and U. Wittstadt, *Solar hydrogen production by water splitting with a conversion efficiency of 18%*, Int. J. Hydrogen Energy, 32 (2007) 3248-3252

[55] M. González Montes, J. C. Martínez-Antón, D. Vázquez Moliní, A. Á. Fernandez-Balbuena and E. Bernabeu, *Achromatic Fresnel lens with improved efficiency for PV systems*, International Journal of Photoenergy, 2014 (2014)

[56] J. Levec and A. Pintar, *Catalytic wet-air oxidation processes: A review*, Catal. Today, 124 (2007) 172-184

[57] S. Chaliha and K. G. Bhattacharyya, *Catalytic wet oxidation of phenol and its derivatives with Fe 2 O 3 and MnO 2*, Indian J. Chem. Technol., 13 (2006) 499-504

[58] F. Stüber, J. Font, A. Eftaxias, M. Paradowska, M. E. Suarez, A. Fortuny, C. Bengoa and A. Fabregat, *Chemical Wet Oxidation for the Abatement of Refractory Non-Biodegradable Organic Wastewater Pollutants*, Process Safety and Environmental Protection, 83 (2005) 371-380

[59] F. P. Miller, A. F. Vandome and J. McBrewster, *Air Mass (Solar Energy)*, International Book Marketing Service Limited, 2011.

[60] E. U. J. R. Center, http://re.jrc.ec.europa.eu/pvgis/apps4/pvest.php, Last update: 10 February 2012 Last access: 20 October 2016

[61] U. S. N. O. website, http://aa.usno.navy.mil/cgi-bin/aa_durtablew.pl?form=2&year=2016&task=-1&place=north+pole&lon_sign=1&lon_deg=0&lon_min=0&lat_sign=1&lat_deg=37&lat_min=00&tz=&tz_sign=-1, Last update: 29 July 2015, Last access: 20 October 2016

[62] J. Cotton, J. Bingert, P. Dunn, D. Butt and R. Margevicius, *Titanium-tantalum alloy development*, Los Alamos National Lab., NM (United States), (1996)

[63] K. Araki, H. Uozumi, T. Egami, M. Hiramatsu, Y. Miyazaki, Y. Kemmoku, A. Akisawa, N. Ekins- Daukes, H. Lee and M. Yamaguchi, *Development of concentrator modules with dome- shaped Fresnel lenses and triple- junction concentrator cells*, Progress in Photovoltaics: Research and Applications, 13 (2005) 513-527

[64] E. Metcalf, H. P. Eddy and G. Tchobanoglous, *Wastewater engineering: treatment, disposal and reuse*, McGraw-Hill, New York, (1991)

[65] G. Luo and I. Angelidaki, *Integrated biogas upgrading and hydrogen utilization in an anaerobic reactor containing enriched hydrogenotrophic methanogenic culture*, Biotechnol. Bioeng., 109 (2012) 2729-2736

[66] I. Bassani, P. G. Kougias, L. Treu and I. Angelidaki, *Biogas upgrading via hydrogenotrophic methanogenesis in two-stage continuous stirred tank reactors at mesophilic and thermophilic conditions*, Environmental science & technology, 49 (2015) 12585-12593

[67] X. Chen, *Batch and Continuous Anaerobic Digestion of Different Organic Waste Streams*, ProQuest, 2008.

[68] R. T. Romano, *Anaerobic digestion of onion processing waste and biochemical methods for enhanced anaerobic digestion*, ProQuest, 2008.

[69] Y. J. Chan, M. F. Chong, C. L. Law and D. Hassell, *A review on anaerobic–aerobic treatment of industrial and municipal wastewater*, Chem. Eng. J., 155 (2009) 1-18

[70] J. Ariunbaatar, A. Panico, G. Esposito, F. Pirozzi and P. N. Lens, *Pretreatment methods to enhance anaerobic digestion of organic solid waste*, Applied Energy, 123 (2014) 143-156

[71] G. D. Zupančič and M. Roš, *Heat and energy requirements in thermophilic anaerobic sludge digestion*, Renewable Energy, 28 (2003) 2255-2267

[72] T. M. LaPara and J. E. Alleman, *Thermophilic aerobic biological wastewater treatment*, Water Res., 33 (1999) 895-908

[73] H. M. Pinheiro, E. Touraud and O. Thomas, *Aromatic amines from azo dye reduction: status review with emphasis on direct UV spectrophotometric detection in textile industry wastewaters*, Dyes and Pigments, 61 (2004) 121-139

[74] A. L. Buikema, M. J. McGinniss and J. Cairns, *Phenolics in aquatic ecosystems: A selected review of recent literature*, Marine Environmental Research, 2 (1979) 87-181

[75] R. Maciel, G. L. Sant'Anna Jr and M. Dezotti, *Phenol removal from high salinity effluents using Fenton's reagent and photo-Fenton reactions*, Chemosphere, 57 (2004) 711-719

[76] K. Turhan and S. Uzman, *Removal of phenol from water using ozone*, Desalination, 229 (2008) 257-263

[77] F. Martínez, J. A. Melero, J. Á. Botas, M. I. Pariente and R. Molina, *Treatment of Phenolic Effluents by Catalytic Wet Hydrogen Peroxide Oxidation over Fe2O3/SBA-15 Extruded Catalyst in a Fixed-Bed Reactor*, Industrial & Engineering Chemistry Research, 46 (2007) 4396-4405

[78] G. Busca, S. Berardinelli, C. Resini and L. Arrighi, *Technologies for the removal of phenol from fluid streams: A short review of recent developments*, J. Hazard. Mater., 160 (2008) 265-288

[79] W. Yun-Hai, C. Qing-Yun, L. Guo and L. Xiang-Lin, *Anodic Materials with High Energy Efficiency for Electrochemical Oxidation of Toxic Organics in Waste Water*, INTECH Open Access Publisher, 2012.

[80] Á. Anglada, A. Urtiaga and I. Ortiz, *Contributions of electrochemical oxidation to waste-water treatment: fundamentals and review of applications*, Journal of Chemical Technology & Biotechnology, 84 (2009) 1747-1755

[81] C. Comninellis and C. Pulgarin, *Anodic oxidation of phenol for waste water treatment*, J. Appl. Electrochem., 21 703-708

[82] D. Fino, C. C. Jara, G. Saracco, V. Specchia and P. Spinelli, *Deactivation and regeneration of Pt anodes for the electro-oxidation of phenol*, J. Appl. Electrochem., 35 405-411

[83] J. Xavier, E. Ortega, J. Ferreira, A. Bernardes and V. Pérez-Herranz, *An electrochemical study of phenol oxidation in acidic medium*, Int. J. Electrochem. Sci, 6 (2011) 622-636

[84] M. Li, C. Feng, W. Hu, Z. Zhang and N. Sugiura, *Electrochemical degradation of phenol using electrodes of Ti/RuO2–Pt and Ti/IrO2–Pt*, J. Hazard. Mater., 162 (2009) 455-462

[85] C. C. Jara, D. Fino, G. Saracco and V. Specchia, *Three-compartment electro-oxidation reactor for bio-refractory organics degradation*, Chem. Eng. Sci., 62 (2007) 5644-5647

[86] I. D. d. Santos, J. C. Afonso and A. J. B. Dutra, *Electrooxidation of Phenol on a Ti/RuO2 anode: effect of some electrolysis parameters*, Journal of the Brazilian Chemical Society, 22 (2011) 875-883

[87] S. Di Giulio, C. Carlesi Jara, D. Fino, G. Saracco, V. Specchia and P. Spinelli, *Fate of Organic Nitrogen during Electrooxidation over Conductive Metal Oxide Anodes*, Industrial & Engineering Chemistry Research, 46 (2007) 6783-6787

[88] A. M. Polcaro, S. Palmas, F. Renoldi and M. Mascia, *On the performance of Ti/SnO2 and Ti/PbO2 anodesin electrochemical degradation of 2-chlorophenolfor wastewater treatment*, J. Appl. Electrochem., 29 147-151

[89] X. Chen, F. Gao and G. Chen, *Comparison of Ti/BDD and Ti/SnO2–Sb2O5 electrodes for pollutant oxidation*, J. Appl. Electrochem., 35 185-191

[90] J. D. Rodgers, W. Jedral and N. J. Bunce, *Electrochemical Oxidation of Chlorinated Phenols*, Environmental Science & Technology, 33 (1999) 1453-1457

[91] R. A. de Souza and L. M. Ruotolo, *Phenol electrooxidation in different supporting electrolytes using borondoped diamond anodes*, International Journal of Electrochemical Science, 8 (2013) 643-657

[92] M. Cataldo Hernández, N. Russo, M. Panizza, P. Spinelli and D. Fino, *Electrochemical oxidation of urea in aqueous solutions using a boron-doped thin-film diamond electrode*, Diamond Relat. Mater., 44 (2014) 109-116

[93] Y.-q. Wang, B. Gu and W.-l. Xu, *Electro-catalytic degradation of phenol on several metal-oxide anodes*, J. Hazard. Mater., 162 (2009) 1159-1164

[94] G. Sotgiu, M. Foderà, F. Marra and E. Petrucci, *Production and characterization of manganese oxide-based electrodes for anodic oxidation of organic compounds*, Chemical Engineering Transactions, 41 (2014) 115-120

[95] G. Sotgiu, L. Tortora and E. Petrucci, *Influence of surface roughening of Titanium substrate in the electrochemical activity of Manganese oxide thin film electrode in anodic oxidation of dye-containing solutions*, J. Appl. Electrochem., 45 (2015) 787-797

[96] G. V. Sokol'skii, S. V. Ivanova, N. D. Ivanova, E. I. Boldyrev, T. F. Lobunets and T. V. Tomila, *Doped manganese (IV) oxide in processes of destruction and removal of organic compounds from aqueous solutions*, Journal of Water Chemistry and Technology, 34 (2012) 227-233

[97] W.-c. Peng, S.-b. Wang and X.-y. Li, *Shape-controlled synthesis of one-dimensional α-MnO2 nanocrystals for organic detection and pollutant degradation*, Sep. Purif. Technol., 163 (2016) 15-22

[98] M. Nakayama, M. Shamoto and A. Kamimura, *Surfactant-Induced Electrodeposition of Layered Manganese Oxide with Large Interlayer Space for Catalytic Oxidation of Phenol*, Chem. Mater., 22 (2010) 5887-5894

[99] S.-W. Lee, C.-W. Lee, S.-B. Yoon, M.-S. Kim, J. H. Jeong, K.-W. Nam, K. C. Roh and K.-B. Kim, *Superior electrochemical properties of manganese dioxide/reduced*

graphene oxide nanocomposites as anode materials for high-performance lithium ion batteries, J. Power Sources, 312 (2016) 207-215

[100] M.-S. Wu, P.-C. J. Chiang, J.-T. Lee and J.-C. Lin, *Synthesis of manganese oxide electrodes with interconnected nanowire structure as an anode material for rechargeable lithium ion batteries*, The Journal of Physical Chemistry B, 109 (2005) 23279-23284

[101] M. Sawangphruk, P. Srimuk, P. Chiochan, A. Krittayavathananon, S. Luanwuthi and J. Limtrakul, *High-performance supercapacitor of manganese oxide/reduced graphene oxide nanocomposite coated on flexible carbon fiber paper*, Carbon, 60 (2013) 109-116

[102] J. Jiang and A. Kucernak, *Electrochemical supercapacitor material based on manganese oxide: preparation and characterization*, Electrochim. Acta, 47 (2002) 2381-2386

[103] J. Wei, M. Cheong, N. Nagarajan and I. Zhitomirsky, *Cathodic electrodeposition of manganese oxides for electrochemical supercapacitors*, ECS Transactions, 3 (2007) 1-9

[104] C. Ottone, M. Armandi, S. Hernández, S. Bensaid, M. Fontana, C. F. Pirri, G. Saracco, E. Garrone and B. Bonelli, *Effect of surface area on the rate of photocatalytic water oxidation as promoted by different manganese oxides*, Chem. Eng. J., 278 (2015) 36-45

[105] F. Zhou, A. Izgorodin, R. K. Hocking, L. Spiccia and D. R. MacFarlane, *Electrodeposited MnOx Films from Ionic Liquid for Electrocatalytic Water Oxidation*, Advanced Energy Materials, 2 (2012) 1013-1021

[106] M. S. El-Deab, M. I. Awad, A. M. Mohammad and T. Ohsaka, *Enhanced water electrolysis: electrocatalytic generation of oxygen gas at manganese oxide nanorods modified electrodes*, Electrochem. Commun., 9 (2007) 2082-2087

[107] K. Izumiya, E. Akiyama, H. Habazaki, N. Kumagai, A. Kawashima and K. Hashimoto, *Anodically deposited manganese oxide and manganese–tungsten oxide electrodes for oxygen evolution from seawater*, Electrochim. Acta, 43 (1998) 3303-3312

[108] M. Seong, S. Kim, H. Yoo and J. Choi, *Doping of anodic nanotubular TiO 2 electrodes with MnO 2 for use as catalysts in water oxidation*, Catal. Today, 260 (2016) 135-139

[109] A. Bergmann, I. Zaharieva, H. Dau and P. Strasser, *Electrochemical water splitting by layered and 3D cross-linked manganese oxides: correlating structural motifs and catalytic activity*, Energy & Environmental Science, 6 (2013) 2745-2755

[110] Y. Chen, L. Hong, H. Xue, W. Han, L. Wang, X. Sun and J. Li, *Preparation and characterization of TiO 2-NTs/SnO 2-Sb electrodes by electrodeposition*, J. Electroanal. Chem., 648 (2010) 119-127

[111] Q. Wang, T. Jin, Z. Hu, L. Zhou and M. Zhou, *TiO2-NTs/SnO2-Sb anode for efficient electrocatalytic degradation of organic pollutants: Effect of TiO2-NTs architecture*, Sep. Purif. Technol., 102 (2013) 180-186

[112] Y. Chen, H. Li, W. Liu, Y. Tu, Y. Zhang, W. Han and L. Wang, *Electrochemical degradation of nitrobenzene by anodic oxidation on the constructed TiO 2-NTs/SnO 2-Sb/PbO 2 electrode*, Chemosphere, 113 (2014) 48-55

[113] G. Zhao, X. Cui, M. Liu, P. Li, Y. Zhang, T. Cao, H. Li, Y. Lei, L. Liu and D. Li, *Electrochemical Degradation of Refractory Pollutant Using a Novel Microstructured TiO2 Nanotubes/Sb-Doped SnO2 Electrode*, Environmental Science & Technology, 43 (2009) 1480-1486

[114] X. Cui, G. Zhao, Y. Lei, H. Li, P. Li and M. Liu, *Novel vertically aligned TiO2 nanotubes embedded with Sb-doped SnO2 electrode with high oxygen evolution potential and long service time*, Mater. Chem. Phys., 113 (2009) 314-321

[115] D. Pugliese, A. Lamberti, F. Bella, A. Sacco, S. Bianco and E. Tresso, *TiO2 nanotubes as flexible photoanode for back-illuminated dye-sensitized solar cells with hemi-squaraine organic dye and iodine-free transparent electrolyte*, Org. Electron., 15 (2014) 3715-3722

[116] S. Hernández, D. Hidalgo, A. Sacco, A. Chiodoni, A. Lamberti, V. Cauda, E. Tresso and G. Saracco, *Comparison of photocatalytic and transport properties of TiO 2 and ZnO nanostructures for solar-driven water splitting*, PCCP, 17 (2015) 7775-7786

[117] S. Hernández, C. Ottone, S. Varetti, M. Fontana, D. Pugliese, G. Saracco, B. Bonelli and M. Armandi, *Spin-Coated vs. Electrodeposited Mn Oxide Films as Water Oxidation Catalysts*, Materials, 9 (2016) 296

[118] G. F. Ortiz, I. Hanzu, T. Djenizian, P. Lavela, J. L. Tirado and P. Knauth, *Alternative Li-Ion Battery Electrode Based on Self-Organized Titania Nanotubes*, Chem. Mater., 21 (2009) 63-67

[119] A. Lamberti, N. Garino, A. Sacco, S. Bianco, A. Chiodoni and C. Gerbaldi, *As-grown vertically aligned amorphous TiO2 nanotube arrays as high-rate Li-based micro-battery anodes with improved long-term performance*, Electrochim. Acta, 151 (2015) 222-229

[120] X. Lu, G. Wang, T. Zhai, M. Yu, J. Gan, Y. Tong and Y. Li, *Hydrogenated TiO2 Nanotube Arrays for Supercapacitors*, Nano Lett., 12 (2012) 1690-1696

[121] S. Yoriya, H. E. Prakasam, O. K. Varghese, K. Shankar, M. Paulose, G. K. Mor, T. J. Latempa and C. A. Grimes, *Initial Studies on the Hydrogen Gas Sensing Properties of Highly-Ordered High Aspect Ratio TiO2 Nanotube-Arrays 20 m to 222 m in Length*, Sensor Letters, 4 (2006) 334-339

[122] A. Lamberti, A. Virga, A. Chiado, A. Chiodoni, K. Bejtka, P. Rivolo and F. Giorgis, *Ultrasensitive Ag-coated TiO2 nanotube arrays for flexible SERS-based optofluidic devices*, Journal of Materials Chemistry C, 3 (2015) 6868-6875

[123] P. Roy, S. Berger and P. Schmuki, *TiO2 Nanotubes: Synthesis and Applications*, Angew. Chem. Int. Ed., 50 (2011) 2904-2939

[124] A. Lamberti, A. Chiodoni, N. Shahzad, S. Bianco, M. Quaglio and C. F. Pirri, *Ultrafast room-temperature crystallization of TiO2 nanotubes exploiting water-vapor treatment*, Scientific Reports, 5 (2015)

[125] A. Ramírez, P. Hillebrand, D. Stellmach, M. M. May, P. Bogdanoff and S. Fiechter, *Evaluation of MnOx, Mn2O3, and Mn3O4 Electrodeposited Films for the Oxygen Evolution Reaction of Water*, The Journal of Physical Chemistry C, 118 (2014) 14073-14081

[126] A. Ramírez, D. Friedrich, M. Kunst and S. Fiechter, *Charge carrier kinetics in MnOx, Mn2O3 and Mn3O4 films for water oxidation*, Chem. Phys. Lett., 568–569 (2013) 157-160

[127] E. Gemelli and N. H. A. Camargo, *Oxidation kinetics of commercially pure titanium*, Matéria (Rio de Janeiro), 12 (2007) 525-531

[128] M. N. Muti, A. Dzilal and J. Dennis, *Effects of Synthesis Parameters on the structure of titania nanotubes*, Journal of Engineering Science and Technology, 3 (2008) 163-171

[129] Z. Lockman, C. H. Kit and S. Sreekantan, *EFFECT OF ANNEALING TEMPERATURE ON THE ANATASE AND RUTILE TiO2 NANOTUBES FORMATION*, (2009)

[130] C. A. Grimes and G. K. Mor, TiO2 Nanotube Arrays: Synthesis, Properties, and Applications, Springer US Boston, MA, 2009, pp. 67-113.

[131] D. Siva Rama Krishna and Y. Sun, *Effect of thermal oxidation conditions on tribological behaviour of titanium films on 316L stainless steel*, Surf. Coat. Technol., 198 (2005) 447-453

[132] J. Niu, X. Liu, K. Xia, L. Xu, Y. Xu, X. Fang and W. Lu, *Effect of Electrodeposition Parameters on the Morphology of Three-Dimensional Porous Copper Foams*, Int. J. Electrochem. Sci, 10 (2015) 7331-7340

[133] M. Sun, B. Lan, T. Lin, G. Cheng, F. Ye, L. Yu, X. Cheng and X. Zheng, *Controlled synthesis of nanostructured manganese oxide: crystalline evolution and catalytic activities*, CrystEngComm, 15 (2013) 7010-7018

[134] M. V. Tran, A. T. Ha and P. M. L. Le, *Nanoflake Manganese Oxide and Nickel-Manganese Oxide Synthesized by Electrodeposition for Electrochemical Capacitor*, Journal of Nanomaterials, 2015 (2015) 12

[135] Y. Feng and X. Y. Li, *Electro-catalytic oxidation of phenol on several metal-oxide electrodes in aqueous solution*, Water Res., 37 (2003) 2399-2407

[136] Y. Zheng, W. Su, S. Chen, X. Wu and X. Chen, *Ti/SnO 2–Sb 2 O 5–RuO 2/α-PbO 2/β-PbO 2 electrodes for pollutants degradation*, Chem. Eng. J., 174 (2011) 304-309

[137] E. Balko and P. Nguyen, *Iridium-tin mixed oxide anode coatings*, J. Appl. Electrochem., 21 (1991) 678-682

[138] Y. Feng, Y. Cui, B. Logan and Z. Liu, *Performance of Gd-doped Ti-based Sb-SnO 2 anodes for electrochemical destruction of phenol*, Chemosphere, 70 (2008) 1629-1636

[139] A. Taguchi, S. Inoue, S. Akamaru, M. Hara, K. Watanabe and T. Abe, *Phase transition and electrochemical capacitance of mechanically treated manganese oxides*, J. Alloys Compd., 414 (2006) 137-141

[140] S. C. Pang, M. A. Anderson and T. W. Chapman, *Novel electrode materials for thin- film ultracapacitors: comparison of electrochemical properties of sol- gel- derived and electrodeposited manganese dioxide*, J. Electrochem. Soc., 147 (2000) 444-450

[141] I. Zaharieva, P. Chernev, M. Risch, K. Klingan, M. Kohlhoff, A. Fischer and H. Dau, *Electrosynthesis, functional, and structural characterization of a water-oxidizing manganese oxide*, Energy & Environmental Science, 5 (2012) 7081-7089

[142] C. Wei, W. Ning, L. Li, C. Yanran, C. Xia, C. Quanjing and G. Lin, *Facile synthesis of manganite nanowires: phase transitions and their electrocatalysis performance*, Nanotechnology, 20 (2009) 445601

[143] G. A. M. Ali, M. M. Yusoff, Y. H. Ng, H. N. Lim and K. F. Chong, *Potentiostatic and galvanostatic electrodeposition of manganese oxide for supercapacitor application: A comparison study*, Current Applied Physics, 15 (2015) 1143-1147

[144] T. Nguyen, M. J. Carmezim, M. Boudard and M. F. Montemor, *Cathodic electrodeposition and electrochemical response of manganese oxide pseudocapacitor electrodes*, Int. J. Hydrogen Energy, 40 (2015) 16355-16364

[145] A. Biswal, B. Tripathy, T. Subbaiah, D. Meyrick, M. Ionescu and M. Minakshi, *Effect of Non-ionic Surfactants and Its Role in K Intercalation in Electrolytic Manganese Dioxide*, Metallurgical and Materials Transactions E, 1 (2014) 226-238

[146] P. M. L. Le, T. A. N. Nguyen and M. Van Tran, *Electrodeposited Manganese Oxide for Electrochemical Capacitor: Effect of Substrates on the Capacitive Behavior of Electrodes*, Meeting Abstracts, (2014) 177-177

[147] T. Takashima, K. Hashimoto and R. Nakamura, *Mechanisms of pH-Dependent Activity for Water Oxidation to Molecular Oxygen by MnO2 Electrocatalysts*, J. Am. Chem. Soc., 134 (2012) 1519-1527

[148] T. Takashima, K. Hashimoto and R. Nakamura, *Inhibition of Charge Disproportionation of MnO2 Electrocatalysts for Efficient Water Oxidation under Neutral Conditions*, J. Am. Chem. Soc., 134 (2012) 18153-18156

[149] E. Saputra, S. Muhammad, H. Sun, H. M. Ang, M. O. Tadé and S. Wang, *Different Crystallographic One-dimensional MnO2 Nanomaterials and Their Superior Performance in Catalytic Phenol Degradation*, Environmental Science & Technology, 47 (2013) 5882-5887

[150] H. Zhao, Y. Dong, P. Jiang, G. Wang, J. Zhang, K. Li and C. Feng, *An [small alpha]-MnO2 nanotube used as a novel catalyst in ozonation: performance and the mechanism*, New J. Chem., 38 (2014) 1743-1750

[151] M. Pimentel, *Oxidation of phenol and cresol by electrochemical advanced oxidation method in homogeneous medium: application to treatment of a real effluent of aeronautical industry*, Université Paris-Est, (2008)

[152] X.-y. Li, Y.-h. Cui, Y.-j. Feng, Z.-m. Xie and J.-D. Gu, *Reaction pathways and mechanisms of the electrochemical degradation of phenol on different electrodes*, Water Res., 39 (2005) 1972-1981

[153] A. Massa, S. Hernández, A. Lamberti, C. Galletti, N. Russo and D. Fino, *Electro-oxidation of phenol over electrodeposited MnOx nanostructures and the role of a TiO2 nanotubes interlayer*, Applied Catalysis B: Environmental, 203 (2017) 270-281

[154] A. R. de Andrade, P. M. Donate, P. P. Alves, C. H. Fidellis and J. F. Boodts, *Ethanol Electro‐oxidation in Ruthenium‐Oxide‐Coated Titanium Electrodes*, J. Electrochem. Soc., 145 (1998) 3839-3843

[155] M. Carmo, D. L. Fritz, J. Mergel and D. Stolten, *A comprehensive review on PEM water electrolysis*, Int. J. Hydrogen Energy, 38 (2013) 4901-4934

[156] R. Horne and G. Frysinger, *The effect of pressure on the electrical conductivity of sea water*, Journal of Geophysical Research, 68 (1963) 1967-1973

[157] F. Allebrod, C. Chatzichristodoulou and M. B. Mogensen, *Alkaline electrolysis cell at high temperature and pressure of 250 C and 42 bar*, J. Power Sources, 229 (2013) 22-31

[158] B. Correa-Lozano, C. Comninellis and A. De Battisti, *Service life of Ti/SnO2–Sb2O5 anodes*, J. Appl. Electrochem., 27 (1997) 970-974

[159] H.-y. Ding, Y.-j. Feng and J.-f. Liu, *Preparation and properties of Ti/SnO 2–Sb 2 O 5 electrodes by electrodeposition*, Mater. Lett., 61 (2007) 4920-4923

[160] D. He and S.-i. Mho, *Electrocatalytic reactions of phenolic compounds at ferric ion co-doped SnO 2: Sb 5+ electrodes*, J. Electroanal. Chem., 568 (2004) 19-27

[161] J.-t. KONG, S.-y. SHI, X.-p. ZHU and J.-r. NI, *Effect of Sb dopant amount on the structure and electrocatalytic capability of Ti/Sb-SnO 2 electrodes in the oxidation of 4-chlorophenol*, Journal of Environmental Sciences, 19 (2007) 1380-1386

[162] L. Lipp and D. Pletcher, *The preparation and characterization of tin dioxide coated titanium electrodes*, Electrochim. Acta, 42 (1997) 1091-1099

[163] C.-S. SHIN and S.-i. MHO, *Electrocatalytic Oxidation of Phenol and Its Derivatives at Sb 5+ Doped SnO 2 Electrodes*, Analytical Sciences/Supplements, 17 (2002) a65-a68

[164] H. Ma, C. Liu, J. Liao, Y. Su, X. Xue and W. Xing, *Study of ruthenium oxide catalyst for electrocatalytic performance in oxygen evolution*, J. Mol. Catal. A: Chem., 247 (2006) 7-13

[165] T. Arikawa, Y. Murakami and Y. Takasu, *Simultaneous determination of chlorine and oxygen evolving at RuO2/Ti and RuO2–TiO2/Ti anodes by differential electrochemical mass spectroscopy*, J. Appl. Electrochem., 28 (1998) 511-516

[166] V. Panic, A. Dekanski, S. Milonjic, V. B. Miskovic-Stankovic and B. Nikolic, *Activity and stability of RuO~ 2 coated titanium anodes prepared via the alkoxide route*, J. Serb. Chem. Soc., 71 (2006) 1173-1185

[167] Y. Yavuz and A. S. Koparal, *Electrochemical oxidation of phenol in a parallel plate reactor using ruthenium mixed metal oxide electrode*, J. Hazard. Mater., 136 (2006) 296-302

[168] N. D. Mu'azu and M. H. Al-Malack, *Influence of some operating parameters on electro-oxidation of phenol using boron doped diamond anode and graphite cathode*, Journal of Environmental Science and Technology, 5 (2012) 460

[169] P. D. Alves, M. Spagnol, G. Tremiliosi-Filho and A. R. d. Andrade, *Investigation of the influence of the anode composition of DSA-type electrodes on the electrocatalytic oxidation of phenol in neutral medium*, Journal of the Brazilian Chemical Society, 15 (2004) 525-533

ACKNOWLEDGEMENTS

I would like to thank my supervisors, prof. Debora Fino and prof. Nunzio Russo, for their help in living this opportunity.

I would like to thank the all the CREST group at the Politecnico di Torino for their help and support during the PhD.

A special thank goes to dott. Simelys Hernández, for her precious advices and for having helped me to improve my knowledge and for my personal growth as a researcher.

Finally, I would like to thank my parents for their support, and Giuliana for having shared with me all the emotions we lived throughout these years.